THÈSE

Pour l'obtention du titre de:

DOCTEUR DE l'UNIVERSITÉ DE LORRAINE ET
DE L' UNIVERSITÉ DE l'ACADÉMIE CHINOISE DES SCIENCES DE CHINE

Mention : Physique

Par : **Mme Ziqi ZHOU**

Optical and Electrical Properties of Two-Dimensional Materials

10/09/2021

Membres du jury :

Directeur(s) de thèse :	M. Yuan Lu	Chargé de Recherche, Université de Lorraine, FRANCE
Président de jury :	M. Henri Jaffrès	Professeur, Unité de mixte de physique CNRS/Thales, FRANCE
Rapporteurs :	Mme. Huanli Dong	Professeur ,Institute of Chemistry, Chinese Academy of Sciences, CHINE
	M. Philippe Schieffer	Professeur, Université de Rennes 1, FRANCE
Co-directeur de thèse :	M. Hervé Rinnert	Professeur -Université de Lorraine/Institut Jean Lamour- FRANCE
	M. Zhongming Wei	Professeur -Instite of semiconductors, Chinese Academy of Sciences - CHINE
Examinateur	M. Huixiong Deng	Professeur -Instite of semiconductors, Chinese Academy of Sciences - CHINE

Résumé élargi

Introduction générale:

Le 21ième siècle est une époque qui connaît une évolution technologique rapide pour laquelle le développement des matériaux est indispensable. Les technologies basées sur les semi-conducteurs traditionnels peinent aujourd'hui à suivre la loi de Moore. La recherche de nouveaux dispositifs électroniques et la conception de nouvelles architectures sont devenues nécessaires pour répondre aux besoins dans de nombreuses applications, notamment dans le domaine du numérique.

Depuis la découverte du graphène, la recherche dans le domaine des matériaux bidimensionnels (2D) est très intense en raison de leurs propriétés optiques et électriques remarquables. Récemment, les chercheurs ont exploré d'autres matériaux caractérisés par des liaisons de type van der Waals similaires au graphène et ont exploré des structures multicouches de matériaux 2D. Ces multicouches sont caractérisées par des liaisons covalentes fortes intra-couches et par des interactions de Van der Walls faibles entre les couches, conduisant ainsi à des propriétés différentes des matériaux massifs tridimensionnels. Les matériaux obtenus peuvent être isolants, semi-conducteurs ou métalliques et présenter des propriétés magnétiques particulières.

Les matériaux 2D sont utilisés dans de nombreux domaines. A titre d'exemples, ceux à caractère semi-conducteur ayant une forte mobilité des porteurs de charge sont utilisés dans les transistors à l'effet du champ, ceux à propriétés semi-métalliques permettent d'obtenir des électrodes flexibles, et ceux qui sont sensibles à la lumière peuvent être utilisés pour réaliser des photo-détecteurs.

Ce travail de thèse s'inscrit dans la recherche de nouveaux matériaux à base de structures 2D et dans l'exploration de nouvelles applications potentielles. Il se concentre plus particulièrement sur le domaine des photo-détecteurs et des émetteurs de lumière présentant une résolution en spin. Dans un premier temps, nous nous

sommes attachés à préparer une couche mince permettant d'obtenir une injection électronique à aimantation perpendiculaire dans le but de développer des diodes électroluminescentes résolues en spin (SPIN-LED), permettant l'émission de lumière polarisée circulairement. Ensuite, nous nous sommes intéressés à la détection de la polarisation de la lumière par des structures capables de générer un courant dépendant de la polarisation. Ainsi nous avons étudié le matériau GeAs, présentant un effet de dichroïsme et avons étudié l'anisotropie de la réponse sous excitation lumineuse de détecteurs de polarisation basés sur GeAs. Enfin nous nous sommes intéressés aux propriétés photo-électriques des dichalcogénures de métaux de transition.

Le manuscrit s'organise selon cinq chapitres, présentés succinctement ci-dessous.

Chapitre 1 : Développement et application des matériaux 2D.

Les matériaux 2D trouvent des applications différentes selon leurs propriétés exploitées. Par exemple, la nature semi-métallique du graphène lui permet de servir comme électrodes transparentes pour les jonctions PN dans les cellules solaires, alors que sa haute mobilité lui permet d'être utilisé dans les circuits intégrés de haute fréquence. Néanmoins, sa structure de bande caractérisée par sa bande interdite de valeur nulle limite son application dans le domaine des semi-conducteurs principalement pour les transistors à l'effet du champ. En revanche, les dichalcogénures de métaux de transition (TMDC) pallient les limites du graphène. En effet la bande interdite est non seulement non nulle mais elle est aussi directe. Les différents composés présentent une gamme de valeurs de la bande interdite allant de 0,1 eV à 3 eV, permettent ainsi d'adapter le semi-conducteur 2D à la gamme de longueur d'onde recherchée. Par ailleurs, l'anisotropie intra-planaire du matériau phosphore noir (Black phosphorus - BP) peut aussi être utilisé pour préparer les détecteurs de polarisation.

La structure de différents matériaux 2D est illustrée ci-dessous. Le graphène correspond au graphite n'ayant qu'une une couche atomique. Présenté dans la figure R1.1(a), le graphène se compose d'atomes de carbone arrangés selon un réseau hexagonal, chaque atome étant relié aux 3 atomes adjacents via une liaison covalente. La distance entre

deux atomes adjacents dans le graphène est environ de 0,142 nm. Faisant l'objet de recherches intenses, d'autres matériaux proches du graphène ont été progressivement synthétisés et étudiés. Parmi eux, le nitrure de bore a la structure la plus proche de celle du graphène, aussi connus comme le « graphène blanc ». La figure R1.1(b) montre que le nombre des atomes d'azote et celui de bore sont égaux. La distance entre les atomes d'azote et de bore adjacents est de 0,25 nm alors que la distance entre les couches est 0,33 nm. C_3N_4 constitue un autre matériau semi-conducteur 2D ayant la structure du graphène, ayant attiré beaucoup d'attention. Il possède deux structures stables, la structure triazine et la structure tris-triazine. Leurs structures cristallographiques sont montrées dans les Figures R1.1(c) et (d). C_3N_4 est un matériau catalytique particulièrement utilisé dans le domaine de la photo-catalyse.

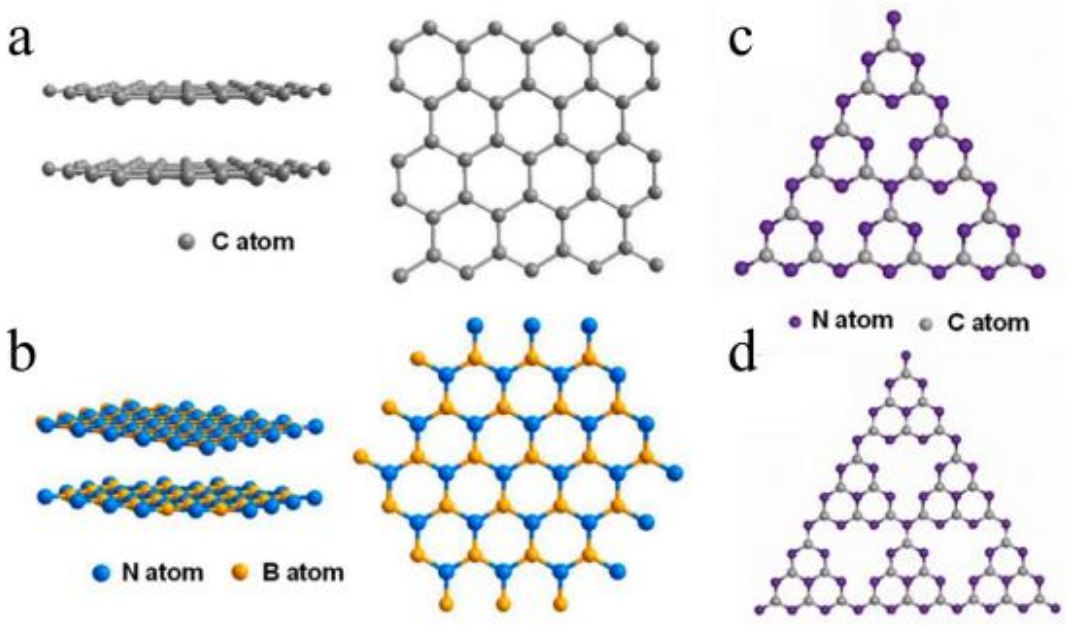

Figure R1.1. Structure cristallographique du graphène et de matériaux proches du graphène. (a) graphène (b) nitrure de bore hexagonal (c) s-triazine (d) g-C_3N_4 ayant la structure de tri-s-triazine

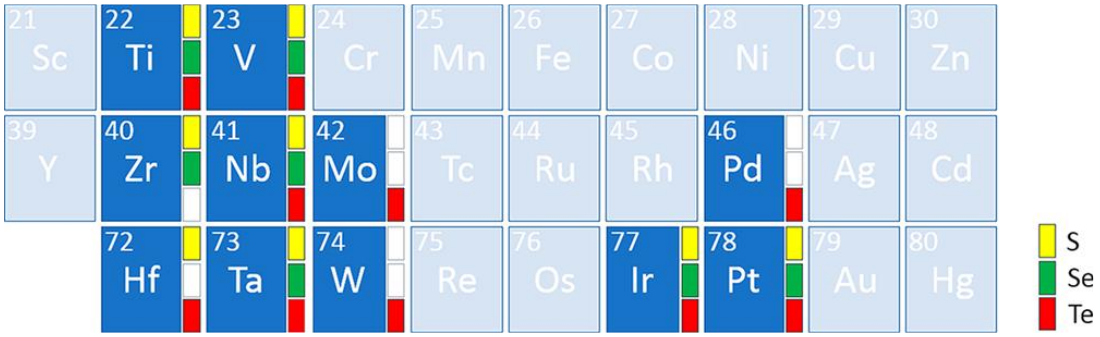

Figure R1.2. Illustration des différents dichalcogénures de métaux de transition majoritaires. Les éléments dans les carrés bleus sont les métaux de transition. Les couleurs jaunes, vertes et rouges représentent respectivement les chalcogénures S, Se et Te.

Chapitre 2 : Techniques expérimentales

Figure R2.1. Four pour croissance CVD

La Figure R2.1 montre le dispositif de dépôt par CVD (chemical vapour deposition). Cette méthode de dépôt met en jeu une réaction chimique entre les réactifs dans la phase gazeuse à haute température. Les éléments nouvellement produits dans la phase gazeuse sont progressivement condensés sur le substrat. La CVD est aujourd'hui la méthode la plus efficace pour élaborer des matériaux 2D en monocouches ou en bicouches à grande

échelle. Avec la CVD, la taille, le nombre de couches, le dopage et les défauts peuvent être contrôlés via les paramètres expérimentaux tels que la température, le temps de réaction, le flux de gaz et la pression du tube, afin de réaliser divers matériaux bidimensionnels.

La Figure R2.2 montre les étapes de structuration permettant la réalisation de contacts sur un matériau 2D. Puisque les matériaux 2D sont en général petits en taille, la technologie de la lithographie optique et électronique est utilisée pour préparer les dispositifs à mesurer

À la première étape, un substrat est recouvert par une couche photorésistante (S1813). Le pattern de fabrication préparé est transféré à la couche photorésistante via un processus de lithographie ultraviolette. Le métal est ensuite déposé sur la surface photorésistante via un processus d'évaporation. Finalement, le métal en excès est supprimé par lift off et un substrat avec les marques de métal est obtenu. La deuxième étape est le transfert du matériau 2D par processus d'exfoliation. Il peut être aussi obtenu directement par dépôt par CVD.

La troisième étape consiste à préparer les électrodes. Une couche de PMMA, sensible au faisceau d'électrons, est déposée sur le matériau 2D. Le motif des électrodes est transféré au PMMA par le processus d'exposition du faisceau électronique. La préparation des électrodes est ensuite complétée via les processus de dépôt de métal, suivi d'une nouvelle étape de lift off. Si la taille du matériau 2D est supérieure à 2 microns, la troisième étape peut aussi être réalisée par lithographie optique.

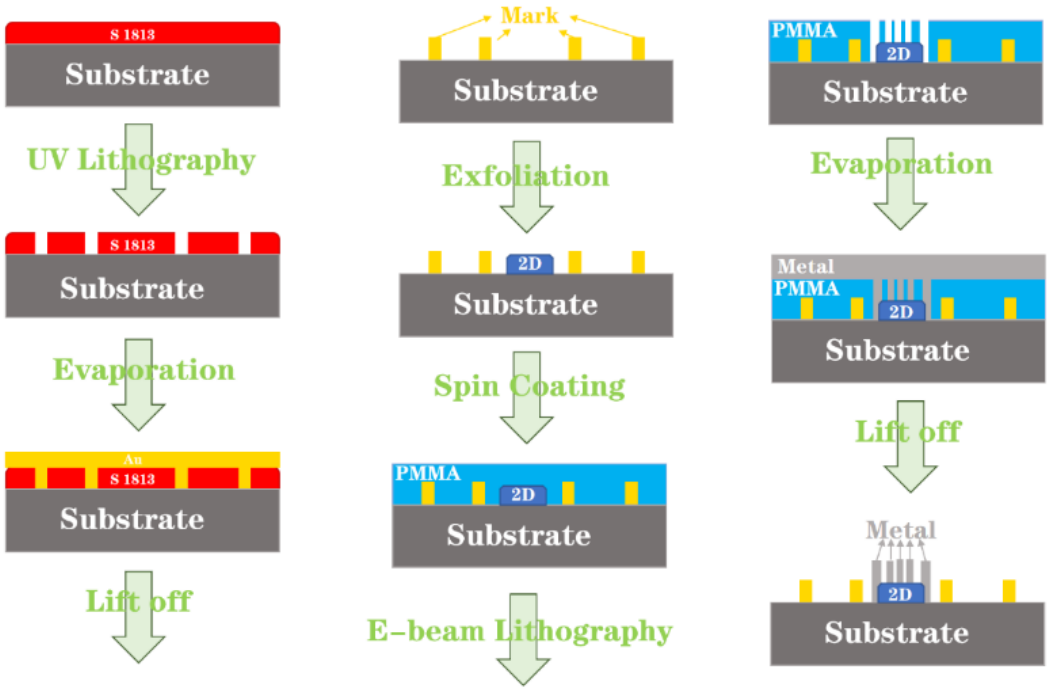

Figure R2.2 Diagramme schématique présentant les étapes de structuration permettant la réalisation de contacts sur un matériau 2D. Le substrat est $SiO_2/n^{++}Si$ de 300 nm.

Chapitre 3 : Ta/CoFeB/MgO sur monocouche de MoS_2

Obtenir un injecteur de spin à aimantation perpendiculaire ayant une haute température de Curie est un prérequis pour développer les dispositifs spin-optoélectroniques qui fonctionnent à la température ambiante sans champ magnétique appliqué.

L'objectif est de déposer une structure Ta/CoFeB/MgO ayant une aimantation perpendiculaire sur une monocouche de MoS_2 complètement couverte, en utilisant la méthode CVD. La **Figure R3.1** montre schématiquement l'empilement réalisé de SiO_2/ML MoS_2/MgO (1.5nm) /CoFeB(1.2nm)/Ta (5nm). En comparaison avec la procédure standard de l'exfoliation bidimensionnelle, la réussite de la fabrication de cette structure aura une influence significative sur le développement de tels composants. Premièrement, cela permettra la fabrication de dispositifs spin-optoélectroniques à haute densité avec lithographie ultraviolette sur un substrat large. Deuxièmement,

puisqu'il est possible d'utiliser une procédure par lithographie de type top-down pour fabriquer les dispositifs, cela préservera une interface propre entre les interfaces CoFeB/MgO et MgO/MoS_2. C'est particulièrement important pour l'injection efficace du spin.

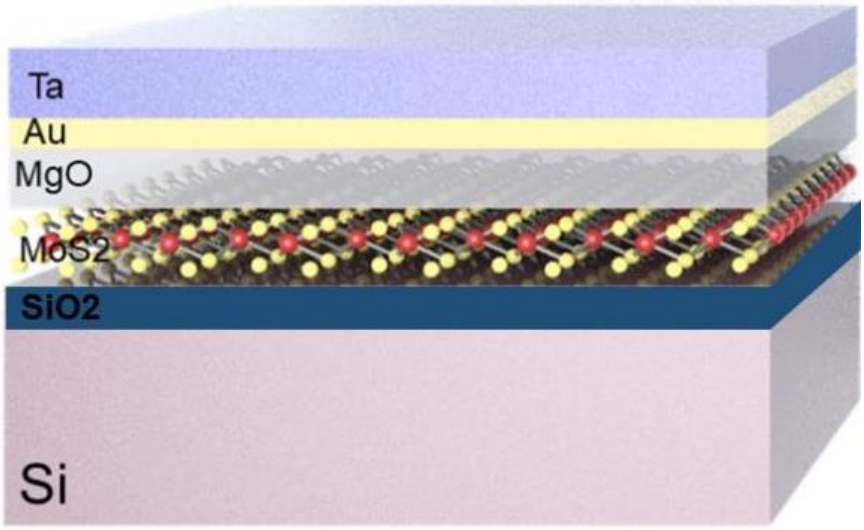

Figure R3.1 Schéma de l'empilement de MoS_2/MgO/CoFeB/Ta sur le substrat de Si/SiO_2.

Afin d'obtenir une couche hyperfine de CoFeB avec aimantation perpendiculaire sur MoS_2, on a optimisé l'épaisseur de CoFeB et la température du recuit (T_{an}). Comme le montre la **figure R3.2a**, le champ de saturation décroit rapidement et la rémanence augmente, en fonction de l'épaisseur de CoFeB allant de 1 nm à 1,2 nm. Avec une épaisseur dépassant 1,2 nm, la couche de CoFeB forme un film continu ferromagnétique.

Le contrôle de la température de recuit, T_{an}, est important pour obtenir une meilleure aimantation. La **figure R3.2b** présente la comparaison des courbes d'aimantation hors du plan pour l'échantillon CoFeB ayant l'épaisseur de 1,2 nm et recuit à différentes températures. La température optimale de recuit se trouve à environ 300 ºC.

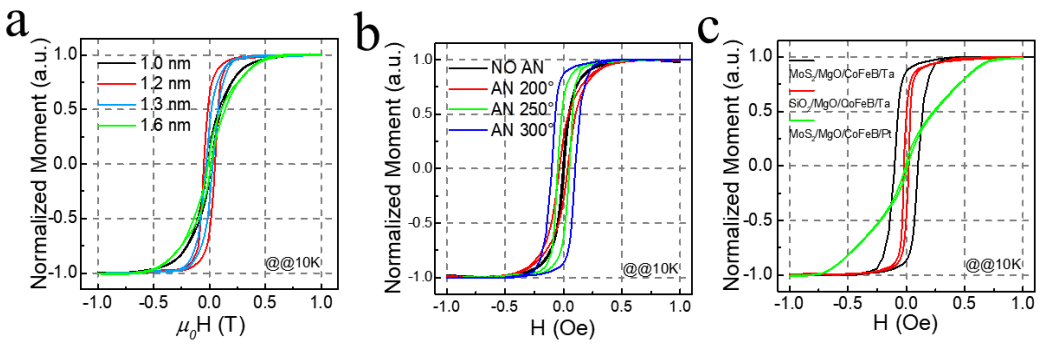

Figure R3.2 (a) Courbes d'aimantation hors du plan des échantillons de CoFeB avec différentes épaisseurs et recuits à T_{an} = 250 ºC, mesurées à 10K. (b) Courbes d'aimantation hors du plan des échantillons de CoFeB à l'épaisseur 1,2 nm non-recuit et recuits à différentes températures, mesuré à 10 K. (c) Comparaison des courbes d'aimantation hors du plan pour 3 échantillons : MoS_2/MgO/CoFeB/Ta, SiO_2/MgO/CoFeB/Ta et MoS_2/MgO/CoFeB/Pt. Tous les échantillons ont la même épaisseur de CoFeB et sont recuits à 300 ºC.

Afin de clarifier le rôle des couches de MoS_2 et de Ta sur l'aimantation, deux échantillons de référence additionnels ont été préparés. Les courbes d'aimantation correspondantes sont présentées dans la **figure R3.2c**. Elles révèlent que l'échantillon élaboré sur SiO_2 présente une rémanence (0,5) et une coercivité (20 mT) plus faibles, impliquant une aimantation perpendiculaire plus faible dans la couche de CoFeB. Ce qui est plus surprenant, c'est que l'échantillon couvert de Pt montre un champ de saturation fort (jusqu'à 0,7 T) avec une rémanence très faible, ce qui indique que l'aimantation de CoFeB dans ce cas est complètement dans le plan.

Les **figures R3.3** et **R3.4** montrent la structure et la caractérisation chimique des empilements de MoS_2/MgO/CoFeB/Ta et MoS_2/MgO/CoFeB/Pt. Pour caractériser la distribution des éléments chimiques, notamment aux interfaces, et afin de comprendre l'inter-diffusion liée au processus de recuit, des mesures par microscopie électronique à transmission à balayage (STEM) combinées à l'analyse par spectroscopie de perte d'énergie électronique résolue spatialement (EELS) ont été menées.

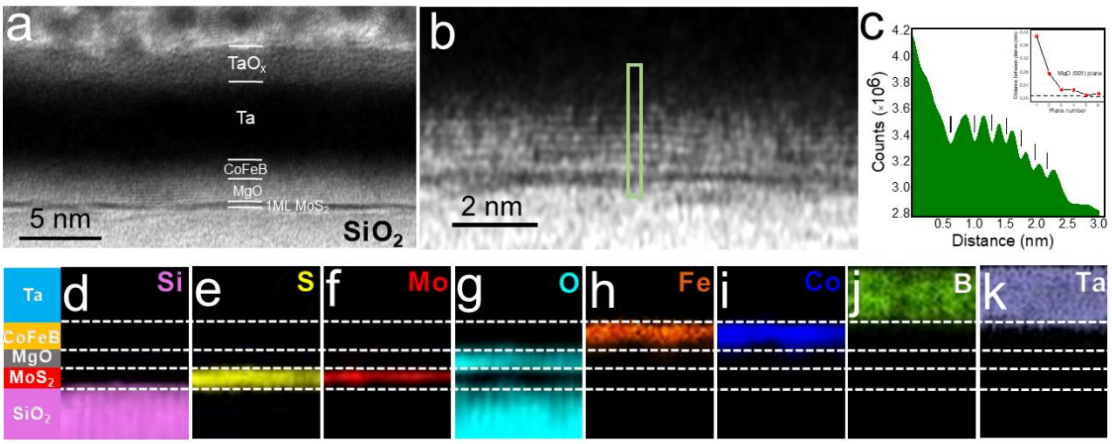

Figure R3.3. Structure et la caractérisation chimique de l'empilement de MoS_2/MgO/CoFeB/Ta. (a) La région claire de l'image HR-STEM à grande échelle montre la structure multicouche. (b) L'image élargie montre la cristallisation de MgO sur MoS_2. (c) Profil de l'intensité intégrée marqué dans la zone verte de la figure (b). L'insert montre la distance entre plans. (d-k) Cartographie des éléments chimiques d'après les spectres images obtenus en STEM EELS.

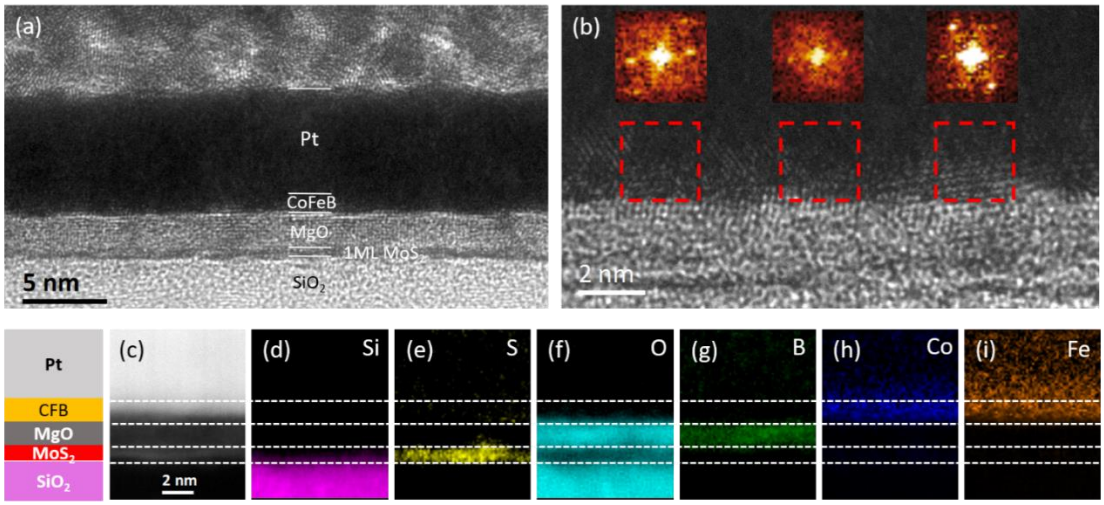

Figure R3.4 Structure et la caractérisation chimique de l'empilement de MoS_2/MgO/CoFeB/Pt. (a) La région claire de l'image HR-STEM à grande échelle montre la structure multicouche. (b) L'image élargie montre la cristallisation de CoFeB sur MoS_2. L'insert représente la transformée de Fourier du signal et montre que CoFeB est cristallisé avec un caractère polycristallin (3 orientations différentes dans les zones différentes). (d-i) Cartographie des éléments chimiques d'après les spectres images

obtenus en STEM EELS.

Sur les **figures R3.3 (g-i)**, la localisation des éléments Fe et Co prouvent l'inexistence de l'inter-diffusion des éléments de la couche FM dans la couche de MoS_2, due à la barrière de diffusion de MgO. L'épaisseur de la couche de Mo est plus mince que celle de la couche de S, ce qui est attendu en lien avec la structure de la couche de MoS_2. Par ailleurs, les atomes de B se trouvent largement diffusés dans Ta, ce qui est dû à la cristallisation de la couche de CoFeB lors de la procédure de recuit.

Les **Figures R3.4 (d-i)** montrent les cartographies des éléments déduits des spectres images obtenus par STEM-EELS. Le signal de Mo dans cet échantillon est trop faible pour obtenir une cartographie fiable de cet élément. En comparaison avec l'échantillon avec la couche de couverture de Ta, la différence la plus marquée est révélée par la cartographie de l'élément de B. Il est clairement démontré que la plupart des atomes de B diffusent dans MgO au lieu d'être absorbés par la couche de Pt après le recuit. De plus, une diffusion importante des atomes de Fe dans la couche de Pt peut être mise en évidence. Les effets combinés de la diffusion de B dans MgO et de la cristallisation désorientée de CoFeB détruisent complètement l'aimantation perpendiculaire à l'interface CoFeB/MgO, qui explique bien l'aimantation dans le plan observée dans l'échantillon couvert de Pt. Cette étude prouve aussi le rôle critique de Ta dans l'absorption des atomes de B dans la couche de CoFeB afin d'établir l'aimantation perpendiculaire.

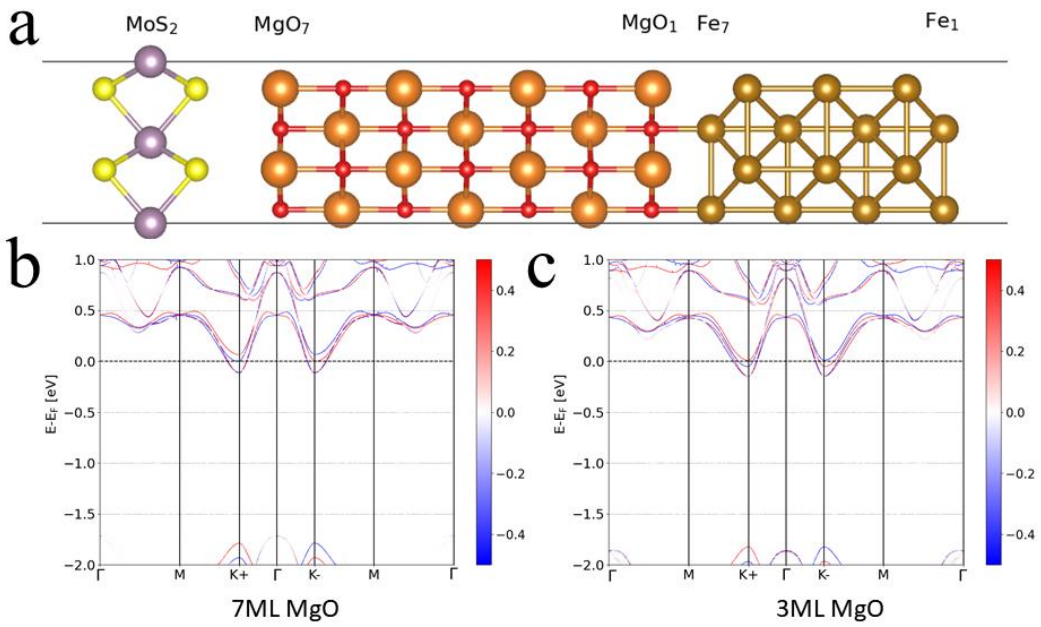

Figure R3.5 (a) Vues de la section et du haut de la cellule unitaire modélisant les multicouches de Fe/MgO/MoS_2. Contribution à la structure de bande de la multicouche provenant de la couche de MoS_2 avec (b) 7 MLs de MgO et (c) 3 MLs de MgO.

Pour mieux comprendre la potentialité de telles hétérojonctions du point de vue de l'injection de spin électrique, on a effectué les calculs ab-initio pour investiguer la structure de bande de CoFeB/MgO/MoS_2. Un caractère intéressant est que la séparation de Zeeman d'environ 10 meV est mise en évidence au point Γ pour le système de Fe/MgO(3MLs)/MoS_2, alors que la séparation est négligeable pour le système de Fe/MgO(7MLs)/MoS_2. La séparation de Zeeman est attribuée à l'effet de proximité dû à la présence du Fe ferromagnétique de l'autre côté de la couche de MgO. Cela signifie que l'épaisseur de la couche de MgO insérée joue un rôle dans les propriétés magnétiques de MoS_2.

Chapitre 4 : Photo-détection polarisée à base de GeAs

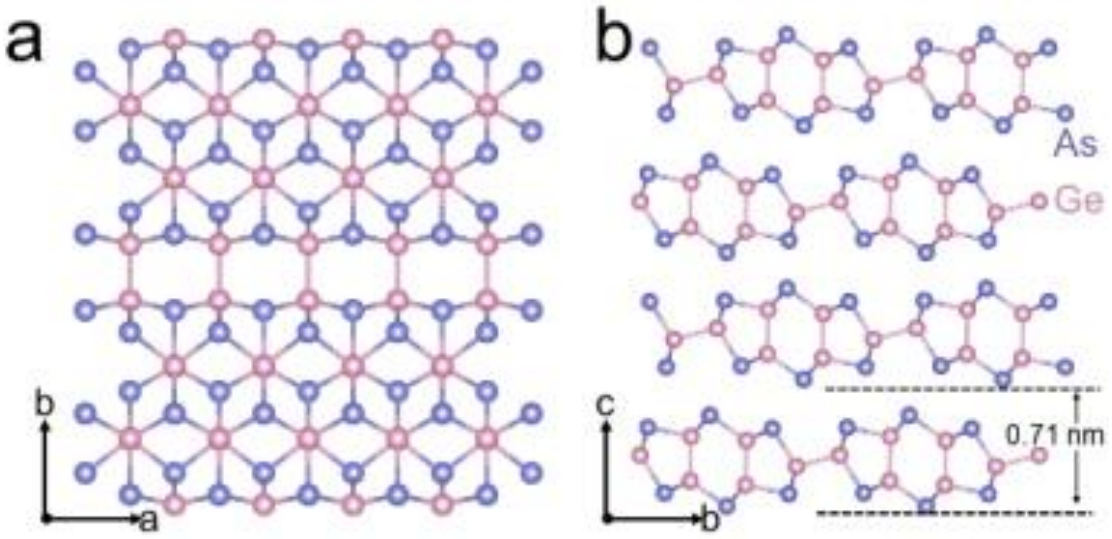

Figure R4.1. Structure cristalline de GeAs. (a) plan ab et (b) plan bc.

L'arséniure de germanium (GeAs) est un matériau récemment étudié ayant une forte anisotropie entre les couches. Il appartient au même type de structure que GaTe avec le groupe spatial C2/m. La structure de GeAs en vues sectionnelles est présentée dans la figure R4.1. Les points rosés représentent les atomes de Ge alors que les points bleus représentent les atomes d'As. Il existe 2 types de liaison Ge-Ge dans le cristal : une suivant l'axe b et l'autre suivant l'axe c, qui induit une forte anisotropie intra-planaire et une réponse optique qui dépend de la polarisation incidente.

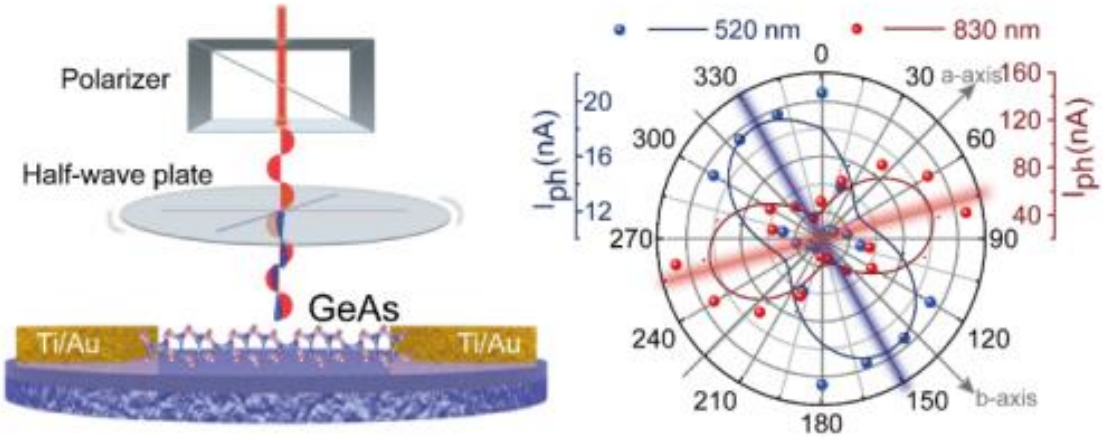

Figure R4.2 (a) Schéma du dispositif expérimental de photo-détection. (b) Photo-

courants sensibles à la polarisation tracés pour deux excitations laser à 520 nm et à 830 nm, représentés avec les coordonnées polaires. I_{ph} est le photo-courant défini comme $I_{ph} = I_{light} - I_{dark}$.

La figure R4.2(a) montre le schéma de principe du dispositif expérimental de mesure du photocourant. Le laser est polarisé linéairement puis passe par une lame demi-onde qui change la direction de la lumière linéairement polarisée. Un objectif de microscope à grande distance de travail et de grandissement x20 permet d'obtenir l'éclairement de l'échantillon de GeAs avec une résolution spatiale satisfaisante.

La Figure R4.2 (b) représente le photocourant mesuré pour différentes directions de polarisation du laser et pour deux longueurs d'onde différentes, en rouge pour le laser à 930 nm et en bleu pour le laser à 530 nm. Le dichroïsme est respectivement caractérisé par un ratio I_{pmax}/I_{pmin} de 1,49 et 4,4 à 830 nm et 530 nm. Un renversement de la direction de la photo-réponse résolue en polarisation est observé entre les deux excitations laser.

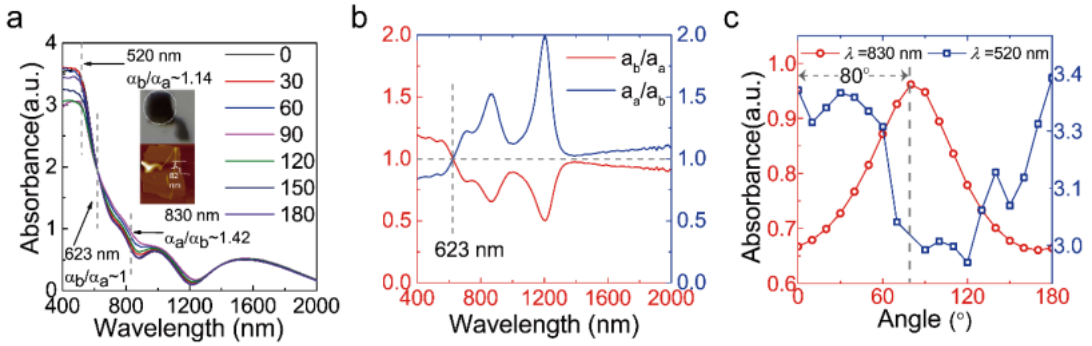

Figure R4.3. (a) Spectre expérimental d'absorption résolu en polarisation avec une échelle de 400 nm à 2000 nm, avec un pas de 30°. (b) Ratio dichroïque, αb/αa(courbe rouge) et αa/αb(courbe bleue), extrait de (a). (c) Intensité d'absorption en fonction de l'angle, pour deux longueurs d'onde, 520 nm (courbe et points bleus) et 830 nm (courbe et points rouges).

La figure R4.3 illustre la dépendance de la réponse en angle de l'absorption avec la longueur d'onde. Les résultats démontrent clairement l'existence d'une anisotropie forte de l'absorption liée à l'anisotropie intra-planaire du cristal de GeAs. Les spectres

d'absorption révèlent un dichroïsme linéaire dont les intensités d'absorption et les directions dépendent de la longueur onde.

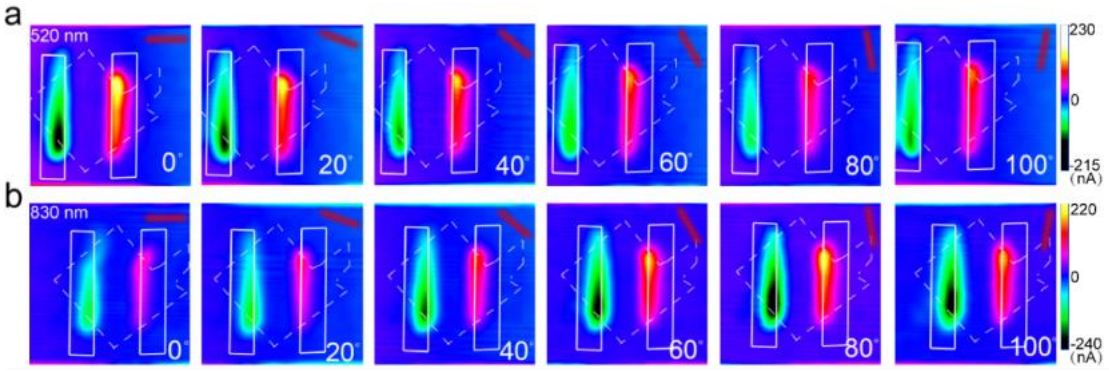

Figure R4.4 Cartographies des photo-courants dépendant de la polarisation pour des échantillons soumis à une polarisation de 30 mV et sous excitation lasers linéairement polarisés à 520 nm (a) et à 830 nm (b), respectivement, montrant la photo-détection dichroïque linéaire. La direction et l'angle du laser polarisé sont illustrés dans chaque cartographie du photo-courant.

Afin de connaitre la réponse des dispositifs sous excitation laser polarisée linéairement, les cartographies de courant ont été mesurées pour différents angles de polarisation et deux longueurs d'onde différentes. La figure R4.4 montre que les signaux du photo-courant se produisent majoritairement à la connexion entre le cristal de GeAs et l'électrode et que les polarités du photo-courant sont opposées dans les deux contacts. Ceci peut s'expliquer par des effets photovoltaïques et photo-thermoélectriques de la jonction de Schottky formée par l'interface entre l'électrode et le cristal de GeAs de type p.

De plus, le renversement optique perpendiculaire du dichroïsme linéaire se révèle dans la cartographie de photo-courant à 520 nm et 830 nm, avec un angle de renversement de 80º. Ce phénomène de renversement est principalement déterminé par la structure cristalline de GeAs de l'échantillon.

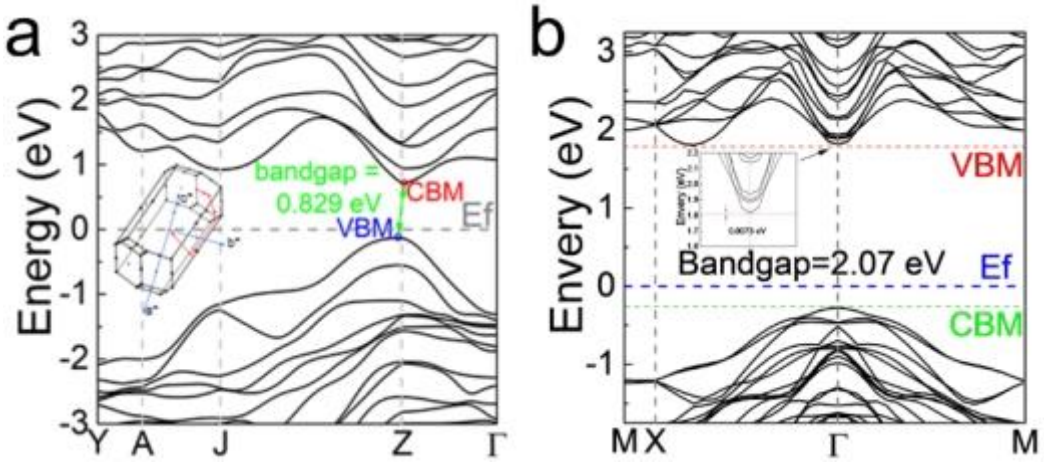

Figure R4.5 Structure de bande électronique (a) de GeAs massif et (b) de la monocouche de GeAs (b) obtenue en utilisant la fonctionnelle HSE06.

Finalement, des calculs de structure électronique de GeAs ont été menés par la méthode de la fonctionnelle de la densité. Dans les calculs, les paramètres du réseau de GeAs obtenus sont *a=3.833* Å, *b=8.543* Å et *c=9.902*Å. La structure de bande électronique, présentée dans la Figure R4.5 (a) montre GeAs massif est un semi-conducteur avec un gap indirect égal à 0.829 eV obtenu au Z, valeur qui est cohérente avec le spectre d'absorption. La structure de bande de la monocouche de GeAs est donnée dans la Figure R4.5 (b). Elle montre une bande interdite de 2.07 eV, directe au point Γ.

Chapitre 5 : La photo-détection basée sur les composés de Sn et S

Come déjà mentionné, les dichalcogénures bidimensionnels de métaux de transition (TMDCs) sont des matériaux fonctionnels prometteurs pour les applications optoélectroniques de la prochaine génération. Ici, nous allons nous intéresser aux propriétés optiques de composés de Sn et S de haute qualité, SnS et $Zn_xSn_{(1-x)}S_2$ (x=0.167) préparés par CVT.

Le composé SnS, dans sa phase orthorhombique, présente une anisotropie remarquable et des propriétés optoélectroniques excellentes. Dans ce chapitre la structure cristalline anisotrope, l'absorption optique polarisée sélective en longueur

d'onde et les caractéristiques optoélectroniques polarisées sont discutées.

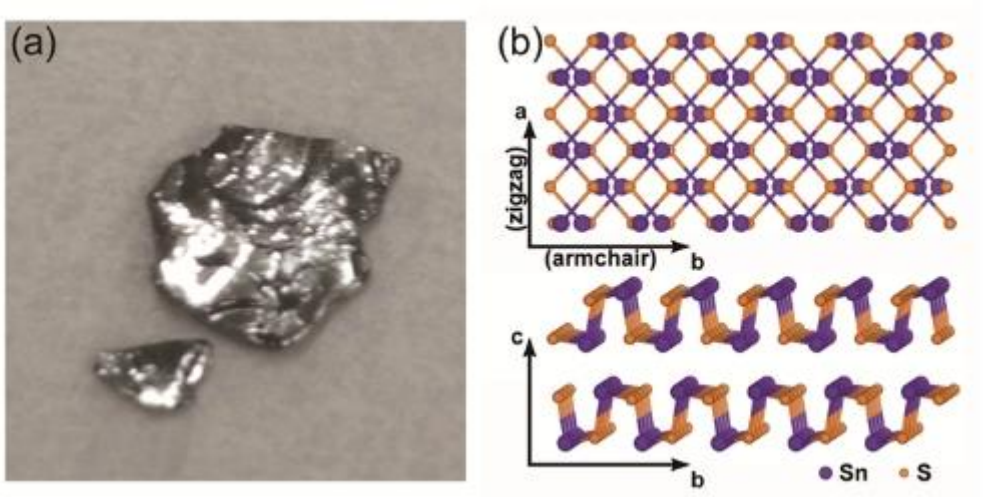

Figure R5.1 (a) Photographie du cristal de SnS ; (b) Structure cristalline de SnS.

SnS possède une structure cristalline qui ressemble à celle du phosphore noir, où les atomes de soufre et d'étain sont arrangés alternativement suivant la direction « fauteuil ». Les axes a et b sont respectivement les directions du réseau du zigzag et du fauteuil, comme illustré dans la **Figure R5.1**.

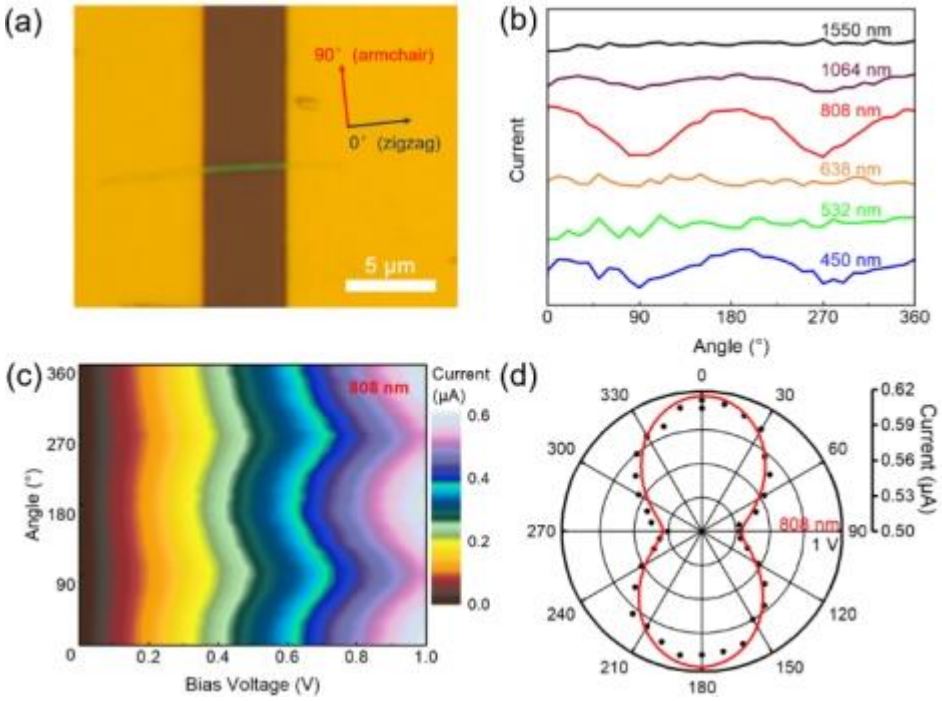

Figure R5.2. Propriétés photo-électroniques polarisées de SnS. (a) Image obtenue par microscope optique. (b) Courbes de la photo-réponse polarisée à des longueurs d'onde différentes. (c) Cartographie du photo-courant sous une excitation de 808 nm illustrant la dépendance avec l'angle de polarisation et la tension de polarisation. (d) Courbes en

coordonnées polaires du photo-courant sou excitation à 808 nm et sous polarisation égale à 1V (points noirs : données expérimentales ; courbe rouge : simulation).

Pour étudier la dépendance du photodétecteur SnS avec la polarisation de la lumière incidente à différentes longueurs d'onde, le photo-courant résolu en angle à des longueurs d'onde d'excitation de 450 nm, 542 nm, 638 nm, 808 nm, 1064 nm et 1550 nm a été mesuré sous un voltage de 1V. Les résultats sont représentés sur la figure R5.2(b). Les courbes des photo-courants à 808 nm et 450 nm présentent une dépendance évidente de la polarisation, alors que la courbe du photo-courant à 1064 nm présente une faible fluctuation périodique. Les ratios dichroïques de l'absorption optique correspondants (αzigzag/αfauteuil) à 450, 532, 638, 808, 1064 et 1550 nm sont respectivement égaux à 1.014, 1.012, 1.024, 1.536, 1.112 et 1.262.

La Figure R5.2(c) montre la carte de couleurs du photo-courant en fonction de la tension de polarisation et de l'angle de polarisation de la lumière incidente à 808 nm. L'ondulation périodique peut être facilement observée. La Figure R5.2(d) représente la trace polaire du photo-courant polarisé avec l'angle résolu sous une tension de polarisation de 1V. Les points noirs sont les données expérimentales. La courbe rouge est approchée via la formule :

$$I_{light}(\theta) = I_{max}\cos^2(\theta+\delta) + I_{min}\sin^2(\theta+\delta)$$

Les déterminations de I_{max} et I_{min} sont respectivement effectuées à 0º et 90º. En comparant l'intensité d'absorption optique polarisée avec l'angle résolu à 808 nm et les résultats de la simulation, on trouve que l'absorbance optique et le photo-courant sont tous maximaux lorsque la direction de polarisation de la lumière incidente est suivant la direction de zigzag (0º) et minimaux si la direction est suivant la direction de fauteuil (90º). On en déduit donc que l'anisotropie de l'absorption optique de l'échantillon de SnS est le facteur principal de la photo-réponse anisotrope. De plus, la sélectivité en longueur d'onde de la sensibilité à la polarisation peut être considérée comme un avantage pour les applications mettant en jeu la photo-détection polarisée.

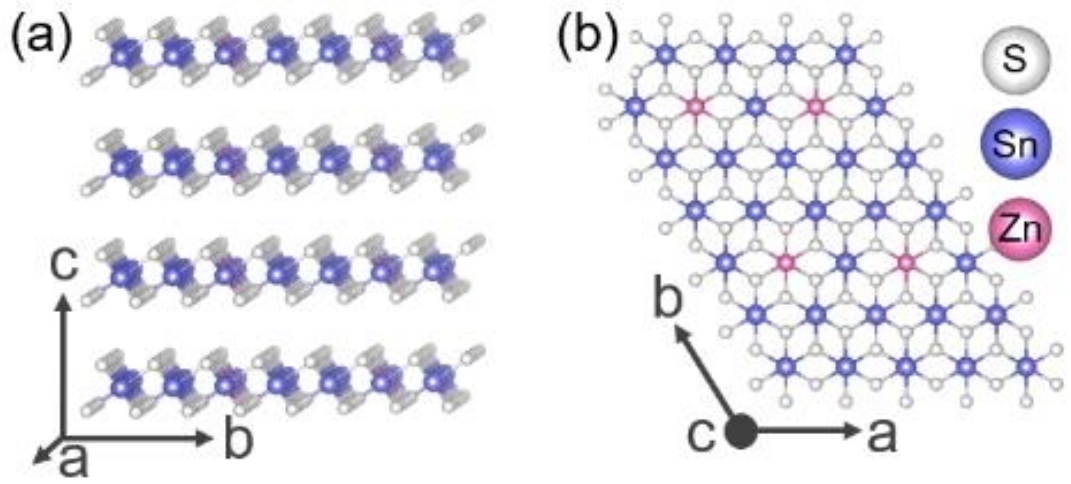

Figure R5.3 (a) Structure cristalline du plan c-b légèrement oblique. (b) Structure cristalline du plan a-b.

Concernant SnS_2, autre composé de Sn et S, ses propriétés photo-électriques sont limitées, en raison de sa structure de bande présentant un gap indirect. Afin d'améliorer la réponse à la lumière de ce matériau, on a élaboré l'alliage $Zn_{0.167}Sn_{0.833}S_2$, qui est un semi-conducteur dont les propriétés photo-électriques sont modifiées par l'ajustement de la structure de bande. La structure cristalline de l'alliage préserve celle de SnS_2 où certains atomes de Sn sont substitués par ceux de Zn, comme l'illustre la figure R5.3.

La Figure R5.4 montre les propriétés optoélectroniques d'un transistor à l'effet du champ basé sur l'alliage $Zn_{0.167}Sn_{0.833}S_2$.

Les courbes I_{ds}-V_{ds} sont mesurées et montrées dans la Figure R5.4(c). Sous une tension Vds de 1V, le courant d'obscurité entre la source et le drain est de 0.1 μA et le courant sous l'illumination par une lumière blanche est de 5.1 μA. Par conséquent, le ratio on/off est de 51. La lumière blanche émise par une LED a été choisie en tant qu'une source d'irradiation pour son application proche dans la vie quotidienne. La courbe de transfert est montrée dans la Figure R5.4(b) balayant les valeurs de V_{gs} de -50 V à 50 V avec la valeur de V_{ds} fixée à 0.01 V. Dans l'image de la courbe de transfert, l'axe des ordonnées à gauche est linéaire et celui à droite est en échelle logarithmique. Le transistor FET basé sur $Zn_{0.167}Sn_{0.833}S_2$ présente les comportements typiques de type n et appartient aux transistors à déplétion. La mobilité de l'effet du champ (μ_m) peut être calculée via la formule :

$$\mu_m = \frac{\partial I_{ds}}{\partial V_g} \cdot \frac{L}{W C_g V_{ds}}$$

où I_{ds} est le courant entre la source et le drain. V_{ds} est la tension du côté du drain au côté de la source. V_g est la tension de grille imposé au substrat de silicium fortement dopé. L est la longueur du canal. W est la largeur du canal. C_g ($C(SiO_2)$ = 11.6 nF cm^{-2}) est le paramètre de la capacitance de la couche de SiO_2 à 300 nm. D'après l'analyse des données dans la Figure R5.4(c), la mobilité calculée des électrons du FET à base de $Zn_{0.167}Sn_{0.833}S_2$ est de 65 cm^2 V^{-1} s^{-1}, qui est plus élevée que celles précédemment rapportées dans les cristaux de SnS_2 et de ZnS_2. Les courbes résultantes du FET de $Zn_{0.167}Sn_{0.833}S_2$, présentées dans la Figure R5.4(d), montrent une relation linéaire due au contact ohmique entre les électrodes d'or et les nano-flocons de $Zn_{0.167}Sn_{0.833}S_2$.

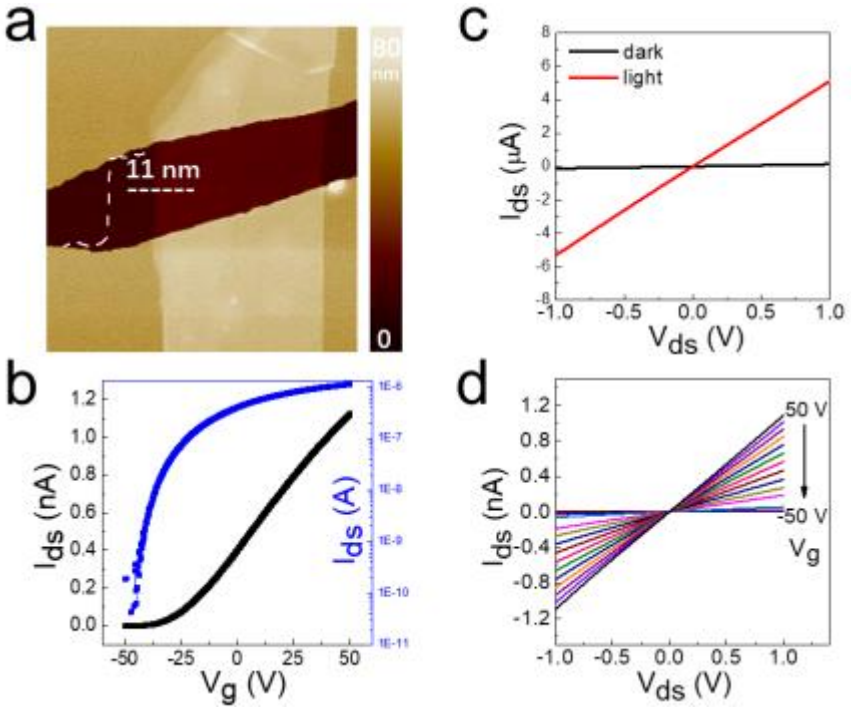

Figure R5.4 (a) Image AFM du dispositif FET $Zn_{0.167}Sn_{0.833}S_2$ avec l'épaisseur du nano-alliage de 11 nm. (b) Courbe courant tension avec et sans lumière. (c) Courbe courant tension Vds/Ids du FET de $Zn_{0.167}Sn_{0.833}S_2$ sous un Vg de 0.01 V. (d) Courbes résultantes de FET de $Zn_{0.167}Sn_{0.833}S_2$.

Finalement, on peut calculer les structures de bande de la monocouche et du matériau massif via les calculs en premiers principes. L'alliage présente un gap direct évalué à 1.458 eV dans la monocouche et 1.507 eV dans le massif. Ce résultat est dû à la présence des atomes de Zn dans l'alliage sous forme Zn^{2+} qui introduit de nombreux

états électroniques qui ajustent le sommet de la bande de valence au point Γ. Par la comparaison des densités d'états de la monocouche de SnS_2, de la monocouche de $Zn_{0.167}Sn_{0.833}S_2$ et de $Zn_{0.167}Sn_{0.833}S_2$ massif, on constate que la densité des atomes de Zn contribue plus aux états de la bande de valence.

Conclusions:

Grâce à leurs propriétés physiques uniques, les matériaux bidimensionnels sont progressivement devenus des matériaux à très fort potentiels. Cette thèse s'est concentrée sur les propriétés optoélectroniques des matériaux bidimensionnels. En particulier le contrôle magnétique de l'hétérojonction MoS2/CoFeB et l'anisotropie de polarisation de GeAs et de SnS ont été étudiés. Les principaux résultats sont rappelés ci-dessous.

Un premier axe a visé à injecter un courant polarisé en spin dans une structure semi-conductrice bidimensionnelle à base de MoS_2 en vue de contrôler la polarisation de l'émission optique. Nous avons élaboré une couche ferromagnétique de CoFeB à aimantation perpendiculaire capable d'injecter des électrons polarisés sans champ magnétique, et sur une grande surface. Pour obtenir la fonction souhaitée nous avons élaboré des structures Ta/CoFeB/MgO ayant une large anisotropie magnétique perpendiculairement à l'axe de croissance. Il a été possible de réaliser un dépôt homogène couvrant toute la surface de la monocouche de MoS_2 sous-jacente, constituant l'émetteur de lumière. En optimisant l'épaisseur de la couche de CoFeB et la température du recuit, on obtient une grande énergie d'anisotropie magnétique perpendiculaire valant 0.975 mJ/m^2. Par l'analyse des propriétés structurales et chimiques de l'hétérostructure, il est montré que l'insertion de MgO entre le métal ferromagnétique et le matériau bidimensionnel peut efficacement bloquer la diffusion des atomes du ferromagnétique. Il est également montré que la couche de Ta joue un rôle critique « d'absorption » des atomes de B de la couche de CoFeB ce qui induit l'aimantation perpendiculaire. D'après les calculs *ab initio*, l'épaisseur de MgO peut être ajustée pour modifier la structure de bande de MoS_2, allant d'un gap indirect avec

pour une couche de MgO de 7 monocouches (MCs) à un gap direct pour une couche de MgO de 3 MCs. L'effet de proximité introduite par le Fe conduit à une modification de la bande de valence au point Γ pour 3 MCs, alors que celle-ci est négligeable pour 7 MCs. Nos résultats expérimentaux et théoriques favoriseront le développement de dispositifs optoélectroniques à spin, à température ambiante, basés sur des semi-conducteurs bidimensionnels à base de dichalcogénures de métaux de transition avec des injecteurs de spin à aimantation perpendiculaire.

Afin d'obtenir un photodétecteur sensible à la polarisation, nous nous sommes intéressés à des cristaux ayant une structure anisotrope. La nature anisotrope intra-planaire du cristal IV-V de GeAs a été investiguée par spectrométrie d'absorption résolue en polarisation entre 400 et 2000 nm. Les échantillons nanométriques bidimensionnels obtenus de GeAs démontrent bien un dichroïsme linéaire et une photo-détection sensible à la polarisation. En comparant le dichroïsme d'absorption du matériau GeAs et le rapport de photocourant anisotrope du détecteur de polarisation, on constate que le rapport de photocourant anisotrope est de 4,4, ce qui est supérieur au dichroïsme (1,42) absorbé par le cristal GeAs lui-même sous l'irradiation d'un laser à polarisation linéaire à 830 nm. Cela est dû à l'existence de la jonction Schottky, à l'interface électrode/GeAs, qui réduit le courant d'obscurité du dispositif, et son champ électrique interne améliore la concentration des porteurs. En résumé, l'excellente performance du cristal de GeAs en fait un matériau favorable à la préparation de détecteurs de polarisation.

Des alliages à base d'éléments des groupes IV-VI tels que SnS et ZnSnS ont également été caractérisés. Il est démontré que SnS présente une mobilité des porteurs valant 37,75 $cm^2 \bullet V^{-1} \bullet S^{-1}$ et une photo-réponse de 310,5 A/W. En raison de l'absorption optique anisotrope, le photo-courant est dépendant de la direction de polarisation de la lumière incidente, émise à 808 nm. L'absorption optique en bord d'absorption présente une sensibilité à la polarisation avec le plus haut ratio dichroïque atteint valant 3,06 à 862 nm. L'alliage ZnSnS bidimensionnel est un semi-conducteur à gap direct et est donc à fort potentiel pour les applications en optique. Il est de type n. La mobilité des

porteurs est de 65 $cm^2 \bullet V^{-1} \bullet S^{-1}$, et le ratio on/off sous l'illumination par une lumière blanche de type LED est élevé et atteint 51.

Perspectives:

Les matériaux à faible dimension font l'objet d'une recherche intense et bénéficient d'un fort développement ce qui devrait permettre de produire des dispositifs optoélectroniques ultraminces, transparents et hautement intégrés, dotés de nouvelles fonctions. Les films magnétiques avec une anisotropie hors du plan sont susceptibles d'améliorer significativement le taux d'injection et de détection des Spin-LEDs. Les résultats obtenus dans cette thèse contribuent à accroitre le potentiel applicatif de tels matériaux. Pour le film à hétérojonction MoS2/MgO/CoFeB, il est envisagé dans un futur proche de réaliser le dispositif Spin-LED et d'en mesurer son taux de polarisation sous injection électrique. L'injecteur développé dans ce travail de thèse pourrait aussi être mis à profit pour injecter un courant polarisé en spin dans d'autres structures LED.

Parmi les matériaux bidimensionnels à fort potentiel, les matériaux semi-conducteurs avec une anisotropie dans le plan, tels que GeAs, pourraient devenir les pixels photosensibles des détecteurs de polarisation. La zone centrale de détection de la polarisation est une photodiode de type Schottky. Il est possible d'augmenter la surface de la jonction Schottky en construisant des électrodes interdigitales pour augmenter l'anisotropie du photocourant sous lumière polarisée. Des dispositifs à matrice à base de GeAs seront réalisés pour obtenir des photodétecteurs performants.

Abstract

2D materials exhibit overwhelming electrical, optical, magnetic, thermal, and other advantages, which enables their great potential applications in ultra-thin, transparent, and highly integrated optoelectronic devices. Searching new two-dimensional materials and exploring their optimal performance, as well as expanding the practical application of two-dimensional materials have been the cores of the researches of two-dimensional materials. This thesis focuses on the vertical magnetic control of the CoFeB film on a large-area single-layer MoS_2 film, which could expand the potential of two-dimensional materials in spin photodetectors, the polarized photodetection based on noval two-dimensional GeAs, and the optical characterizations of group IV-VI compounds like SnS and $ZnSnS_2$. This paper introduces them in details through the following three parts:

1. We fabricate the Ta/CoFeB/MgO structures with large PMA on the full coverage mono-layered MoS_2. By optimizing the thickness of the CoFeB and the annealing temperature, we have obtained a large perpendicular interface anisotropy energy of 0.975 mJ/m^2 at the CoFeB/MgO interface. By analyzing the structural and the chemical properties of the heterostructure, it is found that the insertion of MgO between the ferromagnetic metal (FM) and the 2D material can effectively block the diffusion of the FM atoms into the 2D material. Simultaneously, the Ta layer plays a critical role in efficiently absorbing B atoms from the CoFeB layer to establish the PMA. From the results of *ab initio* calculations, the MgO thickness can be tuned to modify the MoS_2 band structure, from an indirect bandgap with 7 MLs MgO layers to a direct bandgap with 3 MLs MgO layers. The proximity effect induced by Fe results in a 10 meV splitting at Γ point of valence band of the 3MLs MgO structure while it is negligible for the 7MLs MgO structure.

2. we research the anisotropic optical characterization of a group IV-V compound, Germanium Arsenic (GeAs). The in-plane anisotropic optical property of GeAs

crystal is further investigated by the polarization-resolved absorption spectroscopy (400-2000 nm) and the polarization-sensitive photodetectors. In the visible-near infrared spectrum, the 2D GeAs nanoflakes demonstrate the distinct perpendicular optical reversal with an angle of 75~80 degrees on linear dichroism and the polarization-sensitive photodetection. The high angioscopy photocurrent ratio of I_{pmax}/I_{pmin} ~ 1.49 at 520 nm and I_{pmax}/I_{pmin} ~ 4.4 at 830 nm are measured by the polarization-sensitive photodetection. The polarization-dependent photocurrent mapping implied that the polarized photocurrent mainly occurred at the Schottky photodiodes at the electrode/GeAs interface.

3. We research optical characterizations of IV-VI compounds like SnS and ZnSnS. SnS nanosheets exhibit carrier mobility of 37.75 $cm^2 \cdot V^{-1} \cdot s^{-1}$, photoresponsivity of 310.5 A/W and external quantum efficiency of 8.56×10^4% at 450 nm. Optical absorption around the absorption edge presents obvious polarization sensitivity with the highest optical absorption dichroic ratio of 3.06 at 862 nm. Due to the anisotropic optical absorption, the polarized photocurrent appears upon the periodic change affected by the polarized direction of the incident light at 808 nm. The ZnSnS alloys combine the advantageous optical parameters of SnS and ZnS_2, which belong to the direct band structure of n-type 2D material. The carrier mobility of the alloy is 65 cm^2 V^{-1} S^{-1} and the on/off ratio under white-LED illumination is as high as 51.

Keywords: Two-dimensional, Perpendicular magnetic anisotropy, Spin injector, Polarization photodetectors, optical characteristic

Résumé

Les semi-conducteurs bidimensionnels possèdent de nombreuses propriétés fonctionnelles intéressantes telles qu'électriques, optiques, magnétiques, thermiques etc., qui permettent des applications potentielles notamment dans les dispositifs optoélectroniques ultraminces, transparents et hautement intégrés. La synthèse de nouveaux matériaux bidimensionnels et l'exploration de leurs performances optimales, ainsi que le développement de leurs applications font l'objet d'une intense activité de recherche dans le domaine des matériaux. Cette thèse s'inscrit dans la recherche de nouveaux matériaux bidimensionnels.

Un premier axe vise à injecter un courant polarisé en spin dans une structure semi-conductrice bidimensionnelle à base de MoS_2 en vue de contrôler la polarisation de l'émission optique. L'objectif est ici d'élaborer une couche ferromagnétique de CoFeB à aimantation perpendiculaire capable d'injecter des électrons polarisés sans champ magnétique, et sur une grande surface. L'obtention de tels émetteurs optique polarisés doit s'accompagner du développement de photodétecteurs de lumière polarisée à base de matériaux bidimensionnels. C'est l'objet des deux autres axes de cette thèse dans lesquels la photo-détection basée sur les nouveaux semi-conducteur GeAs et des alliages d'éléments des groupes IV-VI tels que SnS et ZnSnS est étudiée.

Concernant l'injecteur de spin, on s'intéresse à la fabrication des structures Ta/CoFeB/MgO ayant une large anisotropie magnétique perpendiculairement à l'axe de croissance. Un point important est la réalisation d'un dépôt homogène couvrant toute la surface de la monocouche de MoS_2 sous-jacente, constituant l'émetteur de lumière. En optimisant l'épaisseur de la couche de CoFeB et la température du recuit, on obtient une grande énergie d'anisotropie magnétique perpendiculaire valant 0.975 mJ/m^2. Par l'analyse des propriétés structurales et chimiques de l'hétérostructure, il est montré que l'insertion de MgO entre le métal ferromagnétique et le matériau bidimensionnel peut efficacement bloquer la diffusion des atomes du ferromagnétique. Il est également

montré que la couche de Ta joue un rôle critique « d'absorption » des atomes de B de la couche de CoFeB ce qui induit l'aimantation perpendiculaire. D'après les calculs *ab initio*, l'épaisseur de MgO peut être ajustée pour modifier la structure de bande de MoS_2, allant d'un gap indirect avec pour une couche de MgO de 7 monocouches (MCs) à un gap direct pour une couche de MgO de 3 MCs. L'effet de proximité introduite par le Fe conduit à une modification de la bande de valence au point Γ pour 3 MCs, alors que celle-ci est négligeable pour 7 MCs.

Afin d'obtenir un photodétecteur sensible à la polarisation, on s'intéresse à des cristaux ayant une structure anisotrope. La nature anisotrope intra-planaire du cristal IV-V de GeAs est investiguée par spectrométrie d'absorption résolue en polarisation entre 400 et 2000 nm. Les échantillons nanométriques bidimensionnels obtenus de GeAs démontrent bien un dichroïsme linéaire et une photo-détection sensible à la polarisation. Les ratios dichroïques obtenus par des mesures de photocourant atteignent des valeurs élevées de $I_{pmax}/I_{pmin} \sim 1.49$ à 520 nm et de $I_{pmax}/I_{pmin} \sim 4.4$ à 830 nm. Les cartographies de photo-courant suggèrent que la dépendance du courant avec la polarisation trouve son origine majoritairement aux interfaces électrode/GeAs qui présentent un caractère de type Schottky.

Des alliages à base d'éléments des groupes IV-VI tels que SnS et ZnSnS ont également été caractérisés. Il est démontré que SnS présente une mobilité des porteurs valant 37,75 $cm^2 \cdot V^{-1} \cdot S^{-1}$ et une photo-réponse de 310,5 A/W. En raison de l'absorption optique anisotrope, le photo-courant est dépendant de la direction de polarisation de la lumière incidente, émise à 808 nm. L'absorption optique en bord d'absorption présente une sensibilité à la polarisation avec le plus haut ratio dichroïque atteint valant 3,06 à 862 nm. L'alliage ZnSnS bidimensionnel est un semi-conducteur à gap direct et est donc à fort potentiel pour les applications en optique. Il est de type n. La mobilité des porteurs est de 65 $cm^2 \cdot V^{-1} \cdot S^{-1}$, et le ratio on/off sous l'illumination par une lumière blanche de type LED est élevé et atteint 51.

Mots clés : semi-conducteur bidimensionnel, anisotropie magnétique perpendiculaire, injecteur de spin, photo-détecteur, lumière polarisée, caractérisation optique

Table of contents

Table of graphs

List of Acronyms

A:
- AFM: Atomic Force Microscopy
- ADF: Annular dark-field

B:
- BN: Boron Nitride
- BF: Bright-field

C:
- CVD: Chemical Vapor Deposition
- CVT: Chemical Vapor Transport

D:
- DP: D'yakonov-Perel
- DOS: Density of states
- DFT: Density-functional theory

E:
- EDS: Energy-dispersive X-ray spectroscopy

F:
- FM: Ferromagnetic
- FIB: Focused ion beam

G:
GeAs: Germanium Arsenic

H:
- HRTEM: High-Resolution Transmission Electron Microscope
- HAADF: High angle annular dark-field

I:
- IBE: Ion beam etching

L:
- LED: Light emitting diode

M:
- MoS_2: Molybdenum disulfide
- MBE: Molecular beam epitaxy
- ML: Monolayer
- MgO: Magnesium Oxide
- MIS: Metal-insulator-semiconductor

O:
- OMFTJ: Organic multiferroic tunnel junction

P:
- PFM: Piezoresponse force microscopy
- PL: Photoluminescence
- PMA: Perpendicular magnetic anisotropy
- PPMS: Physical property measurement system

● PAW: Projector augmented-wave
● PBE: Perdew, Burke, and Ernzerhof

Q:

● QW: Quantum well
● QD: Quantum dot

R:

● RTA: Rapid thermal annealing
● RHEED: Reflection high-energy electron diffraction

S:

● SAED: Selected-Area Electron Diffraction
● SOC: Spin-orbit coupling
● STM: Scanning tunneling microscope
● SQUID: Superconducting quantum interference device
● SIMS: Secondary ion mass spectroscopy
● STEM: Scanning transmission electron microscopy
● SEM: Scanning electron microscope

T:

● TMDs : Transition metal dichalcogenides
● TEM: Transmission electron microscopy

U:

● UHV: Ultra-high vaccum

V:

● VSM: Vibrating-sample magnetometer
● VASP: Vienna ab initio simulation package

X:

● XPS: X-ray photoelectron spectroscopy

Remerciements

Time flies. It's almost been five years since I started my study after graduating from undergraduate student. This thesis would not have been possible without the help and encouragement of many people. I would like to express deep gratitude to many people who have contributed to the completion of my PhD research.

First and foremost, I must thank my Chinese supervisor Prof. Zhongming WEI who is really an expert in semiconductor field providing me the opportunity to start a PhD research at the Institute of Semiconductors. His continuous support during the entire PhD study, his patience and enthusiasm in semiconductor research, and detailed discussions with students have deeply impressed me. Besides, he also gave me a chance of studying in France as a co-mentorship's student. My deepest gratitude is extended to my French supervisor Prof. Yuan Lu who is a specialist of MBE and the field of semiconductor spintronics. Lu picked me up from Nancy railway Station. During the one-year study and life in France, Lu not only taught me how to operate the experiment and build experimental equipment, but also cared about my health. Due to the language barrier, Lu helped me with everything in life. When I left France, due to the COVID-19, I left in a hurry. Lu sent me to the Lorraine train station and then helped me complete the experiment. I acknowledge my French co-supervisor Prof. Hervé Rinnert giving me a big hand during the double-degree application. I would like to thank Paul Marcon and Lionel Calmels from the University of Toulouse for his assistance with the first-principles calculations.

Special thanks belong to Mme Xue GAO and M. Jianying QIN who showed me a lot of experiments at the very beginning of my study in France. I'm grateful for my engineer Stefan Mc-murtry who training for me about E-beam Lithography. I would like to thank my engineer Laurent Badie and Gwladys Lengaine who had an excellent training for me about the different facilities in the clean room. Stéphane Suire is always helpful when people are dealing with the problems of magnetic measurements. I'm

grateful for Christine Sartori and Georges Billant help during my registered and defense. Many thanks to all the people who work in IJL and help me before.

Last and not least, I would like to thank and dedicate this thesis to my family, especially to my grandparent and parents who trust me, care about me and encourage me all the time. Thanks to my boyfriend Xichen CHUAI make me happy. Hope us harmonious union forever. Thanks to my best friend Yuanzhao CHEN and her husband Yuncheng MAO help me translate the French part of this thesis. They make my life in France rich and colorful.

I'm very lucky that I can study in Nancy and I really cherished and enjoyed my life here. The period of pursuing PhD degree will make a difference to the rest of my life.

Ziqi ZHOU

May, 2021

Beijing, CHINA

Chapter 1: Development and application of two-dimensional materials

Since the first discovery of graphene in 2004, the concept of two-dimensional materials has attracted intensive interests and stimulated the research on van der Waals layered materials. In the following ten years, many two-dimensional materials have been discovered, forming a big 2D material family, including graphene, black phosphorus (BP), metal oxides, layered double hydroxides (LDHs), covalent organic framework compounds (COFs), metal organic framework compounds (MOFs), transition metal chalcogenides (TMDCs), hexagonal boron nitride (h-BN), silylene, inorganic perovskite and organic-inorganic hybrid perovskite, etc. [1-14]

Different two-dimensional materials can be used for different application directions. For example, the semi-metallic properties of graphene allow it to be used as a transparent electrode for PN junctions in solar cells, and its high mobility allows it to be applied to high-frequency integrated circuits. However, its zero-band gap limits its application in the semiconductor field, especially in MOSFET. In comparison, transition metal chalcogenide compounds have widely distributed band gap, ranging from 0.1-3 eV. In this case, TMDCs can be used not only in field effect transistors, but also in photo-detectors. Researchers can select two-dimensional materials with different band gaps according to the desired detection light wavelength. In addition, due to the in-plane anisotropy of its own structure, black phosphorous (BP) materials can also be used to polarization detectors. In the following, I will introduce in details the structural characteristics of different two-dimensional materials.

1.1 Graphene

Graphene was discovered by *Andre Geim* and *Konstantin Novoselov* from the University of Manchester in the United Kingdom in 2004. The two scientists won the Nobel Prize in Physics in 2010. Since then, more and more researchers have studied graphene and discovered many good qualities of graphene.

1.1.1 Crystal Structure

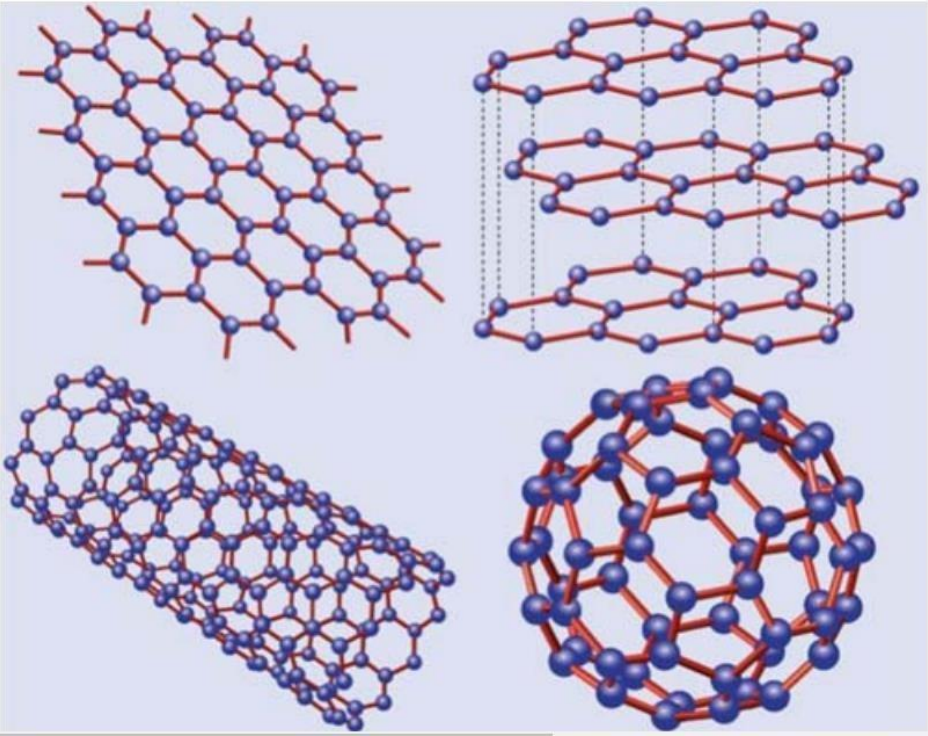

Figure 1. 1 The crystal structure of Graphite, carbon nanotube and fullerene.

Graphene is named by two-dimensional sp^2 hybrid carbon flakes. Graphene is by far the thinnest material. The thickness of graphene is 3.35 Å. It is composed of hexagonal close-packed carbon atoms, where each atom is bonded to three adjacent atoms through covalent bonds. The distance between two adjacent carbon atoms in a single-layer graphene is about 1.42 Å. The extended honeycomb structure of graphene is the cornerstone for the construction of other allotropes. It can be stacked into three-dimensional graphite, crimped into one-dimensional nanotubes, and wrapped to form zero-dimensional fullerenes (as shown in Figure 1.1).

1.1.2 Electrical properties

Single-layer graphene exhibits completely different electrical properties from graphite, such as the bipolar field effect of graphene (Figure 1.2 b), the quantum Hall effect at room temperature (Figure 1.2 e, f), the ultra-high carrier concentration (Figure 1.2 b) and the first detection of single molecule adsorption. Electrons can realize micron-level non-scattering transmission at room temperature. In terms of its electrical conductivity, the current density of graphene is six orders of magnitude higher than that of copper. In addition, it has excellent thermal conductivity and thoughness. These excellent properties of graphene have great application potential in high-speed and high-frequency integrated circuits, thermal and conductive enhanced composite materials, sensors, and solar transparent electrodes.

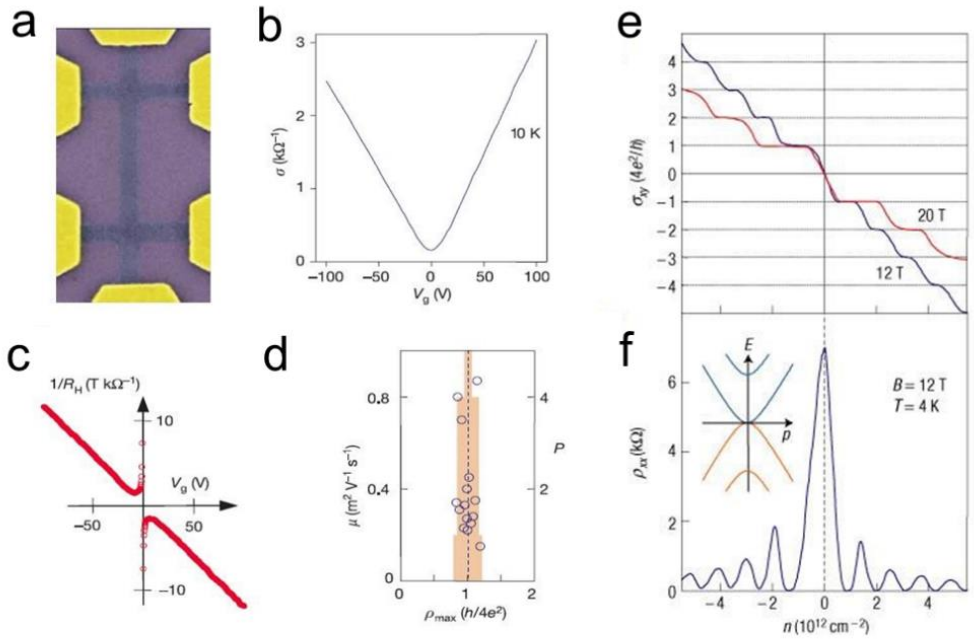

Figure 1. 2 The electric properties of Graphene.

(a) SEM image of graphene device. (b) The conductivity of graphene varies with gate voltage. (c) The Hall coefficient of graphene varies with gate voltage. (d) The maximum resistance value changes with mobility. The carrier of the double-layer graphene Hall conductance (e) and resistance (f) varies with magnetic field and temperature.

The unique electronic properties of graphene come from high-quality 2D atomic structure. High quality represents a low defect state. Defective state is the scattering center of charge transport, high-quality material means low-defect state. In 2008, Columbia's Kim team measured the carrier mobility of single-layer graphene obtained by mechanical exfoliation as high as 200,000 cm^2/Vs. In their experiment, they creatively corroded the substrate under the graphene channel and suspended the graphene between the gold electrodes to minimizing the scattering influence of the substrate on the electrical transmission. Another important transmission characteristic of graphene is bipolarity in the field-effect test. The carriers of graphene can be continuously adjusted to electrons or holes through the gate voltage varies. This is because when the gate voltage is negative, the Fermi level is lower than the Dirac point. There are more holes in the valence band. When the gate voltage is positive, the Fermi level is higher than the Dirac point. There are more electrons in the conduction band.

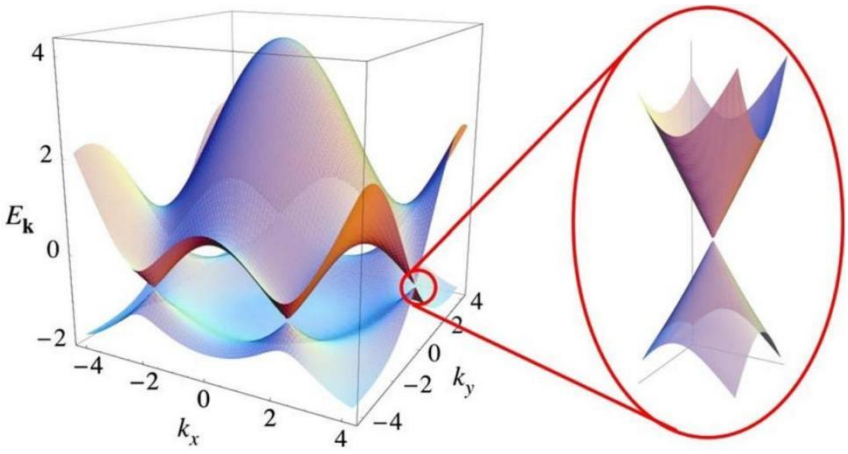

Figure 1. 3 Electron dispersion diagram in graphene.

Graphene has many excellent properties. However, due to the intrinsic zero band gap (Figure 1.3), the switching ratio in the field-effect transistor is very small[15]. In this way, it is very difficult to realize the application of graphene in logic circuits. In contrast, two-dimensional transition metal chalcogenides with different band gaps have naturally attracted the attention of scientists.

1.2 Transition Metal Dichalcogenides (TMDs)

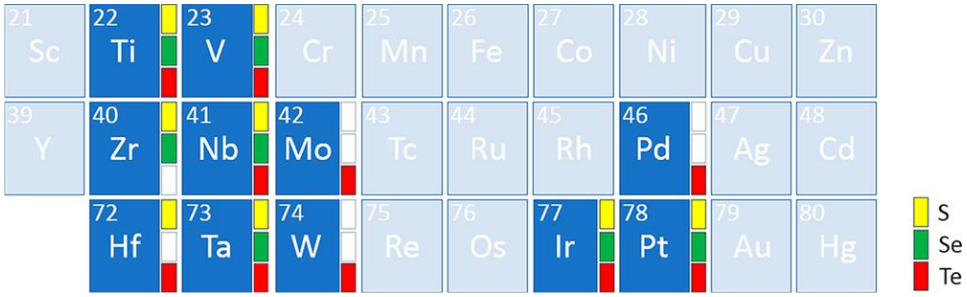

Figure 1. 4 The distribution of the main transition metal chalcogenides. The elements in the blue grid are transition metals, and the colors yellow, green, and red represent the chalcogen S, Se, and Te elements, respectively.

In order to make use of the advantages of two-dimensional materials in the field of traditional semiconductors, researchers have discovered a huge family of TMDCs. Like graphene, TMDCs is a layered material with the layer thickness around 0.7nm. The layered structure is also combined by van der Waals forces. The constituent elements are composed of transition metals and VIA elements (chalcogens) in a ratio of 1:2. The main composition is shown in Figure 1.4. There are many types of compounds in TMDCs, covering related materials such as semiconductors, metals, and insulators.

There are two phases like the H phase and the T phase in TMDCs. Figure 1.5 shows the ball-and-stick model structure of these two phases. The H phase means that the lower tetrahedron and the upper tetrahedron are mirror images of the center plane. The upper and lower tetrahedrons in the T phase are symmetrical to the center, that is, the tetrahedron on the H phase rotates 180° horizontally to obtain the T phase. The top views in both cases are shown in the insets in Figure 1.5. The top view of the H phase is a hexagonal structure, similar to the top view structure of hexagonal boron nitride. The sulfur atoms exist above and below the transition metal in the top view, and the top view structure is through the plane projected.

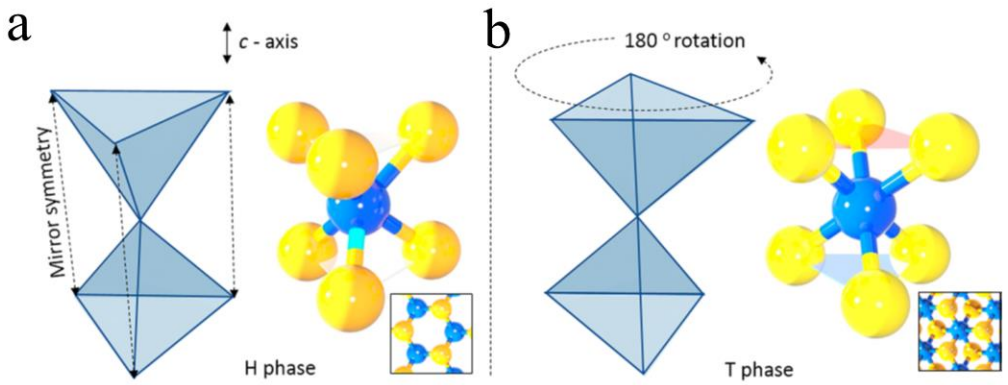

Figure 1. 5 Ball-and-stick model of TMDCs with (a) H-phase and (b) T-phase, the yellow ball is chalcogen element, and the blue ball is transition metal element.

1.2.1 Crystal Structure

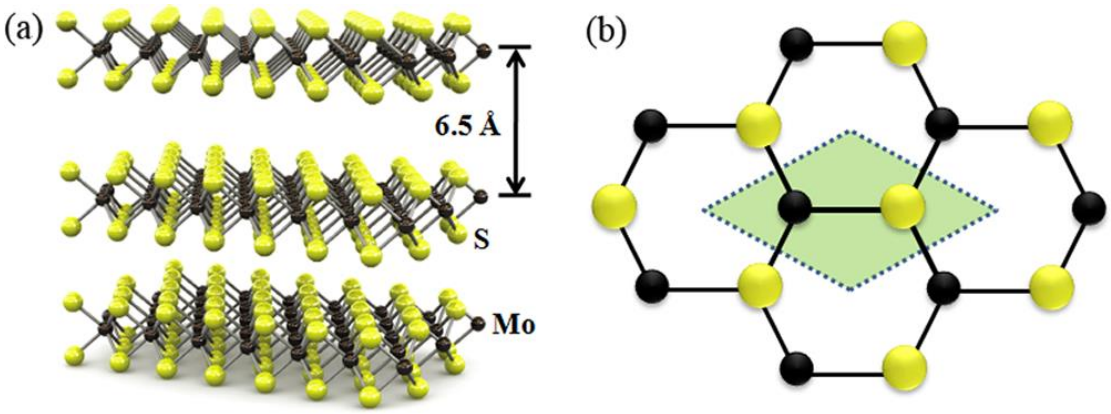

Figure 1. 6 The crystal structure of MoS_2.

(a) the side view structure. (b) the top view.

In the family of TMDCs, MoS_2 is the most typical material with the crystal structure shown in Figure 1.6.[16-19] The Mo atom and two S atoms are located at alternating corners of hexagons. Figure 1.6 (a) shows the bulk crystal structure in side view. The thickness of ML MoS_2 is 6.5Å. Figure 1.6 (b) shows the top view of ML MoS_2 which is similar to graphene.

MoS_2 is semiconductor with the bandgap of 1.2 to 1.9 eV. The ML MoS_2 exhibits a direct bandgap different than its bulk material. This means that ML MoS_2 have a good potential for FET and optoelectronic device applications.

1.2.2 Electrical and Photoelectric Properties

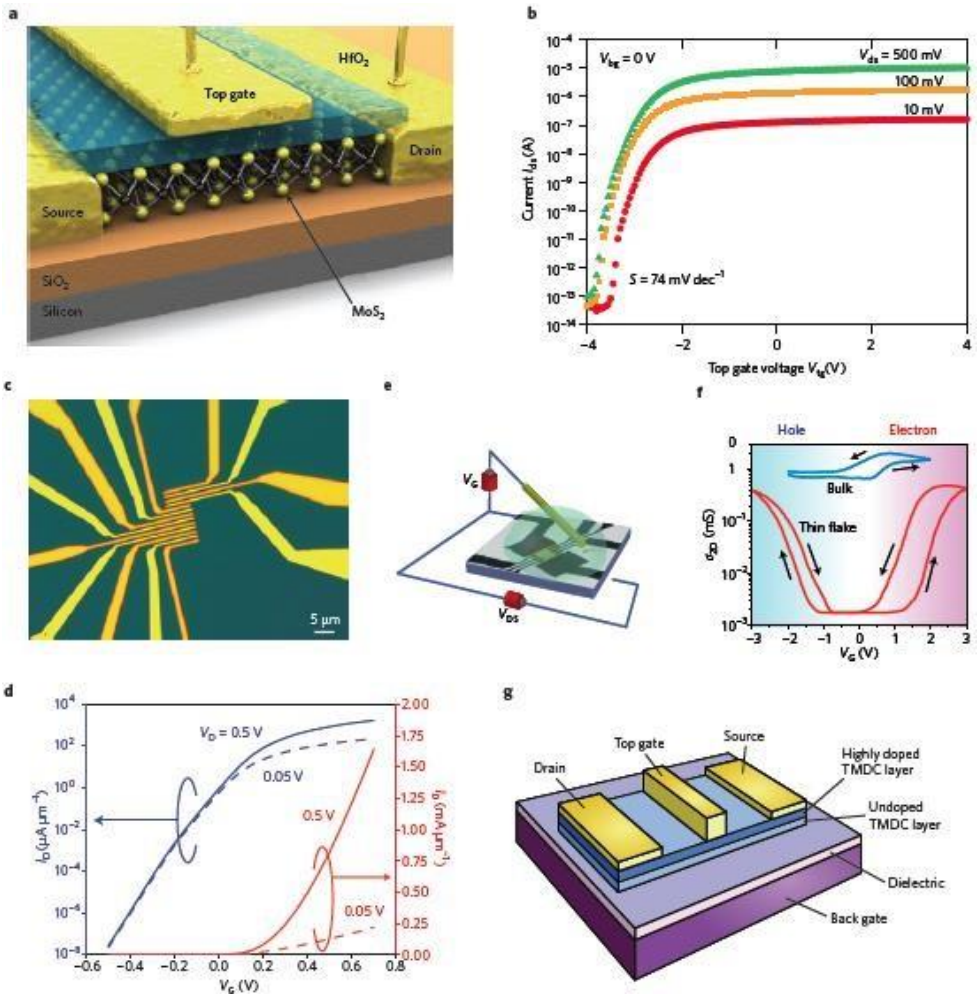

Figure 1. 7 MoS_2 based electrical devices.

(a) and (b) HfO_2-top gate voltage ML MoS_2 field effect device schematic diagram and the corresponding transfer curve. (c) ML MoS_2 integrated circuit. (d) Analog device performance of ML MoS_2. (e) and (f) Schematic diagrams and corresponding electrical properties of electric double layer transistors. (g) Model of high electron mobility based on TMDC. [20-22]

The top gate FET based on ML MoS_2 was reported by the Kis's group for the first time.[22] The device performance shows on-off ratio of 10^8, n-type conductance, a room temperature mobility of up to 200 $cm^2V^{-1}s^{-1}$, and subthreshold swing of 74 mV/dec (Figure 1.7 a, b). HfO_2 is used as a high-k dielectric layer for the device, which can improve the mobility of a single layer of MoS_2 through dielectric optimization. The top gate voltage high-k dielectric is also used in the p-type WSe_2 transistor. The

mobility measured at room temperature is as high as 250 $cm^2V^{-1}s^{-1}$, the subthreshold swing is 60 mV/dec, and the on-off ratio is 10^6. The thin-layer MoS_2 transistor obtained by the liquid lift-off method also obtained similar electrical properties, which indicates that the material can be used for flexible, transparent, two-dimensional electronic device applications. The large-area MoS_2 obtained by chemical vapor deposition also plays an important role in integrated devices (Figure 1.7 c). [23] The theoretical simulation of the performance of a ML MoS_2 transistor quantifies the neglect of the short-channel effect of MoS_2 due to the atomic-scale thickness (Figure 1.7 d).[24] These calculation results show that the top-gate MoS_2 transistor with 15 nm channel can be operated in a ballistic region. The on-state current is as high as 1.6 mA/μm. The sub-threshold swing is close to 60 mV/dec. And the current on-off ratio is 10^{10}. Radisavljevic *et al.* reported that they can build functional electronic integration on multi-layer TMDCs to realize digital logic operations. By photolithography, up to 6 independent switching transistors were fabricated on the same single-layer MoS_2 (Figure 1.7 c).[25]

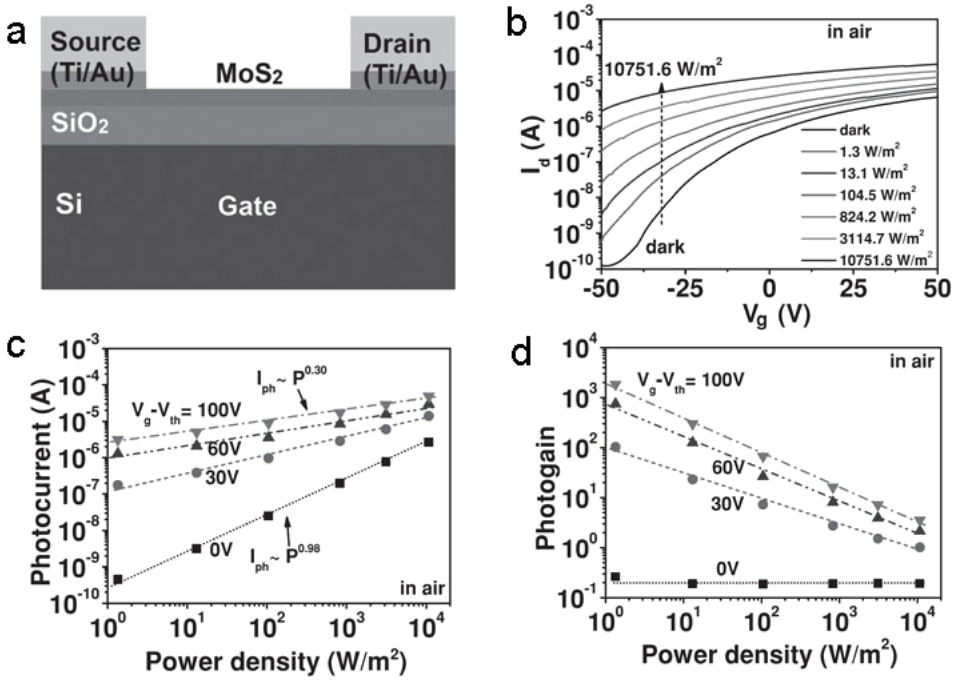

Figure 1. 8 The photodetector based on ML MoS_2.

(a) The Schematic diagram of device. (b) The transfer curves at different light powers. (c) and (d) The power dependence of the photocurrent and photogain. [26]

ML MoS_2 has excellent electrical properties as well as good optoelectronic properties. The photoelectric of MoS_2 is shown in the Figure 1.8. It shows that the photoresponsivity and photogain were up to 2200 A W^{-1} and 5000, respectively. The response time can research 50ms.

1.3 In-plane anisotropy of two-dimensional materials

For the photoelectric properties of 2D materials, the linear polarized photo detection is a novel field. In terms of the in-plane structure of materials, they can be divided into symmetric materials and anisotropic materials. Materials with low in-plane symmetry have high angular sensitivity, and are potential candidate for linear polarized photodetector.

1.3.1 Crystal structure

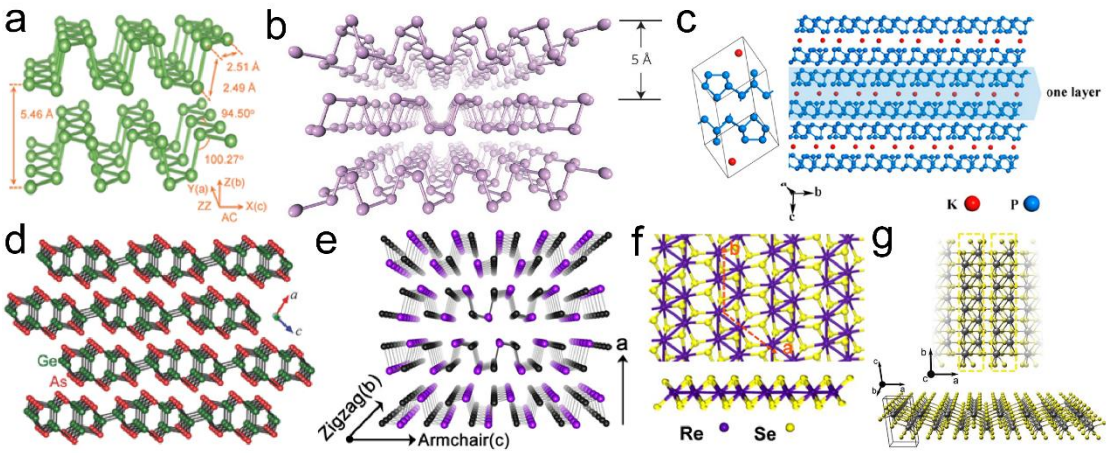

Figure 1. 9 The crystal structure of two-dimensional anisotropic materials.

(a) orthorhombic, black arsenic (B-As) [27, 28]; (b) orthorhombic, black phosphorus (BP) [29]; (c) triclinic crystal, KP_{15}[30]; (d) monoclinic, germanium arsenide (GeAs)[31]; (e) orthorhombic, germanium selenide (GeSe) [31]; (f) triclinic, $ReSe_3$[32]; (g) monoclinic, TiS_3. [33]

B-As and BP are the most representative anisotropic materials, as shown in Figure

1.9 (a) and (b), which are orthorhombic systems and belong to the space groups Bmab and Pcmn, respectively. These two materials belong to natural appearance is black mineral material, so it is called Black-Arsenic and Black-Phosphorus. In a single layer, each As or P atom is covalently bonded to three adjacent atoms. This non-centrosymmetric arrangement results in a strong in-plane anisotropy in the structure. The left side of Figure 1.9 (c) is the unit cell of KP_{15}, and the right side is the triclinic KP_{15} structure. As shown in the structure, one layer is composed of two anti-parallel P tubes, and the four P tubes are coordinated by K atoms. Each K atom is matched with a $[P_{15}]^-$ unit cell. $[P_{15}]^-$ a pentagonal arrangement of P atoms appears inside the unit cell. This arrangement leads to a high degree of anisotropy. GeAs (Figure 1.9 (d)) belongs to the GaTe structure, and its space group is C2/m. It is a new type of two-dimensional intra-layer anisotropic material. In the structure of GeAs, each Ge atom is coordinated by one Ge atom and three As atoms, and each As atom is coordinated by three Ge atoms. Therefore, there are two kinds of Ge-Ge bonds parallel and perpendicular to the b-axis. The two Ge-Ge bonds provide two different channels for electronic transmissions in the material, so that the optical response of the sample is angular and wavelength dependent. As shown in Figure 1.9 (e), GeSe belongs to the Pcmn-D_2h_{16} space group . Its arrangement is the same as that of B-As and BP, so it has strong in-plane anisotropy in terms of structure. ReS_2, $ReS_{2(1-x)}Se_{2x}$, and $ReSe_2$ belong to the twisted 1T structure. The crystal structure of $ReSe_2$ is shown in Figure 1.9 (f), in which diamond-shaped Re_4 aggregates along a zigzag shape due to the Peierls transition. Quasi-one-dimensional titanium trisulfide (TiS_3) is shown in Figure 1.9 (g). There are two lengths of Ti-S bond, the a-axis is 4.97 Å, and the b-axis is 3.43 Å.

1.3.2 Photoelectric Properties

Wang et al. grow the GeSe crystal by CVT and fabric the GeSe based polarization-sensitive photodetector. In Figure 1.10, it shows the photoelectric properties of GeSe. The photo response of GeSe is as high as 4.25 AW^{-1}. The photo currents with different bias are shown in Figure 1.10 (b). Figure 1.10 (c) and (d) are the linear polarized

photoelectric properties of GeAs. The anisotropy ratio of photocurrent is 1.09 at 532 nm, 1.44 at 638 nm, 2.16 at 808 nm. [34]

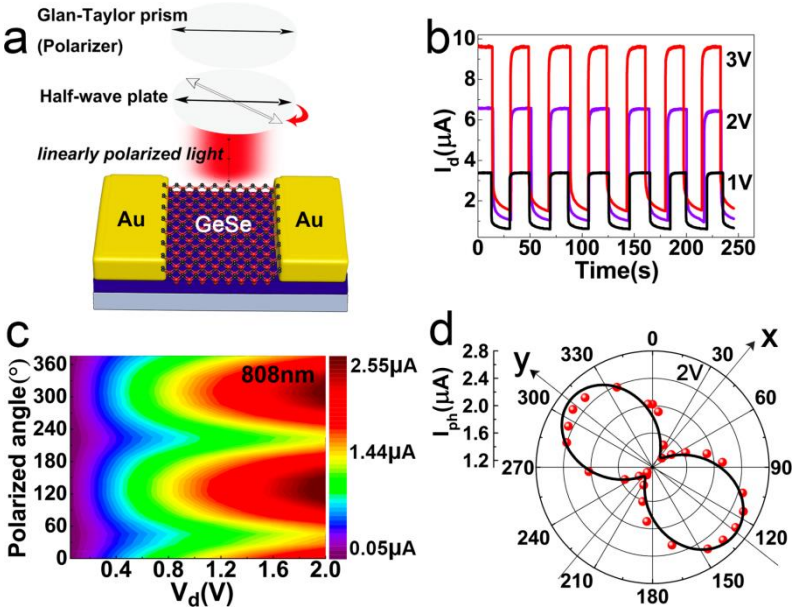

Figure 1. 10 The linear polarized photodetector of GeSe. (a) The Device diagram, (b) the I-T curves under different bais. (c) photocurrent map. (d) polarization-sensitive photocurrent in polar coordinate.[34]

1.4 Application of two-dimensional materials

1.4.1 Spin Light-Emitting Diodes (LED)

1.4.1.1 Principle of spin LED

The spin-LED is a LED with a spin injector deposited on it. The LED is generally a semiconductor heterostructure which includes a source of electrons (n-doped zone), a source of holes (p-doped zone), and intrinsic zone (non-doped). We called this heterostructure a PIN type structure. In spin-LEDs, the radiative recombination of spin-polarized electrons with unpolarized holes results in the emission of circularly polarized light. Figure 1.11 shows the schematic of a spin-LED used for electrical spin injection and optical detection. The analysis of the circular polarization of the emitted light makes

it possible to characterize the efficiency of the spin injection. Researchers often use LED structures comprising quantum wells or quantum dot structure based on InGaAs/GaAs system.

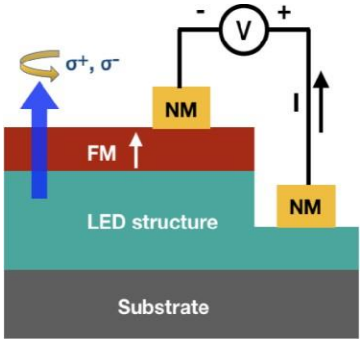

Figure 1. 11 Schematic of the spin-LED used for electrical spin injection and optical detection.

The optical detection of an electrically injected spin polarization in a semiconductor was demonstrated for the first time in 1999 independently by Fiederling et al.[35] and Ohno et al.[36]. Fiederling et al. successful fabric the GaAs-based spin-LED with a spin injector of BeMnZnSe (Figure 1.12 (a)) and measured the circular polarization of 90% under 6K (Figure 1.12(b)). Since the easy magnetization axis of the spin injector was in the plane, a strong magnetic field (1.5T) was applied to orientate the magnetization out of the plane. This is necessary to satisfy the optical selection rules in the case of optical detection from surface emission. A maximum degree of electroluminescence circular polarization noted $P = \frac{I_{\sigma+} - I_{\sigma-}}{I_{\sigma+} + I_{\sigma-}}$,where $I_{\sigma+}$and $I_{\sigma-}$ are the intensities of the right and left circularly polarized components of the luminescence, respectively.

Ohno et al. used a GaMnAs ferromagnetic semiconductor to inject spin-polarized electrons.[37] The device structure schematic and low temperature EL spectral are shown in Figure 1.13 (a) and (b). They obtained a spin injection into the GaAs with a circular polarization of the order of 10% at low temperature. Here, the magnetization of GaMnAs ferromagnetic semiconductor is in-plane. In this case, no need to apply an external magnetic field for edge light detection.

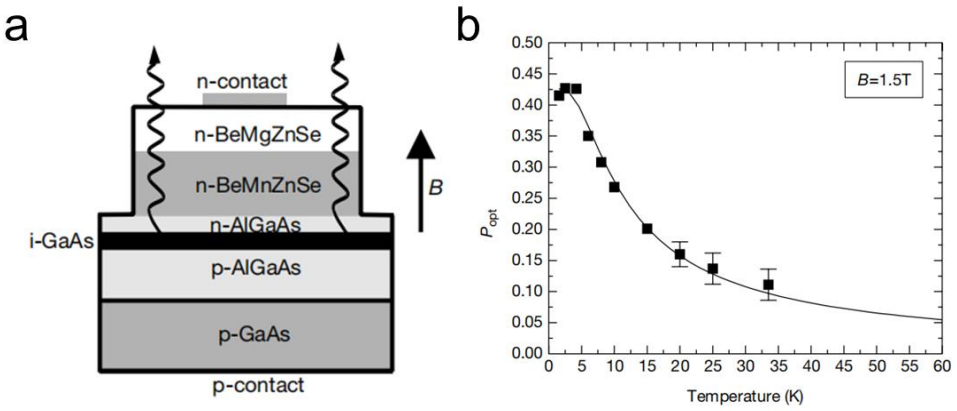

Figure 1. 12 (a)The device structure in side view, (b) Circular polarization of the electroluminescence with temperature varies.

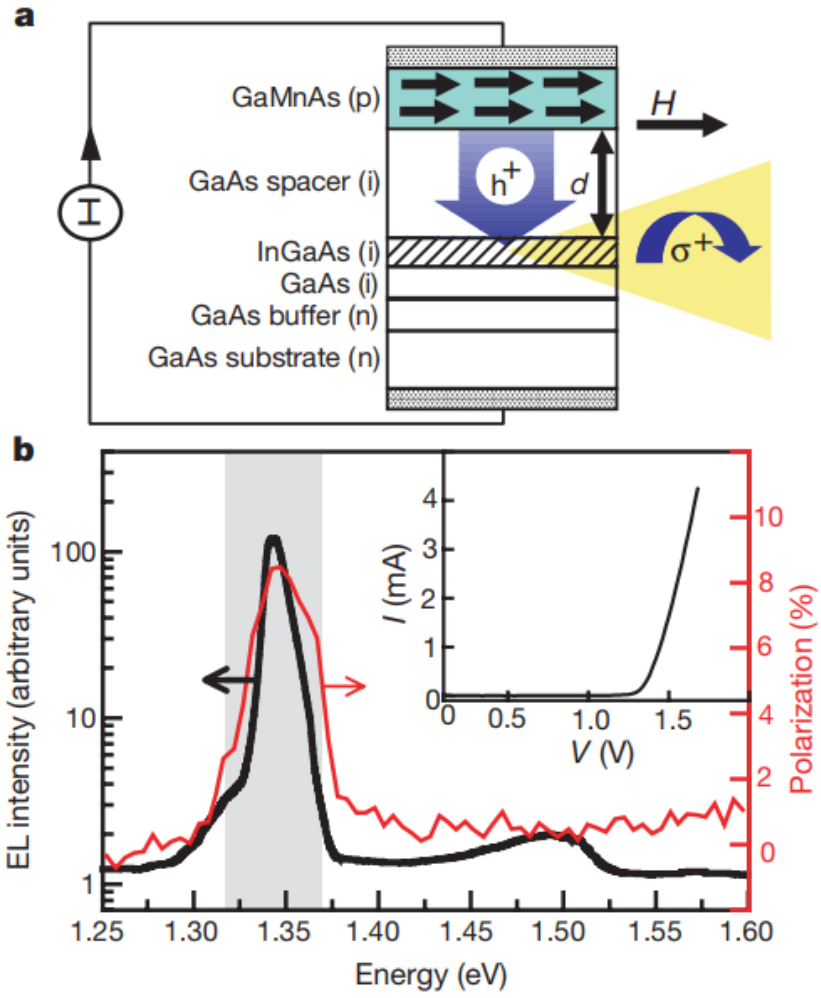

Figure 1. 13 GaAs-based spin-LED.

(a) The device structure, (b) Total EL intensity of the spin-LRD with its corresponding polarization under 6K temperature and 1000 Oe magnetic files.

Since these demonstrations, Spin LED have been extensively studied to enhance the output circular polarization, either by the improvement of spin injector for spin injection efficiency, or by the improvement of semiconductor part for longer spin relaxation time.

1.4.1.2 Spin Relaxation Mechanisms

The spin relaxation mechanisms in semiconductors mainly include the Elliott-Yafet (EY) mechanism, the D'yakonov-Perel (DP) mechanism, and the Bir-Aronov-Pikus (BAP) mechanism. EY mechanism originates from spin-orbit coupling. When electrons are scattered with changing the orbital angular momentum, spin flips may occur. All of impurity scattering, grain boundary scattering and phonon scattering may cause spin flipping. The DP mechanism plays a major role in semiconductor materials that lack inversion symmetry. Electrons will feel an effective magnetic field in the semiconductor. The magnitude and direction of the magnetic field depend on the momentum of the electron. The spin of electron processes around the effective magnetic field resulting in the relaxation of spin. The BAP mechanism origin from the electron-hole exchange interaction. The interaction of electron-hole exchange is determined by the spin carries, which is equivalent to the effective magnetic field acting on electrons. The electron procession along this effective magnetic field causes spin relaxation. In general, the EY mechanism is dominant in narrow band gap and strong spin-orbit coupling semiconductors. The DP mechanism is dominant in low hole concentration and intermediate band gap semiconductor materials. The BAP mechanism plays a major role at low temperature, while the DP mechanism plays a major role at high temperature. The relaxation of the hole spin is generally caused by the EY mechanism.

1.4.1.3 Spin LED in 2D Materials

Spin LED can be also realized by two-dimensional materials. Here, I will introduce some recent reported work in 2D spin LED.

Yu Ye et al. have experimentally demonstrated electrical generation and realized the control of valley polarization. These authors have also proposed new concepts of

electronic devices which combine both spin and valley polarization (Figure 1.14). The electrical excitation and the confinement of the carriers in a set of two non-equivalent valleys are obtained by manipulating the spin polarizations of the injected carriers. The optical selection rules give rise to polarized light emissions, circularly opposed according to the different excited valleys. The (Ga, Mn) As was used as a spin injector to inject spin-polarized holes.

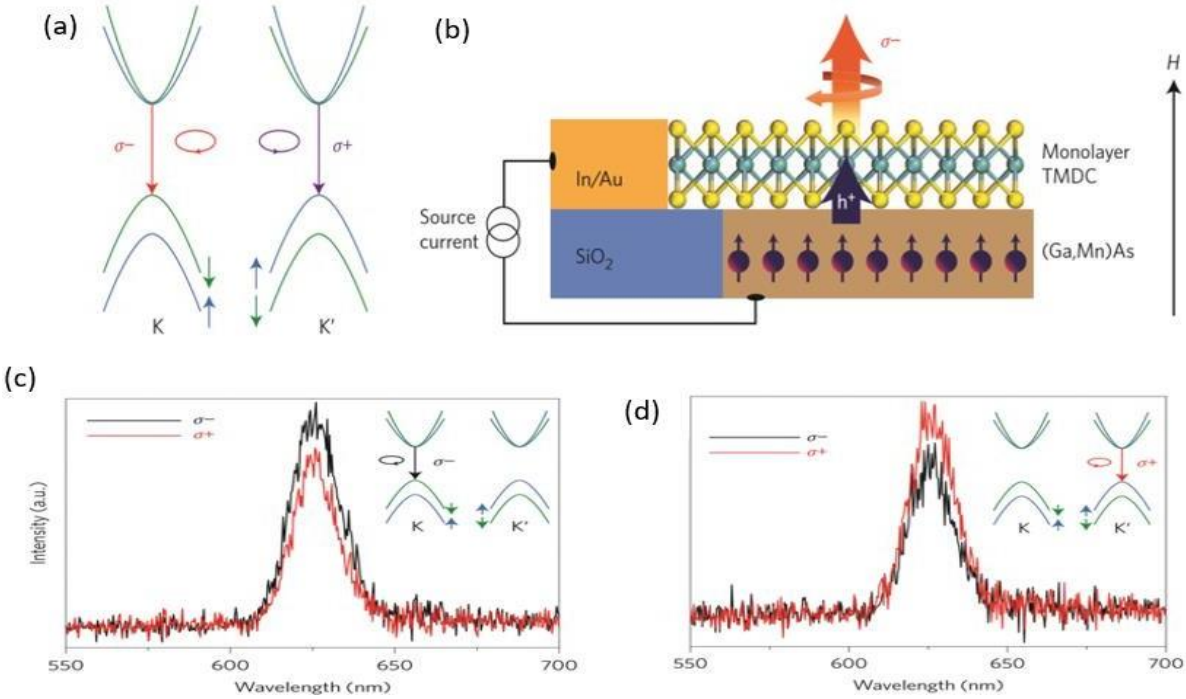

Figure 1. 14: (a) Electronic structure in the K and K 'valleys of the TMDCs monolayer. (b) Schematic of the single-layer TMDCs / (Ga, Mn) As device used for the electrical polarization of valleys. (c) Electroluminescence spectra polarized under an external magnetic field of 400 Oe perpendicular to the surface with a current of 15 µA. (d) Electroluminescence spectra polarized under an external magnetic field of 400 Oe perpendicular to the surface but inverted from (c).[38]

Due to the recombination between the electrically injected spin-polarized holes and the degenerated electrons in the TMDC monolayer, the valley polarization can be determined directly based on the emitted electroluminescence helicity. In the structure of WS_2/(Ga, Mn)As heterostructure, the polarization of electroluminescence is 16.2% at the peak indicating a strong valley polarization in the monolayer of WS_2 following

injections of spin-polarized holes under an external magnetic field of 400 Oe with a current of 15 μA. An opposite value of -14.8% is obtained under an internal magnetic field of 400 Oe applied in the opposite direction. The opposite magnetic field makes it possible to inject “down” spin holes and thus populate the inverted valley K', which results in the emission of σ^+ light[38].

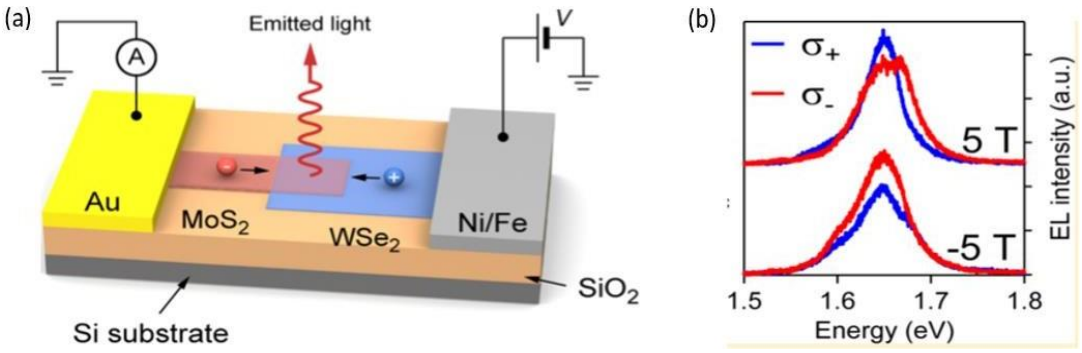

Figure 1. 15: (a) Diagram of the device. Under the application of a positive bias voltage to the Ni / Fe permalloy electrode, holes are injected from the permalloy electrode and recombine in the junction with the electrons injected from the side of the MoS2, which causes light emission. (b) Electroluminescence spectra of a spin valley LED for different values of magnetic fields, acquired for polarizations (σ +) and (σ−)[39].

In 2016, Oriol Lopez Sanchez et al. demonstrated the spin injection from a ferromagnetic electrode of permalloy NiFe into MoS_2 and WSe_2 heterojunctions by the lateral transport of spin-polarized holes in a monolayer of WSe_2 (Figure 1.15). The resulting valley polarization results in circularly polarized light emission, which can be adjusted using an external magnetic field. This demonstration of spin injection and magnetoelectronic control of valley polarization offers a new possibility to realize combined spin and "valletronic" devices based on "spin valley locking" in semiconductor TMDCs. Here, the circular polarization of the light emitted by ferromagnetic contact devices also contains a contribution due to the valley polarization in WSe_2 induced by the external magnetic field. For a 5T magnetic field, a degree of electroluminescence circular polarization of around 20% is achieved. After subtracting the contribution of the valley polarization in WSe_2 caused by the external magnetic field

(approximately 2.5% at 5 T), the spin polarization is approximately 17.5%, indicating the effective injection of spin-polarized carriers. This demonstration of spin injection in a 2D semiconductor-based heterostructure and tunable LED spin-valley via an external magnetic field provides a way to control the polarization of the valley in TMDCs materials without optical excitation. It could allow the emergence of new devices "Valleytronics" based on the electrical and magnetic control of valley polarization in 2D semiconductors. [39]

1.4.2 Spin photodiode

Spin-photodiode is operated in a reverse process as the spin-LED, i.e. an electrical detection of a spin-polarized current when a ferromagnetic/insulator/semiconductor heterojunction is illuminated by a circularly polarized light.

By illuminating a semiconductor with circularly polarized light, it is possible to generate spin-polarized carries. In a spin-LED, it can emit circularly polarized light when spin-polarized carries are injected. It was first identified in 1968 by Lampel [40]. Then, Pierce and Meier [41] used photoemission technology to optically detect spin-polarized electrons generated in GaAs using a Mott detector. For applications, the electrical detection of spin-polarized charge carriers generated by circularly polarized light is more practical. Figure 1.16 shows the schematic of optical spin injection and electrical detection [42]. According to optical selection rules, photo-generated carriers are generated when the semiconductor is irradiated with right or left circularly polarized light with the energy of the band gap. Photo-generated carriers travel to the FM and semiconductor interface and then enter the FM layer. Due to the spin filtering effect, the transmission probability depends on the electron spin direction. Therefore, the measurement of the spin-dependent photocurrent provides information about the spin-dependent transmission from the semiconductor through the interface and into the FM layer.

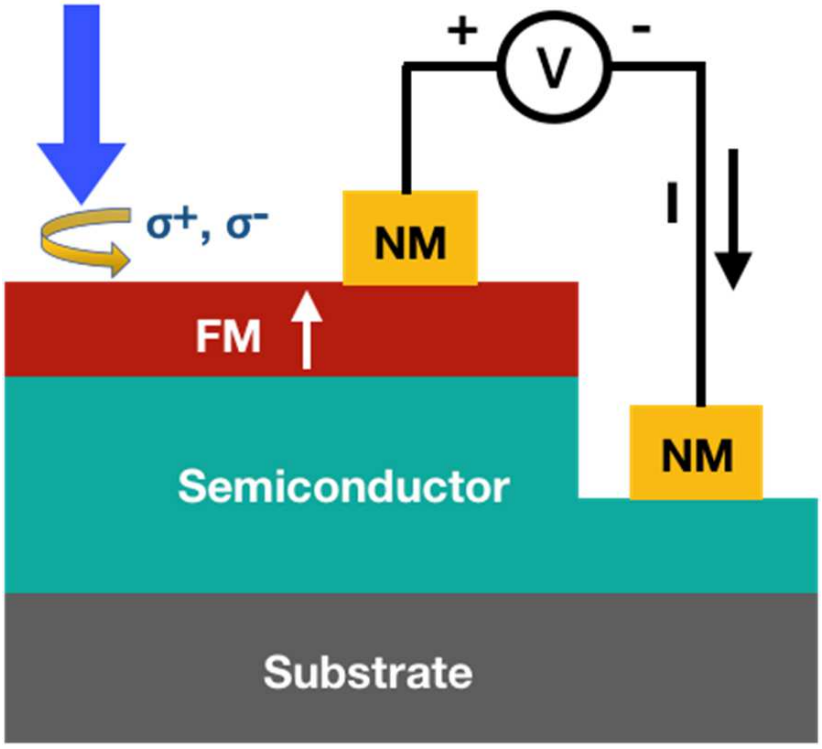

Figure 1. 16 Schematic of optical spin injection and electrical detection.[42]

Lu Xie et al. [43] have firstly report the spin photodiode in 2D WS_2 material.. Figure 1.17 (a) shows optical selection rules with imbalance of electron populations in the valleys K and K′. The spin-polarized photocurrent is obtained thanks to the rules of optical selection valley dependent and spin valley locking in the ML WS_2. In this work, Lu et al. have used a lateral spin valve detector consisting an Al_2O_3 tunnel barrier with Co/Pd ferromagnetic contacts (as shown in Figure 1.17 (b)).

As shown in Figure 1.17 (d), the photocurrent difference ($I_{\sigma+} - I_{\sigma-}$) shows a strong dependence on the FM electrodes magnetization. The photocurrent difference has an obvious spatial distribution pattern. It conforms to the optical selection rules of valley-dependent circular and the spin–valley locking in ML WS_2. The degree of polarization of the photocurrent is defined as the following formular: $P = (\frac{I_{\sigma+} - I_{\sigma+}}{I_{\sigma+} + I_{\sigma+}})$, where $I_{\sigma+}$ is the photocurrent measured under (σ+) and $I_{\sigma-}$under excitation (σ-). A degree of polarization of 15% for the holes and 7% for the electrons was measured, as shown in Figure 1.17 (f). The fit curve (blue lines in Figure 1.17 (f)) obtained by formular $P \sim P_0 e^{-(x/l_s)}$, where P_0 represent the peak polarization, x correspond to the

distance and l_s is the spin-free path. From the fitting curves, it demonstrated the P_0 = 0.15± 0.02, l_s = 1.7± 0.2 μm (holes), while P_0= 0.07± 0.01 and l_s = 1.3± 0.1 μm (electrons).

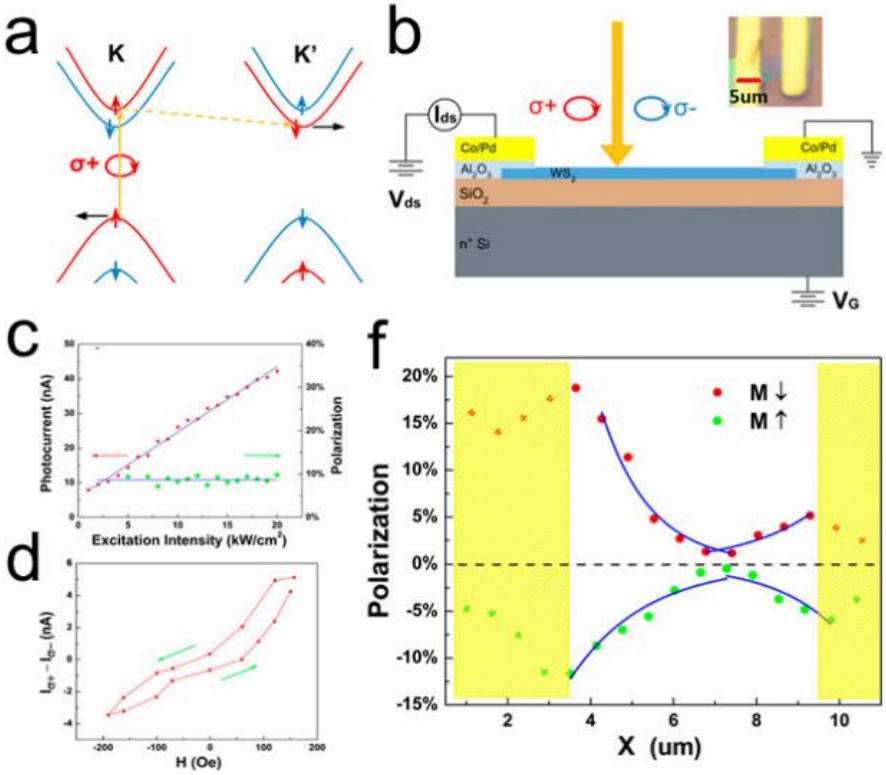

Figure 1. 17 (a) The Schematics of optical selection rules based on valley-dependent. (b) The Schematic of ML WS_2 based spin valve. (c) Photocurrent. (d) The curves of $I_{\sigma+} - I_{\sigma-}$with magnetic field. (f) The photocurrent polarization P with distance.[43]

1.4.3 Linear Polarized Photodetection

Linear Polarization detector is a new type of detector based on Fresnel reflection law. Compared to the traditional detectors, linearly polarized photodetector is angularly sensitive to the linearly polarized light. As shown in Figure 1.18, the light can be defined in two polarization states, that is s-polarization in the horizontal direction (blue light) and p-polarization in the vertical direction (red light).

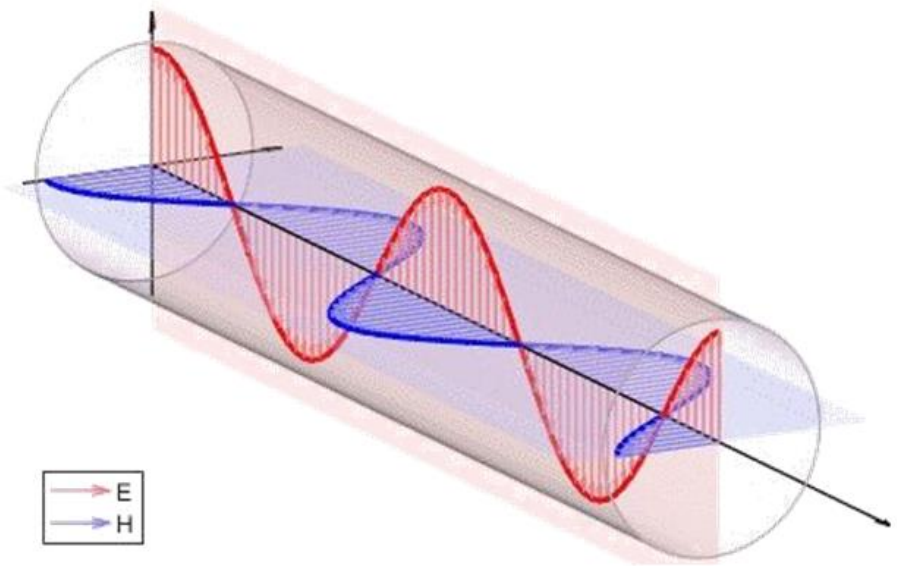

Figure 1. 18 The diagram of light.

According to Fresnel reflection law, the polarization of the light will change when a beam of natural light is reflected and refracted between two media. If a beam of light is incident at Brewster's angle, the reflected light is fully s-polarized light, and the refracted light is mainly polarized with p-polarization (as shown in Figure 1.19 (a)). The Brewster's angle is $\theta_p = \arctan(\frac{n_2}{n_1})$, where n_1 and n_2 are the refractive indices of the medium of the incoming beam and the other medium, respectively. Theoretical model diagrams light reflection and refraction in Bruce's law are shown in Figure 1.19. If a natural light is reflected and refracted by multiple air and glass sheets, the final transmitted light can be fully p-polarized light, as shown in Figure 1.19 (b).

Polarized light is prevalent in daily life, such as the strong light reflected on the road in the afternoon (Figure 1.20(a)). According to Brewster's law, the strong light mainly belongs to s-polarization light. In this case, the camera with the polarized detector which can filter s-polarized light can obtain the clearer road picture like Figure 1.20 (b). Therefore, the linearly polarized photodetector can allow to have a better detection of road in strong natural light environment.

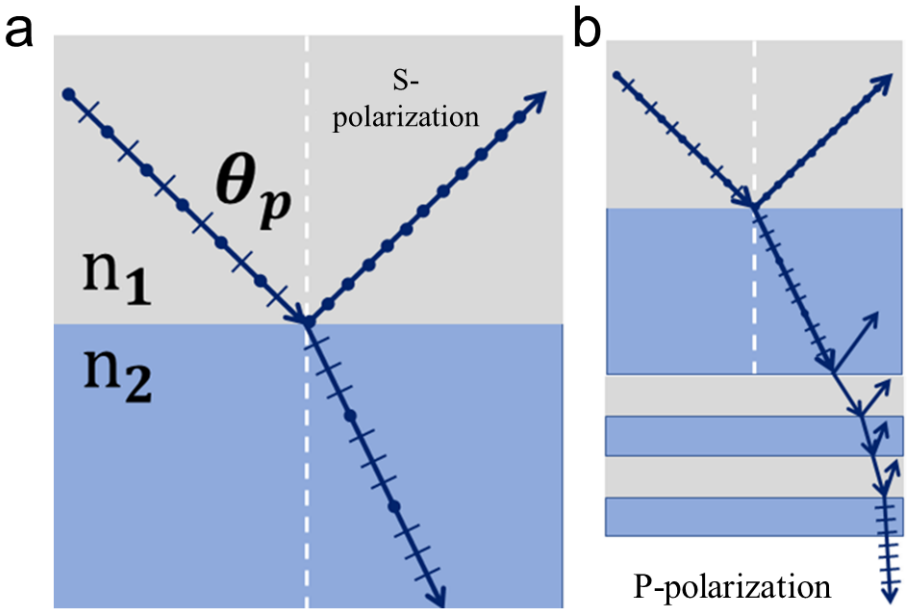

Figure 1. 19 Theoretical model diagrams of light reflection and refraction in Bruce's law. (a) Brewster's angle is θ_p. The reflected light is s-polarized light with incident angle of θ_p. The transmitted light after multiple reflection and refraction is p-polarized light.

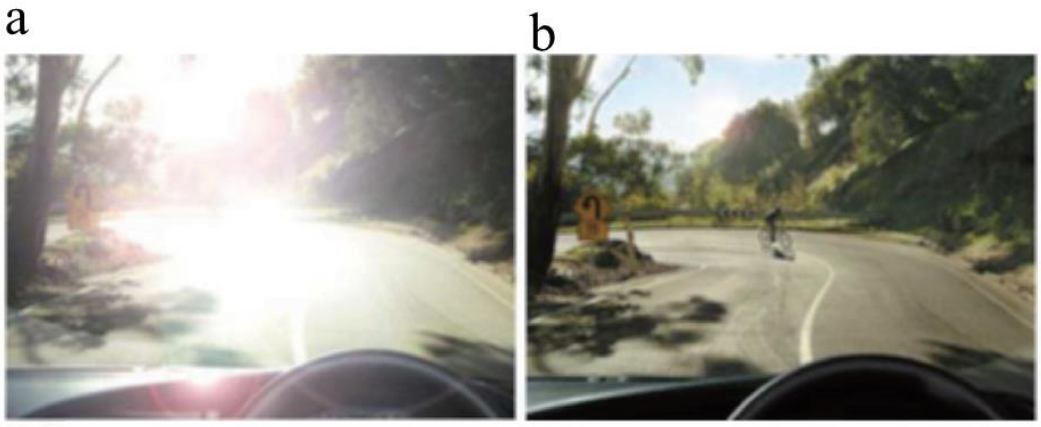

Figure 1. 20 (a) The road photo taken by ordinary cameras. (b) The road photo taken by polarization cameras

We can use polarization chip to obtain the polarization information in order to realize multi-dimensional polarization detection. Polarization chip integrates four sets of polarizers on the traditional detection pixel, with an angular interval of 45°. After detection of light, we can obtain 4 different polarization angle images, and the polarization information image is obtained through the Maitreyan matrix fitting. Polarization chip can detect material, stress, scratches, lesions and so on. One example

is used for polarized biological detection. Figure 1. 21 (a) shows the microscopic imaging of stained cells, which looks homogenous overall. However, the stained cells clearly show the red area where represents the cancerous area by polarization image in Figure 1. 21 (b).

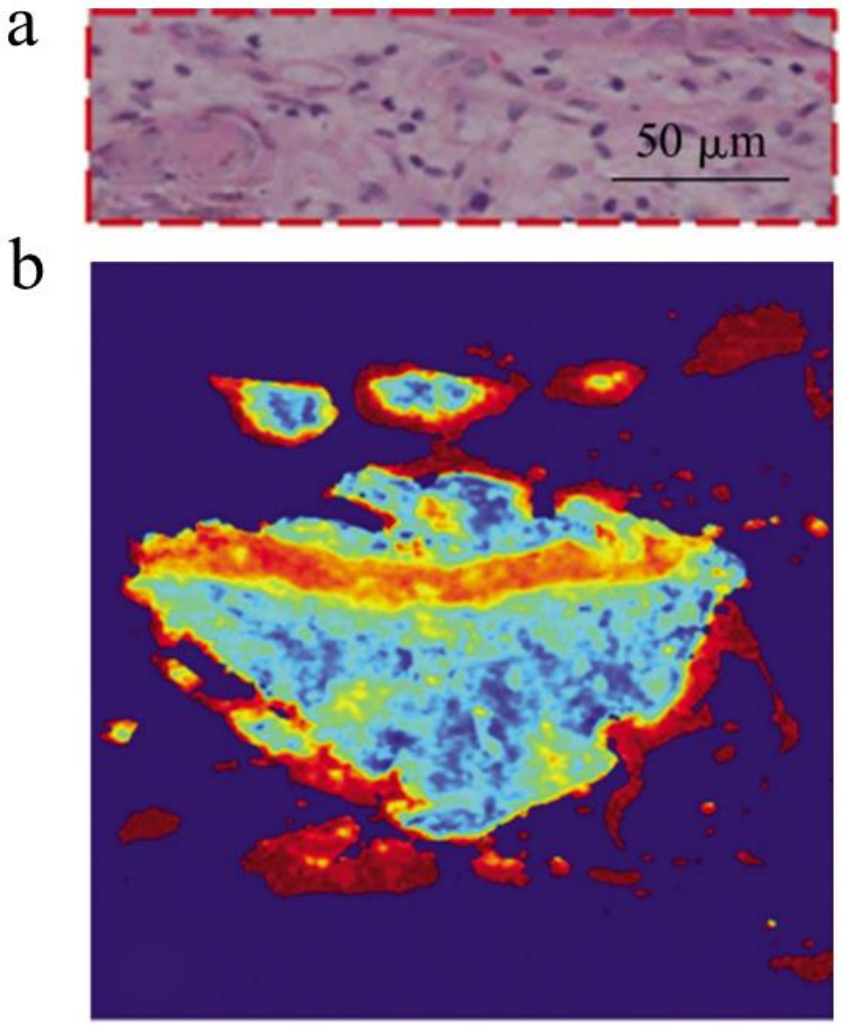

Figure 1. 21 Polarized biological detection. (a) Microscopic imaging of stained cells. (b) Polarization imaging of stained cells, the red area is the cancerous area.

With the gradual development of polarizing chips, researchers wondered whether they could find a kind of material with polarization sensitivity without the need of integrated polarizers. It has been found that low in-plane symmetric two-dimensional materials are angularly sensitive to polarized light and can realize polarization imaging detection. Figure 1. 22 shows the diagram of imaging system based on two-dimensional polarization detector. Polarization detector based on anisotropy 2D material could

detect the polarization state of polarized light, and can achieve precise resolution every 10°.

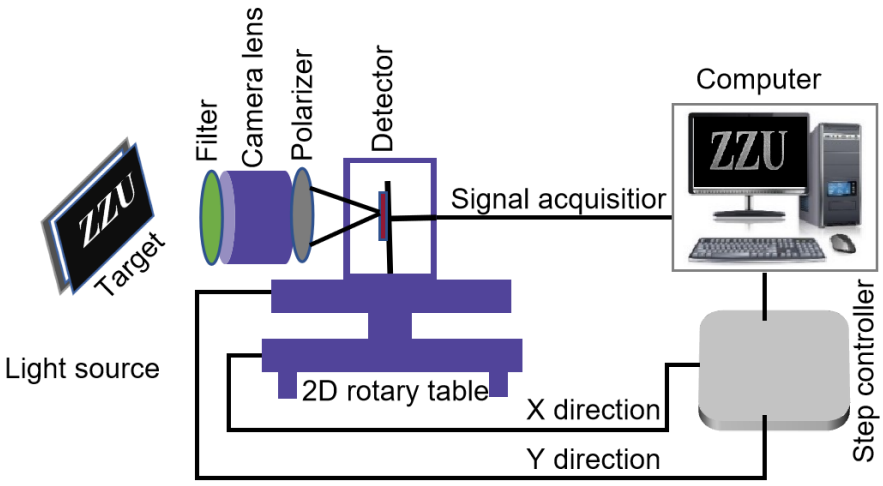

Figure 1. 22 The diagram of imaging system based on two-dimensional polarization detector.

1.5 Summary

This thesis focuses on two-dimensional materials in two aspects. One is the application of two-dimensional materials in Spin LED. We fabricated MgO/CoFeB/Ta heterostructure on monolayer MoS_2. By adjusting the thickness of the CoFeB film, the annealing temperature, and the material of the capping layer, the MgO/CoFeB/Ta structure shows a large perpendicular magnetic anisotropy (PMA) at zero magnetic field. Our experimental and theoretical results will promote the future development of room temperature spin optoelectronic devices based on 2D TMDCs with perpendicular magnetization spin injectors.

The other is the application of two-dimensional materials in linear polarization photodetectors. We chose the materials of GeAs and IV-VI compounds as the linear polarization photosensitive material and studied their optoelectronic properties. 2D materials of GeAs and SnS exhibit the large dichroism and photocurrent anisotropy. Our experimental will advance the application of 2D materials in linearly polarized photodetection.

Chapter 2: Experimental techniques

2.1 Synthesis of two-dimensional materials

2.1.1 Chemical Vapor Deposition (CVD)

Figure 2. 1 CVD sliding tube furnace.

Figure 2.1 shows the machine of the Chemical Vapor Deposition (CVD). The chemical vapor deposition method refers to a reaction process in which a chemical reaction occurs between chemical substances in the gas phase at a high temperature condition. The target compounds are gradually deposited on the substrate. CVD is also the most effective method to directly grow large-scale, single-layer or double-layer two-dimensional materials. The size, number of layers, doping and defect of two-dimensional materials can be controlled through combining different experimental parameters such as temperature, growth time, air flow rate, and tube pressure.

The concentration of reactants is the key to the growth process. The main method of controlling the concentration is to control the ratio of reactants and the flow rate of the gas during growth. For example, during the silicon growth, the precursors of the reaction are SiH_4 and H_2, and the flow rate of the precursors is controlled. High-quality

large-area silicon single crystals can be grown at the flow rate per cubic meter of 7.4×10^{-7} mol/s. For transition metal chalcogenides, the reactants are solid oxides and sulfur (selenium) powder. Taking MoS_2 as an example, the ratio of Mo source and S source directly affects the shape of growing MoS_2. As shown in Figure 1.7, A regular triangle structure (Mo atoms at the edges) is formed when Mo:S is greater than 1:2. When Mo:S equal to 1:2, it is a regular hexagon. When Mo:S is less than 1:2, it is an inverted triangle structure (the edges are S atoms). At this time, the ratio of Mo:S concentration is controlled by the gas flow rate of the carrier gas (Ar). The fast flow rate of Ar gas leads to a slower concentration of sulfur, while the slow flow rate of Ar gas leads to a higher concentration of sulfur.[44]

Temperature is the most important parameter in CVD growth. At the nucleation point of the gas and solid interface, high temperature controls the thermal process, and low temperature controls the mechanical process. In recent reports, when the upper triangle grows from the same nucleation point at the center of the bottom triangle, the temperature is higher than 800°C. In addition, temperature is also an important condition for controlling doping. Taking MoS_2 as an example, its CVD growth temperature is about 650°C. For doped MoS_2, a higher growth temperature is required. As reported by Li Bo et al, the growth temperature of Co-doped MoS_2 is around 680°C[45]。

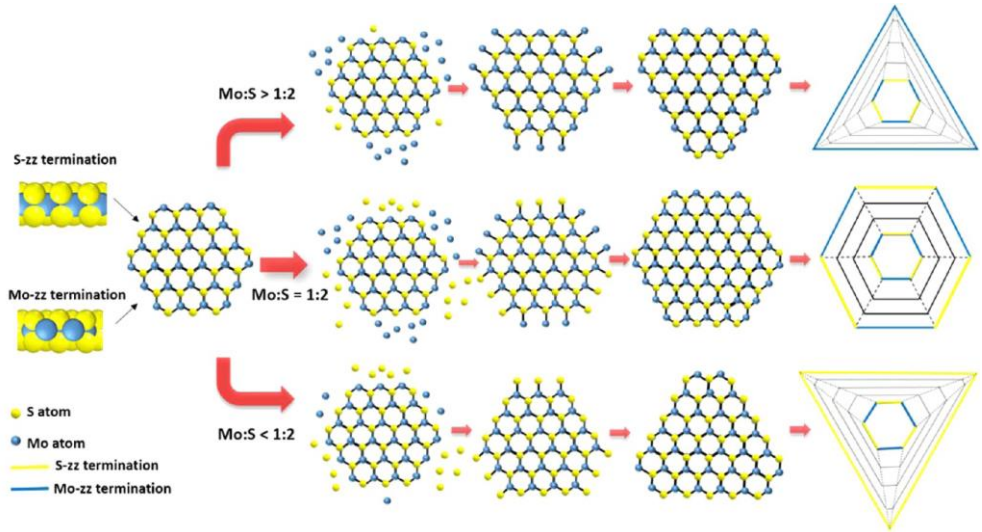

Figure 2. 2 The relationship between the concentration of Mo and S and the final morphology of MoS_2 grown by CVD.

In addition to reactant concentration and temperature, substrate is also the most important part of CVD. The main substrates are silicon wafers, silicon wafers with oxide layers, copper substrates, sapphire substrates, and mica wafers. Heavily doped silicon wafers with an oxide layer on the surface are the first choice for the growth of TMDCs two-dimensional materials. This is for the convenience and quickness of subsequent device preparation. Back-gate field effect transistors can be prepared in one step and the properties of the samples can be quickly obtained. Copper substrate and sapphire substrate are the first choice for large-scale growth. Because copper substrate and sapphire substrate have crystal orientation, the substrate with the same crystal orientation as the growth material can be selected before growth to reduce lattice mismatch and make the material easier deposit on the substrate.

2.1.2 Chemical Vapor Transport (CVT)

Figure 2. 3 Double temperature zone tube furnaces.

Figure 2.3 shows the physical picture of the dual-temperature chemical vapor transport equipment. Most of the chemical vapor transport equipment are dual-

temperature tube furnaces. The function of the dual-temperature zone is to provide a small temperature difference for the reaction zone, so that the sample is vaporized in the high-temperature zone and transported to the low temperature zone for growth. Similar to CVD, the chemical vapor transport (CVT) method is also one of the most important methods for growing materials. Unlike CVD, CVT mainly grows two-dimensional single crystal materials. The size of the bulk material is on the order of centimeters. And the crystal orientation is consistent. In CVT growth, there is no need for a substrate, and the reaction occurs in a high-vacuum (less than 1×10^{-3} Pa) sealed glass tube. The main control parameters are: growth temperature, growth time, reactant concentration, catalyst, etc.

During the CVT growth process, the range of growth temperature and growth time is wide. The selection of growth temperature is mainly determined by the evaporation temperature of the raw material and the growth temperature of the resulting material. In order to fully vaporize the raw materials in the glass tube and fully mixed, the temperature setting should firstly raise the dual temperature zone to be higher than the evaporation temperature of the raw material at the same time. Secondly, we reduce the temperature to near the growth temperature and maintain a temperature difference of 50-100 °C, which is beneficial to the gaseous reactants in the glass tube from high temperature flowing to the low temperature zone. The product will be synthesized near the low temperature zone.

The concentration of the reactants is the decisive factor for the success of the synthesis. The reactants in CVT growth are generally simple substances and a small part of chlorides. Taking SnS_2 as an example, the ratio of Sn:S in the glass tube is 1:5. Excessive S can fully combine with Sn[46] and act as a transport gas to enhance the saturated vapor pressure in the glass tube to obtain high quality SnS_2 crystals. If the ratio of Sn:S in the glass tube is 1:2, a mixture of SnS and SnS_2 can be grown. when the ratio of Sn:S is 1:1, Sn exists in the compound in a sub-state corresponding to SnS crystals. The carrier concentration of CVT grown single crystal is higher than that of CVD growth.

Catalysts are also an indispensable part of the reaction. Commonly used halogen

elements are used as catalysts. For example, high-quality MoS_2 generally uses liquid bromine (Br) as a catalyst. GeSe uses iodine as a catalyst (I_2). Chlorine (Cl_2) is also an catalyst for 2D crystal material growth.

2.1.3 Mechanical Exfoliation

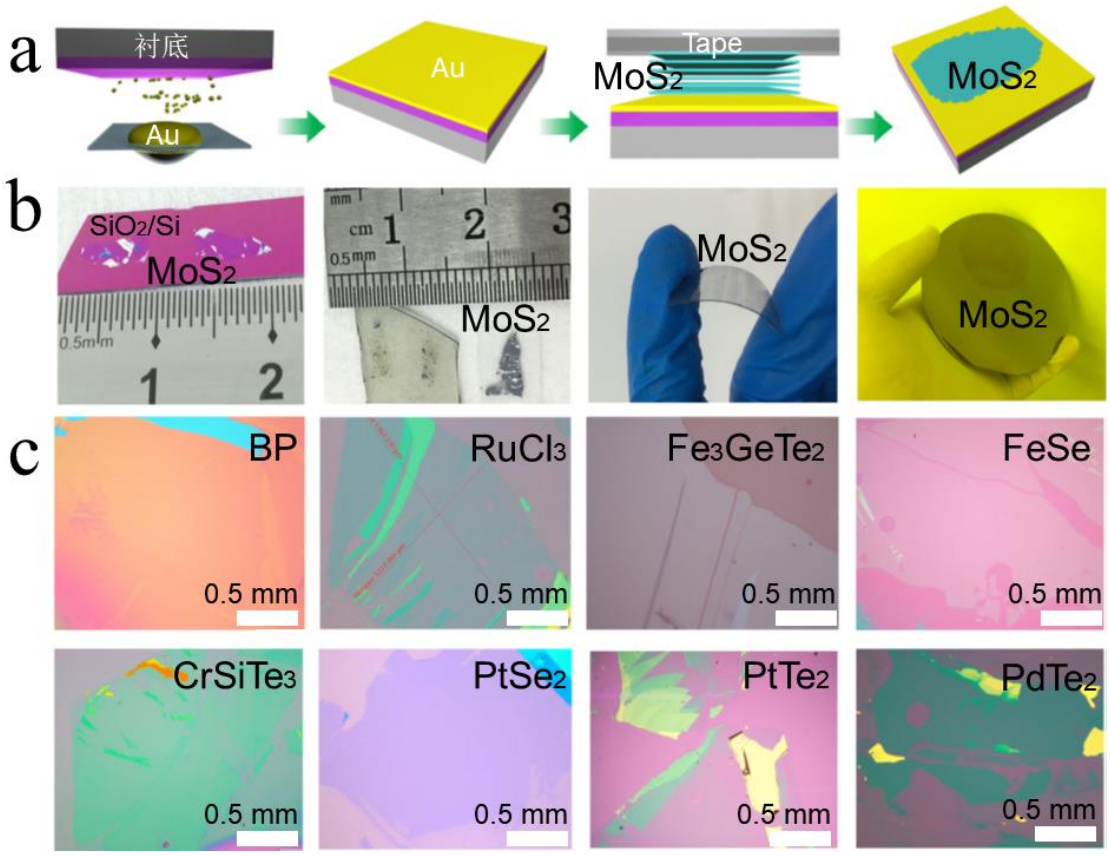

Figure 2. 4 Exfoliating large area of two-dimensional material on a thin gold substrate. (a) Operation process model diagram; (b) MoS_2 peeling experiment under different substrates; (c) Peeling experiment of other common two-dimensional materials.

The discovery of graphene relied on the mechanical exfoliation method. The directional thermally cracked graphite was placed on a transparent Scotch tape and pasted repeatedly to continuously divide the graphite into two sheets. Then the tape with graphite was pasted on the silicon substrate. At this time, since the adhesion force between the silicon substrate and graphite is greater than the van der Waals force between graphite layers, some thin graphite layers will stay on the surface of the silicon substrate.

With the continuous development of people's research, more and more exfoliation methods have been invented, such as high temperature, changing the tape, changing the substrate, and using PDMS. Among them, thin-film gold substrates are widely recognized and used for exfoliate large-area two-dimensional materials. The method is shown in Figure 2.4. Figure 2.4 (a) is the model diagram of the operation flow of the experiment. Firstly, 2 nm Ti/ 2 nm Au is deposited on the substrate successively. After the substrate is prepared, the tape with MoS_2 is placed on the substrate and lightly pasted. Remove the tape, that is, a large area of MoS_2 remains on the surface of the substrate. This experiment has been tried on different substrates as shown in Figure 2.4 (b). In addition, the researchers also tried other common two-dimensional materials in this way (Figure 2.4 (c)). They can obtain a wide range of uniform two-dimensional materials. This is because the binding energy of most two-dimensional materials with the Au (111) surface is greater than 1 eV, which is greater than the Van der Waals force between the molecular layers.

2.2 Synthesis of metal film

2.2.1 Molecular beam epitaxy (MBE)

MBE is a physical vapor deposition technique carried out in ultra-high vacuum. The principle is to use electron beam to evaporate the required materials in an ultra-high vacuum environment. After collimating through the small holes, a molecular beam is formed and sprayed onto a substrate to form a thin film. MBE generally has a very low deposition rate and can achieve epitaxial growth well. It can also be equipped with an in-situ characterization system (such as XRD and STM). During the growth process, the crystalline quality of the film can be monitored in real time (such as RHEED and LEED). MBE is an experimental technique that can realize the growth of single crystal thin films and can precisely control the thickness, composition, and morphology of the thin films.

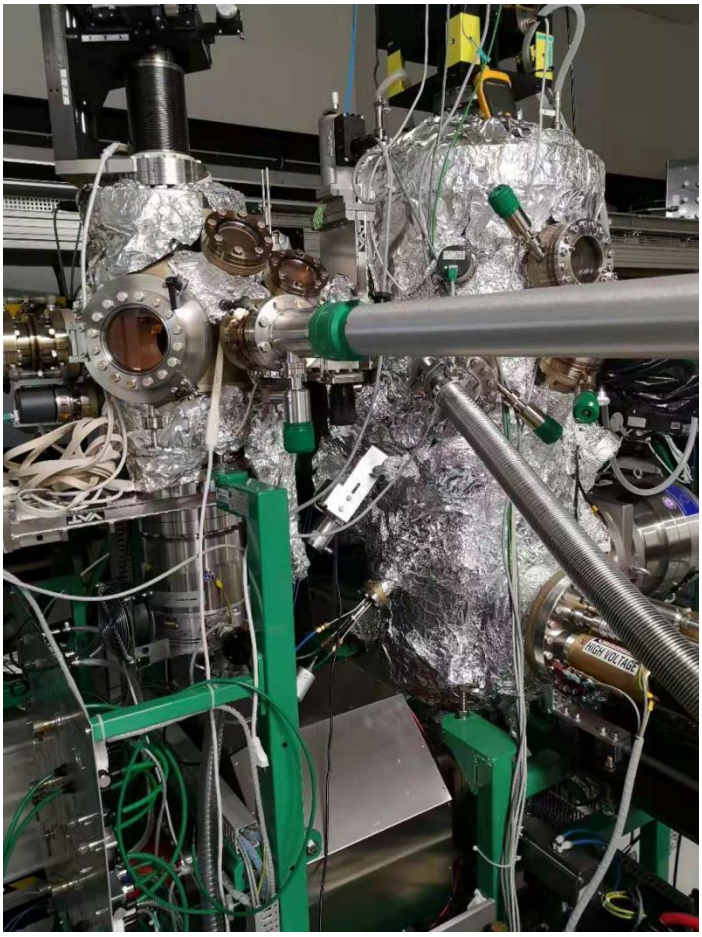

Figure 2. 5 The equipment of Molecular Beam Epitaxy

Figure 2.5 shows the molecular beam epitaxy system in the French Jean Lamour laboratory. Among them, MBE has six electron beam guns, which can grow Fe, Co, Au, MgO, CoFe, and other organic materials. The background vacuum is 10^{-10} torr.

2.2.2 Magnetron sputtering

Magnetron sputtering technology is a physical vapor deposition technology. The principle is to use the electric field between the target and the substrate to ionize the Ar gas. The ionized cations are accelerated under the action of the electric field and bombard the target of the cathode. In this process, ions and electrons will be generated and recollides with Ar to form Ar ions, thereby forming plasma. Finally, the sputtered target particles are deposited on the substrate to form a thin film. Because the efficiency of direct sputtering is very low, magnetron sputtering technology has been developed.

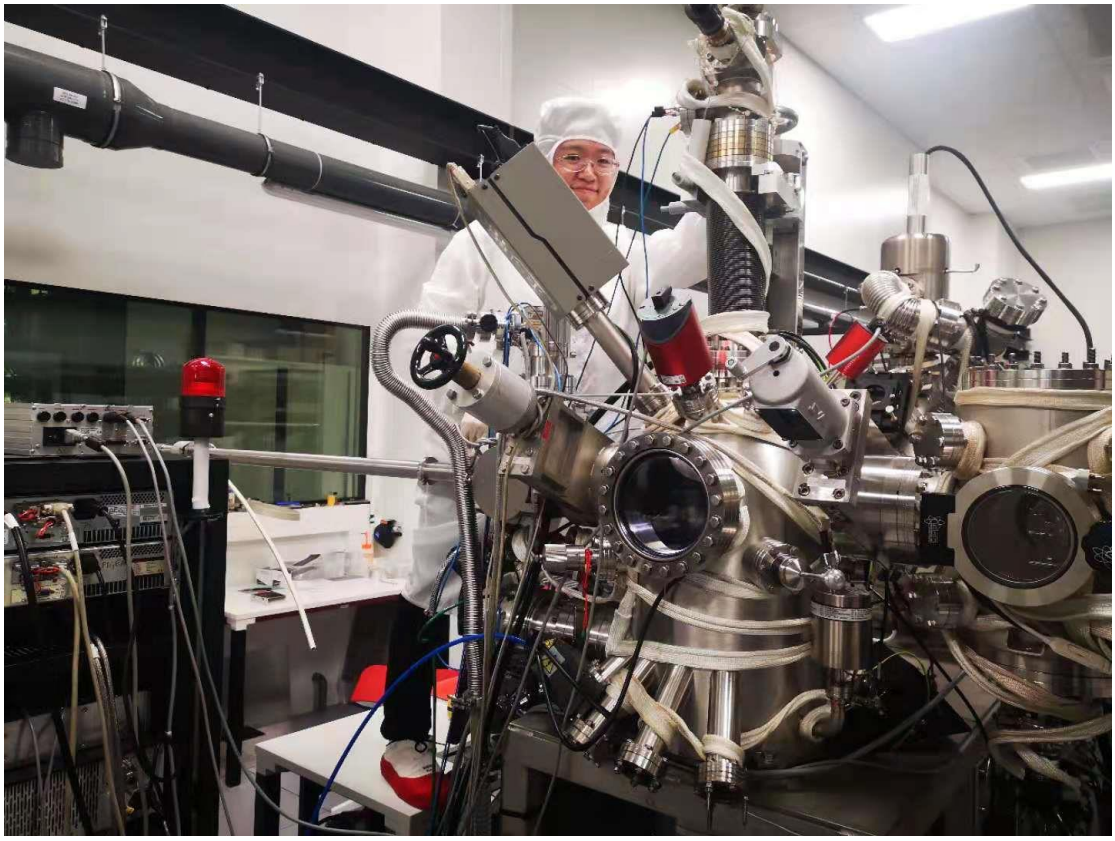

Figure 2. 6 The equipment of Magnetron Sputtering.

A magnetic field parallel to the target is added to the target area, and the electrons make a cyclotron motion under the action of the magnetic field. The electrons are bound near the target, which increases the collision probability with Ar and increases the ionization efficiency of Ar atoms. The bombardment efficiency can be greatly improved under low pressure, thereby improving the sputtering efficiency. Magnetron sputtering has the characteristics of high film formation rate, dense film formation, low substrate temperature, and strong film adhesion. It is widely used in industrial production and scientific research.

In magnetron sputtering equipment, sputtering is divided into two types: DC sputtering and radio frequency sputtering. DC sputtering refers to the addition of a DC electric field between the anode substrate and the cathode target, which requires the target to transfer the positive charge generated during the bombardment process to the cathode, so it is suitable for metal target sputtering. For the insulated target, it cannot neutralize the positive charge generated by the target during the bombardment process.

It will cause the potential on the target to increase, thereby reducing the ionization efficiency and even stopping the sputtering. Therefore, for the insulated target, radio frequency sputtering is required. In this method, a radio frequency voltage with a frequency of 13.56 MHz is generally applied to solve the problem of surface charge accumulation on the insulating target.

Figure 2.6 is the magnetron sputtering equipment used in this paper. The magnetron sputtering apparatus has two chambers: preparation chamber and growth chamber. The preparation chamber is used to prepare samples and connected to the vacuum tube. The growth chamber is used to grow thin films. There are three main targets that is MgO, CoFeB, and Ta. The vacuum of the growth chamber is 10^{-6} Pa. The target sputtering power is 120W. Sputtering pressure is 0.07 Pa. The sputtering rate of the target can be calibrated according to the growth time and the thickness of the grown film.

2.3 Micro-nano processing technology

Figure 2.7 is a schematic diagram of a device based on two-dimensional materials. Because two-dimensional materials are generally small, micro-nano processing technology is used to prepare devices and test them.

In the first step, a substrate with a mark is prepared. A layer of photoresist (S1813) is spin-coated on the substrate. The prepared marking pattern is projectively transferred to the photoresist using an ultraviolet lithography process.Then the metal is vapor-deposited on the surface of the photoresist through an evaporation process. Finally, the metal is stripped through the Lift-off process to obtain a substrate with a marked pattern metal.

The second step is the transfer of two-dimensional materials. The thin layer of two-dimensional material is transferred to the prepared substrate with markings. Here, CVD growth can be used directly, or transfer by the mechanical lift-off method introduced.

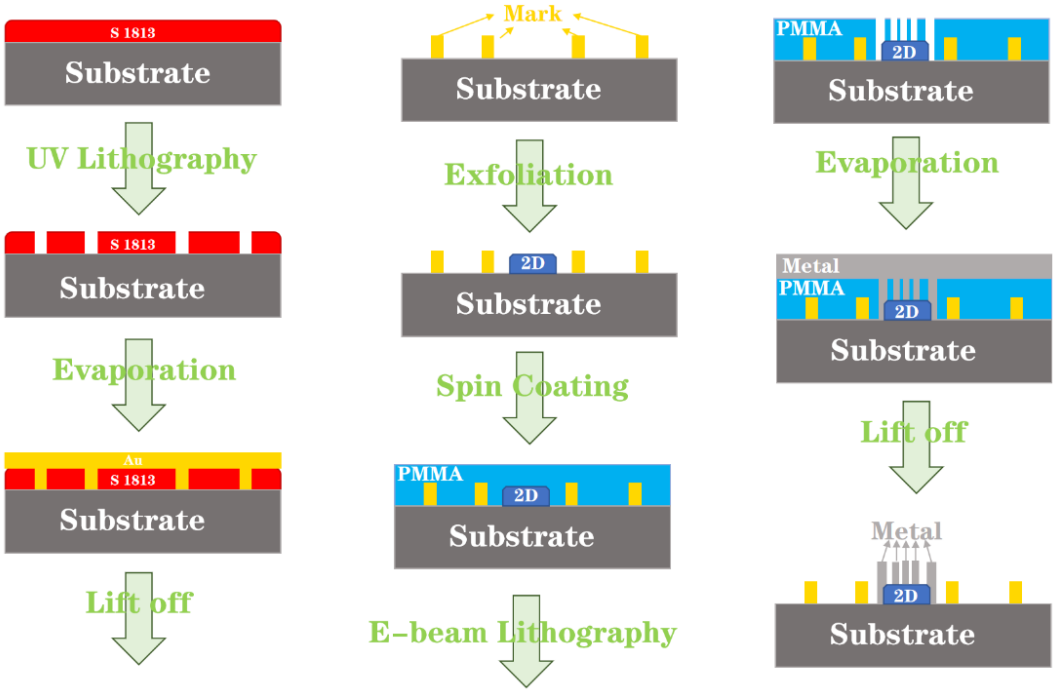

Figure 2. 7 Schematic diagram of two-dimensional material micro-nano processing. The substrate is 300nm SiO_2/n++ Si.

The third step is to prepare electrodes. A layer of PMMA is spin-coated on the two-dimensional materials. The prepared electrode pattern is transferred to the PMMA by the electron beam exposure process. Then the electrode preparation is completed by evaporation coating and Lift-off process. If the size of the two-dimensional material is larger (greater than 2 microns), the third step in the process steps can also be completed by an ultraviolet exposure process.

Below, I will introduce in detail the equipment involved in this process step.

2.3.1 Electron Beam Lithography (EBL)

Electron beam lithography is a high-precision exposure process. The principle is to use electron beams to directly scan, transfer, and copy graphics on the substrate with PMMA. Compared with ordinary lithography technology, electron beam exposure breaks through the diffraction limit of ordinary lithography. According to the theory of diffraction limit, the resolution of the exposure pattern is related to the wavelength of the light used in lithography. The shorter wavelength of light , the higher accuracy can

be achieved by photolithography. According to the matter wave theory, the wavelength of electrons is much smaller than ultraviolet light. The wavelength of an electron with an energy of 100eV is only 0.12nm. Therefore, the resolution of electron beam lithography can be as high as 10nm.

The process EBL includes: substrate cleaning → PMMA spin-coating → heating (130°C/3 minutes) → electron beam lithography→ development → fixing (IPA) → hard film. Figure 2.8 is the physical image of the EBL equipment used in this paper. This equipment includes: sampling chamber, exposure chamber (vacuum degree of 10^{-7} mbar), electron emission chamber (vacuum degree of 10^{-9} mbar). The equipment shown in the picture is the most used electron beam equipment in this paper, and its acceleration voltage can reach up to 30KV.

Figure 2. 8 E-Line Plus electron beam lithography machine.

2.3.2 UV lithography

The UV lithography machine in Figure 2.9 is the most used equipment in this laboratory, with a minimum line width of 2 microns. The photo-lithography process includes seven steps: substrate cleaning, photo-resistant coating, pre-baking (110°C/1 minute), exposure, development (sodium hydroxide solution), fixing (rinsing with

deionized water for 30 seconds), and post-baking. This lithography machine includes: a three-dimensional adjustable substrate platform, an optical alignment system, and an exposure system. The exposure mode is contact exposure. The advantages of photo-lithography are that the exposure time is short and the exposure area is large, which is suitable for large-scale preparation.

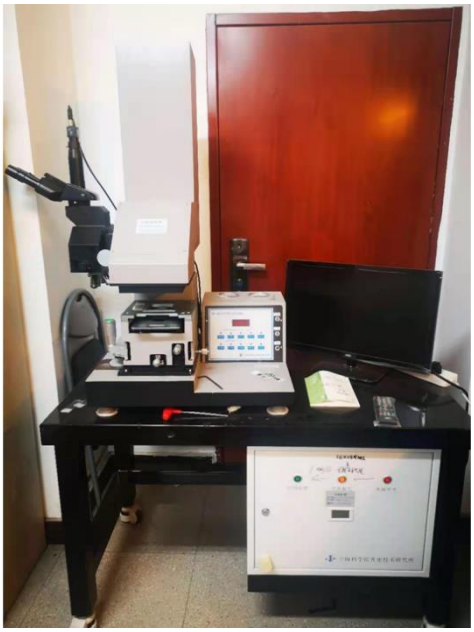

Figure 2. 9 UV lithography machine.

2.4 Basic characteristic parameters

2.4.1 Magnetic Film

Coercive force:

It means that after the magnetic material is saturated and magnetized. When the external magnetic field returns to zero, the magnetic induction intensity B does not return to zero. Only when a certain magnitude of magnetic field is added in the opposite direction of the original magnetization field can the magnetic induction intensity return to zero. This magnetic field is called Coercive magnetic field, also known as coercive force.

Saturation magnetization:

It refers to the maximum magnetization that a magnetic material can achieve when it is magnetized in an external magnetic field, called saturation magnetization. Saturation magnetization is a characteristic of ferromagnetic materials and an extremely important magnetic parameter of permanent magnetic materials. The saturation magnetization M_s is an extremely important magnetic parameter of permanent magnetic materials. For permanent magnet materials, It is better to obtain the high M_s. The saturation magnetization is determined by the number of magnetic atoms, the atomic magnetic moment and the temperature of the material. In the low temperature zone, it follows Bloch's law.

2.4.2 Photodetectors

Characterizing the performance of a detector often requires different characteristic parameters. Below I will introduce some common parameters.

Response time (τ):

The detector has two states, light state and dark state. When receiving light, a photocurrent (I_{ph}) is generated. And the detector output signal is large, which is the light state. When the detector is not illuminated, the current (I_d) generated by the device itself under a specific bias voltage is the dark state. The time required for switching in this state is defined as the response time. In the actual test, the response time is the time required for the dark state to turn into the bright state ninety percents, while the recovery time is the time required for the light state to turn into the dark state ninety percents.

Light response rate (R):

Under the light intensity of unit power, the sensitivity of the photocurrent of the detector, the unit is A/W. The calculated formula is

$$\mathrm{R} = \frac{I_{ph}}{P}(A/W) = (\eta \times q)/(h \times \nu) = \frac{\eta \times \lambda}{1.24}(A/W).$$

Quantum efficiency (η):

It is one of the most important indicators of the detector. It is defined as the ratio of the number of photoelectrons produced by the detector due to the illumination to the number of incident photons. The calculation formula is

$$\eta = (\frac{n_e}{n_{ph}} \times 100\%) = \frac{hc}{q\lambda} R 。$$

In an ideal state, when $\lambda<\lambda_c$, the quantum efficiency is 1. However, in actual tests, due to factors such as light reflection loss and carrier recombination, the quantum efficiency is generally less than 1.

Signal-to-noise ratio (SNR):

Under constant optical power light irradiation, the photoresponse current of the detector will fluctuate irregularly over time. This fluctuation of the photoresponse current is the noise of the detector. In the detector work, we define the optical signal as S, and the noise signal as N. At this time, S/N is the signal-to-noise ratio of the detector. For a single device, the larger photosensitive size of the device, the strongest optical signal and the higher the signal-to-noise ratio can be obtained. However, the high signal-to-noise ratio , which obtained by increasing S, does not indicate that the detector has good performance, so SNR has limitations.。

Noise equivalent power (NEP):

In order to eliminate the above-mentioned limitations in SNR, noise equivalent power is introduced. When the signal of the optical signal generated by the detector receiving the specific light power irradiation is equal to the signal of the noise signal (S/N=1), the specific power is the noise equivalent power. The calculation formula is

$$\mathrm{NEP} = \frac{P}{S/N} = \frac{I_{ph}}{R}.$$

At this time, the smaller the NEP value, the better the performance of the detector

Noise equivalent irradiance (NEI):

Considering the photosensitive area of the detector based on the noise equivalent power, it can be written as

$$\mathrm{NEI}=\mathrm{NEP}\sqrt{S}.$$

Detection rate (D):

According to people's habits (the larger value, the better performance), Jones proposed to use the reciprocal of NEP to determine the performance of the detector, which is defined as the detection rate. The formular is

$$\mathrm{D} = 1/\mathrm{NEP}(W^{-1}).$$

Specific detection rate (D^*):

The specific detection rate is also referred to as the detection rate in most of the current articles. Compared with D, it takes into account the sensitivity of the device . The calculation formula is

$$D^* = (R \times S^{\frac{1}{2}})/(2 \times e \times I_d)^{\frac{1}{2}}。$$

Linear Dichroism (LD):

Anisotropic crystals have angular dependence on the absorption of light. We define this as dichroism, which can be calculated by the formula.

$$LD = AU_{\max} / AU_{\min}$$

In the formula, the AU is the intensity of linear polarization absorption. The dichroism of a crystal is related to the wavelength of light. Generally speaking, the wavelength corresponding to the crystal band gap has the largest dichroism.

Extinction Ratio (EXT):

It is one of the important indexes to characterize the polarization performance of the polarization detector. Polarization detectors are highly sensitive to the angle of polarized light. Therefore, under the incidence of polarized light at different angles, the polarization detector corresponds to different intensities of photoresponse currents. The strongest photoresponse current is I_{phmax} and the weakest current is I_{phmin}. The ratio is the extinction ratio of the detector, and the calculation formula is

$$EXT = 10\log(I_{phmax}/I_{phmin})\ \mathrm{dB}.$$

Chapter 3: Ta/CoFeB/MgO on full coverage monolayer MoS_2

3.1 Background

TMDCs have emerged as a promising 2D crystal family, demonstrating solutions for several novel nano-electronic and opto-electronic applications[20, 47-52]. In contrast to graphene and BN, which are respectively a metal and a wide-gap semiconductor, TMDCs family displays a large variety of electronic properties ranging from semiconductivity to superconductivity[53]. As a representative of TMDs, MoS_2 has a tunable bandgap that changes from an indirect gap of 1.2eV in the bulk to a direct gap of 1.8eV for ML[47]. The ML MoS_2 is characterized by a large spin-orbit splitting of ~0.15eV in the valence band[49, 50] together with a small value of ~3meV for the conduction band[54]. The lack of inversion symmetry combined with the spin-orbit interaction leads to a unique coupling of the spin and valley degrees of freedom, yielding robust spin and valley polarization[20, 50-52].

To realize electron spin optoelectronic device based on monolayer MoS_2 [38, 39, 43, 55], one of the prerequisites is to realize a robust spin injector or detector with perpendicular magnetic anisotropy. There are two main reasons. First, for ML MoS_2, both the intrinsic spin splitting of the valence band and the Rashba-like SOC due to the breaking of the inversion symmetry along the growth direction favor the spin transport through MoS_2 with an out-of-plane spin polarization[56]. This is because that the SOC creates an equivalent perpendicular *k*-dependent magnetic field due to the Dresselhaus effective interactions and associated to the DP spin relaxation mechanism[57]. If electrons with in-plane spin polarization are injected into ML MoS_2, the effective magnetic field can induce an efficient in-plane spin precession along the field[58] as well as the spin-dephasing. Consequently, this yields a predicted short spin lifetime (10-200 ps)[59] together with a small spin diffusion length (~20 nm) [60]. Second, according to the optical selection rules[57, 61]in 2D materials, the magnetization of the

spin injector has to be maintained perpendicular to the sample surface in order to emit a circularly polarized light from the surface emission geometry. This usually requires a strong external magnetic field up to several Tesla to keep the perpendicular magnetization, which is not favorable for practical application. For example, recently, a hole spin injection into ML TMDs has been demonstrated either with perpendicular magnetized GaMnAs injector at zero applied magnetic field[38] or with in-plan magnetized NiFe injector at large perpendicular magnetic field[39] by electrical injection and optical detection method.

Different ways can be used to realize PMA FM layer on 2D materials. One way is to build FM 2D/TMDs VdWs heterojunction by using 2D transfer technology with PMA FM 2D materials such as CrI_3 [62], Fe_3GeTe_2 [63], and Fe-doped SnS_2[46]. This method can obtain a sharp interface and avoid interdiffusion between different layers. However, the Curie temperature (T_c) of these materials are often below room temperature and the size of junction is too small (around tens of microns) due to the exfoliation procedure. Another way is to use high curie temperature 3*d* FM metal on 2D materials, such as CoFeB[64] or Co[65]. However, the direct deposition of FM on 2D materials often introduces metal diffusion into 2D materials, and also the 2D materials will change semiconductor property to metallic property[66-68] due to the penetrating of metal DOS into the 2D materials[68]. An alternative good way is to insert an thin insulating layer between FM and 2D materials. This can one hand avoid the interdiffusion problem and on the other hand circumvent the conductivity mismatch between metal and semiconductor for efficient spin injection[69, 70].

By benefiting the interfacial anisotropy energy, the system of Ta/CoFeB/MgO is well known to exhibit strong perpendicular magnetic anisotropy. The origin of the PMA is due to the hybridization of Co(Fe) with O at the interface of CoFeB/MgO[71]. This system has been already established in metallic MTJ system[72] and GaAs substrate for spin LED[73-77]. However, no report until now on the 2D system. In this work, we report for the first time to elaborate Ta/CoFeB/MgO structure with PMA on full coverage ML MoS_2. The success for fabrication of this structure will have following

important impacts. First, one can fabricate high density spintronics devices with UV lithography on large surface substrate. Second, compared to the exfoliation method, since we can use top to down lithography procedure to fabricate the device, a clean interface between CoFeB/MgO and MgO/MoS_2 can be conserved, which is especially important for efficient spin injection[70, 78] and the contact problem between of FM and 2D can also be definitively resolved[79].

3.2 Heterojunction Processing and characterizations

3.2.1 Heterojunction Processing

Monolayer MoS_2 was grown by chemical vapor deposition (CVD) using highest purity (6N) gases and precursors on SiO_2 substrate (purchased from 2D semiconductor Inc.). The MoS_2 substrate is firstly introduced into an MBE system to perform an annealing at 150°C during 1h to desorb the water and CO_2 on the surface (MBE is shown in Figure 3.1 (b)). When the sample is cooled down to RT, the sample was transferred to another sputtering system (with a base pressure of 5×10^{-8}torr) without breaking the vacuum (sputtering is shown in Figure 3.1(a)). Multilayer stack with the structure of MgO (1.5nm) /$Co_{0.4}Fe_{0.4}B_{0.2}$ (1.2nm) /Ta (5nm) was deposited at RT. After taking out the sample from the vacuum, we have performed RTA treatment on the sample at different temperatures for 3min (The RTA is shown in Figure 3.2).

Figure 3.1(a) shows magnetron sputtering, which includes: transmission chamber, growth chamber, vacuum system, water cooling system, gas path system and control system. One end of the transmission chamber relates to the vacuum tube, and the other end relates to the growth chamber. There are three target positions in the growth chamber of this equipment, like MgO, CoFeB and Ta.

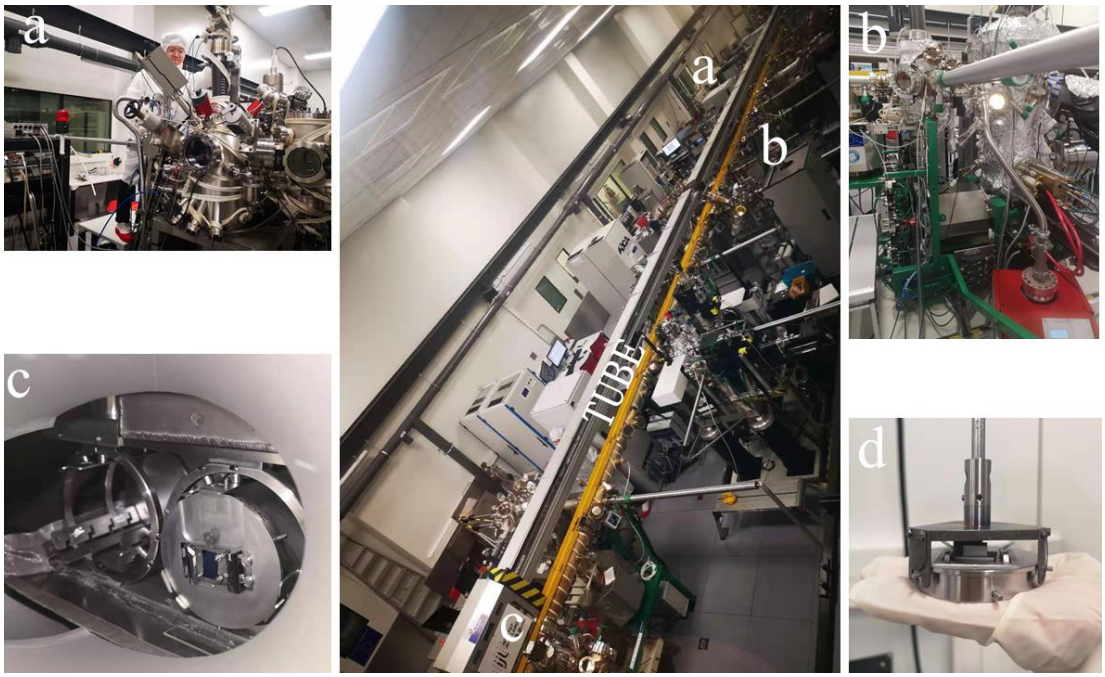

Figure 3. 1 Vacuum interconnection system (a) Magnetron sputtering; (b) MBE; (c) vacuum pipeline transport vehicle; (d) sample transfer system.

Figure 3.1 (b) shows the MBE equipment. The equipment includes: mobile transfer rod, transfer chamber, growth chamber, vacuum system, water cooling system, RHEED and control system. Among them, the mobile transmission rod can be detached from the MBE to connect to the glove box, so that the sample has no air contact during the whole process; the transmission chamber is connected to the mobile transmission rod, the vacuum tube, and the growth chamber, and has the function of transfer and storing samples. The growth chamber is the core of MBE, the vacuum in the growth chamber is 10^{-10} mbar, and it contains 6 crucible positions. MBE can realize temperature-controlled growth. The sample holder can be heated to 800°C or cooled to liquid nitrogen temperature. The sample holder can be rotated to increase the uniformity of the deposited film. The working principle is that the vaporized metal source is heated by the electron beam to evaporate into a gaseous body. The free path of the gas molecules in the growth chamber is longer than the distance between the metal source and the substrate. Therefore, the vaporized gas molecules can follow a straight line to the surface of the substrate.

Figure 3. 2 Rapid thermal annealing equipment (RTA).

The left picture shows the appearance of the RTA, and the right picture shows the annealing chamber.

Figure 3.1 (c) shows the transport trolley in the vacuum pipeline. There are 9 sample positions on each trolley. The method of picking and placing samples on the trolley is shown in Figure 3.1 (d). All devices are equipped with transmission rods. The transmission rod head is set with a three-point buckle, which can stably take the sample holder.

3.2.2 STEM-EELS

HR-STEM combined with spatially resolved EELS was performed by using a probe-corrected microscope JEOL ARM200F (cold FEG) equipped with a GATAN GIF quantum energy filter to reveal the structure and element distribution in the spin-injector before and after annealing. The microscope was operated at 200kV. High angle annular dark-field (HAADF), annular dark-field (ADF) and bright-field (BF) images were simultaneously recorded for structure study while only HAADF signal was recorded during EELS chemical analysis. Thin lamella was extracted by focused ion beam (FIB) milling using an FEI Helios Nanolab dual beam.

3.3 Experimental results and discussion

3.3.1 Monolayer MoS_2 characterization

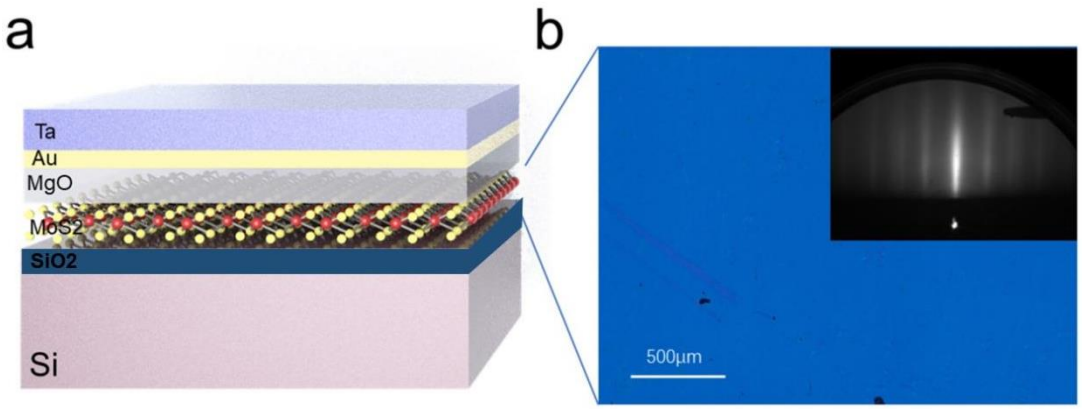

Figure 3. 3 Schematic structure of sample.

(a) Schematics of MoS_2/MgO/CoFeB/Ta stacks on Si/SiO_2 substrate. (b) large scale optic microscopy image of the surface of monolayer MoS_2. Inset: RHEED pattern of MoS_2 surface after annealing at 150°C for one hour. The pattern does not change with different angles.

Figure 3.3 (a) schematically shows the prepared heterostructure of SiO_2//ML MoS_2/MgO (1.5nm) /CoFeB(1.2nm)/Ta (5nm). The full coverage MoS_2 substrate was firstly checked by optical microscope and it shows a uniform contrast on the whole surface ($1\times1cm^2$) (Figure 3.3 (b)).

RHEED has been performed to verify the crystalline properties of MoS_2 ML after annealing at 150°C in an MBE chamber. The RHEED pattern shown in the inset of **Figure 1b** displays a sharp stripe character proving a high crystalline quality of the monolayer MoS_2 and a very smooth surface. Since the RHEED pattern almost does not change with different incident angles of the electron beam, the MoS_2 layer remains mainly in a textured structure with some preferable orientations in the plane[80].

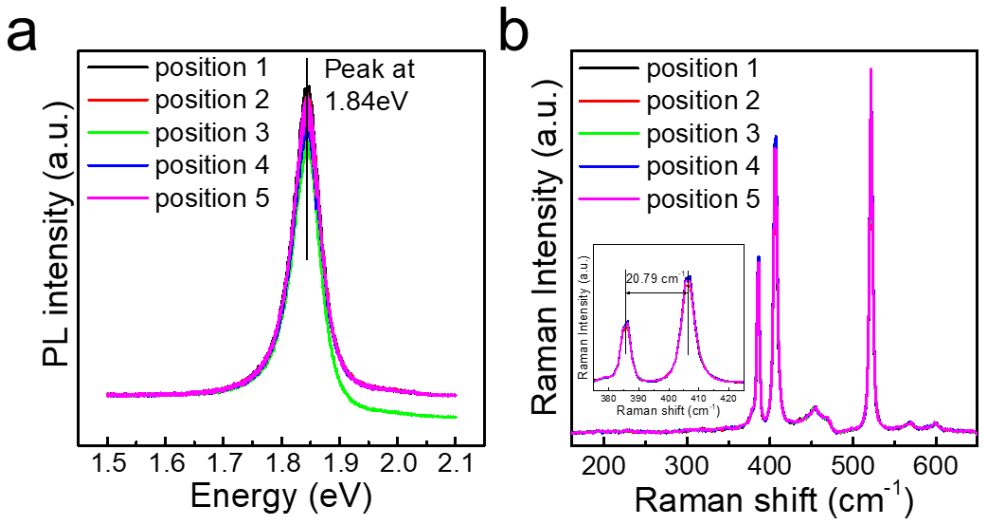

Figure 3. 4 Characterization of monolayer MoS_2.

(a) Room temperature photoluminescence spectra taken on different position of ML MoS_2 surface. (b) Raman spectra taken on different positions of ML MoS_2 surface. Inset: Enlarged spectra to show the distance between E^1_{2g} and A_{1g} modes.

To prove the monolayer character and verify the homogeneity of the MoS_2 film, we have performed characterizations with PL and Raman spectra at room temperature. Figure 3.4 (a) shows the PL spectra in different positions of film. A strong single peak centered at 1.84 eV proves the direct bandgap for the MoS_2 layer, which is almost identical for 5 different positions on the film. Figure 3.4 (b) shows the Raman spectra with laser wavelength of 325 nm. We can find different scattering mode of phonon. The distance between E^1_{2g} mode and A_{1g} mode is about 20.79 cm^{-1}, which is well corresponding the character of monolayer MoS_2 [81].

3.3.2 The Heterojunction of MoS_2/MgO/CoFeB/Ta

The advantage using the full coverage MoS_2 substrate allows us to characterize the magnetic property of sample directly by superconducting quantum interference device (SQUID) magnetometry. To obtain an ultrathin CoFeB layer with PMA on MoS_2, we have optimized CoFeB thickness and annealing temperature (T_{an}).

Figure 3.6 (a) displays the out-of-plane magnetization *vs.* external magnetic field (*M-H*) curves for annealed spin-injectors (T_{an}=250°C) with different CoFeB thicknesses

measured at 10K. From 1nm to 1.2nm, the saturation field quickly decreases and the remanence increases with the increase of CoFeB thickness. However, when the thickness is larger than 1.2nm, the saturation field increases and the remanence decreases with the increase of CoFeB thickness. This can be understood that the CoFeB layer is discontinued and it exhibits a superparamagnetic character with a thickness lower than 1.2nm. When the thickness is larger than 1.2nm, the CoFeB can form continuous film exhibiting ferromagnetic property.

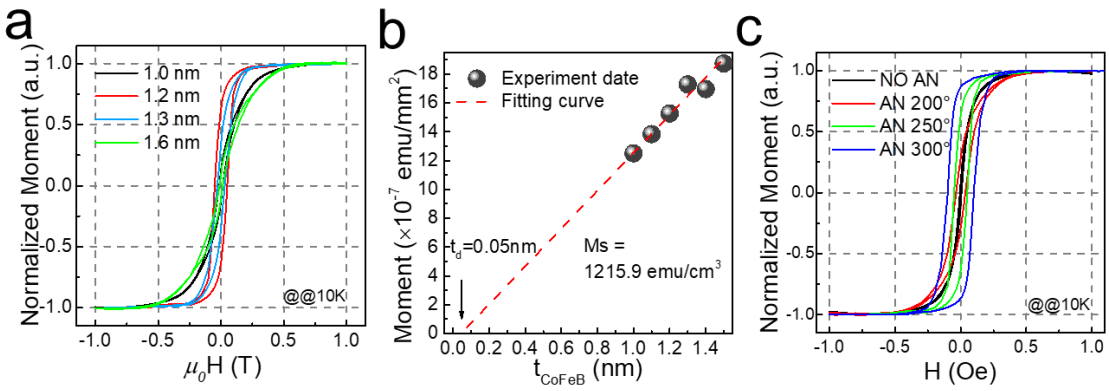

Figure 3. 5 Magnetic characterization of MoS_2/MgO/CoFeB/Ta heterostructure. (a) Out-of-plane M-H curves for samples with different CoFeB thicknesses with Tan=250°C measured at 10K. (b) Extrapolation of CoFeB magnetic dead layer td from the CoFeB thickness dependent saturation magnetization Ms. (c) Out-of-plane M-H curves for the sample with 1.2nm CoFeB before and after different temperature annealing measured at 10K.

To understand the role of interface anisotropy to establish PMA, we need to study the effective anisotropy energy as a function of CoFeB thickness. Since it is reported that there exists a magnetic dead layer which is attributed to the intermixing at the top Ta/CoFeB interface during deposition or upon annealing[82], we need firstly extract the thickness of dead layer (t_d) and the saturation magnetization (M_s) from the fitting of magnetization as a function of CoFeB thickness. As shown in Figure 3.5 (b), the M_s is extracted to be 1216 emu/cm^3 from fitting the thickness dependent magnetization. The dead layer thickness t_d is determined by extra-plotting the fitting line to zero magnetization, and is found as thin as 0.05nm, which is much smaller than the reported

value of 0.5nm[74]. This could be related to our specific deposition condition of film.

A precise control over the annealing temperature T_{an} is also an important factor to obtain a good PMA property. Figure 3.5 (c) displays the comparison of the out-of-plane M-H curves for the 1.2nm thick CoFeB sample with different T_{an}. The optimized annealing temperature is found to be around 300°C. The CoFeB coercivity and remanence gradually increase with the annealing temperature up to 300°C, then decrease after the annealing at 350°C. As already investigated theoretically by Yang et al., the PMA is very sensitive to the Fe(Co)/MgO interface chemical structure. The improvement of PMA at Tan up to 300oC could be attributed to an optimization of the interfacial chemical structure and crystallization of CoFeB at CoFeB/MgO interface. When T_{an} exceeds 300°C, Ta species start to diffuse through the ultrathin CoFeB to MgO interface and significantly damage PMA.

In order to observe the changes of PMA in detail, I will give the *M-H* curves of CoFeB thickness and annealing temperature at room temperature and low temperature in Figure 3.6 and Figure 3.7.

The thickness of CoFeB is one of the important parameters in PMA. The *M-H* curves of 1nm to 1.6nm are measurement in 10K and RT and shown in Figure 3.6 (a) to Figure 3.6 (g). Figure 3.6 (h) is the magnetic anisotropy between out-plane and in-plane. As shown in Figure 3.6 (h), the effective anisotropy energy density per unit volume (K_{eff}) *vs.* the effective CoFeB thickness (t_{eff}=t_{CoFeB}-t_d) can then be plotted from the integrated difference between the out-of-plane and in-plane *M-H* curves. It can be observed that the 1.2nm CoFeB is the optimal thickness to obtain PMA.

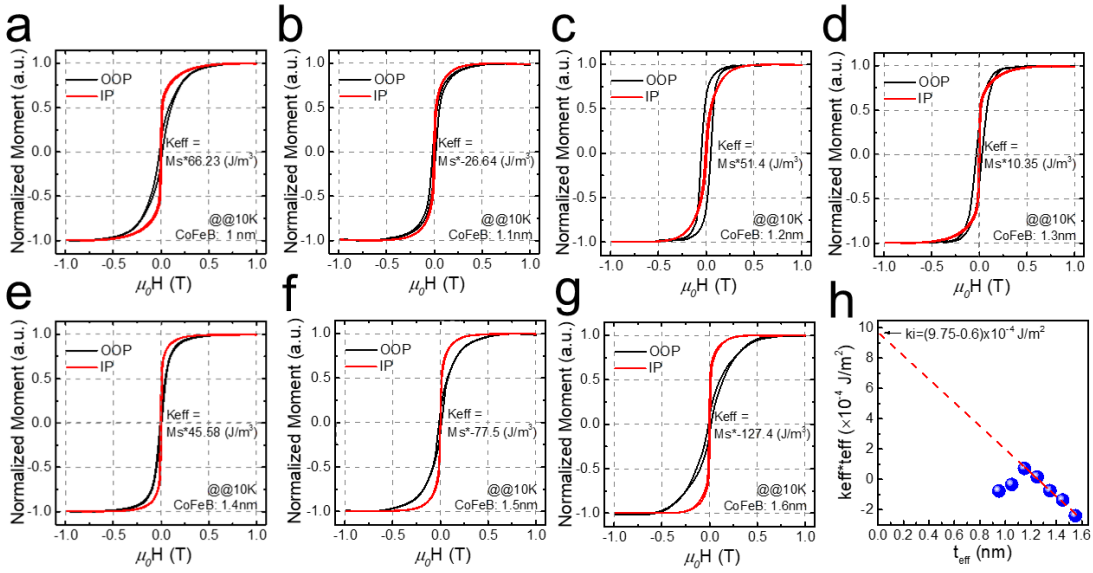

Figure 3. 6 (a-g) Out-of-plane and in-plane M-H curves for samples with different CoFeB thicknesses with Tan=250°C measured at 10K. (a) 1nm, (b) 1.1nm, (c) 1.2nm, (d) 1.3nm, (e) 1.4nm, (f) 1.5nm, (g) 1.6nm. (h) teff dependence of the product of K_{eff} and t_{eff}, where the intercept to the vertical axis of the linear extrapolation corresponds to interface anisotropy Ki.

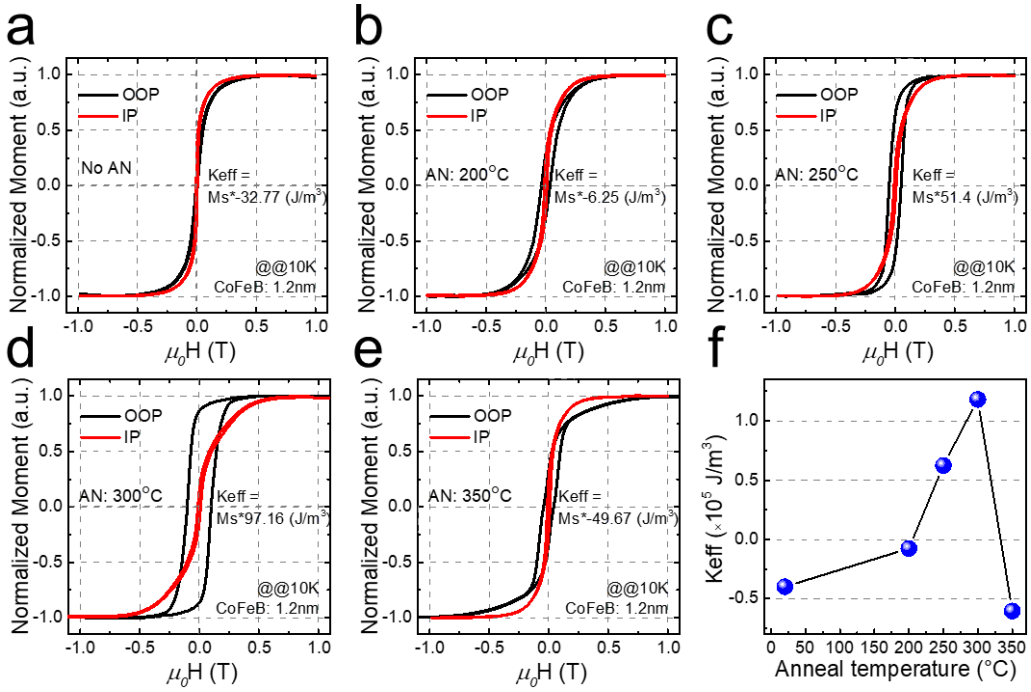

Figure 3. 7 (a-e) Out-of-plane and in-plane M-H curves for the sample with 1.2nm CoFeB before and after different temperature annealing measured at 10K. (a) no annealing, (b) 200°C annealing, (c) 250°C annealing, (d) 300°C annealing and (e) 350°C annealing. (f) Keff as a function of annealing temperature.

A precise control over the annealing temperature T_{an} is also an important factor to obtain a good PMA property. Figure 3.7 (a-e) displays the comparison of the out-of-plane *M-H* curves for the 1.2nm thick CoFeB sample with different T_{an}. The corresponding K_{eff} *vs.* T_{an} plotted in Figure 3.7 (f**)**. The contribution of the MgO/CoFeB interface anisotropy (K_i) scaling with a resulting '1/*t*' volume anisotropy can overcome the CoFeB bulk in-plane shape anisotropy (K_b) and establish the perpendicular magnetic anisotropy of the CoFeB layer[74]. The optimized annealing temperature is found to be around 300°C. The CoFeB coercivity and remanence gradually increase with the annealing temperature up to 300°C, then decrease after the annealing at 350°C. As already investigated theoretically by Yang *et al.* [71], the PMA is very sensitive to the Fe(Co)/MgO interface chemical structure. The improvement of PMA at T_{an} up to 300ºC could be attributed to an optimization of the interfacial chemical structure and crystallization of CoFeB at CoFeB/MgO interface[83]. When T_{an} exceeds 300ºC, Ta species start to diffuse through the ultrathin CoFeB to MgO interface and significantly damage PMA[75]. Figure 3. 8 shows the curves of 1.2 nm CoFeB with inplane and out of plane direction. We can observe that although the coercivity is much reduced at RT, the perpendicular magnetic anisotropy can well persist at RT.

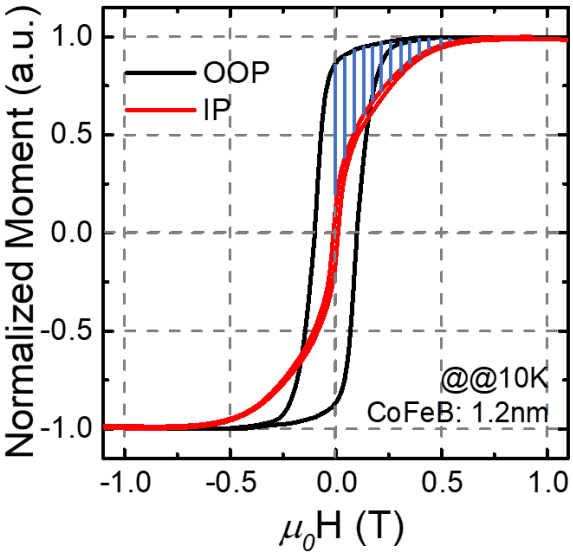

Figure 3. 8 Out-of-plane and In-plane M-H curves for 1.2 nm CoFeB sample measured at 10K.

The effective anisotropy constant (K_{eff}) is an important parameter for

characterizing the anisotropy of the sample, which can be calculated by $K_{eff}=M_{s\text{-}eff}\times\Delta/\mu_0$. In the above formula, $M_{s\text{-}eff}$ is the effective saturation magnetization per volume; Δ is the shaded area of the blue lines, which represents the difference in the area of the in-plane (IP) and out-of-plane (OOP) MH curves in the first quadrant, as shown in Figure 3.8.

From the fitting curve of thickness dependent magnetization, $M_{s\text{-}eff}$ can be extracted as 1216 emu/cm^3. Δ is 0.09716T for 1.2nm CoFeB. Furthermore, $\mu_0=4\pi\times10^{-7}$ H/m and 1emu/cm^3=$4\pi\times10^{-4}$T. By injecting all parameters into the formula, the value of K_{eff} can be calculated as follow.

$$K_{eff}=M_{s\text{-}eff}\times\Delta/\mu_0=(1216\times4\pi\times10^{-4})\times(0.09716)\div(4\pi\times10^{-7})=118136.844\ J/m^3$$

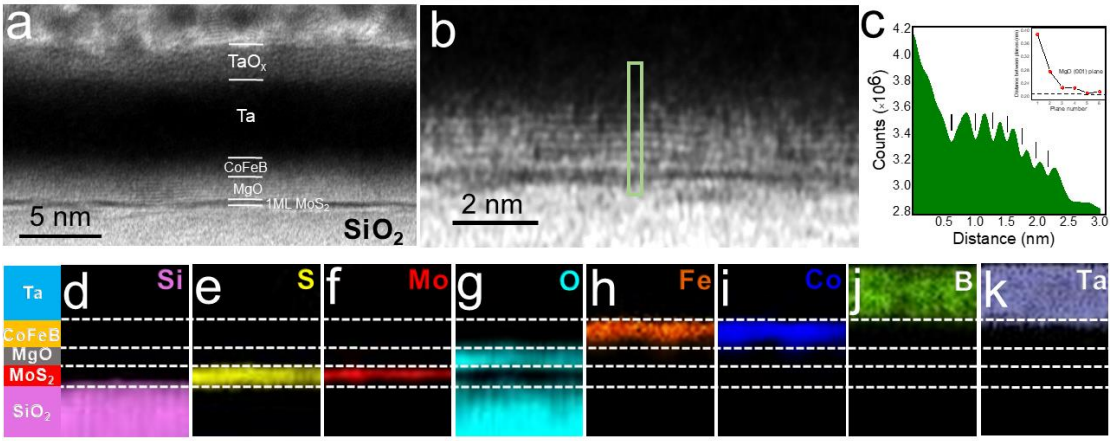

Figure 3. 9 Interfacial structure and chemical characterization of MoS_2/MgO/CoFeB/Ta heterostructure.

(a) Large scale HR-STEM bright field image shows the multilayer structure. (b) Enlarged image shows the crystallizations of MgO on MoS_2. (c) The profile of integrated intensity marked in the green zone in panel (b). Inset: The distance of interval of valley of oscillations. (d-f) Chemical element mapping from EELS spectrum images by extracting the signals of (d) Si L3 (99 eV), (e) S L3 (165 eV), (f) Mo M5 (227 eV), (g) O K (532 eV), (h) Fe L3 (708 eV), (i) Co L3 (779 eV), (j) B K (188 eV) and (k) Ta N5 (229 eV) edges, respectively. As shown in Figure 3.5 d-k, the chemical elements are mapped from EELS spectrum images.

When $K_{eff}>0$, the CoFeB layer is characterized with an out-of-plane easy-axis of magnetization. When $K_{eff}<0$, the CoFeB is characterized by an in-plane easy-axis of

magnetization. Since the interface anisotropy (K_i) can be obtained from the intercept of $K_{eff} \cdot t_{eff}$ *vs.* t_{eff} linear fitting. The value found from our results is about 0.97±0.10 mJ/m^2, which is comparable to the value of 1.3 mJ/m^2 given by Ikeda *et al.* for metallic MTJ[72] , and larger than the value of 0.63 mJ/m^2 reported for GaAs substrate[74].

Through experiments, we have obtained the optimal PMA condition, which is 1.2 nm CoFeB and 300°C rapidly annealing temperature. We use IBE to cut this sample into thin flake to measure the TEM. HRTEM and STEM were performed to characterize the interfacial structure. Figure 3.9 (a) displays the STEM bright field image at Ta/CoFeB/MgO/MoS_2 interface. We can distinguish different layers from the contrast of image. On the top surface of sample, 2nm TaO_x layer is formed due to the oxidation of Ta layer. The thickness of Ta and CoFeB layer is about 4.8nm and 1.2nm, respectively. The interface between Ta and CoFeB is rather diffused, and both exhibit amorphous feature. On the contrary, some crystalline structures can be found in MgO layer. Under the MgO layer, 1 ML MoS_2 can be clearly observed with the dark contrast. Figure 4.5 (b) shows a magnified STEM image where the MgO layer exhibits a textured structure. Since MgO has a fcc structure, the observed MgO planes could correspond to MgO (001) or MgO (111) planes. To clarify this point, we have extracted the profile of integrated intensity in the green zone in Figure 3.9 (b). As shown in Figure 3.9 (c), the intensity profile shows a regular oscillation. For the bright field image, the dark contrast corresponds to the atomic plane. Therefore, one can obtain the distance between two planes from the interval between the two valleys in the oscillation. We have shown in the inset of Figure 3.9 (c) the interval distance with the corresponding number. It is interesting to find that the interval distance decreases from 3.8Å (No.1) to 2.1Å (No.6). The first interval is between the first MgO plane and ML MoS_2. The large distance of 3.8Å well indicates a Van-der-Waals bonding between MgO and MoS_2. With the increase of thickness of MgO, the interval saturates to the value of 2.1Å, which is well consistent with the value of MgO (001) plane (2.1Å) and far from the value of MgO (111) plane (2.43Å). Therefore, we can conclude a MgO (001) texture is formed on the MoS_2 layer, probably due to the annealing procedure.

We have performed STEM combined with spatially resolved electron energy loss spectroscopy (EELS) to characterize the interfacial element distribution in the atomic level so that the inter-diffusion related to the annealing process can be understood. Figures 3.9 (d-f) show the chemical element mapping from EELS spectrum images. The clear layered structure of Fe, Co and O proves that no important interdiffusion of elements from FM layer into the MoS_2 owing to the diffusion barrier of MgO. The thickness of Mo layer is thinner than that of S layer and sites in the center of MoS_2 layer, which again validates the structure of MoS_2 is not influenced by Ta/CoFeB/MgO deposition. More interesting, the B is found to largely diffuse into Ta, which is due to the crystallization of CoFeB layer during the annealing procedure. This is critical to establish the PMA property at MgO/CoFeB interface[74, 75].

3.3.3 The Heterojunction of MoS_2/MgO/CoFeB/Pt

From the results of STEM, we are conscious of the important of the capping layer. In order to compare the Ta capping layer, we chose another inert metal Pt as the masking layer. We have fabricated a MoS_2/MgO/CoFeB/Pt heterojunction with a thickness of 1.2nm CoFeB and 300°C RTA. Figure 3. 10 shows the *M-H* curves of Ta capping and Pt capping. The sample with Pt layer displays a large saturation field up to 0.7T and almost zero remanence, which indicates that the CoFeB magnetization is completely in-plane.

To understand why the PMA is completely lost in the reference sample replaced by Pt, we have also performed HR-STEM structural characterizations combined with EELS analyses, with details in Figure 3.11.

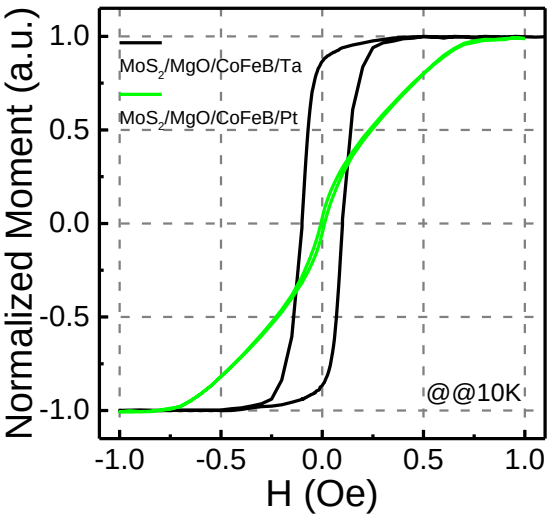

Figure 3. 10 Comparisons of out-of plane *M-H* curves for two samples: MoS_2/MgO/CoFeB/Ta and MoS_2/MgO/CoFeB/Pt. All samples have the same CoFeB thickness and were annealed at 300°C.

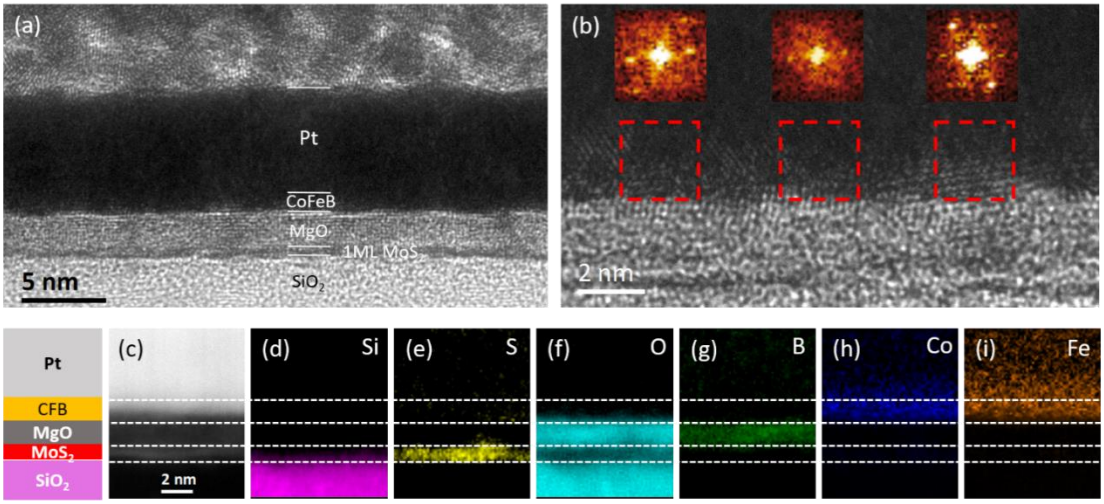

Figure 3. 11 Interfacial structure and chemical characterization of MoS_2/MgO/CoFeB/Pt heterostructure.

(a) Large scale HR-TEM image shows the multilayer structure. (b) Enlarged image shows the crystallization of CoFeB on MgO. Insets: FFT patterns show that the CoFeB is crystallized with a polycrystaline feature (3 different orientations in different zones). (c)STEM HAADF image of the zone where EELS analyses are performed. (d-i) Element maps drawn from STEM-EELS spectrum image, respectively for (d) SiK, (e) SL, (f) OK, (g) BK, (h) CoL and (i) FeL edges.

Figure 3.11 (a) and (b) display the large scale and magnified HRTEM images of the Pt/CoFeB/MgO/MoS_2 interfaces after annealing at 300°C, respectively. It is found that the MgO layer contains many small crystalline structures with disordered orientations. CoFeB layer also exhibits a crystalline feature. The insets of Figure 3.11 (b) display the FFT analyses of the CoFeB structure in three different zones (marked with red dashed squares), which show different diffraction patterns indicating a polycrystalline feature of CoFeB. Figures 3.11 (d-i) show the chemical element mapping deduced from the EELS spectrum images. The Mo signal in this sample is too weak to construct the element mapping. Compared to the sample with Ta capping layer, the most distinct difference is revealed by the mapping of B element (Figure 3.11 (g)). It is clearly that most of B atoms diffuse inside the MgO instead of being absorbed by the Pt layer after annealing.

Moreover, an important diffusion of Fe atoms into Pt layer can be also evidenced. More details for the profile of the element distribution and B diffusion in MgO can be found in Figure 3.12. Compared to Ta, Pt is more difficult to react with boron to form the boride, which needs high temperature and high pressure conditions[84]. Therefore, the Pt capping layer is quite difficult to absorb the B atoms during the annealing at 300°C. On the contrary, it is well known that Pt and Fe can easily react with each other to form the alloy[85], which can explain the observed important diffusion of Fe in Pt. Since Pt layer is already textured in the as-grown state, it can serve as a template for the CoFeB crystallization during the annealing, leading to a disorientated (non *bcc*) structure of the CoFeB layer. This phenomenon has already been observed when a Ru layer is contacted with CoFeB. Consequently, the MgO layer absorbs all B atoms repelled from the CoFe matrix after annealing. The combination effects of the diffusion of B inside MgO and the disorientated CoFeB crystallization destroy the PMA at the CoFeB/MgO interface, which well explains the observed in-plane magnetization in the Pt capping sample. This study also proves the critical role of Ta to efficiently absorb B atoms from the CoFeB layer to establish the PMA.

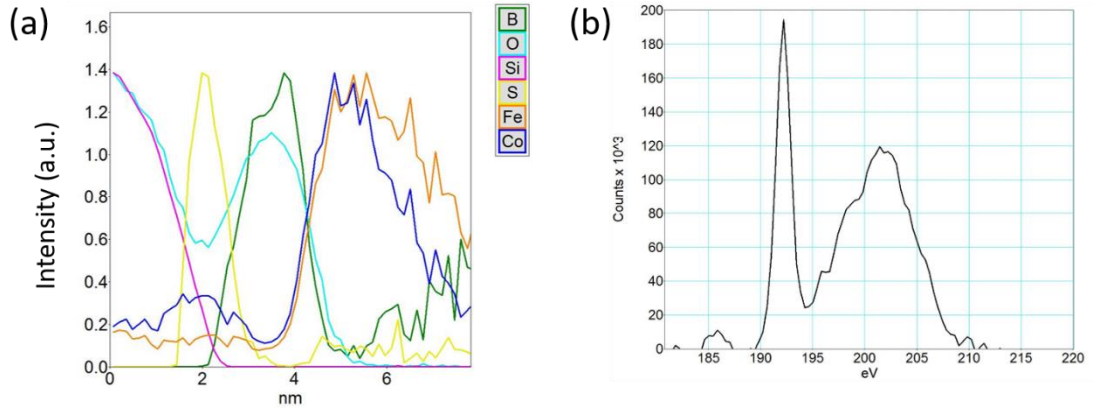

Figure 3. 12 (a) The maximum-normalized element concentration profiles from EELS drawn perpendicularly to the MoS_2 layer shows the diffusion of B completely inside the MgO barrier. (b) EELS spectrum of BK edge extracted from spectrum image in the MgO layer. The fine structure is typical of B III, showing the oxidation of boron simultaneously to its diffusion.

3.3.4 The Heterojunction of MgO/CoFeB/Ta

To clarify the role of MoS_2 on the establishing of PMA, we have prepared another two reference samples. One is with the same Ta/CoFeB/MgO structure on SiO_2 substrate and the other is on ML MoS_2 but Ta layer is replaced by Pt layer. Figure 3.13 displays the out-of-plane M-H curves at 10K for the two samples after annealing at 300°C. It is found that the sample on SiO_2 substrate shows a much smaller remanence (0.5) and a small coercivity about 20mT, indicating a smaller PMA in the Ta/CoFeB/MgO system.

For the change in coercivity, we have no intuitive evidence to prove the cause. Theoretically, we analyzed the following reasons that may affect the coercivity.

Firstly, the flatness of the interface affects the coercive force. For the substrate of Si and 2D material, 2D material belong to the crystal with flat surfaces. Therefore, the preparation of MgO and CoFeB on the two-dimensional material can obtain a flatter film. The flatter film exhibits the large PMA.

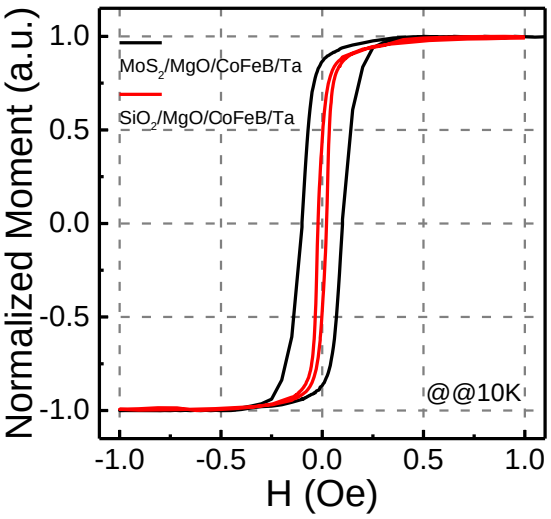

Figure 3. 13 Comparisons of out-of plane M-H curves for three samples: SiO_2/MgO/CoFeB/Ta and MoS2/MgO/CoFeB/Pt. All samples have the same CoFeB thickness and were annealed at 300°C.

Secondly, compared to the amorphous SiO_2 substrate, the crystalline ML MoS_2 layer favorize the crystallization of textured MgO (001) structure as well as a bcc crystallization of CoFeB layer after annealing procedure, which is an indispensable condition to create the large interface anisotropy at MgO/CoFeB interface to establish the PMA of CoFeB. Therefore, it is reasonable that the PMA in the reference sample without MoS_2 is much reduced, which validates the important role of the ML MoS_2 layer.

3.4 First-principles calculation

3.4.1 Calculation method

The theoretical analysis and calculations were completed by Paul Marcon and Lionel Calmels from CEMES, CNRS, Université de Toulouse.

The electronic structure of the multilayer described by this supercell has been calculated with the VASP[86, 87], based on the DFT and the PAW method[88]. The

generalized-gradient approximation developed by PBE was used to calculate the exchange and correlation potential[89]. We chose a basis size corresponding to a cut-off energy of 550 eV. The first Brillouin zone was sampled with a 16×20×1 Monkhorst-Pack grid[90] for structural optimizations and for calculating the band structure and with a denser mesh (45×45×1) to calculate the DOS. The atom internal coordinates have been optimized until all forces are below 10 meV/Å and Van-der-Waals corrections have been taken into account within the DFTD3 formalism[91, 92]. A dipole correction has been used to avoid non-physical charge transfer across the slab.

3.4.2 MoS_2/7ML MgO/7ML Fe Heterojunction

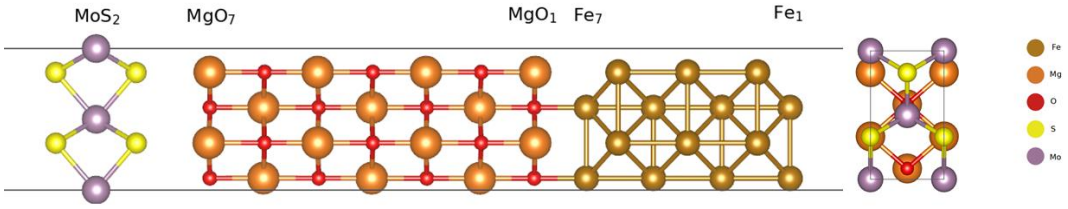

Figure 3. 14 Section and top view of the unit cell used to model the Fe/MgO/MoS_2 multilayers.

To better understand the potentiality of such FM/oxide/2D hetero-junction in view of electrical spin injection, we have performed *ab-initio* calculations to investigate the band structure and spin resolved DOS at the interfaces of a Fe/MgO/MoS_2 slab, which simulates our experimental CoFeB/MgO/MoS_2 structure. Figure 3.14 shows the section and top view of the unit cell that we have used to model the Fe/MgO/MoS_2 multilayer. It contains 7 MLs of Fe, followed by 7 MLs of MgO and a single 1H-MoS_2 layer. The O_z axis is the direction perpendicular to the Fe/MgO and MgO/MoS_2 interfaces. The MgO conventional cubic cell is rotated in the *xy*-plane by 45° with respect to the Fe conventional cubic cell, Fe atoms being on top of oxygen atoms at the Fe/MgO interface. The Fe/MgO/MoS_2 supercell that we used for the calculations imposes the same periodicity in *x*- and *y*-directions for the Fe, MgO and MoS_2 layers. This common periodicity may be responsible for structural distortions in the heterostructure unless huge supercells are used. Therefore, we had to find a compromise between reasonable

distortions and reasonable supercell size. After relaxation of the atomic positions, the distance of 0.441 nm is found between the Mo layer and the first MgO layer, confirming the weak Van-der-Waals bonding between MoS_2 and the rest of the stacking. This is also in a good agreement with the value of 0.38 nm determined in our TEM characterizations.

Figure 3.15 shows the integrated DOS over atomic spheres belonging to the successive atomic layers of the supercell. The DOS curves calculated at the center of the Fe layer (Fe4) and at the center of the MgO layer (MgO 4 layer) resemble those calculated from undistorted *bcc* Fe and *fcc* MgO, respectively. This indicates that the artificial distortion that we imposed does not strongly change the physical properties of the Fe and MgO layers. The spin polarization at the Fermi level E_F ($P_s(E_F)$), defined as the relative difference between the DOS values calculated for the two spin states at E_F, is negative (the majority spin DOS is lower than the minority spin DOS) for the interface Fe ML (Fe 7 layer). Most importantly, the bottom of the conduction band of MoS_2, which was clearly above the Fermi level E_F for an isolated MoS_2 layer, is now shifted below E_F. It means that electrons have been transferred from the Fe/MgO interface to the MoS_2 layer and the resulting charge distribution induces an internal electric field in MgO (shown as a continuous shift of the successive MgO DOS curves). This internal electric field is partly screened by a small buckling (between 0.0025 and 0.005 nm) between Mg and O atoms of the same MgO layer.

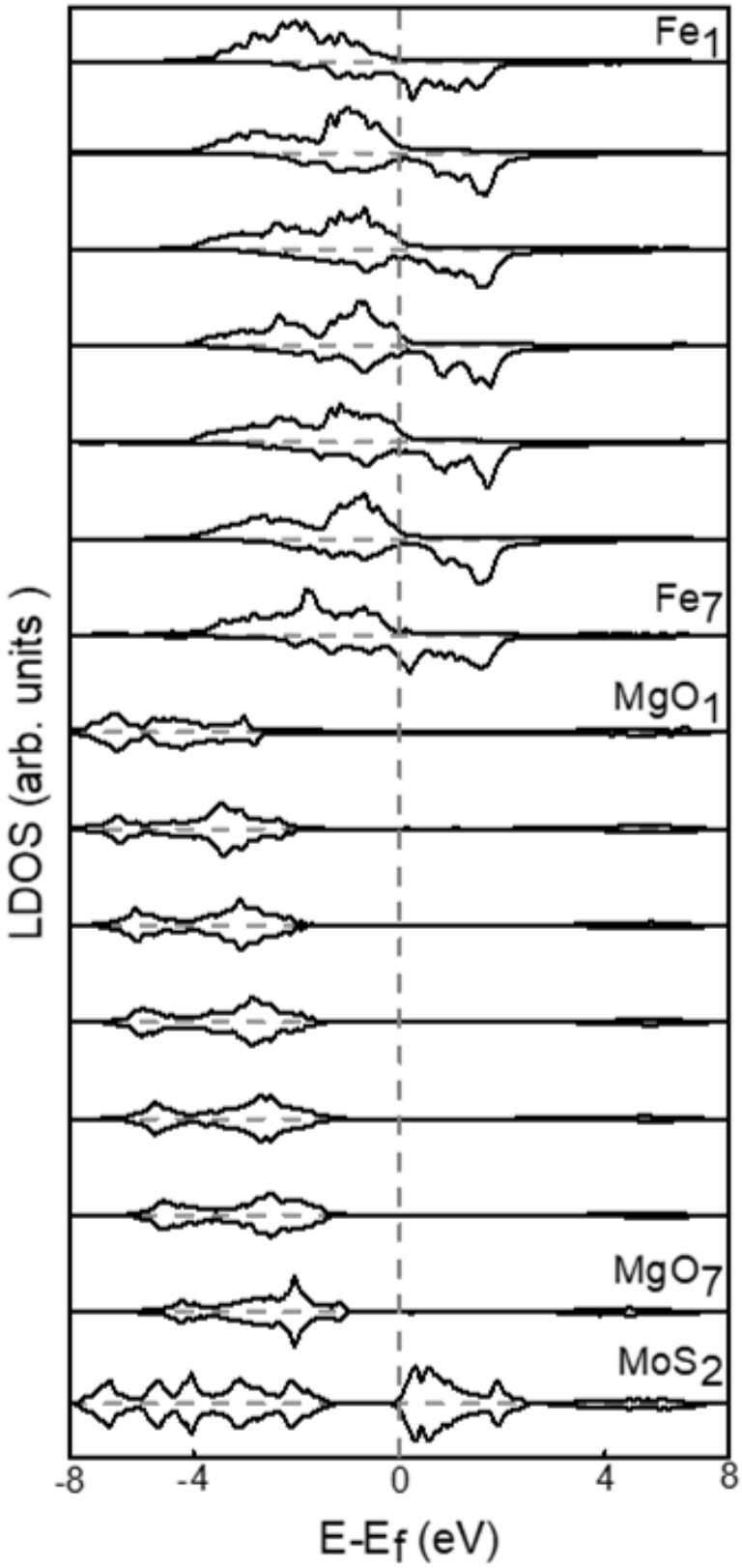

Figure 3. 14 Integrated majority and minority DOS over atomic spheres belonging to the successive atomic layers of the supercell.

Figure 3.16 (a), which shows the z-variations of the xy-averaged electrostatic potential, confirms that the internal electric field only exists in the MgO layer. Figure 3.16 (b), which shows the electron charge allocated to each atomic layer, reveals that the charge transfer mainly occurs between the MgO layer at the Fe/MgO interface and the S layer at the MgO/MoS_2 interface. The charge transfer in this MIS structure is due to the different work function of electrons in bulk Fe and in the MoS_2 ML. The values of the Fe work function and the MoS_2 ML electron affinity and band gap energy that we calculated are indeed of 3.91 eV, 3.65 eV and 1.74 eV[93], respectively (while the values of 4.5 eV, 4 eV, and 1.8 eV1 have respectively been measured in experiments) [18, 23]. A similar charge transfer has also been experimentally observed in Fe/MgO/GaAs system[94]. The charge transfer induced by the insertion of MgO can effectively reduce the Schottky barrier height for FM/2D contact[17, 70, 95], which is in favor of the spin-polarized electron injection from the FM metal to the 2D conduction band.

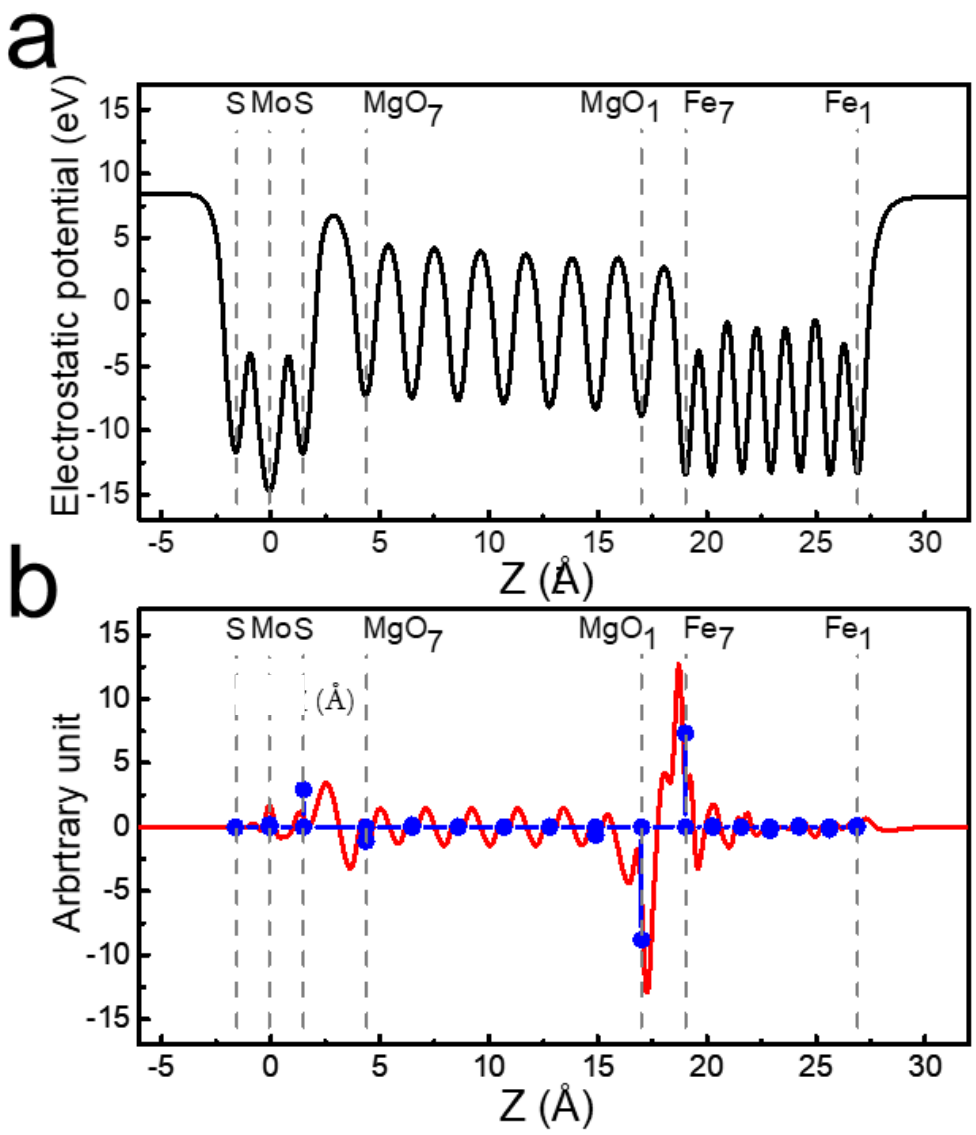

Figure 3. 15 (a) z-variations of the xy-averaged electrostatic part of the potential energy. (b) Red curve is the electron charge density allocated to each atomic layer. Each blue dot corresponds to the z-integration of the red curve between the two mid-perpendicular planes separating an atomic layer and its neighbors on the right and left sides.

Figure 3.17 (a) shows the z-dependence of the DOS at the Fermi level, calculated for majority and minority spin electrons. The DOS values decrease exponentially in MgO, both from the Fe/MgO and MgO/MoS_2 interfaces. Figure 3.17 (b) shows the corresponding profile of spin polarization at EF calculated from the spin-resolved DOS. The spin polarization at the Fermi level rapidly vanishes away from the MgO/Fe interface, and the electron gas transferred in the MoS_2 layer does not show significant

spin polarization. The sign of spin polarization is changed in the middle of MgO. This is because the characteristic length of the exponential decay of electron states near the Fe/MgO interface is smaller for minority spin than for majority spin electrons, in agreement with the results obtained by Butler et al. for the Fe/non-distorted MgO interface[96].

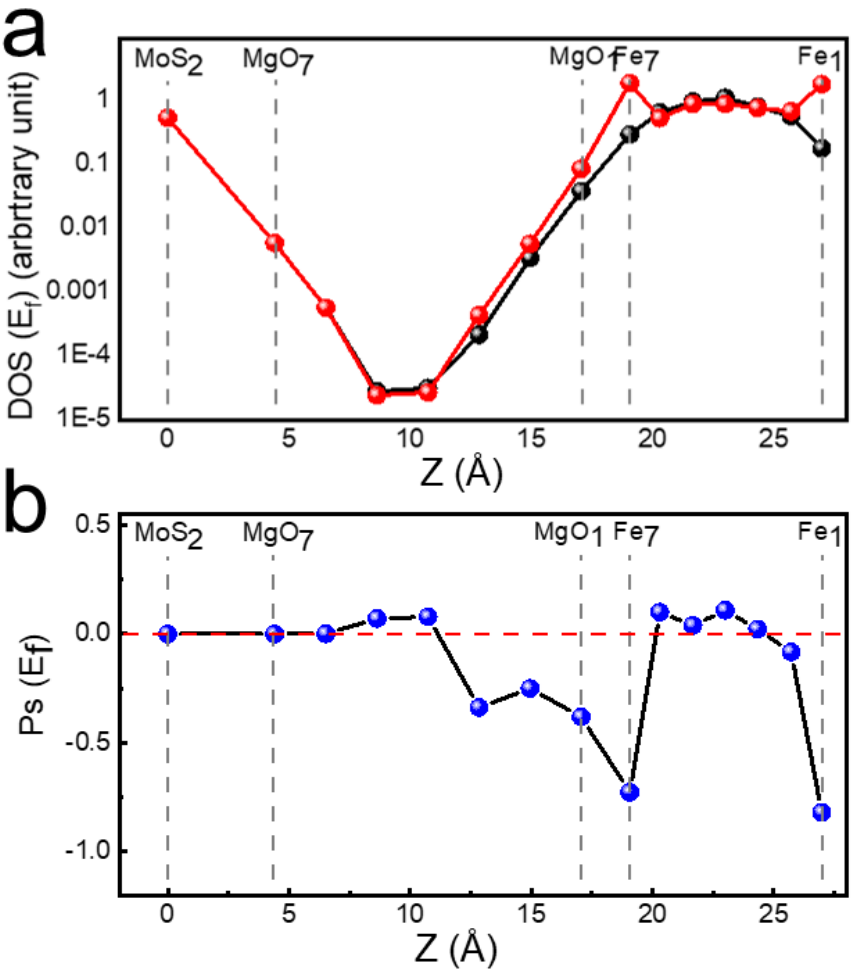

Figure 3. 16 (a) z-dependence of the DOS at the Fermi level, calculated for majority and minority spin electrons. (b) Profile of spin polarization calculated from the spin-resolved DOS.

3.4.3 MoS_2/3ML MgO/7ML Fe Heterojunction

To better understand the origin of the modification of the band structure, we have also performed calculations in a similar structure with 3MLs of MgO.

Comparing the two local projected state densities (7-layer MgO and three-layer MgO), LDOS of the iron atomic layer unchange with the change in the number of magnesium oxide layers. while for the magnesium oxide layer, the internal electric field of the three-layer MgO is smaller than that of the seven-layer MgO.

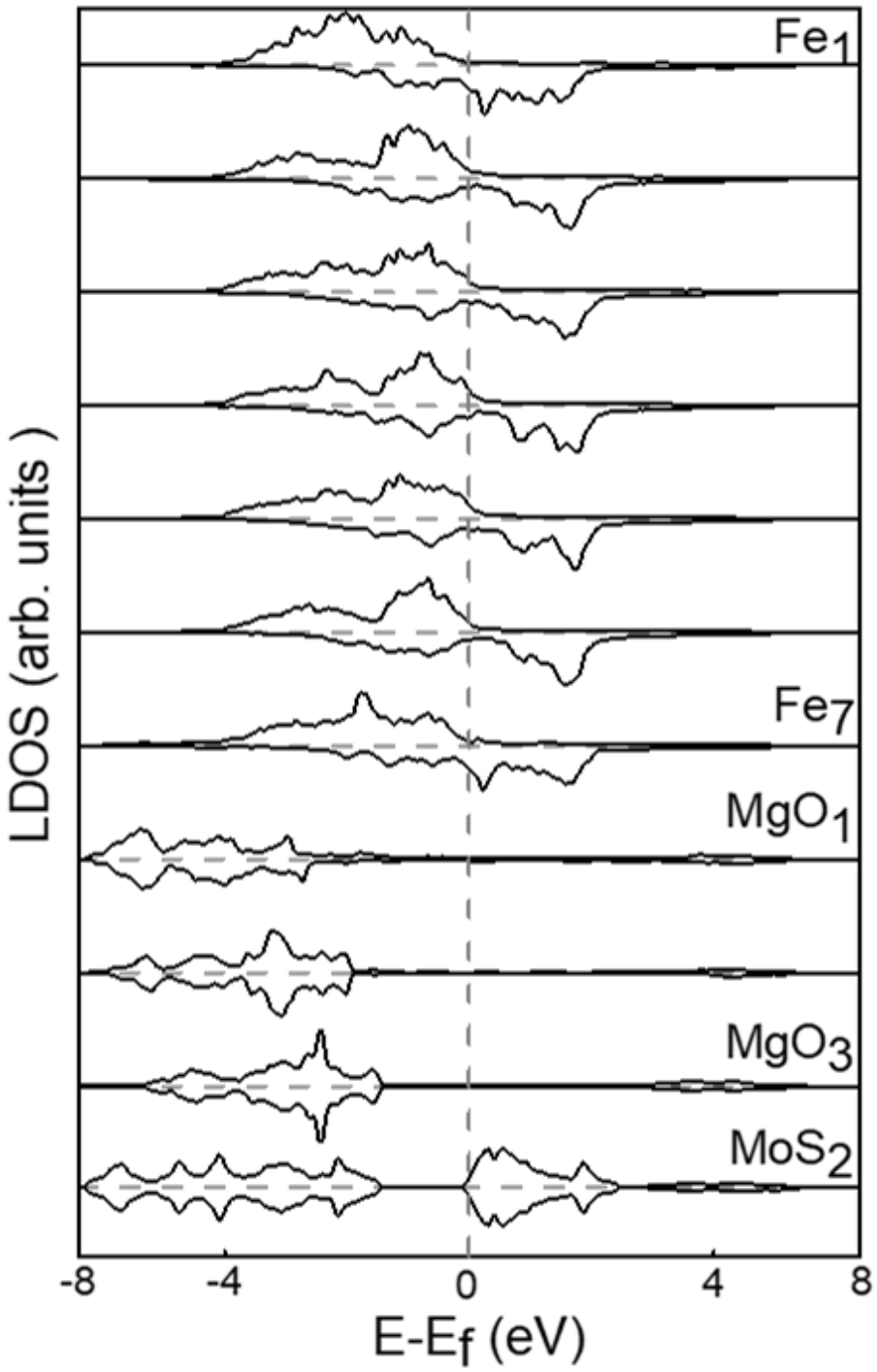

Figure 3. 17 Integrated majority and minority DOS over atomic spheres belonging to the successive atomic layers of the supercell.

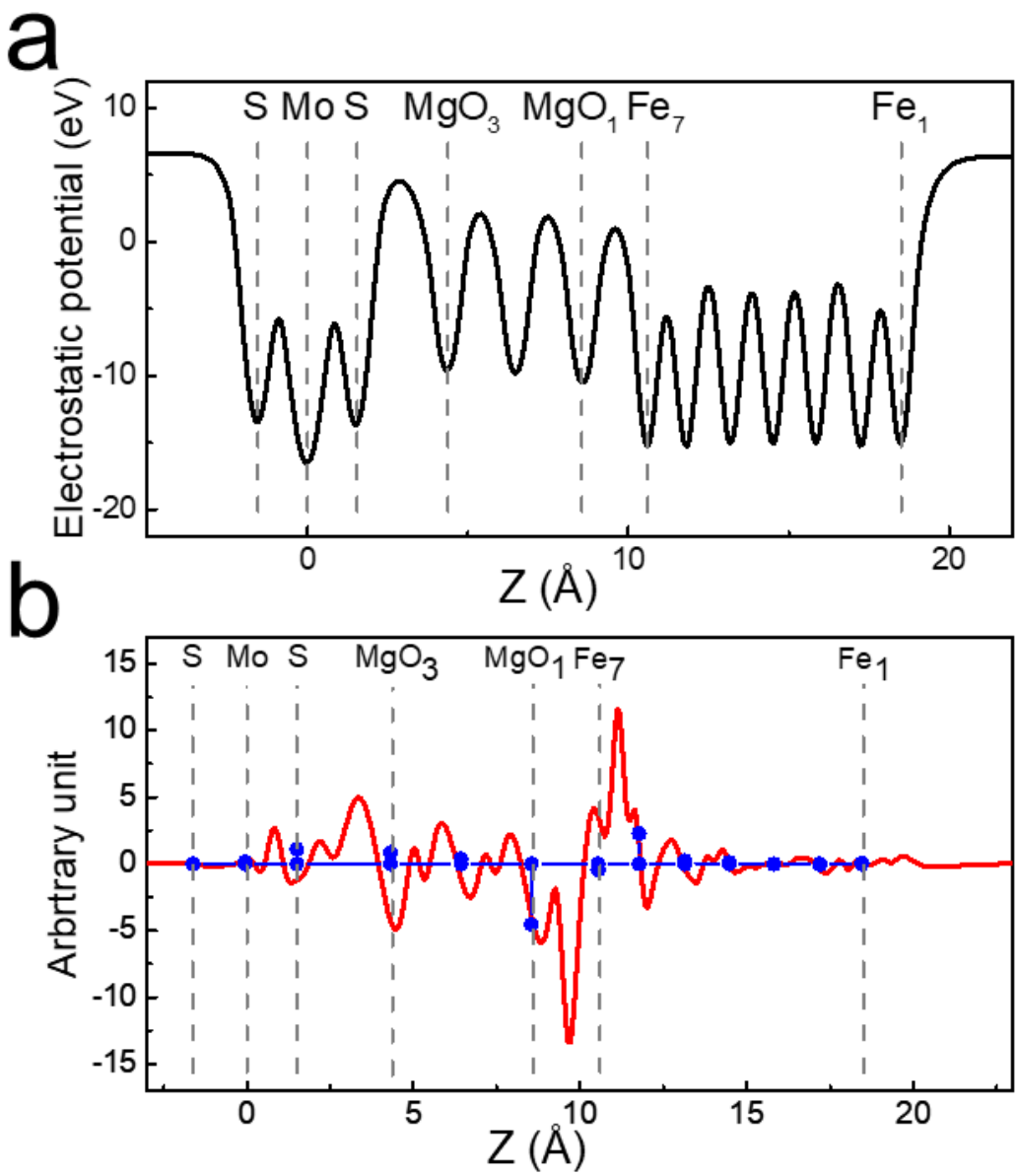

Figure 3. 19 (a) z-variations of the xy-averaged electrostatic part of the potential energy. (b) Red curve is the electron charge density allocated to each atomic layer. Each blue dot corresponds to the z-integration of the red curve between the two mid-perpendicular planes separating an atomic layer and its neighbors on the right and left sides.

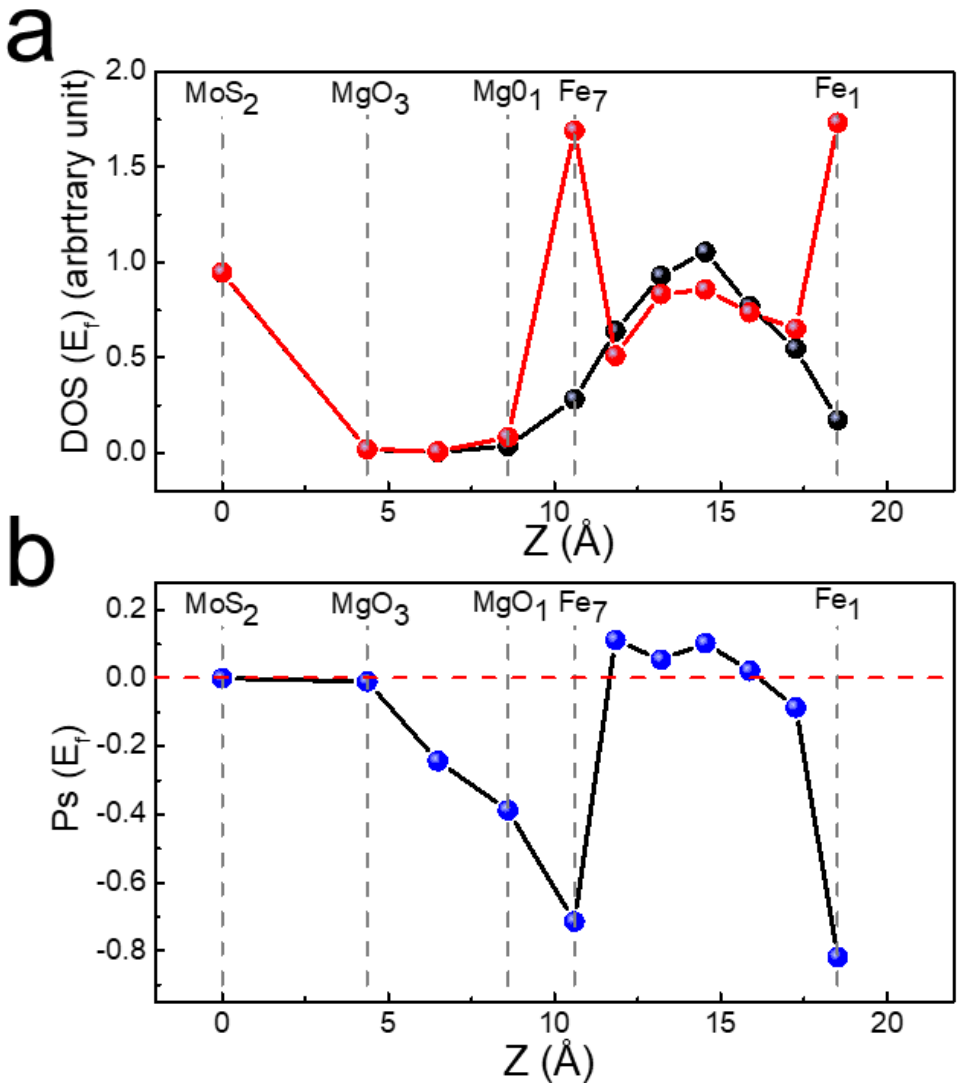

Figure 3. 18 (a) z-dependence of the DOS at the Fermi level, calculated for majority and minority spin electrons. (b) Profile of spin polarization calculated from the spin-resolved DOS.

The two-color dots shown in Figure 3.20 (a) represent the charge density values of electrons in two spin directions. From the DOS diagram in the Z direction, the spin polarization direction in the iron film is reversed, while the spin polarization direction remains consistent in the magnesium oxide layer.

It can be seen from the spin polarization curve that the spin polarization retention rate in the iron atom film is relatively high. Among them, the spin polarization rate is the highest at the boundary of the iron film, and at the interface of iron and magnesium oxide, the spin polarization rate is the extreme speed drops and continues to drop in the

magnesium oxide layer. When the spin-polarized electrons enter the MoS_2 layer, the spin polarization rate is almost zero.

3.4.4 Band structure of Fe/MgO/MoS_2

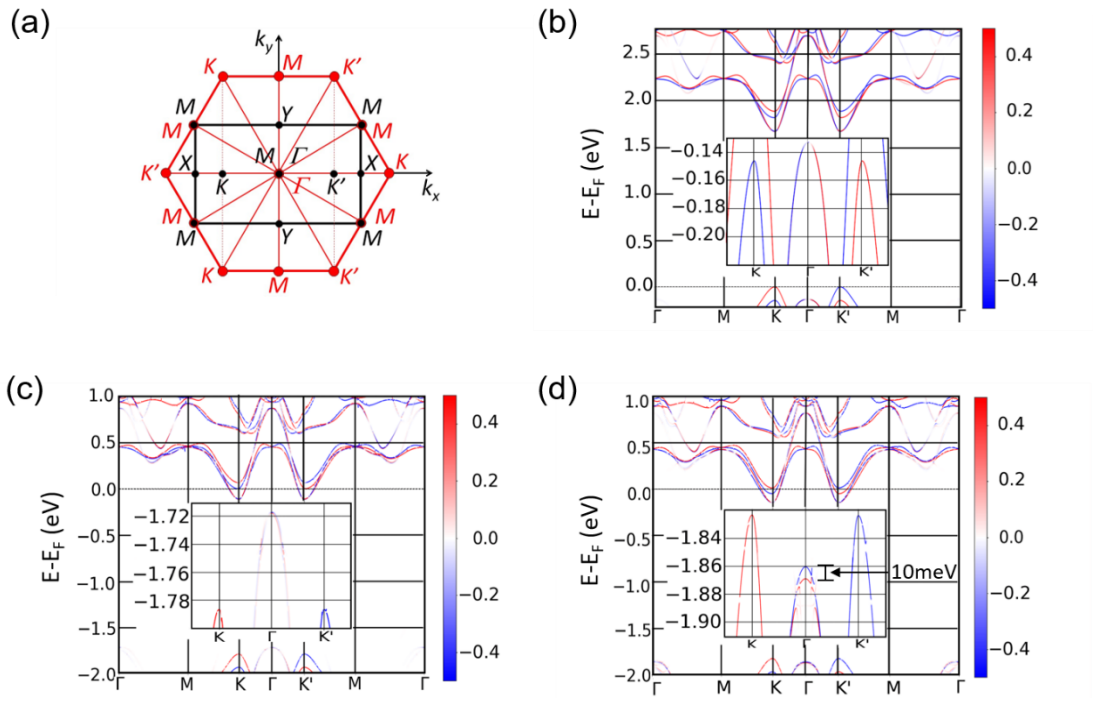

Figure 3. 19 Band structure of the MoS_2 ML in the multilayer structure. (a) Brillouin zone of the unit cells. The red lines represent the hexagonal Brillouin zone of the primitive unit cell of the MoS_2 ML. The black lines represent the rectangular Brillouin zone of the multilayer structure. (b) Band structure of monolayer MoS_2 calculated with a conventional rectangular unit cell. Inset: Magnified valence band structures. (c, d) Contribution of the MoS_2 layer to the band structure of the multilayer with (c) 7 MLs of MgO and (d) 3 MLs of MgO. The red and blue lines respectively show the positive and negative values of the spin projection s_z (in units of $\hbar$). Insets: Magnified valence band structures show a meglectable Zeeman splitting for 7 MLs of MgO but a large splitting of 10mV at Γ point for 3 MLs of MgO.

To clarify the influence of the Fe/MgO stack on the band structure of MoS_2, we have compared the band structures of the MoS_2 ML and the Fe/MgO/MoS_2 multilayer.

Figure 3.21 (a) shows the rectangular first Brillouin zone of the Fe/MgO/MoS_2 multilayer (black lines) and the hexagonal Brillouin zone of the MoS_2 ML (red lines). To understand where the K and K' valleys of MoS_2 are located in the rectangular Brillouin zone, the pieces of the MoS_2 ML hexagonal Brillouin zone located outside the rectangular one must be translated inside the black rectangular zone: the location of the K, K' and M points after these translations are indicated with black letters. This helps to understand how the band structure of MoS_2 is folded, when represented along the high symmetry directions of the multilayer Brillouin zone. Figure 3.21 (b) shows the calculated band structure of the MoS_2 ML with a rectangular conventional cell, which clearly indicates a direct band gap of 1.7 eV at K and K' points. Figure 3.21 (c) shows the contribution of the MoS_2 layer to the band structure of the multilayer containing 7 MLs of MgO. The band structure of MoS_2 confirms that electrons transferred from the Fe/MgO interface to the MoS_2 layer occupy the minima of the conduction bands of MoS_2 at the K and K' points. Furthermore, we find that the band gap of the MoS_2 ML is no longer direct. The maximum of the valence band is found at the Γ point instead of the K and K' points. To better understand the origin of the modification of the band structure, we have also performed calculations in a similar structure containing only 3 MLs of MgO. As shown in Figure 3.21 (d), we observe that MoS_2 still keeps its direct bandgap in the multilayer with 3 MLs of MgO (the top of the valence band at Γ being shifted to a lower energy), which shows that the influence of the MgO layer on the band structure of MoS_2 is not trivial and strongly depends on its thickness.

Another interesting feature is that a Zeeman splitting of about 10meV is evidenced at the Γ point for the Fe/MgO(3 MLs)/MoS_2 system (inset of Figure 3.22 (d)), while this splitting is negligible for the MoS_2 ML (inset of Figure 3.21 (b)) and the Fe/MgO(7 MLs)/MoS_2 system (inset of Figure 3.21 (c)). The Zeeman splitting is attributed to a proximity effect due to the presence of ferromagnetic Fe on the other side of the MgO layer. The proximity effects have been also recently evidenced in the cases of CoFeB/MgO/Si junction by spin-pumping measurements and CrI_3/WSe_2 systems by photoluminescence measurements. It is quite interesting that the thickness of the

inserted MgO layer plays a role on the magnetic properties of MoS_2 by the proximity effect. Compared to the case of the direct contact between FM metals and 2D materials, the insertion of a thin insulating layer can prevent the hybridization at the metal/TMD interface and enable room temperature controlled proximity effects. For 2D spin optoelectronic applications, thick MgO barrier will enhance the spin filtering effect to increase the injected spin polarization58. However, the band gap of the MoS_2 layer will become indirect. On the contrary, with a thin MgO, MoS_2 preserves a direct band gap and the proximity effects will enhance the spin lifetime in MoS_2.

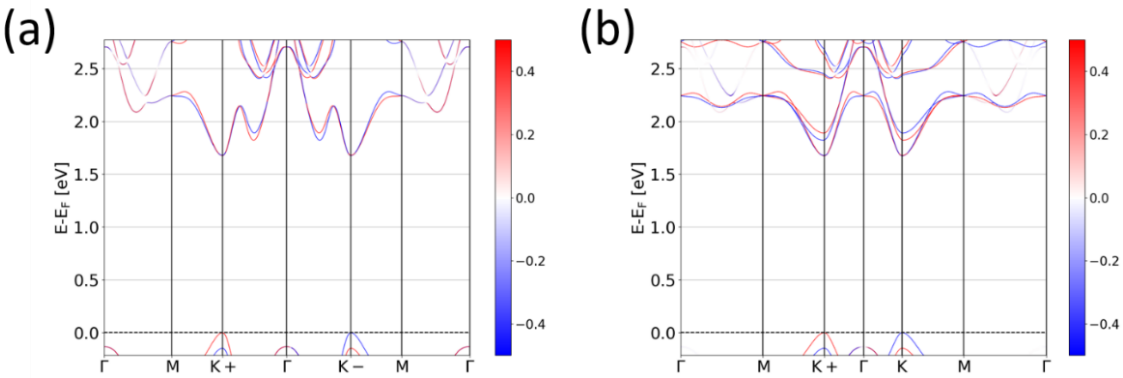

Figure 3. 20 (a) Band structure of monolayer MoS_2 defined in a hexagonal lattice. (b) Band structure of monolayer MoS_2 defined in a rectangular lattice.

3.5 Conclusion

We have reported a large perpendicular magnetic anisotropy in Ta/CoFeB/MgO structure on full coverage monolayer MoS_2. The large PMA has been obtained after a precise control of the CoFeB thickness and post-annealing procedure. It is found that the insertion of a thin insulating MgO layer can effectively block the metal diffusion into the 2D material during the annealing treatment. MgO can be crystallized to the (001) *fcc* texture on the MoS_2 ML. During the annealing at 300°C, the Ta layer shows a high efficiency to absorb B atoms from the CoFeB layer. This avoids the diffusion of B atoms into MgO and the suppression of the PMA, as evidenced with the Pt capping layer. All these factors ensure the large PMA established in the Ta/CoFeB/MgO/MoS_2 system. Furthermore, first principle calculations have also been performed in

Fe/MgO/MoS_2 structures to understand the electronic and spin properties in such FM/oxide/2D systems. It is interestingly to find that the thickness of the MgO layer can modify the MoS_2 band structure from an indirect bandgap with 7MLs of MgO to a direct one with 3MLs of MgO. The latter multilayer also shows a proximity effect with a Zeeman splitting of 10meV in the MoS_2 valence band at the Γ point. These findings suggest that the magnetic and electronic properties of MoS_2 can be modulated by the MgO thickness. Our experimental and theoretical results will promote the future development of room temperature spin optoelectronic devices based on 2D TMDs with a perpendicularly magnetized spin injector.

Chapter 4: GeAs based polarized photodetector

4.1 Background

In recent years, high-performance photodetectors working at the spectral range from ultraviolet to infrared have sprung up in succession[30, 97-103]. Among them, the polarization-sensitive photodetectors based on anisotropic semiconductor exhibit overwhelming advantages in practical applications, such as orthogonal polarization spectroscopy imaging, polarization sensors, remote sensing and optical radar [104-108]. For the active layer of polarization-sensitive photodetectors, primary research works focused on one-dimensional (1D) nanowires and nanobelts including Indium Phosphide (InP)[109], ZnO,[102] Sb_2S_3[100] and Barium Titanium Sulfide ($BaTiS_3$) [110] due to their macroscopic anisotropy. But the aspect ratios of 1D materials still limit the diverse device application. 2D materials, for example graphene and the family of transition metal dichalcogenides, have rapidly developed for their electronic, spintronic, and photonic phenomena superior to their bulk materials. [111-113] Compared to the conventional 2D materials with in-plane hexagonal lattice, 2D materials with in-plane rectangular lattice including Black Phosphorus (B-P),[114] ReS_2, $ReSe_2$, Black Arsenic (B-As),[28] Germanium Selenide (GeSe),[34] and MoO_3[115] have anisotropy in their structure and optoelectronic properties along the a-axis and b-axis directions. Among these anisotropic materials, polarized photodetection has already been demonstrated in B-P,[116] ReS_2, [117] $ReSe_2$, [106] B-As, [27] B-AsP,[30, 118] and GeSe[34, 119, 120]. Discovering new stable anisotropic materials with excellent anistropic photoresponse has attracted intensive interests for future polarized photodetection applications.

Germanium Arsenic (GeAs) is a new 2D material with strong intralayer anisotropy, belonging to the GaTe structure type with C2/m space group. GeAs crystal is deemed to a potential candidate for polarization photodetectors due to its narrow band gap (less than 1 eV) and the typical in-plane anisotropic layered structure. In 2016, Prof. Kovnir

and co-workers successfully synthesized GeAs crystal and demonstrated its highly anisotropic thermoelectric properties.[121] Furthermore, Prof. Duan and co-workers systematically showed that GeAs crystal is a semiconductor of high hole-carrier mobility (100 $cm^2 V^{-1}s^{-1}$) with highly anisotropic electronic properties (anisotropic mobility ratio of 4.8). [122] And they also investigated the excellent infrared photo-response of GeAs flakes. Recently, Prof. Ajayan and co-workers reported the optical and electronic anisotropy of GeAs in details. [123] The crystal growth, band structure, electric properties and thermoelectric performance of the GeAs crystal have been investigated [40-42]. However, due to the limitation of detection methods, the high anisotropic polarization photodetection with GeAs 2D material is still not reported.

4.2 GeAs crystal structure

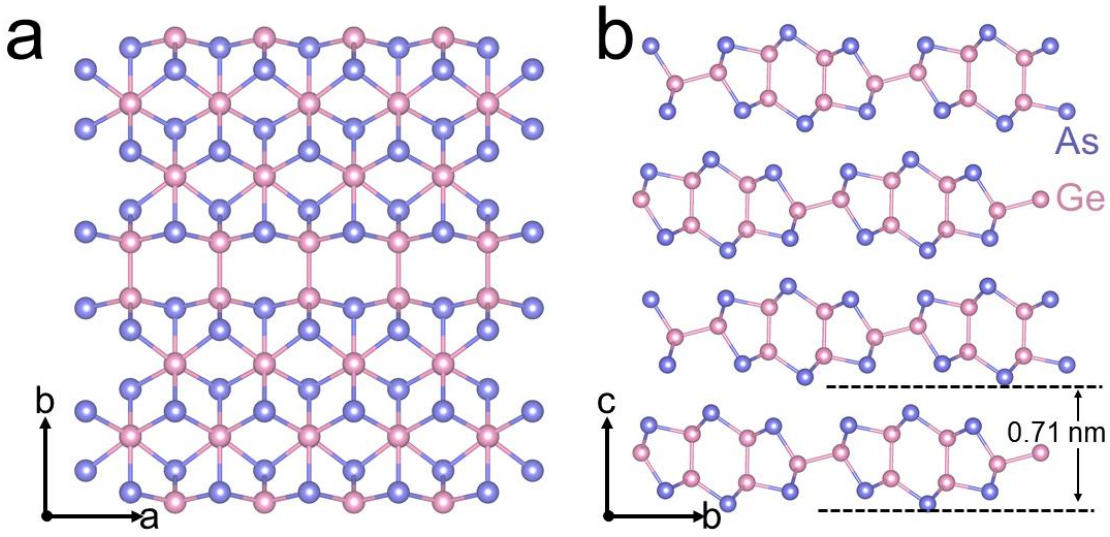

Figure 4. 1 The schematics of GeAs crystal.

(a) shows ab-plane; (b) shows bc-plane.

The crystal structure of layered GeAs is shown in Figure 4.1. The pink balls are Ge atoms, coordinated by one Ge atom and three As atoms, while the blue balls are As atoms, coordinated by three Ge atoms. Figure 4.1 (a) is a top view of a single-layer GeAs crystal (a-b plane). From the top view, the structure is composed of Ge-Ge bond-connected repeating units. Therefore, the structure is asymmetric along the a-axis and

b-axis in the plane. It can be seen from the side view of the interlayer structure (Figure 4.1 (b)) that there are two kinds of Ge-Ge bonds in the material, one Ge-Ge bond is along the b axis, and the other Ge-Ge bond is along the c axis, which proves once again GeAs crystals have strong in-plane anisotropy. In addition, it can be seen from the side view that GeAs crystals are stacked in two layers in a cycle of AB stacking, and the AB stacking mode is the tightest stacking mode. In the two layers, one As atom in the upper layer is located on the lateral Ge-Ge bond of the under layer. In this case, it is difficult for GeAs crystals to peel off to form a single layer. At the same time, it can be seen from the interlayer crystal structure that the thickness of a single-layer GeAs is 0.71nm.

4.3 Characterization of samples and devices

4.3.1 Transmission electron microscope (TEM)

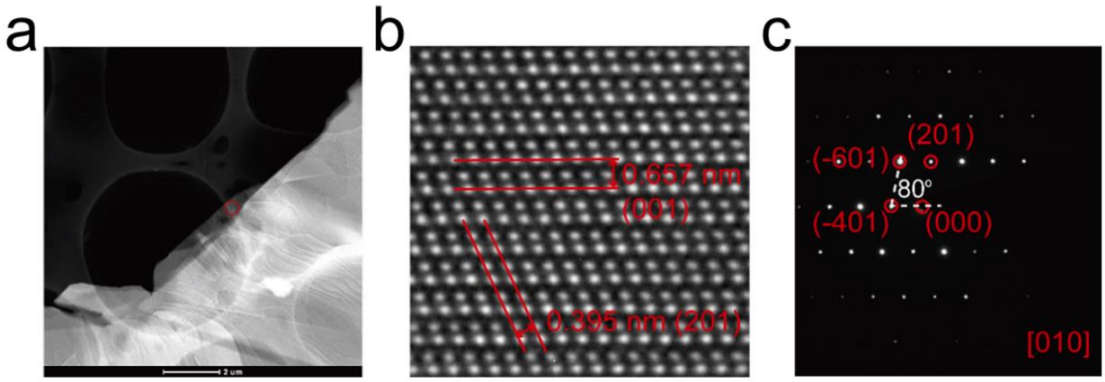

Figure 4. 2 Structure characterization.

(a) the TEM image of GeAs nanolayer, (b) HRTEM of the GeAs nanolayer, (c) Corresponding SAED pattern of GeAs nanolayer, The zone axis is along [0 1 0].

We have studied the atomic structure of GeAs by TEM. Figure 4.2 (a) is the collected low-magnification TEM image and it exhibits a layered structure of GeAs. HRTEM and SAED characterizations were performed on the zone with a few layers of GeAs at the edge (red dotted circle), as shown in Figure 4.2 (b) and (c), respectively. HRTEM image shows that in the two directions with an angle of 80° , the lattice spacing is 0.657 nm and 0.395 nm, respectively. By comparing the XRD diffraction

card of GeAs material (Figure 4.4), these two spacings correspond to GeAs (001) and (201) planes. To The bright electron diffraction spots in Figure 4.2 (c) indicate that the sample is a single crystal material with good crystallinity. By comparing the distance between the diffraction spots with the parameters in Figure 4.4, the diffraction spots near the origin correspond to (2 0 1), (-6 0 1), (-4 0 1) planes. Finally, we can determine the out-of-plane crystal axis in the selected area corresponds to [0 1 0] direction.

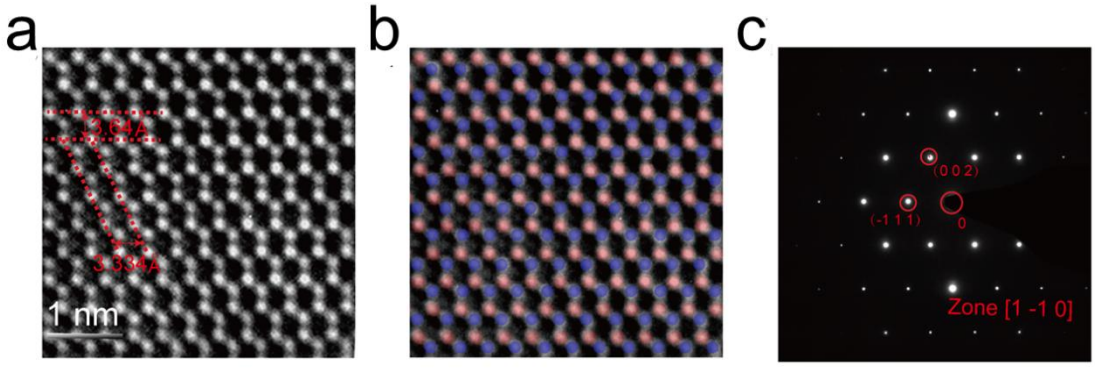

Figure 4. 3 Structure characterization.

(a) TEM image of GeAs nanolayer, (b) Pseudo color of HRTEM. Pink dots represent bright atoms and blue dots represent dark atoms. (c) SAED pattern of GeAs nanolayer. The zone axis is along [1 −1 0].

In order to observe more details of the crystal structure, we rotated the crystal axis with to another direction, as shown in Figure 4.3 (a). For the two directions with an angle of 60°, the lattice spacing is 3.64 Å and 3.334 Å, respectively. In order to further determine the crystal axis of this test plane, the area electron diffraction pattern was measured, which can be analyzed from the corresponding SAED image. The diffraction spots near the origin correspond to the (0 0 2) and (-1 1 1) planes, so the out-of-plane crystal axis can be determined to be the [1 -1 0] direction. Meanwhile, a shading analysis on the HRTEM image in Figure 4.3 (a) shows a contrast between the atoms, which has been rendered with a color atomic map in Figure 4.3 (b). Here we can clearly see the alternating arrangement of Ge atoms and As atoms.

#	2-Theta	d(?)	I(f)	(h k l)	Theta	1/(2d)	2pi/d
1	9.522	9.2803	2.1	(0 0 1)	4.761	0.0539	0.6770
2	11.611	7.6152	2.3	(2 0 0)	5.805	0.0657	0.8251
3	13.546	6.5315	12.2	(-2 0 1)	6.773	0.0766	0.9620
4	16.396	5.4019	5.5	(2 0 1)	8.198	0.0926	1.1631
5	19.111	4.6402	0.6	(0 0 2)	9.555	0.1078	1.3541
6	20.401	4.3495	13.0	(-2 0 2)	10.201	0.1150	1.4446
7	23.343	3.8076	5.7	(4 0 0)	11.672	0.1313	1.6502
8	23.477	3.7862	10.5	(-4 0 1)	11.738	0.1321	1.6595
9	24.276	3.6633	0.1	(2 0 2)	12.138	0.1365	1.7152
10	24.276	3.6633	0.1	(1 1 0)	12.138	0.1365	1.7152
11	25.704	3.4630	0.5	(-1 1 1)	12.852	0.1444	1.8144
12	26.540	3.3558	7.8	(1 1 1)	13.270	0.1490	1.8724
13	26.935	3.3074	11.0	(4 0 1)	13.468	0.1512	1.8997
14	27.285	3.2658	24.1	(-4 0 2)	13.643	0.1531	1.9240
15	28.837	3.0935	33.9	(0 0 3)	14.419	0.1616	2.0311
16	28.978	3.0787	23.3	(-2 0 3)	14.489	0.1624	2.0408
17	29.461	3.0293	100.0	(3 1 0)	14.731	0.1651	2.0741
18	29.940	2.9819	16.6	(-3 1 1)	14.970	0.1677	2.1071
19	30.353	2.9423	1.1	(-1 1 2)	15.177	0.1699	2.1355
20	31.780	2.8134	3.4	(1 1 2)	15.890	0.1777	2.2333
21	32.084	2.7874	23.1	(3 1 1)	16.042	0.1794	2.2541
22	33.140	2.7009	6.7	(4 0 2)	16.570	0.1851	2.3263
23	33.253	2.6920	23.3	(2 0 3)	16.627	0.1857	2.3340
24	33.400	2.6806	13.5	(-3 1 2)	16.700	0.1865	2.3440
25	33.624	2.6632	0.9	(-4 0 3)	16.812	0.1877	2.3592
26	34.782	2.5771	2.1	(-6 0 1)	17.391	0.1940	2.4380

Figure 4. 4 The PDF card of GeAs crystal.

Card number: PDF#89-1502

4.3.2 Angle-resolved polarized Raman spectroscopy

4.3.2.1 Measurement principle

Raman scattering spectroscopy is the most common measurement to characterize two-dimensional material structure. The type of crystal can be identified by the characteristic peak, and the in-plane anisotropy of the crystal can be studied by comparing the angle-dependence of the intensity of the characteristic peak. Angle-resolved polarization Raman spectroscopy is the most direct measurement method to detect the symmetry of the material lattice. In this chapter, we use angle-resolved polarized Raman spectroscopy to study the in-plane anisotropy of GeAs materials. The schematic diagram of the optical path is shown in Figure 4.5. The orange double arrow represents the polarization direction of the incident laser. The green arrow represents

the signal receiving direction of the analyzer. Before the entrance of the spectrometer, the analyzer is set to be vertical and horizontal to the direction of the incident laser. When the orange arrow is parallel to the green arrow, it indicates the parallel configuration; when the orange double arrow and the green double arrow are perpendicular to each other, it indicates the cross configuration. The angle dependence of the intensity of the Raman peak is obtained by rotating the sample.

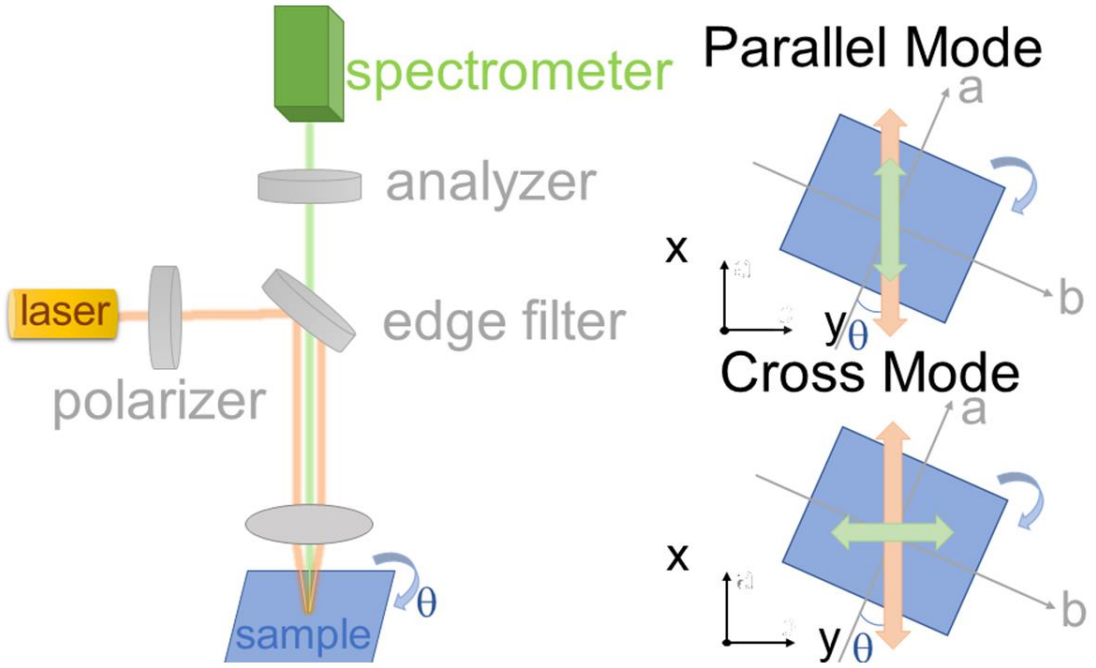

Figure 4. 5 Schematic diagram of angle-resolved Raman spectroscopy

For the GeAs crystals in this chapter, the Raman tensor (R) of all Raman modes can be expressed by the formula $R = \begin{vmatrix} a & d & e \\ d & b & f \\ e & f & c \end{vmatrix}$. The intensity of the Raman mode can be expressed by the formula $I \propto |e_s R e_i|^2$ where $e_s = [cos\theta \quad sin\theta \quad 0]$ is scattered light and $e_i = \begin{matrix} cos\theta \\ [sin\theta] \\ 0 \end{matrix}$ is unit polarization vector. Taking the e_s and e_i into I formula, the intensity of the Raman mode can be expressed by the formula $I \propto |acos^2\theta + bsin^2\theta + dsin2\theta|^2$.

4.3.2.2 Results and analysis

As shown in Figure 4.6 (b), the black curve is the measurement in the traditional Raman spectroscopy mode. Seven Raman peaks can be observed in the Raman shift from 100 cm^{-1} to 350 cm^{-1}, which are consistent with the previous reports[123]. The Raman peaks at 147, 172, 274, 283, and 307 cm^{-1} belong to the A_g mode, while the Raman peaks at 242 and 256 cm^{-1} belong to the B_g mode. In addition, we measured the angle-dependence Raman spectroscopy with the analyzer parallel to the laser polarization direction (parallel mode) and perpendicular to the laser polarization (cross mode), respectively. Six Raman peaks can be observed in the parallel mode (blue curve) while only two peaks are present in the cross mode (red curve). By comparing the Raman spectra of these three modes, it can be confirmed that GeAs crystals have strong in-plane anisotropy. The angle-resolved polarization Raman spectrum in parallel mode is measured by rotating the sample every 10°, as shown in Figure 4.6 (a). The intensity of all Raman peaks in the polarized Raman spectrum image varies with the sample angle.

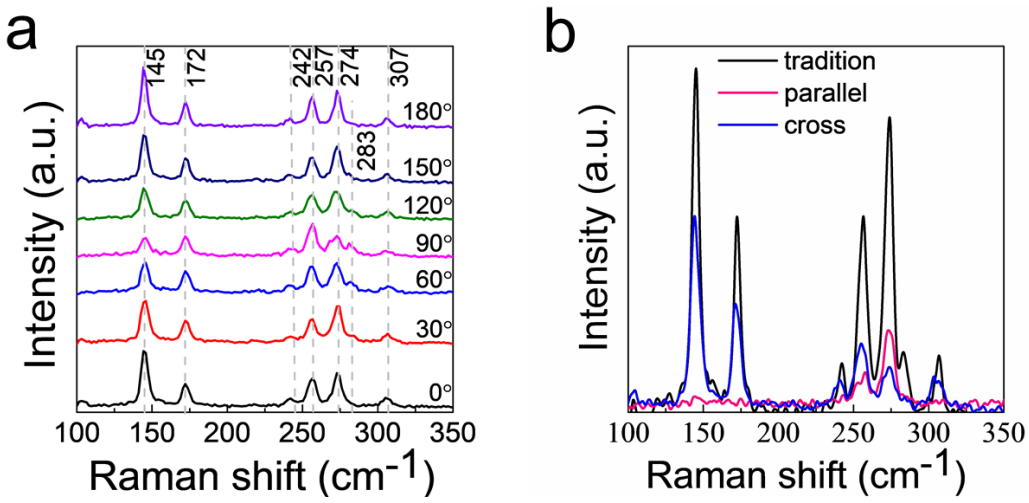

Figure 4. 6 Raman scattering spectrum based on GeAs nanosheets. (a) Angle-resolved Raman scattering spectrum; (b) Raman scattering spectrum in traditional, parallel, vertical, and three modes.

We extracted the Raman peak intensity at different angles from Figure 4.6 (a). As shown in Figure 4.7 (c,d,g,h), the peaks in A_g mode (147 cm^{-1}, 172 cm^{-1}, 274 cm^{-1} and

283 cm^{-1}) are fitted by the formula $|b|^2 cos^4\theta + |c|^2 sin^4\theta + 2|b||c| cos\varphi_{bc} sin^2\theta cos^2\theta$. It is found that the period of the anisotropy of the Raman peak is 180° corresponding to two-leaf type. As shown in Figure 4.7 (e, f), the peaks in the B_g vibration mode (242 cm^{-1}, 256 cm^{-1}) are fitted with the formula $|f|^2 \sin^2 2\theta$. It is found that the period of the anisotropy of the Raman peak intensity is 90° corresponding to four-leaf type.

Figure 4.7 (a) and (b) are the microscope and AFM images of the sample used to measure Raman spectroscopy. The white circle in Figure 4.7 (a) is the sample area where Raman spectroscopy signals are collected. It can be seen from AFM that the thickness of the sample is 36 nm. In the experiment, the two edges of the sample are used for position calibration to ensure that the measuring point remains unchanged during rotating sample angle.

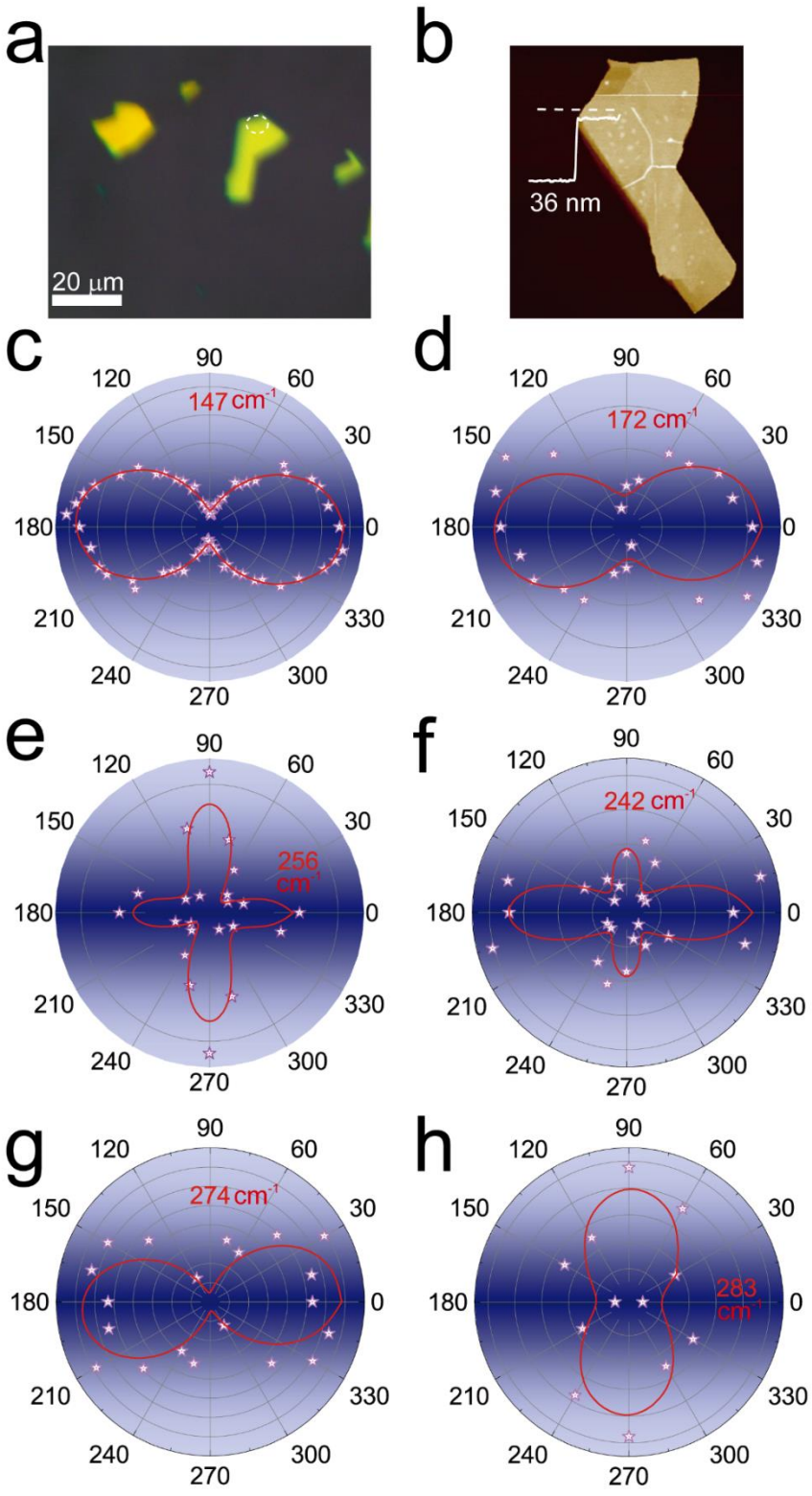

Figure 4. 7 The angle-dependent Raman peak intensity in polar coordinates.

(a) Microscope image of GeAs nanosheets used in the Raman test; (b) AFM image of GeAs nanosheets; 147 cm^{-1} (c), 172 cm^{-1} (d), 242 cm^{-1} in polarization configuration The angle-dependent Raman peak intensity of 256 cm^{-1}(e), 242 cm^{-1} (f), 274 cm^{-1} (g), and 283 cm^{-1} (h).

4.3.3 Polarization absorption spectrum of GeAs

4.3.3.1 Measurement Principle

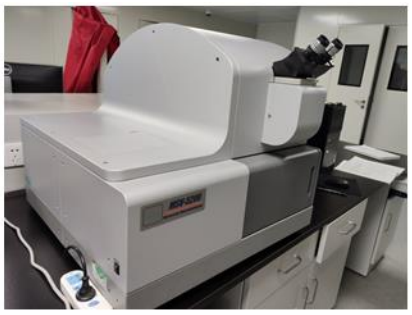

Figure 4. 8 Polarization Absorption Spectrometer.

The micro-absorption spectrum was characterized by the instrument of MSV-5200 produced by JASCO, as shown in Figure 4.8. The minimum size of spot is a 20μm in diameter. The schematic optical path diagram is shown in Figure 4.9, where the left half is the light emitting device. The Xenon lamp can emit the full spectrum of unpolarized light. After passing through the filter and diffraction grating, a signal wavelength of light is selected. The unpolarized light will pass through the polarizer to be polarized into linearly polarized laser, following by separating into two paths. One path is to be detected directly by detectors, and the other path is to be focused on the sample. The light penetrating the sample can be collected by the detectors.

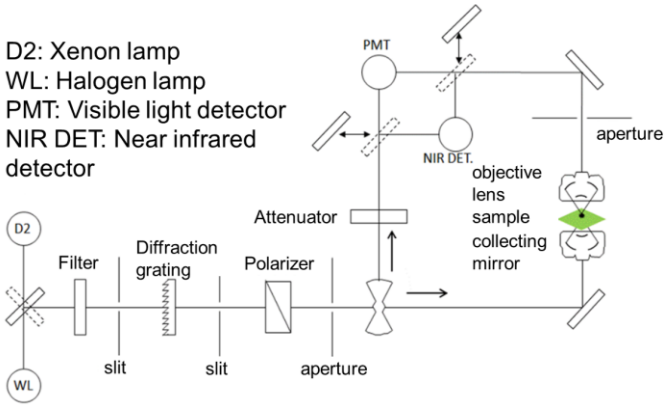

Figure 4. 9 The schematic optical path diagram of the slightly curved polarization absorption spectrum measurement

4.3.3.2 Results and analysis

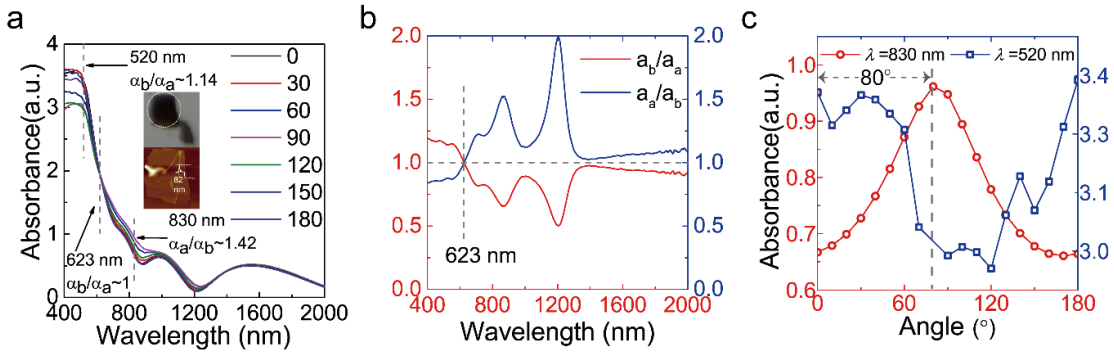

Figure 4. 10 Polarization-resolved absorption spectra. (a) Polarization-resolved absorption spectra in experimental with the spectral range from 400 to 2000 nm in steps of 30°. The microscope image and AFM image of GeAs are inset. (b) The dichroism ratios αb/αa (red line) and αa/αb (blue line) are extracted from (a). (c) Absorption intensity as a function of angle varies under 520 nm (blue plots and line) and 830 nm (red plots and line), respectively

In order to further study the optical absorption properties of GeAs nanosheets, we prepared GeAs on a transparent quartz substrate and measured the polarization absorption spectrum in the wavelength range of 400 nm to 2000 nm, as shown in Figure 4.10. The sample size is 50×50 μm and a thickness of 82 nm (shown in the inset in Figure 4.10 (a)). It can be seen from Figure 4.10 (a) that from 400 nm to 520 nm, the absorption intensity is relatively high, and the dichroism is also large. When wavelength is larger than 520 nm, the absorption intensity gradually decreases, and the change of intensity as a function of angle decreases. [106, 124, 125] The absorption at 632 nm has almost no change of intensity, while a maximum absorption anisotropy of 1.42 is found at around 830 nm. According to first-principles calculations, the band gap of the GeAs material is about 0.83 eV, corresponding to the absorption wavelength of 850 nm. Therefore, the absorption peaks from 1200 to 2000 nm are not due to the absorption of the GeAs itself. The absorption spectra in mid-infrared and far-infrared are attributed to the exciton, defects, and impurity absorption in the GeAs crystal. The dominant polar direction of GeAs flake is along b-axis at the wavelength of 400 nm to 500 nm, whereas when wavelength is larger than 623 nm the dominate polar direction change to be along the a-axis direction. In order to clearly observe the reverse phenomenon, the dichroism ratio is extracted from the absorption spectra and displayed in Figure 4.10 (b). Two

kinds of dichroism ratios, α_a/α_b (the blue line) and α_a/α_b (the red line) intersects at 623 nm, which indicates the reverse point. The angle-dependent absorptions under 520 nm and 830 nm wavelengths, are extracted from Figure 4.10 (a) and shown in Figure 4.10 (c). It is clearly that the dominate direction of polar absorption is different between visible (along b-axis) and near-infrared range (along a-axis) with a change angle of about 80°.

4.4 Photoelectric properties

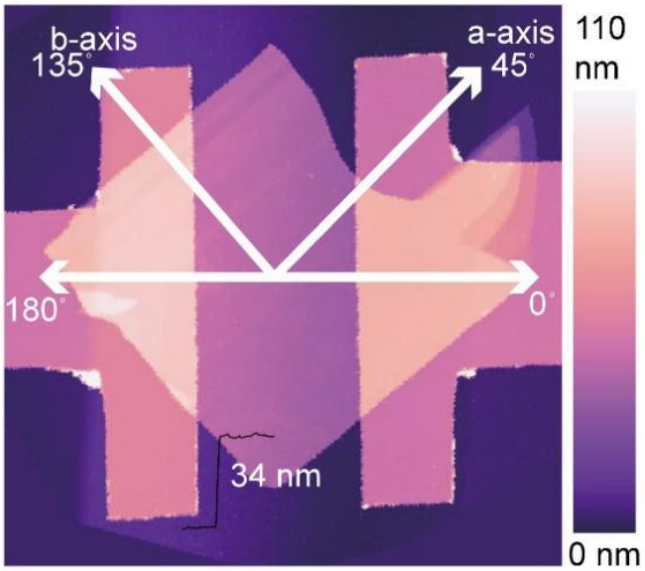

Figure 4. 11 Atomic force microscope image of the device based on GeAs nanoshets.

Firstly, the GeAs nanosheets are transferred to the SiO_2/Si substrate by mechanical peeling and the PMMA is spin-coated onto GeAs (with a thickness of about 300nm). After electron beam exposure, the prepared electrode pattern is transferred to the PMMA film. Subsequently, Ti/Au metal was deposited by electron beam evaporation equipment. Finally, the device is obtained through a lift-off process. As shown in Figure 4.11, 34 nm GeAs flake is used to prepare two-terminal devices, and the crystal axis of the sample has been calibrated in the image.

4.4.1 Ordinary photoelectric properties

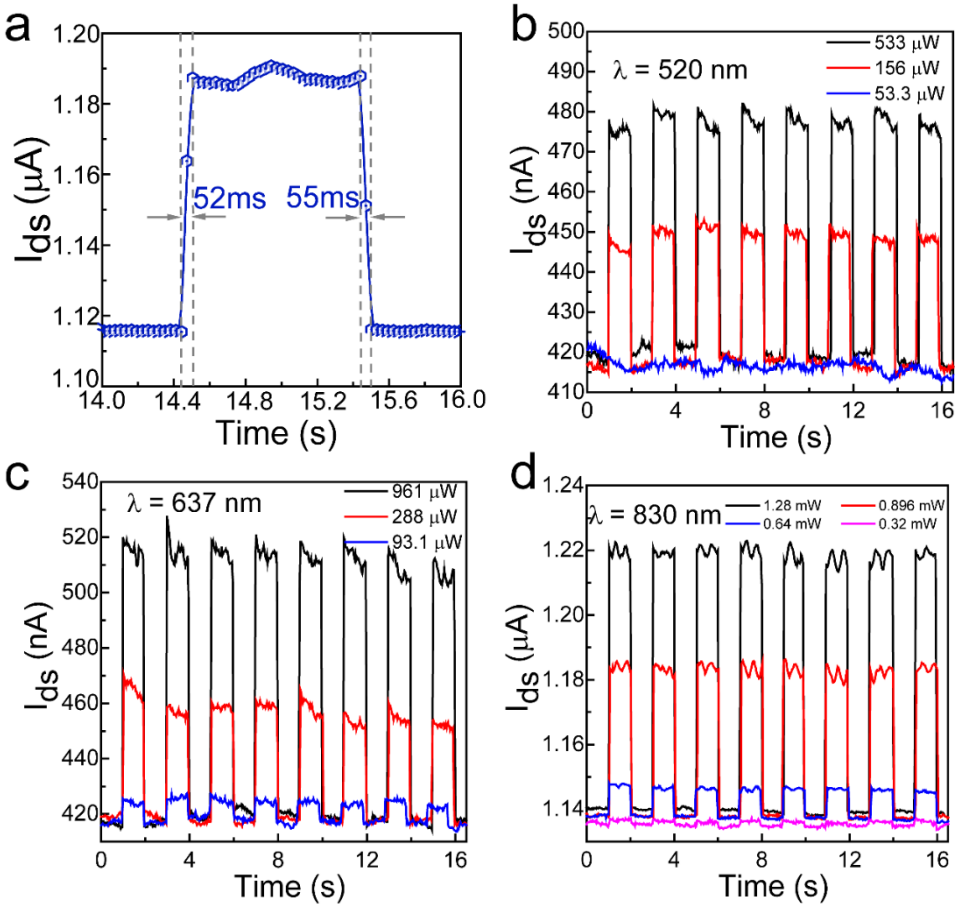

Figure 4. 12 Optoelectronic properties of the GeAs based device.

(a) Photoresponse time of the device. Time dependent I_{ds} of the transistor based on the GeAs under the drain-source voltage V_{ds} of 10 mV. The Ids under the laser of 520 nm (b), 637 nm (c), 830 nm (d) with different power.

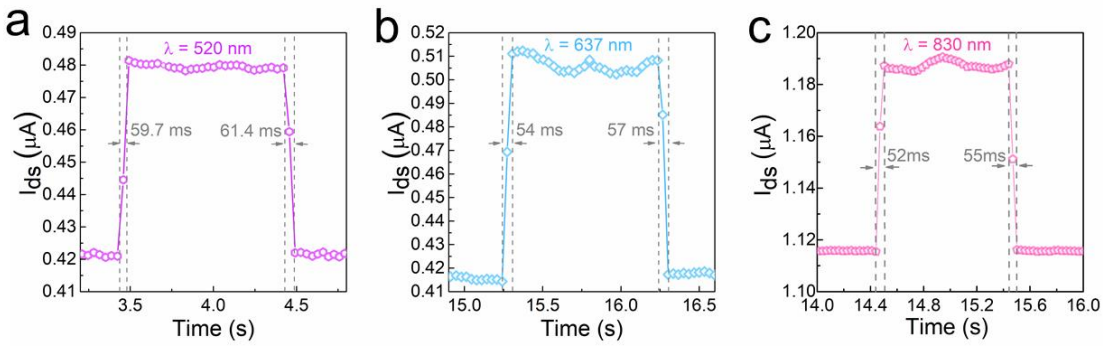

Figure 4. 13 Photo response speed of the GeAs based device.

Under (a) 520 nm (b) 637 nm (c) 830 nm laser irradiation, the light response and recovery of the device.

We have studied the optical response I-t curve of the device under different

wavelengths and different illumination power, as shown in Figure 4.12. At the same time, the light response time and recovery time of the device were measured under the wavelength of 520 nm, 637 nm, and 830 nm. For the lasers, we used solid-state lasers with themselves photo response time of 10ms. The results are shown in Figure 4.13. When the wavelength increases, the response time and recovery time becomes shorter. The optical response is the fastest at the laser wavelength of 830 nm. In addition, it is found that the recovery time is slightly longer than the light response time.

4.4.2 Polarized photoelectric properties

4.4.2.1 Measurement Principle

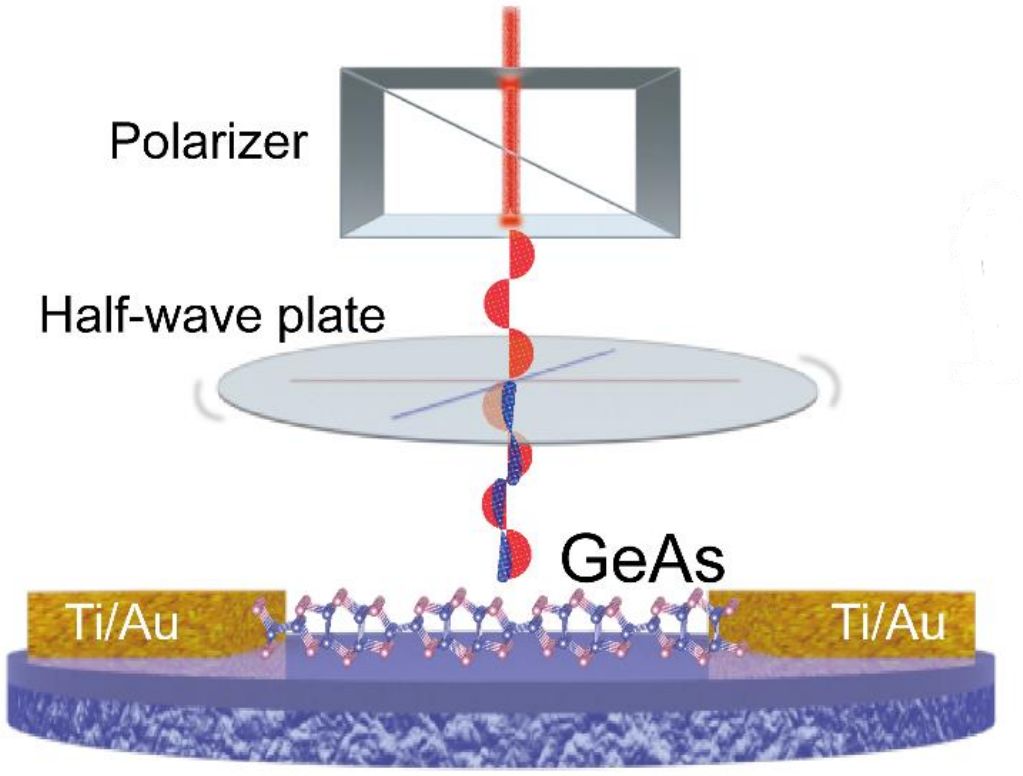

Figure 4. 14 Schematic diagram of photodetection device based on GeAs

We have also studied the optical properties of the polarization detector based on GeAs nanosheets. Figure 4.14 is a schematic diagram of the characterization of the polarized light response. After the light is emitted by the laser, it passes through the Green prism to form a linearly polarized light, following by a half-wave plate. The half-

wave plate can change the polarization angle of the linearly polarized light. In the experiment, the angle of the half-wave plate is rotated to obtain the angle-dependent photocurrent. Then the linearly polarized light is focused through the eyepiece and finally irradiated on the surface of the sample. During the measurement, the laser irradiation position is fine-tuned to get the maximum light response.

4.4.2.2 Results and analysis

Figure 4.15 shows the polarization-sensitive photocurrents with 520 nm and 830 nm wavelengths in the polar coordinates. The blue and red data are the light response values under the 520nm and 830nm wavelengths, respectively. The data are fitted by the formular of $I_{ph}(\theta) = I_{pmax}cos^2(\theta + \varphi) + I_{pmin}sin^2(\theta + \varphi)$, where θ is the incident direction of polarized light, I_{pmax} and I_{pmin} are the maximum current and minimum current of the light response, respectively, and φ is the fitting parameter. From the fitting, it is easily found that the two photocurrents present the two lobes shape, but the polarization directions are different. The polarization response of the 520 nm laser is dominated by the b axis, and the polarization response of the 830 nm laser is dominated by the a-axis, and the deflection angle is 75°, which is consistent with the phenomenon of absorption reversal. The dichroism of the polarization detector under 520nm and 830nm laser irradiation is 1.49 and 4.4, respectively, which is much larger the dichroism of absorption. Theoretically, since the anisotropy of the device comes from the material itself, the anisotropy of absorption should be bigger than the light response. The Schottky junction of the gold electrode on GeAs could enhance the dichroism of the light response.

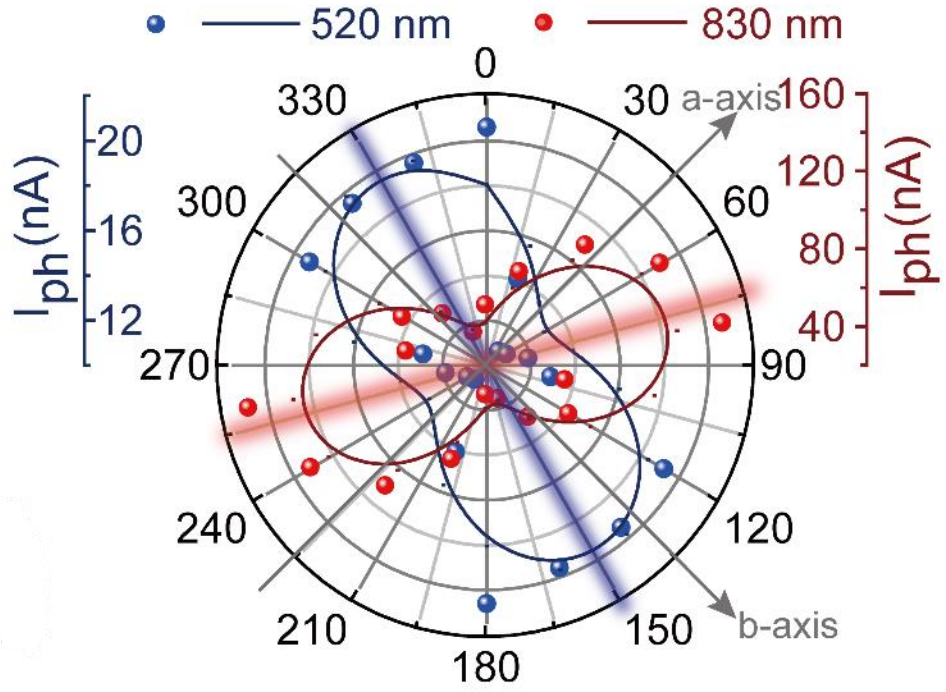

Figure 4. 15 Experimental polarization-sensitive photocurrents are plotted with the linear-polarization laser of 520 nm and 830 nm in the polar coordinates. I_{ph} is photocurrent defined as $I_{ph}=I_{light}-I_{dark}$.

The photo-response of GeAs photodetector was fast enough to be measured by the polarization-dependent photocurrent mapping on the device to understand the working mechanism. The 100X focal length eyepiece was used to obtain a smaller focus spot. The 30 mV of drain-source voltage (V_{ds}) is added between the drain electrode and source electrode. The 0°was defined as the direction of linear-polarization laser which is perpendicular with the electrode direction. The polarization-dependent photocurrent mappings under the irradiation of 520 nm laser are shown in Figure 4.16 (a), and the light polarization directions have been marked in each photocurrent mapping. From Figure 4.16 (a), we observe that the photocurrent signals occur in the contact zones between GeAs crystal and Au electrodes. The photocurrent has opposite polarity at the two contacts. This is due to the photovoltaic and photo thermoelectric effect of the Schottky junction formed by the Ti/Au electrode contact on p-type GeAs crystal. In addition, the spatial photocurrent mappings show a linear dichroism photodetection

behavior. The photocurrent reaches its maximum value at 0° polarization and decreases gradually with the variation of polarization direction. In the case of 830 nm laser irradiation, the photocurrent signals are similar as the case of 520nm, which mainly occurs in the contact regions, as shown in Figure 4.16b. But the photocurrent increases when the polarization angle increases and it reaches a maximum value at 80°. The distinct angle difference for the maximum photocurrent between 520 and 830 nm wavelength could be attributed to the polarization dependent absorption reversing from b-axis to a-axis happening in 623 nm as shown in Figure 4.10b. This further validates the wavelength dependent polarization reverse nature of GeAs crystal.

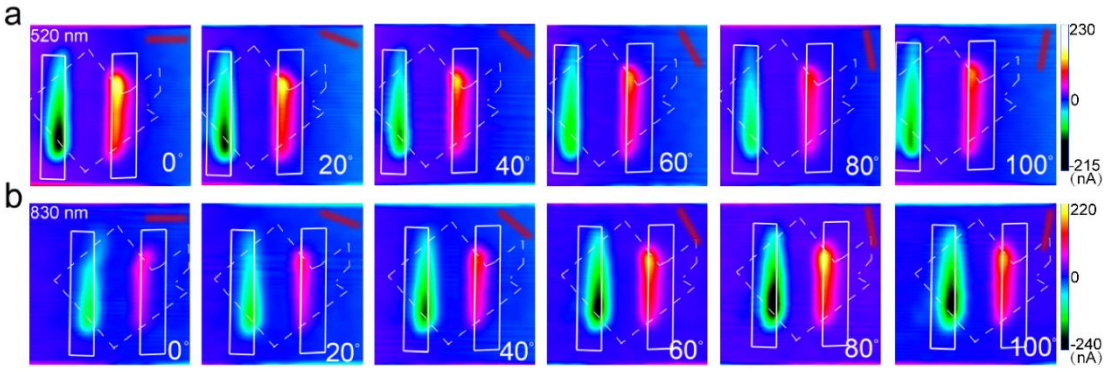

Figure 4. 16 The polarization-dependent photocurrent mapping of device under a V_{ds} of 30 mV. The linear-polarization laser of 520 nm (a) and 830 nm (b), respectively, showing the linear dichroic photodetection. The direction and angle of polarization laser is illustrated in each photocurrent mapping. The color bars are in the right side.

The slight difference of the photocurrent intensity for left and right contact could be due to the bias applied for the measurement. To further prove this point, we have measured the photocurrent mappings under zero bias voltage for both wavelengths, as shown in Figure 4.17. The mappings show a similar angle dependence as the case with the bias of 30mV, which further proves that the angle dependence of photo-response is due to the absorption anisotropy of the GeAs material.

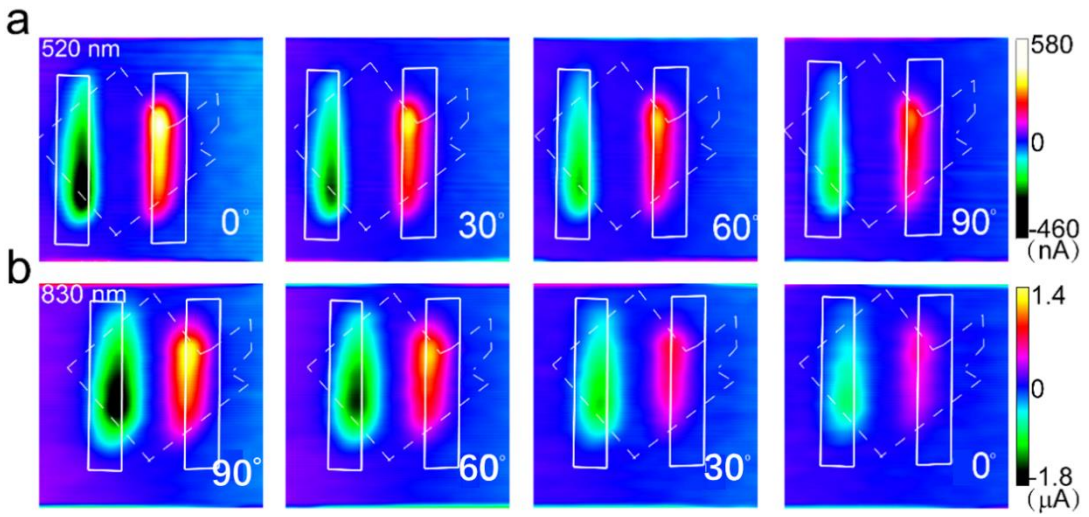

Figure 4. 17 The polarization-dependent photocurrent mapping of device under zero bias. The linear-polarization laser of 520 nm (a) and 830 nm (b), respectively

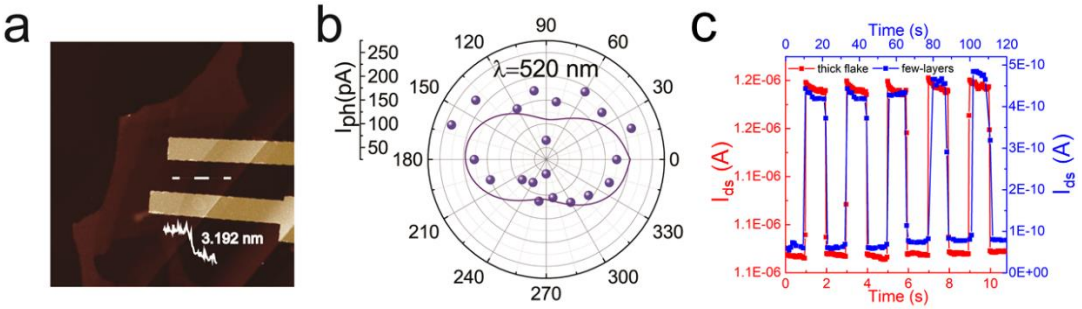

Figure 4. 18 Photo response of thin GeAs based device. (a) AFM image of the few-layer GeAs device. (b) Experimental polarized photocurrent under the linear-polarization laser of 520 nm. (c) Time dependent Ids of thick flake GeAs and few-layers GeAs under the zero Vds and 520 nm laser of 541 μW power.

To investigate the photoelectronic properties of the few-layer GeAs crystal, we prepared photodetectors based on GeAs few-layer. Figure 4.18 (a) shows the device image of AFM. The thickness of GeAs few-layer is 3.192 nm, nearly 4 layers. The results of angle-resolved photocurrent under the laser of 520nm is extracted and fitted in polar coordinates by the formula of $I_{ph}(\theta) = I_a cos^2(\theta + \varphi) + I_b sin^2(\theta + \varphi)$. It clearly shows that the photocurrent of 4-layer GeAs is significantly smaller than the bulk material. However, the device based on 4-layer GeAs crystal exhibits similar anisotropic characteristics, as shown in Figure 4.18 (b). Figure 4.18 (c) also show the similar light response time and recovery time for thick and 4-layer samples.

4.5 First-principles calculation

To understand the experimental results, we have used the projection enhanced plane wave (PAW) method in density functional theory (DFT) to calculate GeAs structure [126-128]. In the whole calculation, the hybrid function method (HSE06) is mainly used, and the method of Perdew, Burke, and Ernzerhof (PBE) is used as a supplementary method to calculate the electron exchange and relaxation processes [87]. In the whole process, 500 eV is used as the plane wave attached energy. All structures are fully relaxed with a tolerance of 0.02 eV/A. The lattice parameters of the GeAs after relaxation are a=3.833Å, b=8.543Å, and c=9.902Å[129]. We have calculated the band structure, density of states, and absorption spectrum of GeAs for single layer and bulk materials.

4.5.1 Band structure calculation

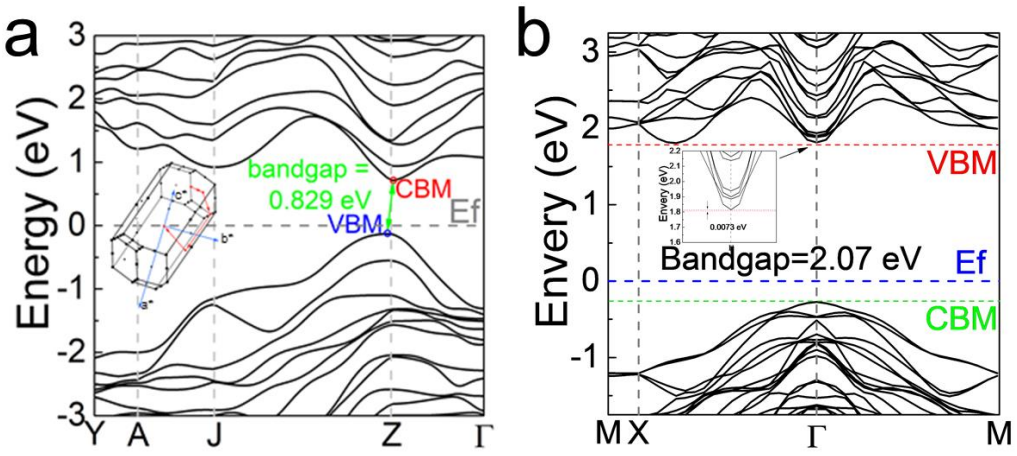

Figure 4. 19 Electronic Band structure with the HSE06 functional method.

(a) bulk GeAs; (b) monolayer GeAs

The electronic band structure of bulk GeAs (Figure 4.19 (a)) exhibits that the bandgap of bulk crystal is indirect bandgap semiconductor with 0.829 eV with VBM and CBM locating at two sides of Z point, while the integral path of the band structure is illustrated. At the same time, the band structure of GeAs monolayer is given in Figure 4.19 (b), which shows an indirect bandgap of 2.07 eV. The secondary energy valley locates at with 0.0073 eV higher than conduction-band minimum energy. Different band

structures of monolayer and bulk GeAs crystal led to different optical and electrical properties.

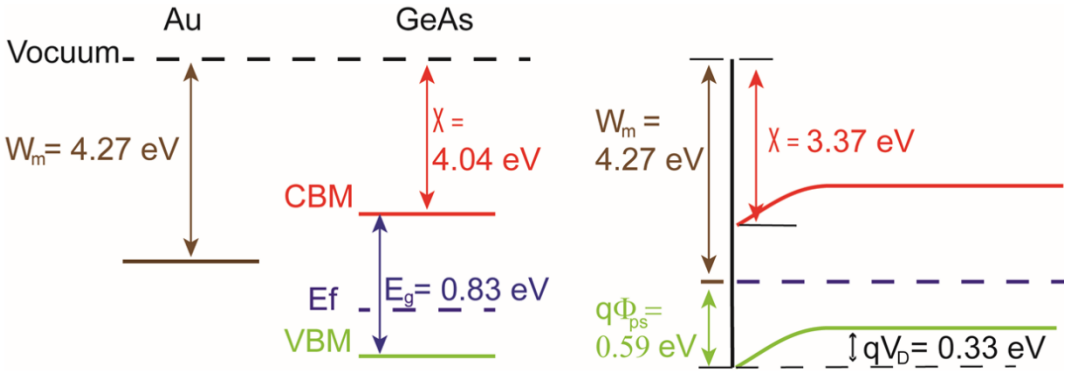

Figure 4. 20 The band realignment of two layers GeAs contacting with Au electrode. The picture on the left shows the band alignment of metal and two-dimensional material themselves. The picture on the right is the overall band alignment after contact. $q\Phi_{ps}$ is the height of Schottky barrier, W_m is the function work of the metal and X is the electron affinity of the GeAs.

The Schottky barrier forms when Au electrode contacts with GeAs. This phenomenon generally occurs between two-dimensional materials and metallic electrodes with high work function when existing relatively low interface density of states.[126, 127] Figure 4.20 displays the discrete energy bands of two layers of GeAs and Au and the realignment of GeAs in contacting with Au. It is clearly to see that a strong built-in electric field is formed in the Schottky barrier, with a Schottky barrier height of $q\Phi_{ps} = 0.59\text{eV}$. The photo-generated carriers at the Au/GeAs interface ransfer to the two sides of the Schottky contacts under the action of the field. Then a potential difference is formed at both contacts, resulting in the photocurrent. The photo-generated minority holes inside the GeAs nanoflake are blocked by the Schottky barrier and contributes less to the photo-generated current. It can explain why we observe in experiment (Figure 4.15 and 4.16) that the photocurrent signals of the device mainly occur close to the Schottky contact regions.

4.5.2 Calculation of absorption spectrum

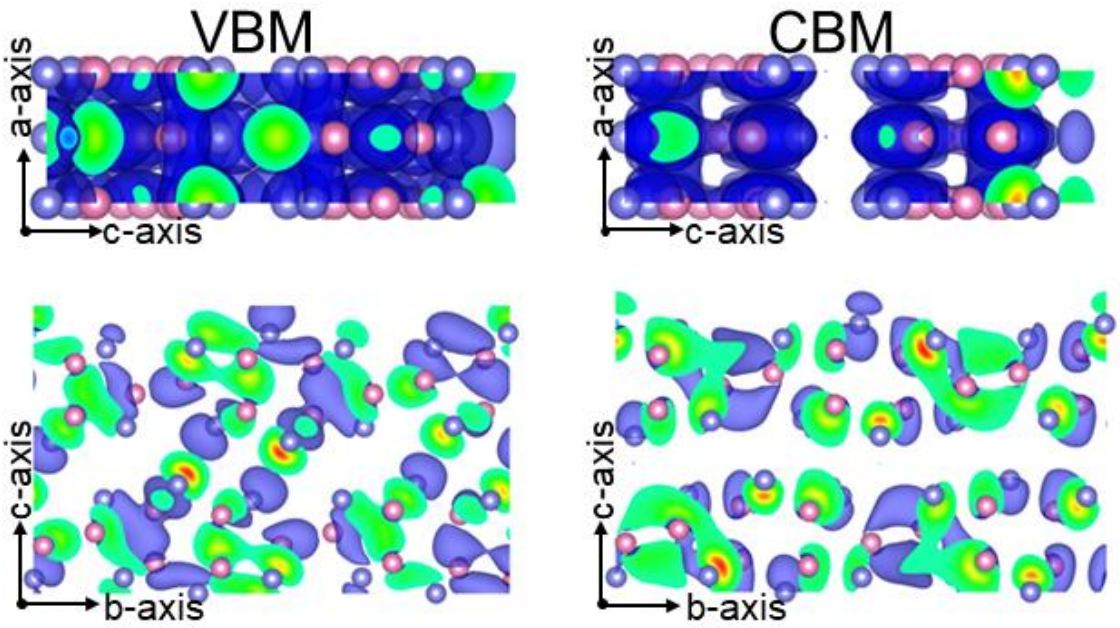

Figure 4. 21 Partial charge density of nanoflake GeAs at the state of VBM and CBM.

To analyze the anisotropic absorption of GeAs crystal, the partial charge density (PCD) was calculated by VASP. The most typical PCD of VBM and CBM were extracted and displayed in Figure 4.21 on the ac-plane and bc-plane, respectively. The spatial distribution of VBM and CBM wave functions are distinct along the a-axis and b-axis. The Fermi Golden Rule was used to obtain the formula

$$|< c|H_{eR}|v >|^2 = \frac{|E|^2}{4q^2}|\int u^*_{c,k_c}\exp\left[i(q-k_c)\cdot r\right](e\cdot p)u_{v,k_v}\exp\left(ik_v\cdot r\right)dr\,|^2,$$

where |v> is the valence band state with energy Ev and wavevector k_v and |c> is the conduction band with corresponding energy Ec and wavevector k_c. From the image of PCD, we can obtain the two states wavefunction $u^*_{c,k_c}\exp\left[i(q-k_c)\cdot r\right]$ and $u_{v,k_v}\exp\left(ik_v\cdot r\right)$ possessing different value along x-axis and y-axis. Therefore, the value of the matrix element $|< c|H_{eR}|v >|^2$ varying with angle can demonstrate the polarization dependent absorption with in-plane anisotropy.

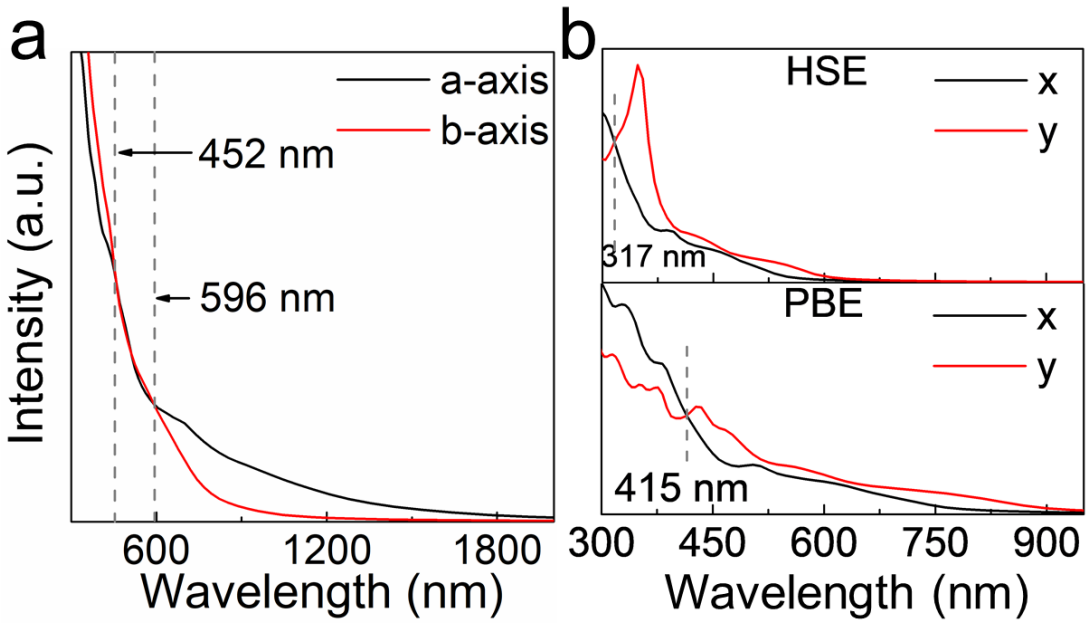

Figure 4. 22 The absorption spectrum of bulk GeAs (a) and monolayer GeAs (b) in theory. The reverse range of strongest absorption direction is between 452 nm and 596 nm.

Furthermore, the theoretical optical absorbance of 1L GeAs (Figure 4.22 (b)) and nanoflake GeAs (Figure 4.22 (a)) was calculated by the formula $\alpha(\omega) = \sqrt{2}[\sqrt{\varepsilon_1^2(\vartheta) + \varepsilon_1^2(\vartheta)} + \varepsilon_1(\omega)]^2$ with the method of PBE. In the formula, the frequency of the incident photon is shown as ω and the real part and imaginary part of the dielectric function are shown as $\varepsilon_1(\vartheta)$ and $\varepsilon_1(\vartheta)$, respectively. From Figure 4.22 (a), we observed that the b-axis direction has larger absorption between 400 nm and 452nm, however, a-axis has stronger absorption when the wavelength is larger than 596 nm. This can explain the experimentally observed polarization reversal phenomenon as a function of wavelength. In Figure 4.22 (b), the theoretic calculations also predict that the GeAs monolayer could undergo a similar polarization absorption direction reversal phenomenon by PBE and HSE method. Compare the two methods, the HSE method uses a denser integration path and considers the hatree-fock exchange interaction. Therefore, the HSE hybrid functional assess the actual electric structure. For the calculated electric structure, the calculation result of HSE method is slightly larger, the calculation result of PBE is smaller. In this case, the inversion point could locate between 317 nm (calculated by HSE method) and 415 nm (PBE method).

4.6 Conclusion

Polarization detection has an important potential for applications for biological tumor imaging and aerosol detection etc. Actually, the polarization detection are usually realized by adding optical polarizer in front of the detector to obtain polarization information. The high cost, short lifetime of optical components, and large detector volume limit the application. Here, we have demonstrated a new type of two-dimensional material (GeAs) with large in-plane anisotropy for the polarized light detector

First, a single crystal GeAs material was prepared by the chemical vapor transport method. The GeAs crystal has excellent stability in the air, and then we used the mechanical exfoliation method to obtain the few-layer GeAs crystals and characterize them by using scanning electron microscopy and Raman spectroscopy to confirm the crystal structure.

Secondly, the in-plane low symmetry of GeAs crystals is studied. From the angle-resolved Raman spectrum, it can be concluded that GeAs crystals have strong in-plane asymmetry. From the polarization absorption spectrum, not only the wavelength dependence but also the angle dichroism of absorption can be obtained. It reaches a maximum absorption dichroism near 830nm with a ratio of 1.42. Meanwhile, it is found that the visible and near-infrared wavebands have different angle for the maximum absorption dichroism, which are separated with an angle of 80°.

Thirdly, we prepared GeAs nanosheets into two-terminal photodetectors for polarized light detection. The dichroism ratios measured at 532nm and 830nm are as high as 1.49 and 4.4, respectively. The angle difference for the maximum photocurrent between 532nm and 830nm is about 75 degrees, which is consistent with the absorption reversal phenomenon. We further studied the source of this reversal phenomenon and found that it is related to the arrangement of the crystal. The HR-STEM image under the [010] crystal axis shows that Ge atoms appear in pairs with As atoms. There are two arrangements of atoms, and the angle between these two arrangements is also 80°.

Therefore, it can be concluded that the two directions of the two arrangements (001) and (201) directions correspond to the maximum response direction of polarized light in the visible and infrared wavelengths, respectively.

Finally, we have also studied the photo-response mapping of GeAs photodetectors. It is found that the maximum light response occurs at the Schottky contact between the semiconductor GeAs crystal and the metal electrode. This Schottky junction also contributes to the improvement of the dichroism of the polarization detector [1]compared to the absorption dichroism of the GeAs material. At 830nm under linearly polarized laser irradiation, the dichroism reaches 4.4, which is greater than the dichroism (1.42) absorbed by the GeAs crystal itself. This is due to the existence of the Schottky junction, which reduces the dark current of the device, and its built-in electric field enhances the photocurrent. In summary, the excellent performance of GeAs crystal is favorable for polarization detectors applications.

Chapter 5: IV-VI compounds based Photodetector

5.1 ZnSnS alloy based Photodetector

Most of two-dimensional metal chalcogenides have similar crystal structures and can form alloy compounds by dissolving two or more compound components together. These alloy compounds have adjustable stoichiometry, along with tunable physical properties of based on their stoichiometry. Recently, a lot of two-dimensional metal chalcogenide alloys that can stably exist have attracted the attention of researchers, including $W_xMo_{1-x}S_2$, $W_xMo_{1-x}Se_2$, $MoS_{2x}Se_{2-2x}$, WS_2Se_{2-2x}, SnS_2Se_{2-2x}, $ReS_{2x}Se_{2-2x}$, $HfS_{2x}Se_{2-2x}$, CdS_xSe_{1-x}, $GaSe_xTe_{1-x}$, etc. By changing the composition of the alloy compounds, most of these compounds can achieve continuous adjustment of band structure, as well as tunable electrical or optoelectronic properties over a wide range Therefore, they can be used in different application scenarios by selecting alloy compounds with appropriate component ratio. Table 5.1 lists the energy band gap of some two-dimensional metal chalcogenide alloys adjusted with the composition.

Table 5.1 Variation of the band gap with the composition of two-dimensional metal chalcogenides

	Compound (x)	Bandgap[eV]	Ref.
$W_xMo_{1-x}S$	0 → 1	1.85 → 1.99	215
$MoS_{2x}Se_{2-2x}$	0.6 → 1	1.73 → 1.86	213
$WS_{2x}Se_{2-2x}$	0 → 1	1.61 → 1.97	214
$SnS_{2x}Se_{2-2x}$	0 → 1	1.37 → 2.27	218
$ReS_{2x}Se_{2-2x}$	0 → 1	1.32 → 1.62	212
$HfS_{2x}Se_{2-2x}$	0 → 1	1.94 → 2.64	217

CdS_xSe_{1-x}	0 → 1	1.8 → 2.3	219
$GaSe_xTe_{1-x}$	0 → 0.33	1.66 → 1.78	211
	0.34 → 1	1.35 → 2.01	

5.1.1 Crystal structure and characterization

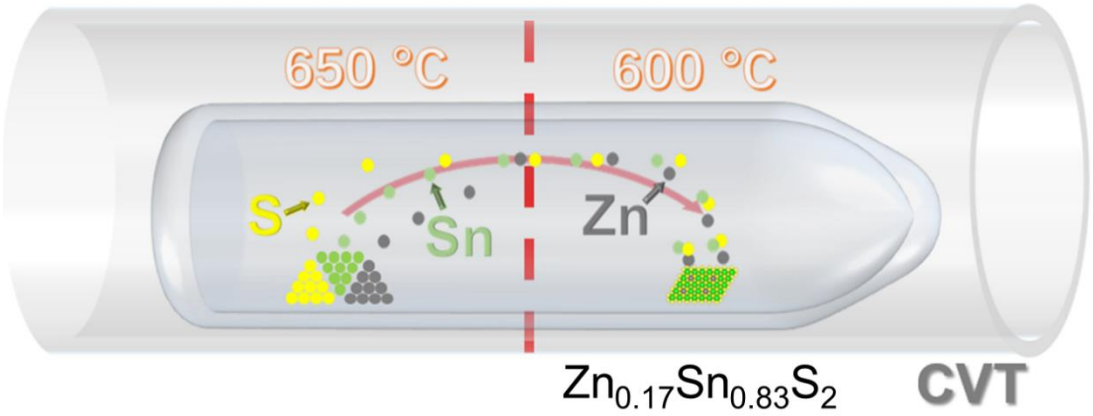

Figure 5. 1 Diagram of $Zn_{0.17}Sn_{0.83}S_2$ alloy grown by the CVT.

High quality $Zn_{0.17}Sn_{0.83}S_2$ alloy bulk crystals were grown by CVT reaction technique. The schematic diagram of synthetic process is shown in Figure 5.1. Sulfur (S), Stannum (Sn) and $ZnCl_2$ compound were utilized as reactants and mixed completely into vacuum evacuated glass ampoule under the mass ratio of 10: 30: 0.6. Then, the glass ampoule was maintained in two-zone furnace for three days with the reactants place at the high temperature-zone (T=650°C), enabling the growth of $Zn_{0.17}Sn_{0.83}S_2$ crystal at the low temperature-zone (T=600°C). After the growth stage, the furnace was cooled down at a rate of 10°C per hour, while maintaining 50°C temperature difference between the two zones. After cooling down to room temperature, $Zn_{0.17}Sn_{0.83}S_2$ alloy crystals were taken out for further analysis.

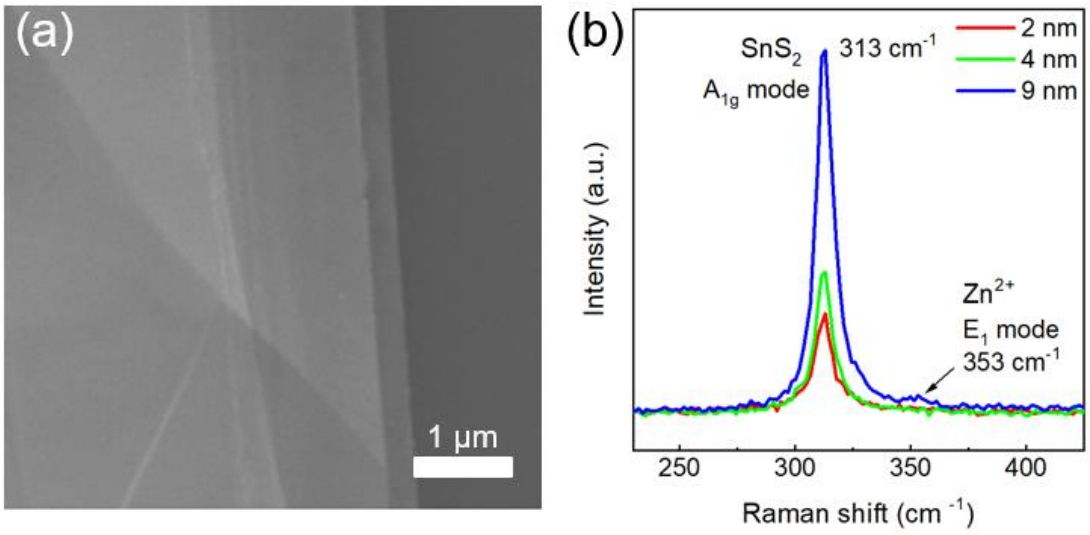

Figure 5. 2 Raman spectrum.

(a) SEM image of $Zn_{0.17}Sn_{0.83}S_2$. (b) Raman spectrum of $Zn_{0.17}Sn_{0.83}S_2$ nanosheets with different thicknesses.

The SEM image of the $Zn_{0.17}Sn_{0.83}S_2$ nanosheets (Figure 5.2 (a)) shows its layer structure and easy-to-exfoliate characteristic like other 2D materials. Raman spectroscopy is a typical method for determining the crystal structure of 2D materials by analyzing lattice vibration peaks.[31, 130-132] The Raman spectra of $Zn_{0.17}Sn_{0.83}S_2$ nanosheets with different thickness were measured and presented in Figure 5.2(b). There are two Raman peaks in the range of 200~400 cm^{-1}, 313 cm^{-1} and 353 cm^{-1}, under the 532nm excitation. The 313 cm^{-1} peak corresponds to the A_{1g} photo mode of SnS_2 nature, while the 353 cm^{-1} peak corresponds to the E_1 mode of Zn^{2+}.[133] The intensity of the characteristic peak of Si substrate decreases with increasing $Zn_{0.17}Sn_{0.83}S_2$ thickness.

In order to accurately obtain the element composition and element ratio of the alloy, we measured and analyzed the EDS spectrum and the XPS of the alloy crystal, which are presented in Figure 5.3 (a) and Figure 5.3 (b-d), respectively. From the EDS spectrum (Figure 5.3 (a)), the sums of the Sn M-shell, L-shell and K-shell, and Zn L-shell and K-shell and S K-shell signals were monitored.[134] It clearly exhibits the Sn, S and Zn elements in the range of 0 to 30 keV. The Sn 3d electron peaks (Figure 5.3 (b)) are located at 486.8 eV and 495.3 eV with low binding energy arising from Sn $3d^{5/2}$, in accordance with SnS_2 value. In Figure 5.3 (c), the binding energies 161.9 eV and

162.8 eV corresponds to S $2p^{3/2}$ and S $2p^{1/2}$ core level orbitals, respectively. The building energy of 1023.1 eV and 1046.2 eV are attributed to Zn $2p^{3/2}$ and Zn $2p^{1/2}$, which consists with the XPS peaks of Zn^{2+} (Figure 5.3 (d)). Furthermore, the XPS measurement determined that the value of x is 0.17 at the $Zn_xSn_{(1-x)}S_2$ alloys.

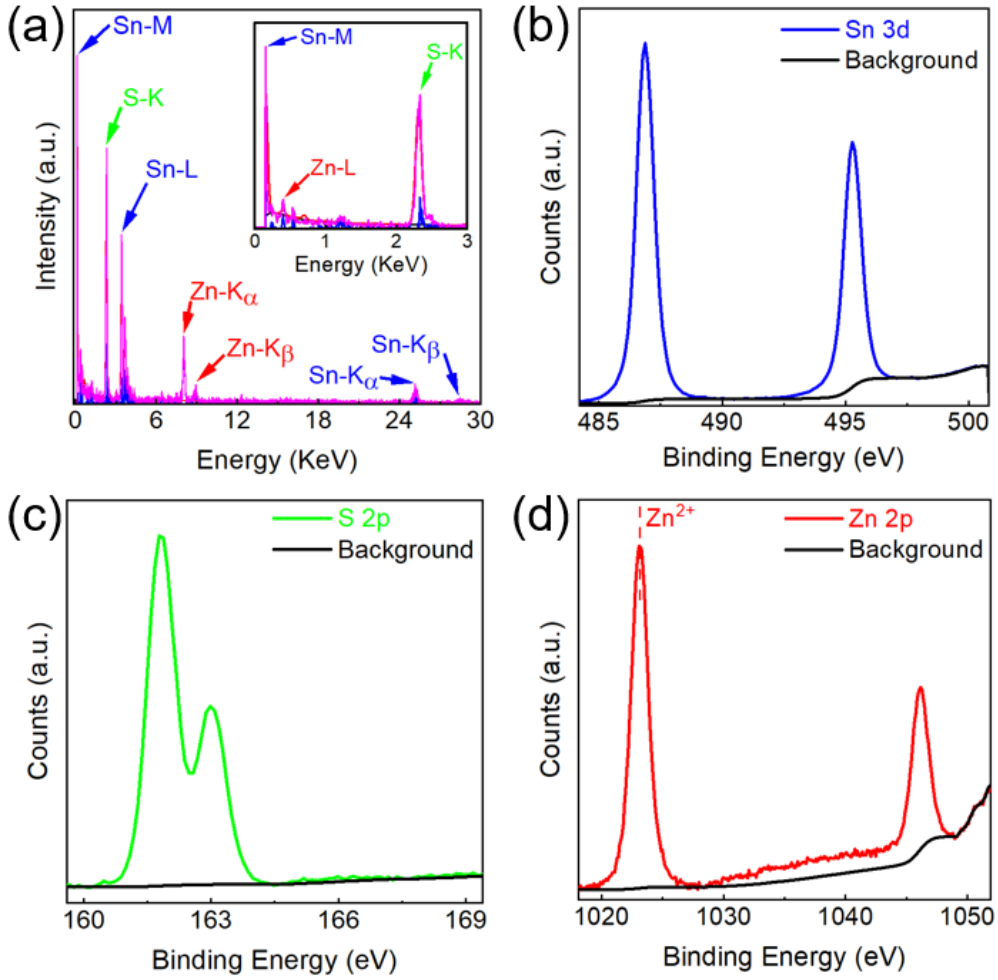

Figure 5. 3 Energy spectrum analysis.

(a) EDS of $Zn_{0.17}Sn_{0.83}S_2$ (inset: zoom-in EDS for 0-3 KeV region). (b) Fine XPS spectrum of Sn 3d electrons. (c) Fine XPS spectrum of S 2p electrons. (d) Fine XPS spectrum of Zn 2p electrons (dotted line is at the XPS position of Zn^{2+}).

$Zn_{0.17}Sn_{0.83}S_2$ is a typical two-dimensional (2D) semiconductor alloy material. Figure 5.4 (a, b) shows the crystal structures of $Zn_{0.17}Sn_{0.83}S_2$ from top view and side view, where the silver, blue and pink balls correspond to S, Sn and Zn atoms respectively, as shown in the right side of Figure 5.4 (b). The side view shows the layer-by-layer structure. In the top view, it is easy to observe that the Zn atoms take up the

positions of Sn atoms. The crystal structure of the $Zn_{0.17}Sn_{0.83}S_2$ alloys, based on SnS_2 structure, belongs to triclinic crystal system with P $\bar{3}$m1 space group.

To characterize the microstructure and crystallinity of $Zn_{0.17}Sn_{0.83}S_2$ alloy crystals, TEM and STEM were utilized. HRTEM image (Figure 5.4 (c)) reveals that the $Zn_{0.17}Sn_{0.83}S_2$ alloy crystal has lattice spacing of 0.184 nm and 0.32 nm, assigning to the (1 1 0) and (1 0 0) planes respectively. The SAED pattern (Figure 5.4 (d)) exhibits hexagonally arranged spot pattern, which is assigned to the triclinic crystal system along the [0 0 -1] zone plane of $Zn_{0.17}Sn_{0.83}S_2$ alloy crystal, proving the high crystallization quality.

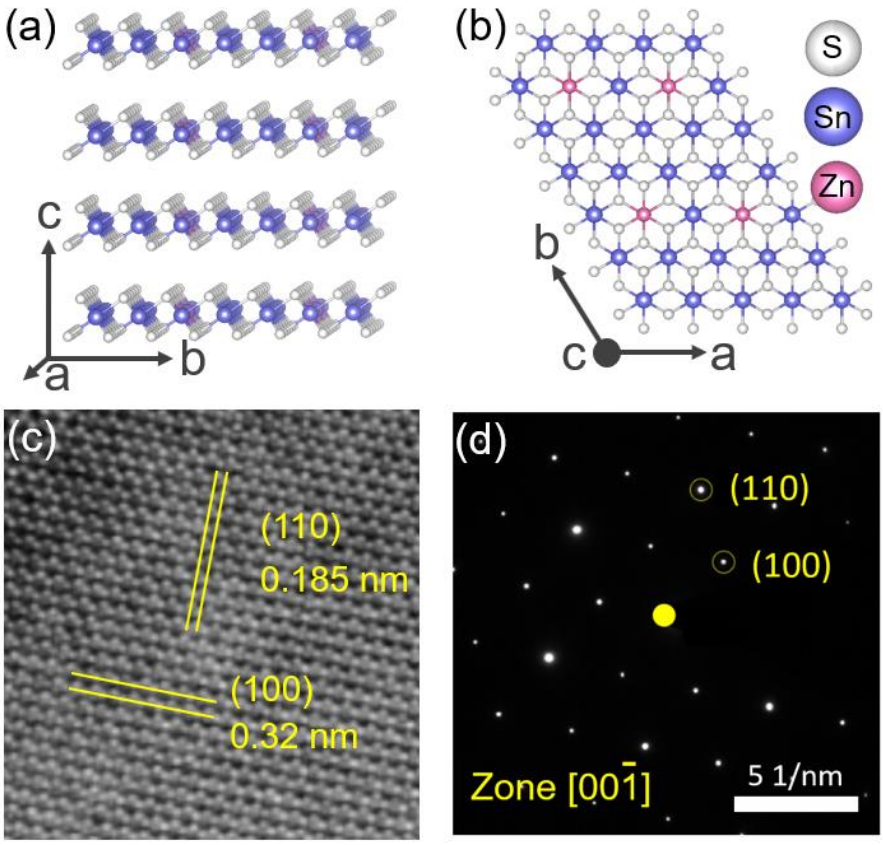

Figure 5. 4 Crystal structure.

(a) Schematic diagram of crystal structure for slightly oblique c-b plane. (b) Schematic diagram of crystal structure for a-b plane. (c) HRTEM image. (d) SAED pattern along [00-1] crystal axis.

The HAADF-STEM image is shown in Figure 5.4 (e). The large size HAADF image demonstrates non-clusters in the alloy crystal. Further, the EDS mapping of S,

Sn, Zn element are displayed in Figure 5.5 (b-d). The EDS mapping image of Zn element (Figure 5.5 (d)) indicates that the Zn elements are homogeneously distributed throughout the alloy crystal.

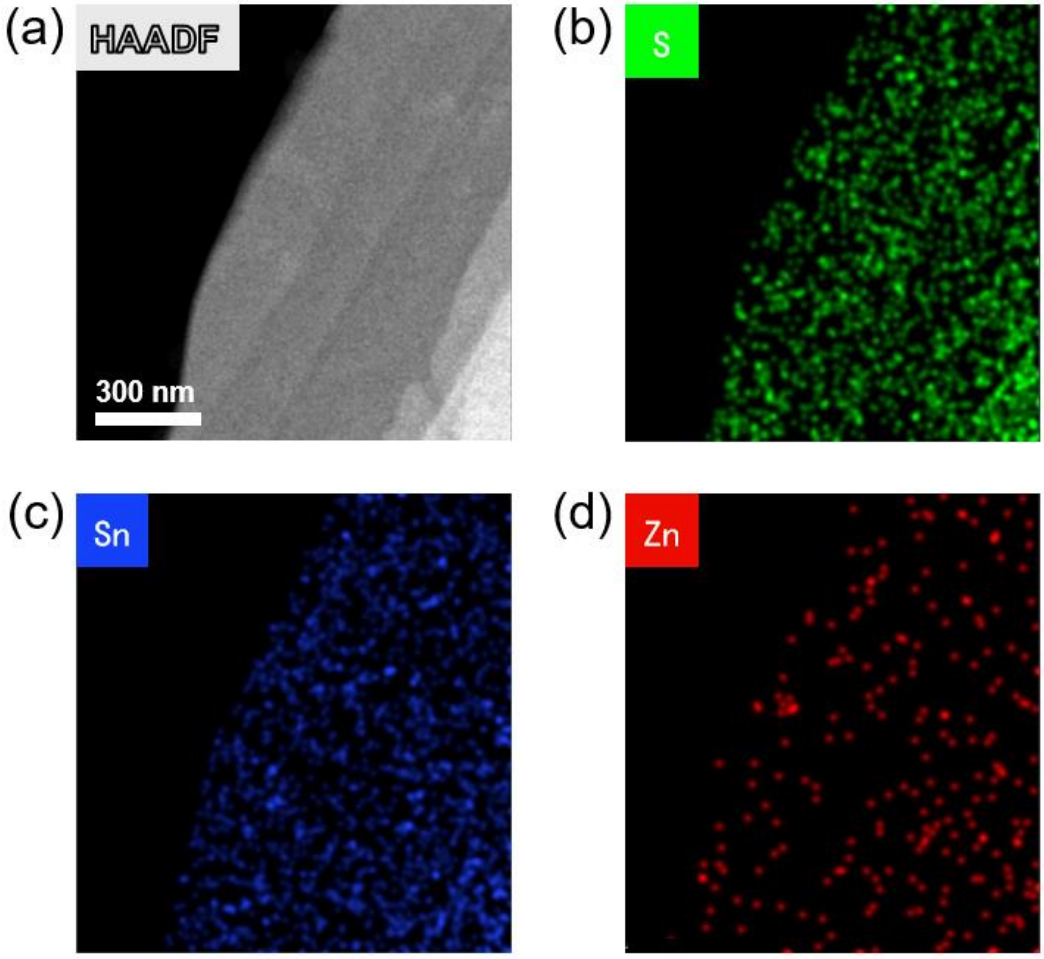

Figure 5. 5 Distributions of different elements.

(a) HAADF STEM image of $Zn_{0.17}Sn_{0.83}S_2$ nanosheet. (b) Distribution of S. (c) Distribution of Sn. (d) Distribution of Zn.

5.1.2 Optical properties

The electrical properties of the $Zn_{0.17}Sn_{0.83}S_2$ alloy material were probed by fabricating and measuring the few-layer $Zn_{0.17}Sn_{0.83}S_2$ based field-effect transistors (FETs) device. To prepare the $Zn_{0.17}Sn_{0.83}S_2$ FETs, the few-layer material was first mechanically exfoliated on the SiO_2/Si substrate (heavily n-doped, 300 nm SiO_2) by the adhesive tape. Then, one gold stripe mask was transferred onto the $Zn_{0.17}Sn_{0.83}S_2$

few layers before deposition gold electrodes. After lifting off the gold stripe mask, the channel was obtained. Next, the electrodes of source and drain were separated by the probe station. This kind of method of fabricating devices has been widely used in the research of two-dimensional materials and organic materials.

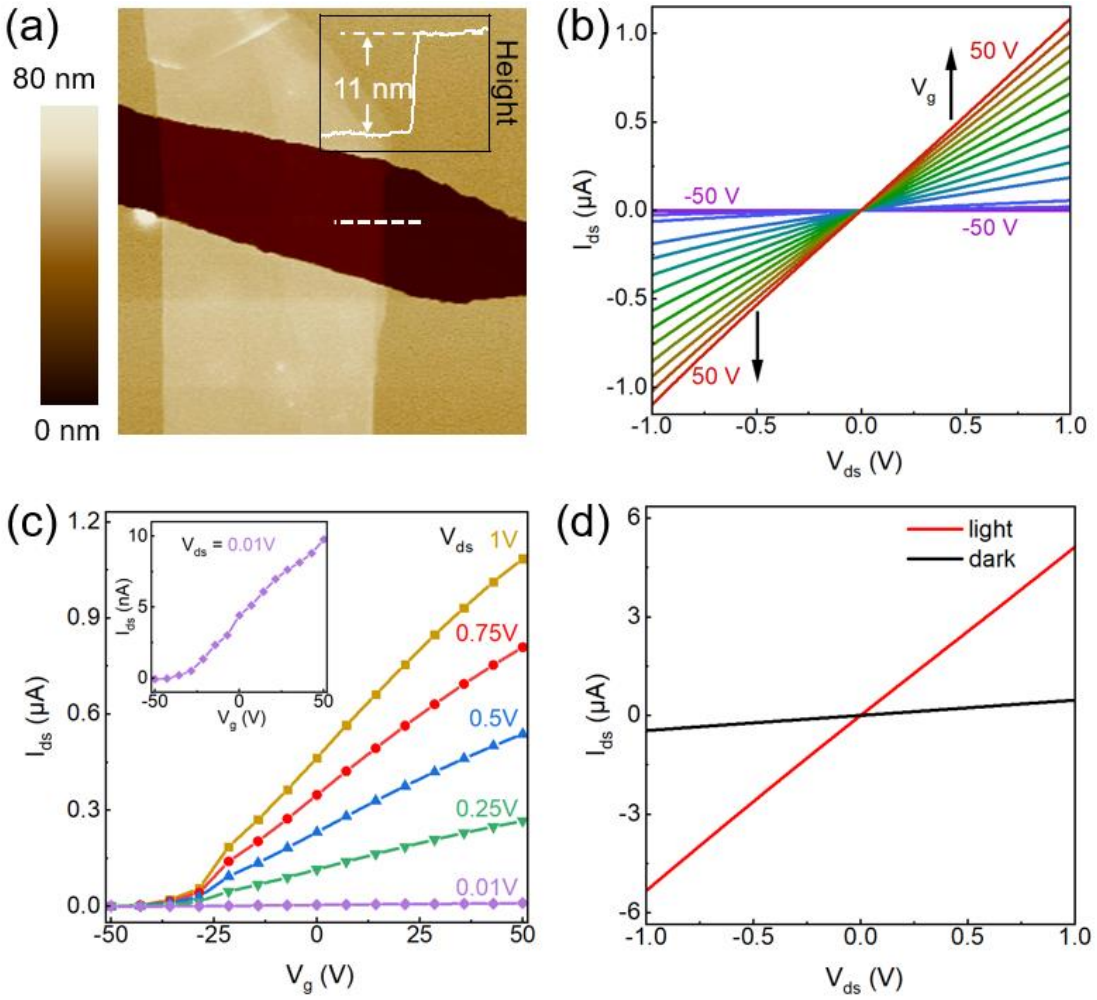

Figure 5. 6 Electronic and photoelectronic measurement.

(a) AFM image (inset: height curve in the position marked by white dotted line). (b) Output curves. (c) Transfer curves under different bias voltages (inset: zoom-in transfer curve for V_{ds} = 1 V). (d) IV curves under dark atmosphere and white LED illumination.

AFM image of $Zn_{0.17}Sn_{0.83}S_2$ FET, as shown in Figure 5.6 (a), proves that the thickness of $Zn_{0.17}Sn_{0.83}S_2$ nanoflake is 11nm, the length and width of the FET channel is 2.6 μm and 5 μm. The I_{ds}-V_{ds} curves was measured and shown in Figure 5.6 (d). At V_{ds} of 1V, the dark current is 0.1 μA. Upon illumination of LED white light, we obtained 5.1 μA. Therefore, the on/off ratio is as high as 51. The LED white light was chosen as

the irradiation source for its closer to daily life and application. The transfer curve is shown in Figure 5.6 (d) sweeping the V_g value from -50 V to 50 V with the V_{ds} value of 0.01V. In the image of transfer curve, the left y-axis is linear coordinate system, and the right is Log10 system. The $Zn_{0.17}Sn_{0.83}S_2$ based FET shows typical n-type behavior and belongs to depletion transistor. The field-effect mobility (μ_m) could be calculated by the formula of

$$\mu_m = \frac{\partial I_{ds}}{\partial V_g} \cdot \frac{L}{W C_g V_{ds}}$$

where I_{ds} is the current between source and drain, V_{ds} is the voltage from drain side to source side, V_g is the gate voltage added on the high doping silicon substrate, L is the length of channel, W is the width of channel, and C_g ($C(SiO_2)$ = 11.6 nF cm^{-2}) is gate capacitance parameter of 300 nm SiO_2 layer. By analyzing the data in figure 5.6 (c), the electron mobility of $Zn_{0.17}Sn_{0.83}S_2$ FET is calculated to be 65 $cm^2 V^{-1} s^{-1}$, which is higher than SnS_2 and ZnS_2 crystal as shown in Table 5.2. The output curves of $Zn_{0.17}Sn_{0.83}S_2$ FET, shown in Figure 5.6 (b), exhibit the linear relationship, resulting from the Ohmic contact between gold electrodes and $Zn_{0.17}Sn_{0.83}S_2$ nanoflakes.

Comparing with Table 4.2, the $Zn_{0.17}Sn_{0.83}S_2$ device has an ultra-high photocurrent response, which is one order of magnitude higher than that of pure SnS_2 (10 nm) with a similar thickness. The result is also higher than Fe doped SnS_2.samples. The improvement of the photocurrent response of the $Zn_{0.17}Sn_{0.83}S_2$ device comes from the influence of Zn doping on the SnS_2 band structure, which greatly improves its photoelectric performance. This will be verified in the following theoretical calculations and analysis.

Table 5.2 Carrier mobilities, photoresponsivity and light ON/OFF ratios of SnS2, Fe doped SnS2 and ZnS in the prior literatures and $Zn_{0.17}Sn_{0.83}S_2$ nanosheet in this thesis

	electron mobility [$cm^2 \cdot V^{-1} \cdot s^{-1}$]	R [$A \cdot W^{-1}$]	on/off ratio	Ref.
SnS_2 (bulk)		8.8 m		85
SnS_2 (10nm)	5	100		167
SnS_2 (1L)	3.43	83 m		32

SnS_2	2.34			218
ZnS	10-17	1.6 m	9.7	248-249
$Fe_{0.021}Sn_{0.979}S_2$	8.15	206 m	10	32
$Zn_{0.17}Sn_{0.83}S_2$ (11 nm)	65	1026.4	11	here

5.1.3 Calculations

The first principles calculation based on Density Functional Theory (DFT) were used to calculate the electric band structure and density of states.[135, 136] The generalized gradient approximation (GGA) of Perdew, Burke, and Ernzerhof (PBE) were bring to electron exchange and correlation.[137-139] Figure 5.7 (a) is the electric structure and DOS of monolayer showing the indirect band gap with 1.507 eV, as the previous reports. To adjust the band structure, the Zn atom doping into 2×3 super cell of SnS_2 at Sn position with the Zn: Sn ratio of 1: 5, which is consistent with the experimental conditions. The electric structure and DOS of monolayer and bulk $Zn_{0.17}Sn_{0.83}S_2$ alloy are shown in Figure 5.7 (b) and 5.7 (c) respectively. It is easily to observe that the direct band gap in monolayer and bulk alloy crystal with the bandgap of 1.458 eV and 1.507 eV. This is due to the presence of Zn atoms in the alloy belonging to Zn^{2+} state which introduces many defective states and adjust the top of valence band to Γ point. Comparing with the DOS images of monolayer SnS_2, monolayer $Zn_{0.17}Sn_{0.83}S_2$ and bulk $Zn_{0.17}Sn_{0.83}S_2$, the density of states of Zn atom contributes more in the valence band.

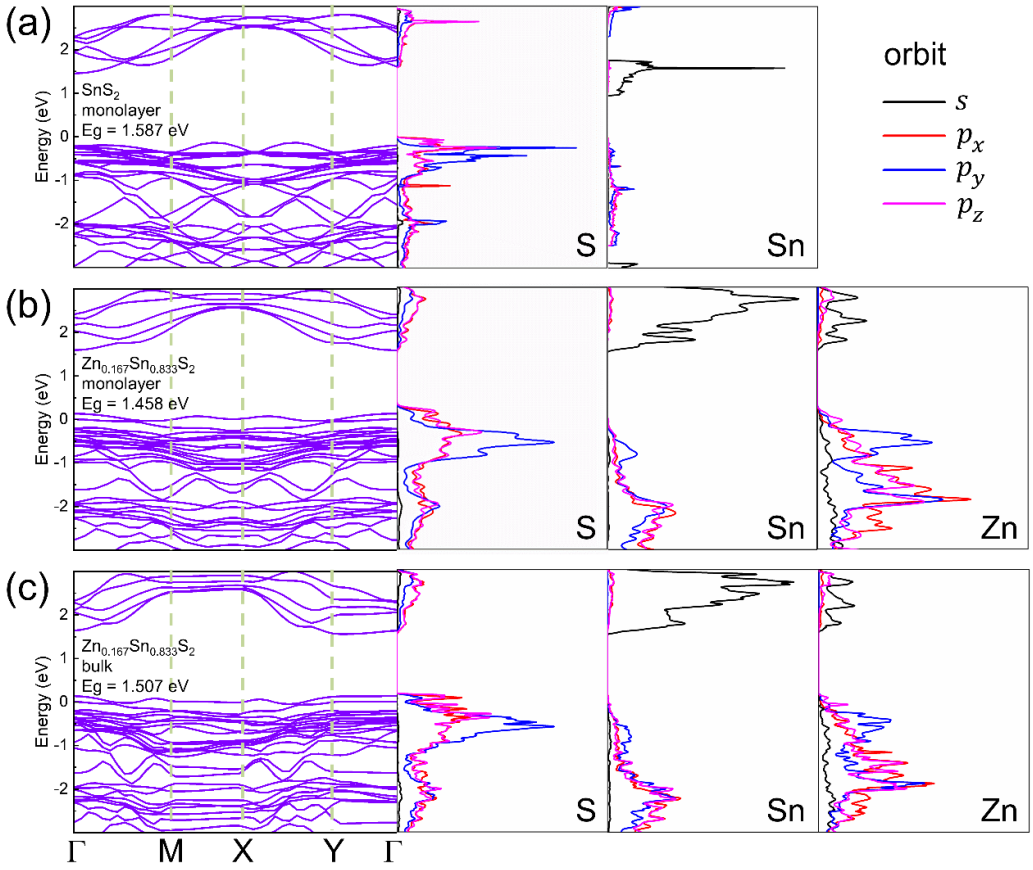

Figure 5. 7 Theoretical calculation results.

(a) Electronic band structure and distributions of DOS for different atoms in monolayered SnS2. (b) Electronic band structure and distributions of DOS for different atoms in monolayered $Zn_{0.17}Sn_{0.83}S_2$. (c) Electronic band structure and distributions of DOS for different atoms in bulk $Zn_{0.17}Sn_{0.83}S_2$.

5.2 SnS based Photodetection

5.2.1 Crystal structure and characterization

SnS is an orthorhombic system, which has low crystal structure symmetry. Figure 5.8 (a) is a photograph of a large piece of SnS crystal. Figure 5.8 (b) is crystal structure of SnS. The orange atoms are sulfur atoms, and the purple atoms are tin atoms. SnS is stacked along the c-axis. The a-axis and b-axis are the zigzag direction and the armchair direction of the crystal lattice, respectively. The part is a top view along the c-axis, and the lower half is a side view slightly inclined along the a-axis. SnS has a corrugated

crystal structure, like black phosphorus, with sulfur atoms and tin atoms alternately arranged along the direction of the crystal handrails. The number of SnS JCPDS is PDF#01-0984, which belongs to the space group Pmcn (62), and the unit cell parameters are: a = 3.99 Å, b = 4.34 Å, and c = 11.2 Å. Figure 5.8 (c) is the data of the different interplanar spacing of its PDF.

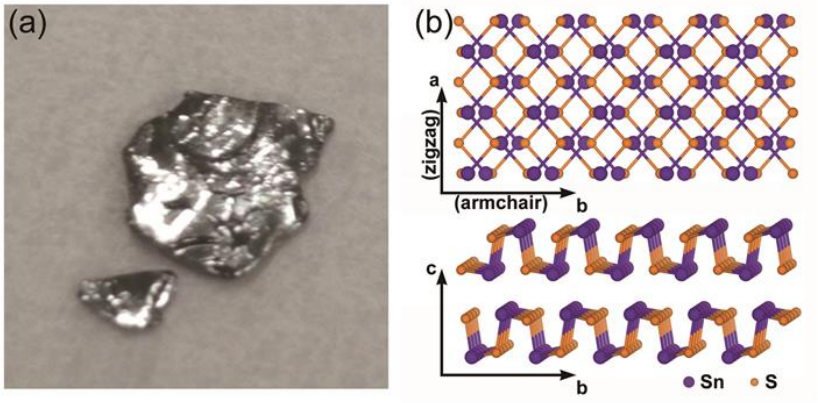

(c)

d(A)	I(f)	I(v)	h	k	l	n^2	2-Theta	Theta	1/(2d)	2pi/d
4.0400	16.0	11.0	0	1	1		21.983	10.991	0.1238	1.5552
3.4200	40.0	33.0	0	1	2		26.033	13.016	0.1462	1.8372
3.2400	40.0	35.0	1	0	2		27.506	13.753	0.1543	1.9393
2.9300	32.0	31.0	1	1	0		30.484	15.242	0.1706	2.1444
2.8300	100.0	100.0	0	1	3		31.589	15.794	0.1767	2.2202
2.3000	32.0	39.0	1	0	4		39.133	19.567	0.2174	2.7318
2.1200	11.0	15.0	0	2	1		42.611	21.305	0.2358	2.9638
2.0200	24.0	34.0	0	2	2		44.832	22.416	0.2475	3.1105
1.9900	24.0	34.0	0	1	5		45.545	22.773	0.2513	3.1574
1.8700	32.0	48.0	0	0	6		48.650	24.325	0.2674	3.3600
1.7800	16.0	25.0	1	1	5		51.283	25.642	0.2809	3.5299
1.7200	16.0	26.0	2	1	2		53.210	26.605	0.2907	3.6530
1.6900	16.0	27.0	1	0	6		54.231	27.116	0.2959	3.7179
1.6200	20.0	35.0	2	0	4		56.781	28.391	0.3086	3.8785
1.5600	3.0	5.0	0	2	5		59.177	29.589	0.3205	4.0277
1.4500	20.0	39.0	1	2	5		64.177	32.088	0.3448	4.3332
1.4000	13.0	26.0	0	0	8		66.761	33.381	0.3571	4.4880
1.3600	13.0	27.0	1	3	0		68.997	34.498	0.3676	4.6200
1.2900	10.0	22.0	0	2	7		73.327	36.664	0.3876	4.8707
1.2600	10.0	22.0	3	1	1		75.372	37.686	0.3968	4.9867
1.2200	10.0	23.0	1	3	4		78.304	39.152	0.4098	5.1502
1.2000	3.0	7.0	2	1	7		79.867	39.934	0.4167	5.2360

Figure 5. 8 Photograph of crystals and schematic of the crystal structure.

(a) Photograph of SnS crystals. (b) Crystal structure of SnS. (c) PDF interplanar spacing datasheet of SnS.

Figure 5.9 shows the picture of transmission electron microscopy measurement of SnS nanosheets. Figure 5.9 (a) is a low-resolution TEM image of SnS transferred on a carbon film. The electron diffraction pattern of SnS (Figure 5.9 (b)) clearly and regularly distributes diffraction spots of parallelogram structure, which matches the crystal structure of orthorhombic SnS along the [001] crystal direction. Figure 5.9 (c) is the HRTEM image. The distance between the (110) and (-110) crystal planes is 2.93 Å and 2.91 Å, respectively. The angle between (110) and (-110) crystal planes is 85°.

In Figure 5.9 (d), the armchair direction and the zigzag direction are marked on the enlarged HRTEM image, and the pseudo-HRTEM of the single-layer SnS is marked with purple tin atoms and orange sulfur atoms. The TEM image proves that the SnS flakes have high crystalline quality.

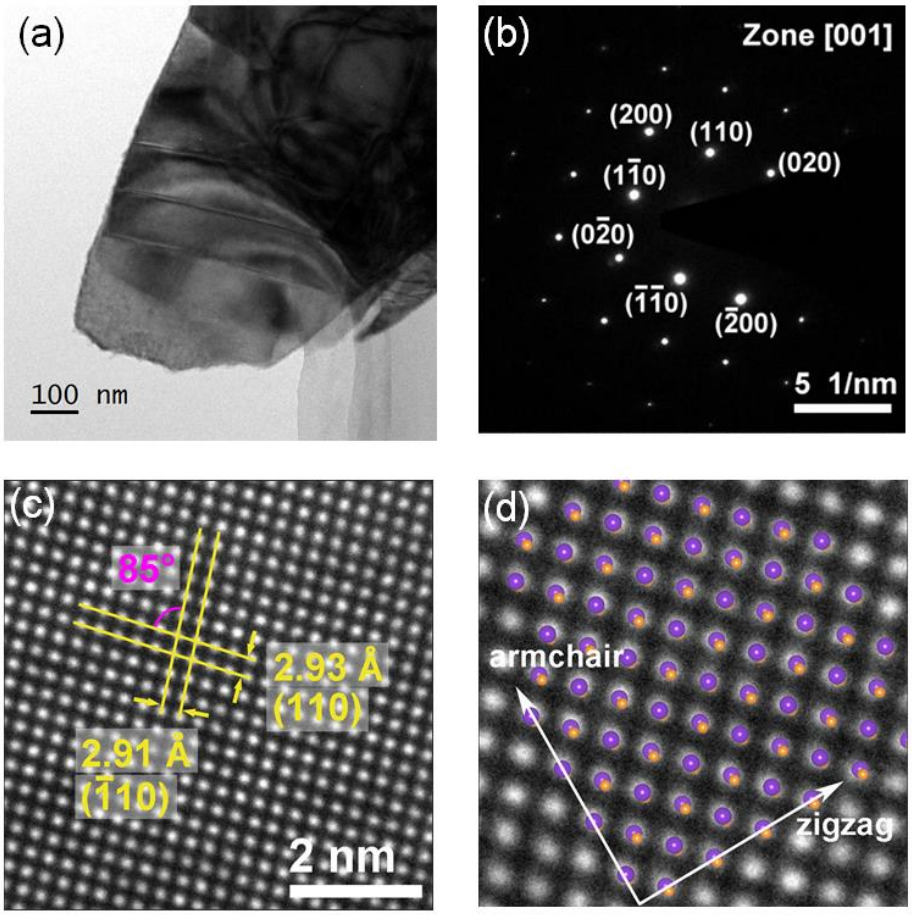

Figure 5. 9 Pictures of TEM.

(a) TEM image. (b) SAED pattern for the [001] zone axis. (c) HRTEM image of the SnS nanosheet. (d) Zoom-in HRTEM image with corresponding purple tin and orange sulphur atomic distribution in a monolayer.

Figure 5.10 shows Raman spectrum of the SnS nanosheet. The Raman peaks locate at 95.8 cm^{-1}, 163.1 cm^{-1}, 190.9 cm^{-1} and 218.6 cm^{-1}. Among them, the Raman peak at 163.1 cm^{-1} corresponds to the B_{3g} phonon vibration mode, while the other three peaks are A_g mode phonons. The positions of these Raman peaks are basically consistent with the SnS Raman spectra reported in the literature [140]. Figure 5.11 shows the angle-resolved polarization Raman spectrum. The upper figure is the contour map of the

Raman scattering intensity. In the angle-resolved Raman polarization spectrum, it can be clearly seen that the peak intensities of A_g and B_{3g} vary periodically with the light polarization angle. In the parallel polarization configuration, the A_g (190.9 cm^{-1}) Raman peak has a maximum at 90°, and the peak at 0° and 180° is the minimum. The Raman peak of B_{3g} mode has a maximum value at 45° and 135° with the four-leaf type. In the angle-resolved Raman spectra with parallel configuration, the other two A_g peaks can be vaguely seen at the positions of 95.8 cm^{-1} and 218.6 cm^{-1}, which vary with the polarization angle of the incident light. For the vertical configuration, the A_g Raman peaks at 95.8 cm^{-1} and 218.6 cm^{-1} are basically not observed for the weak intensity of the A_g Raman peak. In the angle-resolved Raman spectrum of SnS, the two peaks of A_g (190.9 cm^{-1}) and B_{3g} (163.1 cm^{-1}) are sensitive to angle. The following discussion mainly focuses on the phonon vibrations corresponding to these two Raman peak modes.

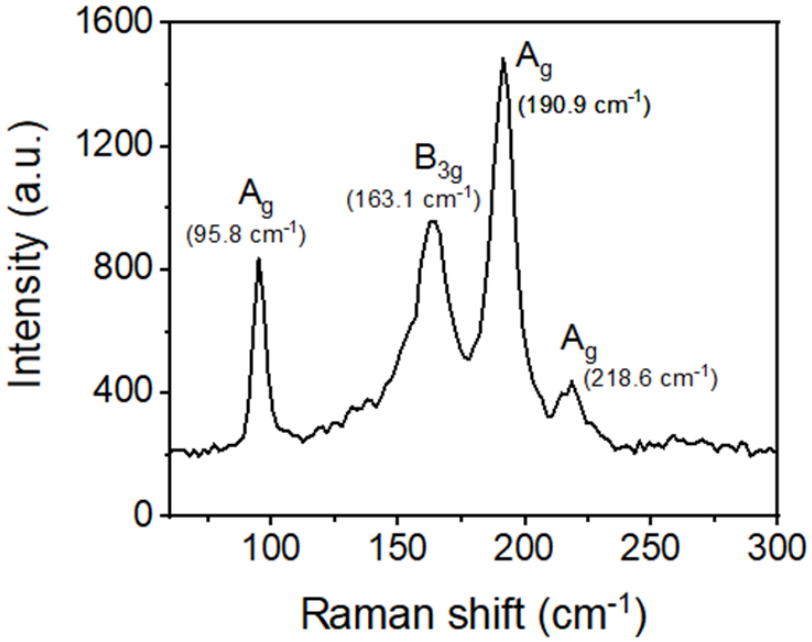

Figure 5. 10 Raman spectrum of SnS nanosheet.

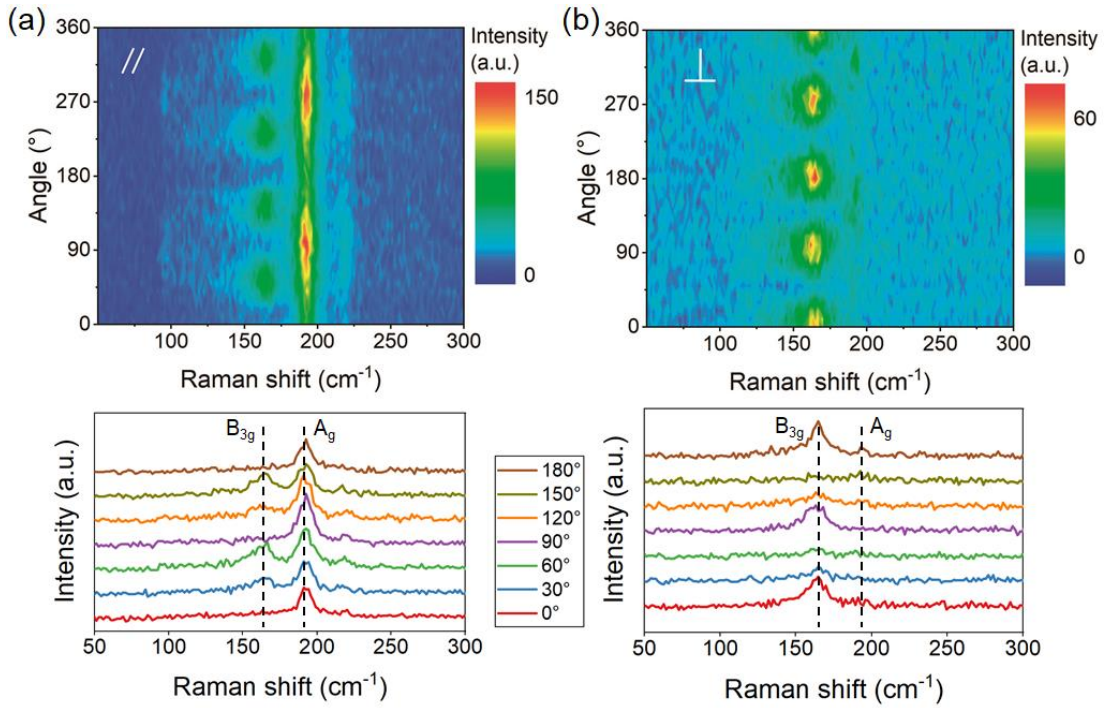

Figure 5. 11 Angular-resolved polarization Raman spectrum of SnS.

(a) Parallel-polarization configuration of ARPR. (b) Cross-polarization configuration of ARPR.

According to the Placzek model, the intensity of Raman scattered light (I) can be expressed as $I \propto | e_i \cdot \mathrm{R} \cdot e_s |^2$, where R is the second-order Raman tensor corresponding to the Raman vibration mode, and e_i and e_s are the incident light and the electric polarization unit vector of the scattered light, respectively. For SnS, the Raman tensor of the vibration modes of A_g (190.9 cm^{-1}) and B_{3g} (163.1 cm^{-1}) can be expressed as

$$\mathrm{R}(\mathrm{A}_g) = \begin{bmatrix} |a|e^{i\phi_a} & 0 & 0 \\ 0 & |b|e^{i\phi_b} & 0 \\ 0 & 0 & |c|e^{i\phi_c} \end{bmatrix}, \quad \mathrm{R}(\mathrm{B}_{3g}) = \begin{bmatrix} 0 & 0 & 0 \\ 0 & 0 & |f|e^{i\phi_f} \\ 0 & |f|e^{i\phi_f} & 0 \end{bmatrix}.$$

Taking the zigzag direction as the Y direction and the armchair direction as the Z direction, the incident light is irradiated on the YZ plane, and the angle between the polarization direction of the incident light and the Y axis is θ. The unit vector of the polarization direction of the incident light $e_i = (0, \cos\theta, \sin\theta)$, the scattered light e_S is $(0, \cos\theta, \sin\theta)^T$ in the parallel configuration, and $(0, -\sin\theta, \cos\theta)^T$ in the cross configuration.

Table 5.3 Raman scattering intensity expressions of SnS

$A_g^{//}$	$A_g^{\perp}$	$B_{3g}^{//}$	$B_{3g}^{\perp}$
$\|b\|^2\cos^4\theta+\|c\|^2\sin^4\theta+2\|b\|\|c\|\cos\varphi_{bc}\sin^2\theta\cos^2\theta$	$\frac{(\|b\|^2+\|c\|^2-2\|b\|\|c\|\cos\varphi_{bc})\sin^2 2\theta}{4}$	$\|f\|^2\sin^2 2\theta$	$\|f\|^2\cos^2 2\theta$

* $\varphi_{bc}=\phi_b-\phi_c$

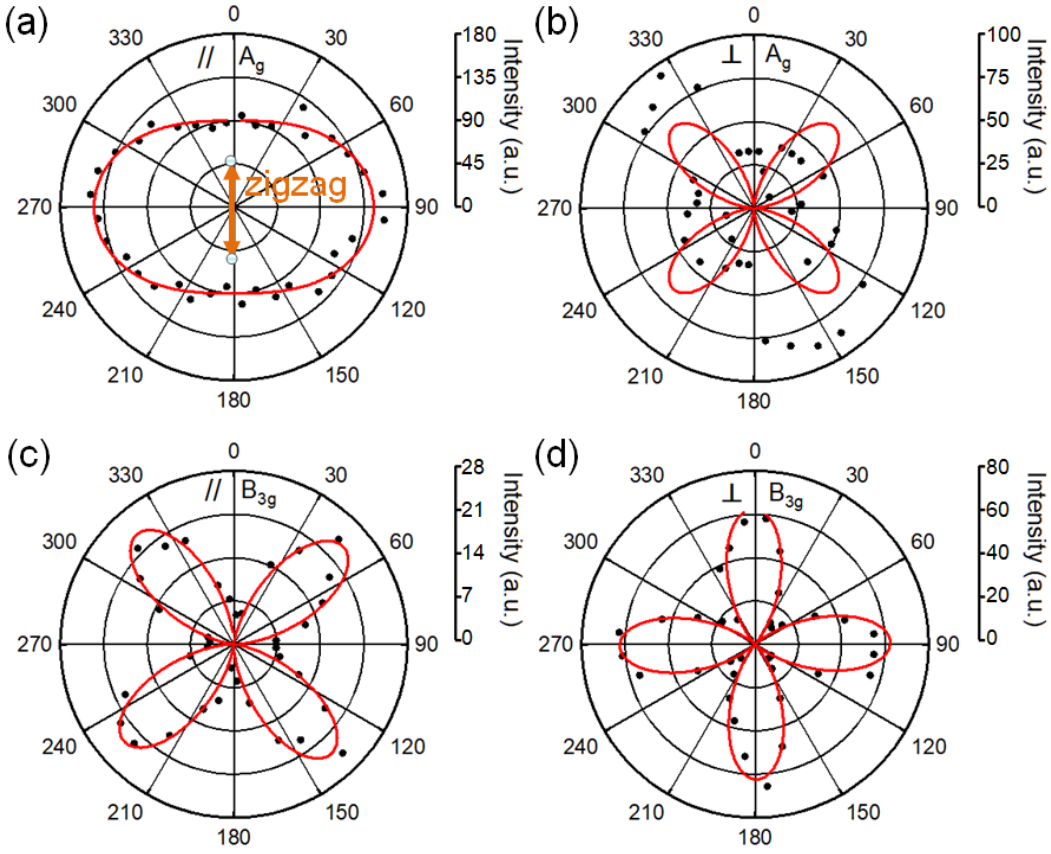

Figure 5. 12 Polar plots of A_g (190.9 cm-1) and B3g (163.1 cm-1) peaks intensities with the polarization direction of incident light (black point: experimental data, red line: the fitting data).

According to the Raman scattering intensity formula of A_g and B_{3g} modes in Table 5.3, the intensity value changes periodically with the polarization angle of the incident light, which is consistent with the phenomenon observed in the experiment. Figure 5.12 shows Polar plots of A_g (190.9 cm^{-1}) and B_{3g} (163.1 cm^{-1}) peak intensities with the polarization direction of incident light. Among them, the fitted curve (red curve) perfectly fits the data points (black dots). In the fitted curve, the intensity of Raman

scattering parallel to the armchair direction is $|b|^2$, and the intensity parallel to the ZigZag direction is $|c|^2$. Therefore, the crystal orientation information can be inferred from the A_g peak of SnS in parallel mode. For example, 0° is parallel to the armchair direction of the SnS lattice. This method is very important in the study of anisotropic properties of materials.

5.2.2 Optical properties

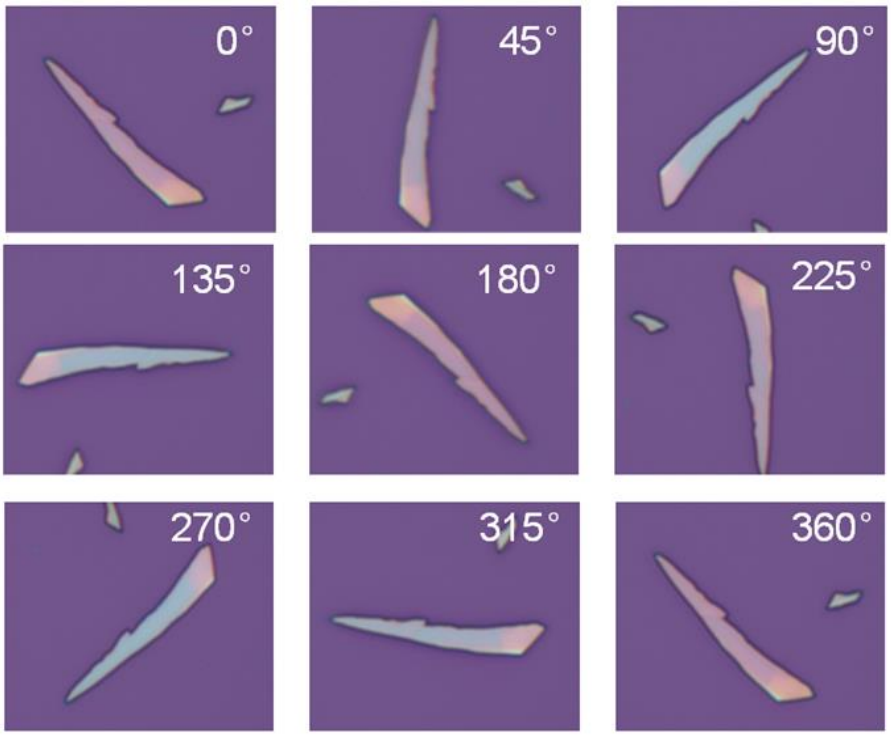

Figure 5. 13 Polarization optical microscope photographs.

Figure 5.13 are a polarized optical microscope image of SnS crystal. By rotating the sample to change the polarization direction of the incident light relative to the SnS crystal, it can be clearly seen that the same crystal exhibits different colors under different angles of polarized light. At 90°, 135°, 270°, 315°, the sample is greenish, while the sample at other angles appears red. During the rotation of the sample, the color transits between the two colors. This color transition shows that SnS has different absorption or reflection characteristics for light with different polarization directions.

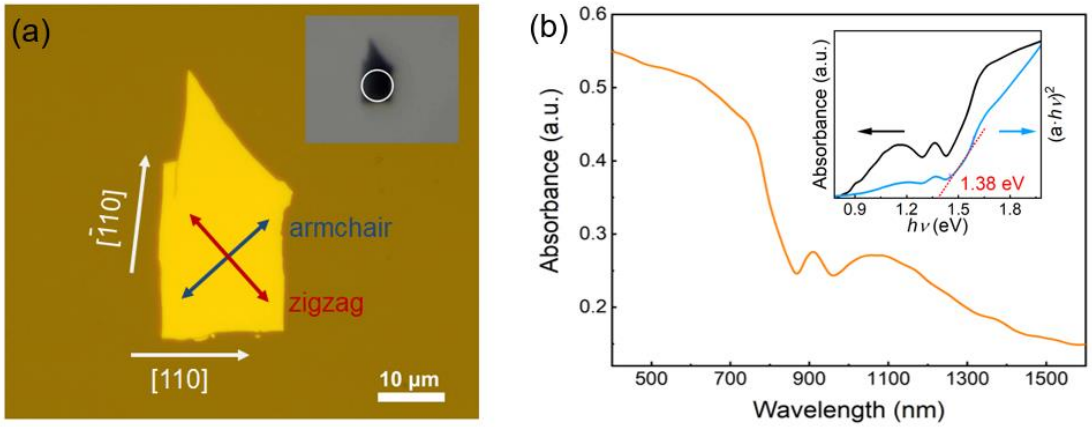

Figure 5. 14 Optical absorption spectrum.

(a) Optical microscope photograph of the sample used for optical absorption spectrum testing. (b) Optical absorption spectrum of SnS nanosheet (inset: curves at the absorption edge of hν-absorbance and hν-$(a \cdot hν)^2$, red line is the fitting line of the absorption edge).

The optical absorption spectrum can effectively reflect the optical characteristics of SnS. Due to the small size of the SnS nanosheets, a micro-area optical absorption spectrum system with a spot diameter of 20 μm is used to characterize the SnS nanosheets on the quartz glass sheet. Figure 5.14 (a) is an optic image of the sample used for the micro-area light absorption spectrum measurement. According to the angle-resolved Raman spectrum data, the zigzag (crystal a-axis) and armchair (crystal b-axis) crystal orientations are marked. The small picture in the illustration is an optical microscope photo of the absorption spectrum of the micrometer area. The test area is marked by the white circlet. Figure 5.14 (b) shows the light absorption spectrum of SnS nanosheets in the range of 400-1600 nm. One can clearly see the steep absorption edge at 750 nm to 850 nm, which corresponds to the optical band gap of SnS nanosheets reported in the literature[141]. This absorption edge corresponds to the light absorption of the 1.3 eV direct band gap. For the direct band gap semiconductors, the relationship between the light absorption coefficient and the photon energy at the absorption edge is as follows:

$$(a \cdot hv)^2 = \mathrm{A}(hv - \mathrm{E_g}).$$

where a is the light absorption coefficient measured by the absorption spectrum, h_v is the energy of the corresponding wavelength photon, Eg is the band gap, and A is a

constant. The band gap can be calculated based on the light absorption spectrum. The inset in Figure 5.14 (b) is the light absorption coefficient and $(a \cdot h_v)^2$ corresponding to the change curve of different photon energies. By fitting the above formula at the absorption edge, the optical band gap is about 1.38 eV, which matches with the literature. In more detail, there are two small absorption peaks adjacent to the SnS absorption edge, which may be caused by the exciton absorption of the hole-electron pair.

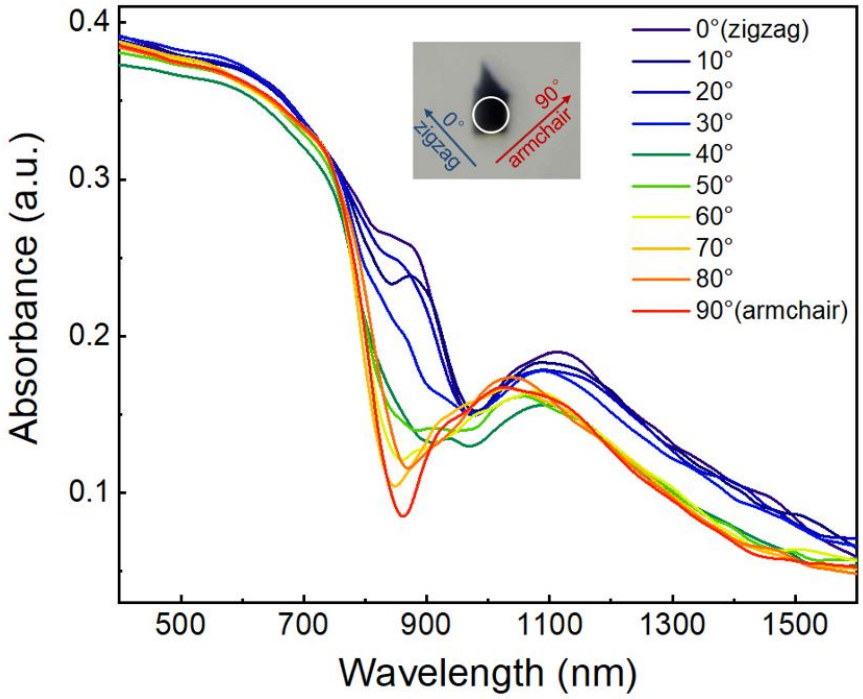

Figure 5. 15 Angle-resolution polarization optical absorption spectra.

Anisotropic SnS material has different physical properties in different lattice directions. Figure 5.15 is an angle-resolved polarization absorption spectrum. The polarization angle between polarized light and the crystal varies from 0° to 90°. The polarization direction of light is parallel to the zigzag direction of the crystal structure at 0°, and parallel to the direction of the armchair at 90°. In the 750 nm to 1600 nm band, the light absorption coefficient is great in the zigzag direction. 750 nm is just near the absorption edge, and the photon energy corresponding to 1.29 eV at 960 nm is close to the direct band gap of SnS nanosheets reported in the literature.

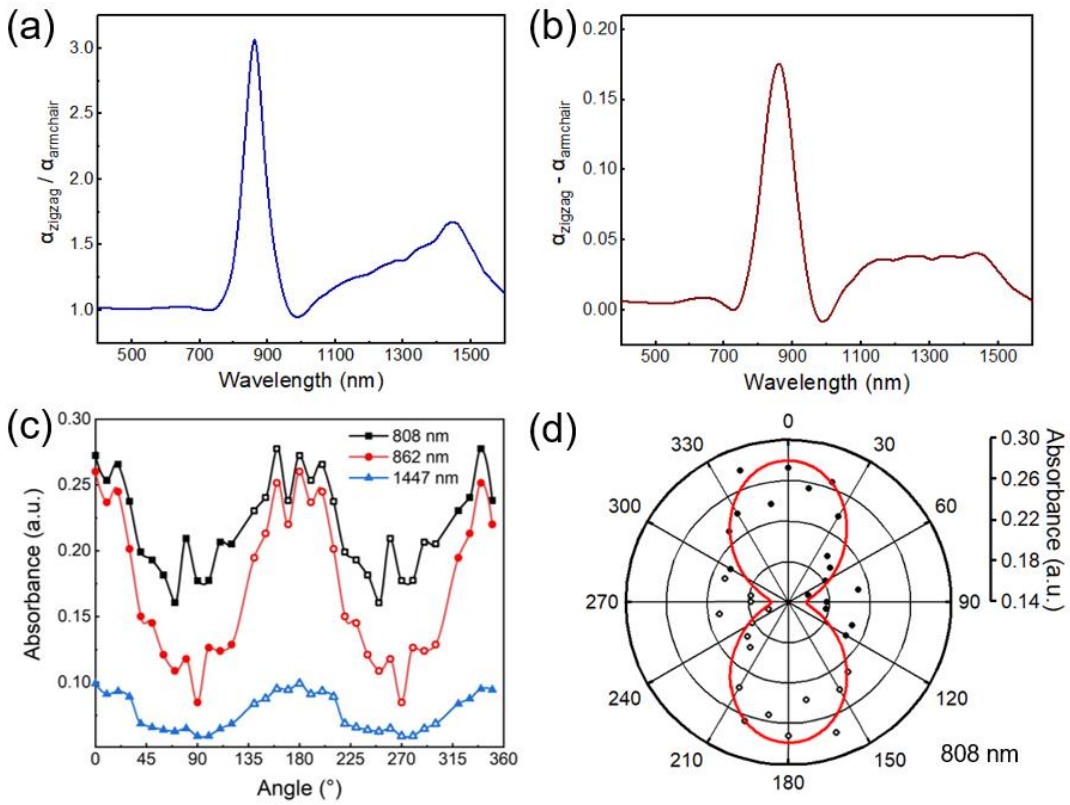

Figure 5. 16 Variations of optical absorption spectra with the polarization angle of incident light.

(a) Linear dichroism ratio. (b) Linear dichroism amplitude. (c) Variations of optical absorption intensities for different wavelengths (filled dots: experimental data, hollow dots: experimental data of symmetrical angles). (d) Variations of optical absorption intensities for 808 nm with polarization angle (filled dots: experimental data, hollow dots: experimental data of symmetrical angles, red line: fitted curve).

In order to clearly show the difference in anisotropic absorption of SnS nanosheets, Figure 5.16 (a) exhibit the ratios between the zigzag direction and the armchair direction ($\alpha_{zigzag}/\alpha_{armchair}$). Two peaks at 862 nm and 1447 nm can be found with the corresponding dichroic ratios of 3.06 and 1.67, respectively. In Figure 5.16 (b), the amplitude of the dichroism is shown with a similar peak at 862 nm while the peak in the 1030-1060 nm band is gentle. Figure 5.16 (c) is the curve of the polarization absorption coefficient at 808 nm, 862 nm and 1447 nm as a function of the polarization angle. The three curves have a similar change trend, showing a 180° change period. Figure 5.16 (d) is the polar coordinate form of the angle-resolved polarization

absorption coefficient at 808 nm. The black dots in the figure are the experimental data and the red curve is the fitting curve. The fitted curve follows the formula:

$$\alpha(\theta) = \alpha_{max} \cos^2(\theta + \varphi) + \alpha_{min} \sin^2(\theta + \varphi).$$

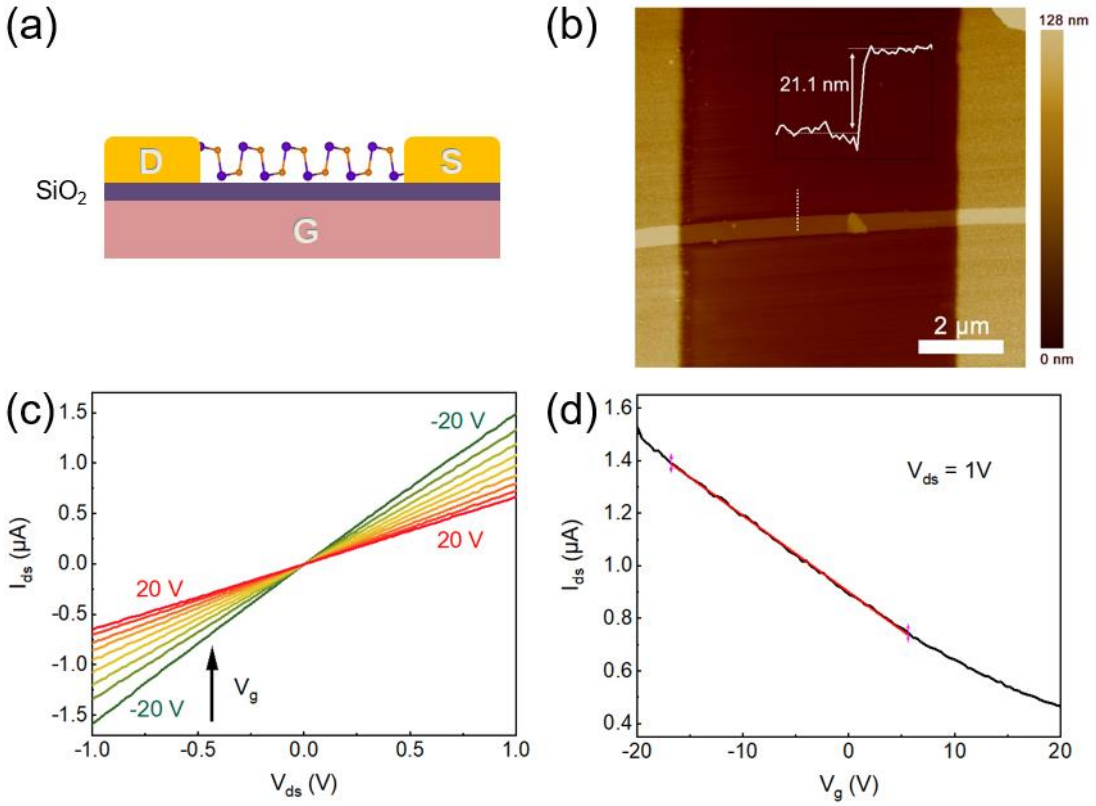

Figure 5. 17 Electronic measurement of SnS.

(a) Device structure. (b) AFM image (inset: hight curve of SnS nanosheet on SiO2 medium layer). (c) Output curves. (d) Transfer curve for Vds = 1 V (red line: fitting line).

Figure 5.17 (a) is the schematic diagram of the SnS based photodetector. Figure 5.17 (b) is an AFM image of the SnS device. The thicker left and right areas are the electrode areas, and the thinner strips in the lateral direction are the SnS crystals with thickness of about 21.1 nm. Figure 5.17 (c) is the output curves. The source-drain voltage is between -1 V and 1 V. The SnS device exhibits a strong field effect under the adjustment of the gate control voltage in the range of -20 V to 20 V. The I-V curve of the SnS device is straight and has good symmetry in the positive and negative bias region, indicating that there is a good ohmic contact between the gold electrode and the SnS crystal. In order to further analyze the electrical transport characteristics of the SnS device, Figure 5.17 (d) shows its transfer curve at a source-drain voltage of 1 V. The

SnS device exhibits P-type conduction behavior. In the range of -20 V to 20 V gate voltage, it mainly works in the linear region. The carrier mobility can be calculated by the following formular:

$$\mu = \frac{L}{WC_iV_{ds}} \cdot \frac{\partial I_{ds}}{\partial V_g} .$$

The red straight line in the transfer curve is the fitted line. According to the slope of the fitted line and the above formula, the field-effect hole mobility of SnS is about 37.55 $cm^2 \cdot V^{-1} \cdot s^{-1}$.

Figure 5.18 describes the optical and electrical properties of SnS devices. The photocurrent response (R_λ) reflects the intensity of the photocurrent response of the photodetector to unit light power and it is an important photoelectric performance index. The photocurrent response can be calculated according to the formula:

$$R_\lambda = \Delta I_{ph}/(P_\lambda S).$$

where ΔI_{ph} represents the photocurrent (I_{light}-I_{dark}), P_λ is the optical power density of incident light, and S is the effective area of the photodetector device. Figure 5.18 (a) is the photocurrent response with bias voltage under 450 nm, 638 nm, 808 nm, 1064 nm and 1550 nm wavelength lasers (the polarization direction of the laser is parallel to the zigzag direction of the SnS crystal). These wavelength ranges basically cover the band gap width of SnS nanosheets. The photocurrent response gradually weakens as the wavelength increases. Compared with other wavelengths, the photocurrent responses are negligible at 1064 nm and 1550 nm. The inset in Figure 5.18 (a) is the photocurrent response under 1 V bias voltage. It has a photocurrent responsivity of 310.5 A/W at 450 nm and 198.6 A/W at 808 nm. The external quantum efficiencies of the 450 nm and 808 nm are respectively 8.56×10^4% and 3.05×10^4%. In the I-V curve of Figure 5.18 (b), it can be seen that both the light and dark current are straight lines and are basically symmetrical in the positive and negative bias regions. Figure 5.18 (c) shows the light response switching curve of a period of 20 s. The device has good light response repeatability, but the second half of the light response will have a longer time lag, especially in the fall stage. We observed that the light on and off response times are 0.45 s and 3.14 s, respectively. Figure 5.18 (d) is the 808 nm photocurrent curve

controlled by the gate voltage under 1 V bias. With the increase of the gate voltage, the photocurrent response of the SnS nanosheets rises from 175.8 A/W to 298 A/W. Compare to SnS_2 crystal, SnS optoelectronic devices have a large dark current and a relatively long photo response time, but have a higher photo responsivity.

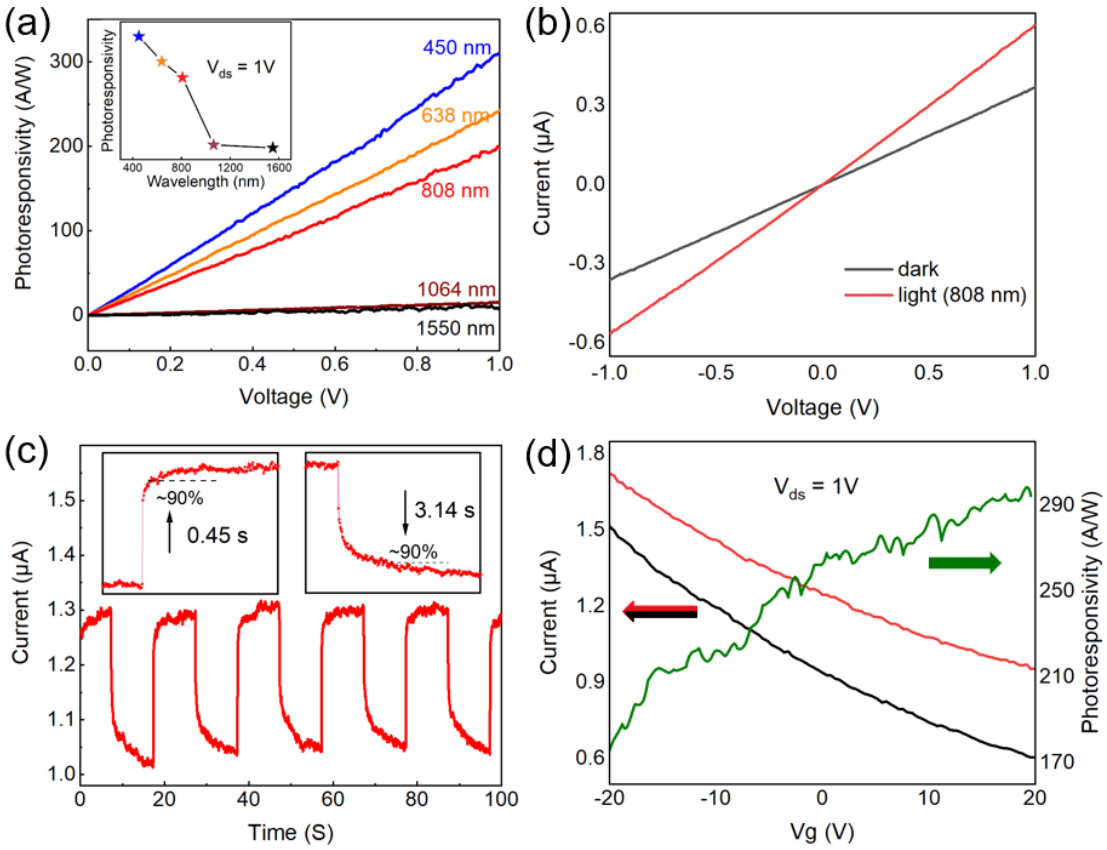

Figure 5. 18 Optoelectronic characteristics of SnS.

(a) Photoresponsivity for different incident light wavelengths (inset: photoresponsivity for the bias voltage of 1 V). (b) IV photoresponse for 808 nm laser. (c) Switching curve of photocurrent at 808 nm (inset: zoom-in curves of the rising and falling edges in a cycle). (d) Variations of photocurrents and photoresponsivity at 808 nm controlled by the gate voltage (black line: dark current, red line: light current, green line: photoresponsivity).

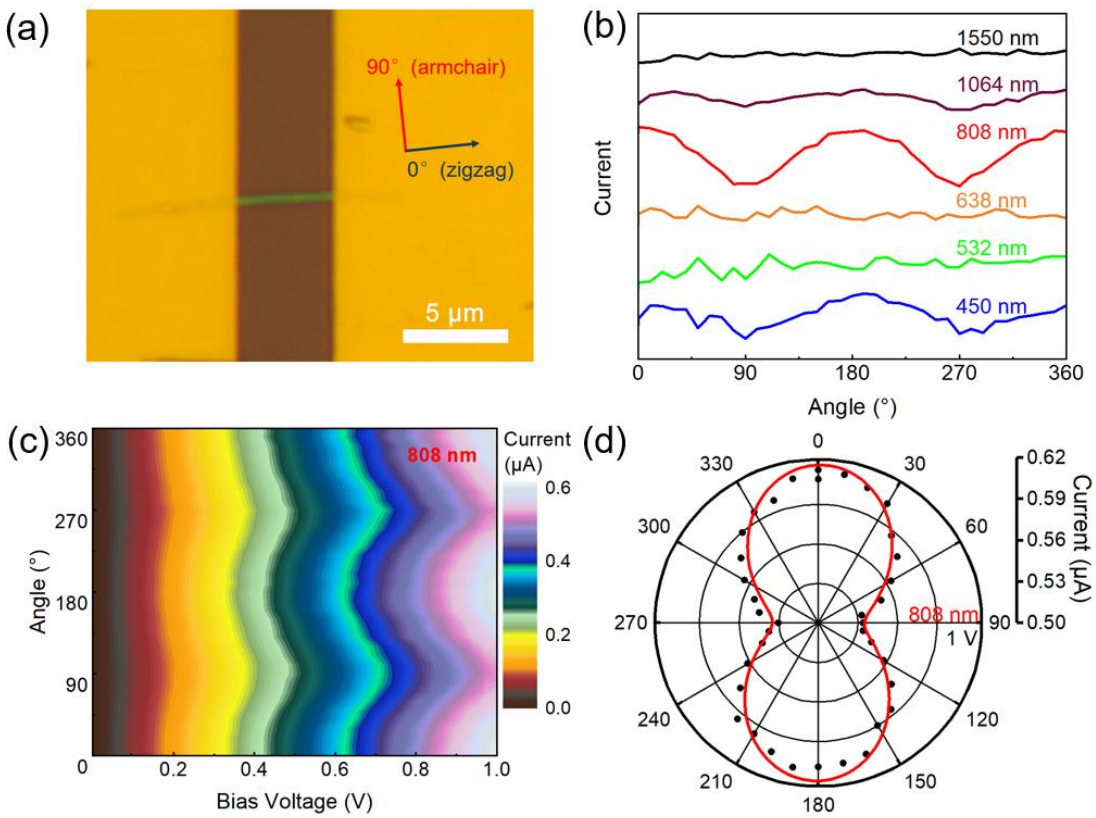

Figure 5. 19 Polarizd photoelectronic properties of SnS.

(a) Optical microscope image. (b) Polarized photoresponse curves of different wavelengths. (c) 2D colormap of photocurrent with the polarization angle of 808 nm incident light and bias voltage. (d) Polar coordinate curve of photocurrent with the polarization angle of 808 nm incident light under 1 V bias voltage (black dots: experimental data, red line: fitting curve).

Figure 5.19 (a) is the optical microscope picture of the SnS device. It shows the crystal orientation information determined according to the angle-resolved polarized Raman spectroscopy. The 0° and 90° directions correspond to the zigzag and armchair directions of the SnS lattice, respectively. The polarization direction of the incident light is consistent with the angle marked. In order to compare the polarization dependence of SnS nanosheets on the photocurrent of different wavelengths of light, figure 5.19 (b) plots the corresponding wavelengths (450 nm, 532 nm, 638 nm, 808 nm, 1064 nm and 1550 nm) under bias of 1 V. Figure 5.19 (c) shows the contour color map of the photocurrent with the polarization angle varies under 808 nm incident light. It exhibits the obvious photocurrent anisotropy. Figure 5.19 (d) is the polar coordinate diagram of

the angle-resolved polarization photocurrent under bias of 1 V. The black dots are the experimental data, and the red curve is the fitting curve by the formula:

$$I_{light}(\theta) = I_{max}\cos^2(\theta+\delta) + I_{min}\sin^2(\theta+\delta),$$

where I_{max} and I_{min} are the maximum and minimum values of the fitted photocurrent curve, and the angles of I_{max} and I_{min} in the fitting result are 0° and 90°, respectively. Compared with the introduction of the polarized light absorption spectrum section above, the fitting curves of the polarized light current at 808 nm and the polarized absorption spectrum are similar. Both have a maximum value in the zigzag direction (0°) and a minimum value in the armchair direction (90°). Compare the two values of dichroic and photocurrent anisotropy ratio, we can find the highest anisotropy ratio located at around 800nm. For the 808nm, the dichroic ratio is 1.75, while the photocurrent anisotropy ratio is 1.2.

5.2.3 Calculations

In order to analyze the anisotropic characteristics of SnS crystals, the local charge density of SnS was calculated by VASP. Figure 5.20 shows the distribution of SnS space charge density on the c-a (zigzag) and c-b (armchair) crystal planes at the edge of the conduction band and the edge of the valence band. It can be seen that the charge density distribution at VBM and CBM are obviously different. According to the Fermi Gold Rule:

$$P_{i\to f} = \frac{2\pi}{\hbar}\left|\langle\varphi_f|H_{eR}|\varphi_i\rangle\right|^2 \delta(E_f(k_f) - E_i(k_i) - \hbar\omega)$$

For a specific light absorption transition, the electron energy changes before and after the transition is fixed, and the transition probability $P_{v\to c}$ is related to the matrix element $\left|\langle\varphi_c|H_{eR}|\varphi_v\rangle\right|^2$. The transition matrix element can be expressed as

$$\left|\langle\varphi_c|H_{eR}|\varphi_v\rangle\right|^2 = \frac{|E|^2}{4q^2}\left|\int u^*_{c,k_c}\exp[i(q-k_c)r](ep)u_{v,k_v}\exp(ik_v r)\,dr\right|^2$$

Where $|\varphi_v\rangle$ and $|\varphi_c\rangle$ are the states in the valence band with energy E_v (wave vector k_v) and the state in the conduction band with energy E_c (wave vector k_c) before and after the light absorption transition of the electron. The wave functions in the two bands are denoted as $u_{v,k_v}\exp[i\,k_v r]$ and $u^*_{c,k_c}\exp[i(q-k_c)r]$, respectively. There is the following relationship between the wave function of electrons and the space charge density:

$$\rho(r) = q\cdot|\varphi(r)|^2$$

Therefore, the distribution of space charge density in Figure 5.20 reflects the distribution of the wave function, and the wave function is also completely different in the zigzag direction and the armchair direction. The theoretical results explain the observed strongest direction of absorption and photo response along the zigzag direction.

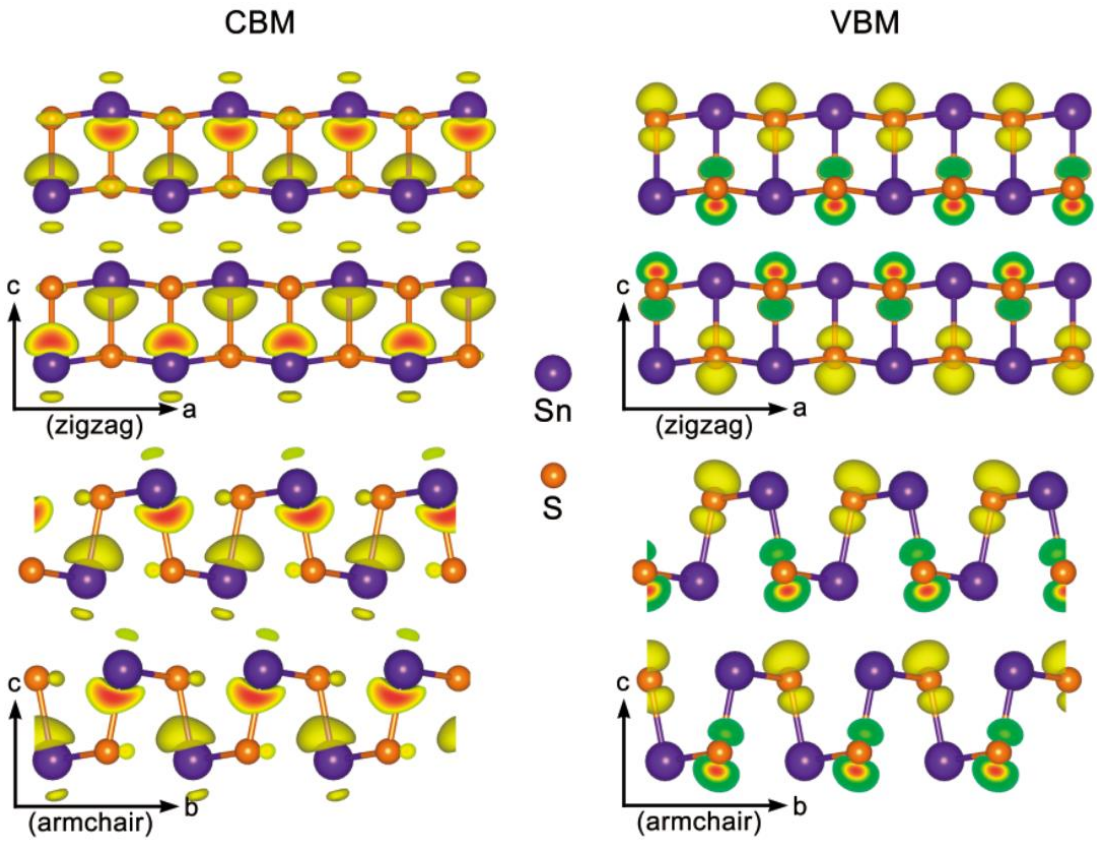

Figure 5. 20 Partial charge density in a (zigzag)-c and b (armchair)-c planes of SnS nanosheet at the state of CBM and VBM.

5.3 Conclusion

In summary, the 2D semiconductor alloy $Zn_xSn_{1-x}S_2$ with x = 0.17 have been investigated comprehensively. The XPS and EDS spectrums confirmed the element composition and element ratio of the alloy, the HRTEM and SAED images proved the high quality of alloy materials, while EDS mappings reveal the random arrangement of Zn, Sn and S atoms in the 2D alloys. The FETs based on $Zn_{0.17}Sn_{0.83}S_2$ alloy exhibited a clear photoelectronic effect with high carrier mobility of 65 cm^2 V^{-1} S^{-1} and photocurrent/ dark current ratio larger than 50. The First principle calculation results indicated the electric structure wasadjusted to direct band gap by doping Zn atoms into SnS_2. Our study suggests that $Zn_{0.17}Sn_{0.83}S_2$ is a high quality 2D semiconductor alloy material, which presents significant optoelectronics application prospects.

For SnS crystal, we have investigated the anisotropic crystal structure, optical characteristics, and optoelectronic properties of SnS nanosheets mechanically exfoliated from their bulk materials. Angle-resolved polarized Raman spectra revealed the anisotropy of SnS crystal structure, and could be used to nondestructively determine the crystal orientation. SnS nanosheets had a direct optical band gap of about 1.38 eV. The polarized optical absorption of SnS nanosheets presented the polarization sensitivity at the absorption edge, which had the wavelength selectivity in the meantime. The highest optical absorption dichroic ratio ($\alpha_{zigzag}/\alpha_{armchair}$) was approximately 3.06. Theoretical calculation qualitatively explained the polarization-dependent optical absorption. The SnS nanosheets based FETs had the carrier mobility of about 37.55 $cm^2 \cdot V^{-1} \cdot s^{-1}$ and photoresponsivity of 310.5 A/W under the 450 nm laser illumination. The photocurrent of the SnS device presented the obvious polarization dependence for 808 nm wavelength. Both polarized optical absorption and photocurrent had the maximum for the polarized direction along the zigzag direction and the minimum for the armchair direction. The anisotropy of optoelectronic properties of SnS nanosheets were mainly caused by the optical absorption characteristics. These studies reveal the potential of SnS applied to the polarized photodetection with specific wavelength.

Chapter 6: Summary and Prospects

6.1 Summary

This thesis focuses on the study of the polarization dependent photo-response of two-dimensional materials and the growth of Ta/CoFeB/MgO/MoS_2 heterostructure. The polarization anisotropy of GeAs and SnS and a large perpendicular magnetic anisotropy in Ta/CoFeB/MgO/MoS_2 heterojunction were demonstrated. The main results are presented in the following three parts:

A large perpendicular magnetic anisotropy in MgO/CoFeB/Ta on full coverage monolayer MoS_2:

We have reported the large out-of-plane magnetic anisotropy in the Ta/CoFeB/MgO structure on a fully covered monolayer MoS_2. After precise control of the CoFeB thickness and post-annealing procedure, a larger PMA was obtained. It was found that during the annealing process, inserting a thin insulating MgO can effectively prevent the metal diffusing into the 2D material. MgO can be crystallized into (001) bcc crystal on ML MoS_2. During the annealing at 300°C, the Ta layer showed a high efficiency of absorbing B from the CoFeB layer. This can prevent B from diffusing into the MgO barrier and destroying the ML MoS_2. All these factors ensure the large PMA established in our system. In addition, first-principles calculations have also been performed in the Fe/MgO/MoS_2 structure to understand the spin transport properties in this FM/oxide/2D system. Interestingly, it is found that the thickness of MgO can change the semiconductor performance of MoS_2, from the indirect band gap of 7MLs MgO to the direct band gap of 3MLs MgO. The 3ML MgO structure shows a proximity effect revealed by a Zememan splitting of 10 meV at the Γ point of the MoS_2 valence band. These findings indicate that the magnetic and semiconductor properties of MoS_2 can be adjusted by the thickness of MgO. Our experimental and theoretical results will promote the future development of room temperature spin optoelectronic devices based on 2D TMDCs with perpendicular magnetization spin injectors.

The optical properties of the polarization detector based on two-dimensional GeAs:

The photo response of the GeAs photodetector is studied. The polarization-dependent photocurrent mapping shows that the polarized photocurrent mainly occurs in the Schottky photodiodes. The Schottky junction also contributes to the improvement of the anisotropic photocurrent ratio of the polarization detector. It is found that the anisotropic photocurrent ratio is 4.4, which is larger than the dichroism (1.42) absorbed by the GeAs crystal itself under the irradiation of 830 nm linearly polarized laser. This is owing to the existence of the Schottky junction, which reduces the dark current of the device, and its built-in electric field enhances the carrier concentration. In summary, the excellent performance of GeAs crystal is a favorable material for the application of polarization detectors.

IV-VI Compounds based photodetectors:

We have investigated the crystal structure, optical characteristics, and optoelectronic properties of IV-VI Compounds, like $ZnSnS_2$ alloys and SnS nanosheets. For the $ZnSnS_2$ alloy, the carrier mobility of is 65 $cm^2 \cdot V^{-1} \cdot s^{-1}$ and the on/off ratio under the white LED illumination is as high as 51. For the SnS crystal, the photodetector based on SnS nanosheets exhibits the carrier mobility of 37.75 $cm^2 \cdot V^{-1} \cdot s^{-1}$, photoresponsivity of 310.5 A/W and external quantum efficiency of 8.56×10^4% at 450 nm. Optical absorption around the absorption edge presents obvious polarization sensitivity with the highest optical absorption dichroic ratio of 3.06 at 862 nm.

6.2 Prospects

Low-dimensional materials are widely used and are expected to produce ultra-thin, transparent, highly integrated optoelectronic devices with new functionalities. Among them, 2D materials with in-plane anisotropy are expected to be used as polarization detectors for the photosensitive pixels, and realizing a robust spin injector or detector with perpendicular magnetic anisotropy is a prerequisite to obtain a spin optoelectronic device based on 2D materials with zero applied magnetic field. The results in this thesis are promising for the following future developments:

1. For the MoS_2/MgO/CoFeB heterojunction film, it is expected to realize Spin LED and spin photodiode application in two-dimensional materials under zero magnetic field. Further, we will fabricate LED or photodiode structures with perpendicularly magnetized Ta/CoFeB/MgO for spin injection and detection.

2. For the low-dimensional semiconductor material GeAs, since the core structure of the polarization detector is a Schottky junction, we can increase the area of the Schottky junction by building interdigital electrodes to enhance the anisotropic photocurrent ratio. Furthermore, we will fabricate the GeAs array devices to realize a system for the application of polarization detection.

Reference

[1]L. Chen, J. C. Du, W. Zhou, H. Z. Shen, L. X. Tan, C. L. Zhou and L. C. Dong, Microwave-Assisted Solvothermal Synthesis of Covalent Organic Frameworks (COFs) with Stable Superhydrophobicity for Oil/Water Separation, Chem-Asian J,2020,15,21,3421-3427

[2]P. L. Cheung, S. K. Lee and C. P. Kubiak, Facile Solvent-Free Synthesis of Thin Iron Porphyrin COFs on Carbon Cloth Electrodes for CO2 Reduction, Chemistry of Materials,2019,31,6,1908-1919

[3]L. G. Christie, Captivating COFs, Nat Chem,2016,8,5,406-406

[4]X. Gao, Y. Dong, S. W. Li, J. W. Zhou, L. Wang and B. Wang, MOFs and COFs for Batteries and Supercapacitors, Electrochem Energy R,2020,3,1,81-126

[5]X. L. Hu, H. G. Li and B. E. Tan, COFs-based Porous Materials for Photocatalytic Applications, Chinese J Polym Sci,2020,38,7,673-684

[6]G. A. Leith, A. A. Berseneva, A. Mathur, K. C. Park and N. B. Shustova, A Multivariate Toolbox for Donor Acceptor Alignment: MOFs and COFs, Trends Chem,2020,2,4,367-382

[7]O. Yaghi, MOFs and COFs for carbon capture and conversion, Abstr Pap Am Chem S,2015,250,

[8]R. M. Zhu, J. W. Ding, L. Jin and H. Pang, Interpenetrated structures appeared in supramolecular cages, MOFs, COFs, Coordin Chem Rev,2019,389,119-140

[9]A. Dankert, B. Karpiak and S. P. Dash, Hall sensors batch-fabricated on all-CVD h-BN/graphene/h-BN heterostructures, Scientific Reports,2017,7,12277

[10]T. R. Fan, A. H. Hosseinnia, H. Moradinejad, A. A. Eftekhar and A. Adibi, Hybrid h-BN/Graphene/h-BN Silicon Device for Electro-optic Modulation, Conference on Lasers and Electro-Optics (Cleo),2018,

[11]P. Fu, J. Wang, R. Jia, S. Bibi, R. I. Eglitis and H. X. Zhang, Theoretical study on hydrogen storage capacity of expanded h-BN systems, Computational Materials

Science,2017,139,335-340

[12]Q. Huang, D. Yu, Z. Zhao, S. Fu, M. Xiong, Q. Wang, Y. Gao, K. Luo, J. He and Y. Tian, First-Principles Study of O-BN: A Sp^3-Bonding Boron Nitride Allotrope, J. Appl. Phys.,2012,112,053518

[13]C. Li, X. Yan, W. Z. Bao, S. J. Ding, D. W. Zhang and P. Zhou, Low sub-threshold swing realization with contacts of graphene/h-BN/MoS2 heterostructures in MoS2 transistors, Applied Physics Letters,2017,111,19,193502

[14]J. H. Los, J. M. H. Kroes, K. Albe, R. M. Gordillo, M. I. Katsnelson and A. Fasolino, Extended Tersoff potential for boron nitride: Energetics and elastic properties of pristine and defective h-BN, Physical Review B,2017,96,18,184108

[15]L. Cheng, C. Yuan, S. Shen, X. Yi, H. Gong, K. Yang and Z. Liu, Bottom-Up Synthesis of Metal-Ion-Doped WS(2) Nanoflakes for Cancer Theranostics, ACS Nano,2015,9,11,11090-101

[16]J. Biscaras, Z. Chen, A. Paradisi and A. Shukla, Onset of two-dimensional superconductivity in space charge doped few-layer molybdenum disulfide, Nat Commun,2015,6,8826

[17]J.-R. Chen, P. M. Odenthal, A. G. Swartz, G. C. Floyd, H. Wen, K. Y. Luo and R. K. Kawakami, Control of Schottky Barriers in Single Layer MoS_2 Transistors with Ferromagnetic Contacts, Nano Lett.,2013,13,7,3106-3110

[18]S. Das, H.-Y. Chen, A. V. Penumatcha and J. Appenzeller, High Performance Multilayer MoS_2 Transistors with Scandium Contacts, Nano Lett.,2012,13,1,100-105

[19]O. Lopezsanchez, D. Lembke, M. Kayci, A. Radenovic and A. Kis, Ultrasensitive photodetectors based on monolayer MoS2, Nat Nanotechnol,2013,8,7,497

[20]T. Cao, G. Wang, W. Han, H. Ye, C. Zhu, J. Shi, Q. Niu, P. Tan, E. Wang, B. Liu and J. Feng, Valley-selective circular dichroism of monolayer molybdenum disulphide, Nat. Commun.,2012,3,1,887

[21]Y. Yoon, K. Ganapathi and S. Salahuddin, How good can monolayer MoS(2) transistors be?, Nano Lett,2011,11,9,3768-73

[22]F. Schwierz, Graphene transistors, Nat Nanotechnol,2010,5,7,487-96

[23]K. Lee, H.-Y. Kim, M. Lotya, J. N. Coleman, G.-T. Kim and G. S. Duesberg,

Electrical Characteristics of Molybdenum Disulfide Flakes Produced by Liquid Exfoliation, Adv. Mater.,2011,23,36,4178-4182

[24]L. Liu, S. B. Kumar, Y. Ouyang and J. Guo, Performance Limits of Monolayer Transition Metal Dichalcogenide Transistors, IEEE Transactions on Electron Devices,2011,58,9,3042-3047

[25]Branimir Radisavljevic, Michael Brian Whitwick and A. Kis, Integrated Circuits and Logic Operations__Based on Single-Layer MoS_2, ACS Nano,2011,5,9934-9938

[26]W. Zhang, J. K. Huang, C. H. Chen, Y. H. Chang, Y. J. Cheng and L. J. Li, High-gain phototransistors based on a CVD MoS(2) monolayer, Adv Mater,2013,25,25,3456-61

[27]Y. Chen, C. Chen, R. Kealhofer, H. Liu, Z. Yuan, L. Jiang, J. Suh, J. Park, C. Ko, H. S. Choe, J. Avila, M. Zhong, Z. Wei, J. Li, S. Li, H. Gao, Y. Liu, J. Analytis, Q. Xia, M. C. Asensio and J. Wu, Black Arsenic: A Layered Semiconductor with Extreme In-Plane Anisotropy, Adv. Mater.,2018,30,1800754

[28]M. Zhong, Q. Xia, L. Pan, Y. Liu, Y. Chen, H.-X. Deng, J. Li and Z. Wei, Thickness-Dependent Carrier Transport Characteristics of a New 2D Elemental Semiconductor: Black Arsenic, Adv. Funct. Mater.,2018,1802581

[29]H. Yuan, X. Liu, F. Afshinmanesh, W. Li, G. Xu, J. Sun, B. Lian, A. Curto, G. Ye, Y. Hikita, Z. Shen, S. Zhang, X. Chen, M. Brongersma, H. Hwang and Y. Cui, Polarization-Sensitive Broadband Photodetector Using A Black Phosphorus Vertical P-N Junction, Nat. Nanotechnol.,2015,10,707-713

[30]M. Long, A. Gao, P. Wang, H. Xia, C. Ott, C. Pan, Y. Fu, E. Liu, X. Chen, W. Lu, T. Nilges, J. Xu, X. Wang, W. Hu and F. Miao, Room Temperature High-Detectivity Mid-Infrared Photodetectors Based on Black Arsenic Phosphorus, Sci. Adv.,2017,3,e1700589

[31]Z. Zhou, M. Long, L. Pan, X. Wang, M. Zhong, M. Blei, J. Wang, J. Fang, S. Tongay, W. Hu, J. Li and Z. Wei, Perpendicular Optical Reversal of the Linear Dichroism and Polarized Photodetection in 2D GeAs, ACS Nano,2018,12,12,12416−12423

[32]Y. C. Lin, H. P. Komsa, C. H. Yeh, T. Bjorkman, Z. Y. Liang, C. H. Ho, Y. S. Huang, P. W. Chiu, A. V. Krasheninnikov and K. Suenaga, Single-Layer ReS(2): Two-

Dimensional Semiconductor with Tunable In-Plane Anisotropy, ACS Nano,2015,9,11,11249-112457

[33]N. Tian, Y. Yang, D. Liu, X. Liu, P. H. Tan, D. Zhang, K. Chang, H. Li, M. Zhao, J. R. Li, X. Tang, D. Zhang, Z. Zhang, W. Xiao, H. Yan and Y. Zhang, High Anisotropy in Tubular Layered Exfoliated KP_{15}, ACS Nano,2018,12,2,1712-1719

[34]X. Wang, Y. Li, L. Huang, X. Jiang, L. Jiang, H. Dong, Z. Wei, J. Li and W. Hu, Short-Wave Near-Infrared Linear Dichroism of Two-Dimensional Germanium Selenide, J. Am. Chem. Soc.,2017,139,14976-14982

[35]R. Fiederling, M. Keim, G. Reuscher, W. Ossau, G. Schmidt, A. Waag and L. W. Molenkamp, Injection and detection of spin-polarized current in light- emitting diode, Nature,1999,402,790

[36]I. Appelbaum, B. Huang and D. J. Monsma, Electronic measurement and control of spin transport in silicon, Nature,2007,447,7142,295-8

[37]Y. Ohno, D. K. Young, B. Beschoten, F. Matsukura, H. Ohno and D. D. Awschalom, Electrical spin injection in a ferromagnetic semiconductor heterostructure, Nature,Nature,402,790

[38]Y. Ye, J. Xiao, H. Wang, Z. Ye, H. Zhu, M. Zhao, Y. Wang, J. Zhao, X. Yin and X. Zhang, Electrical generation and control of the valley carriers in a monolayer transition metal dichalcogenide, Nat. Nanotechnol.,2016,11,7,598-602

[39]O. L. Sanchez, D. Ovchinnikov, S. Misra, A. Allain and A. Kis, Valley Polarization by Spin Injection in a Light-Emitting van der Waals Heterojunction, Nano Lett.,2016,16,9,5792-5797

[40]G. Lampel, Nuclear Dynamic Polarization by Optical Electronic Saturation and Optical Pumping in Semiconductors, Physical Review Letters,1968,20,10,491-493

[41]D. T. Pierce and F. Meier, Photoemission of spin-polarized electrons from GaAs, Physical Review B,1976,13,12,5484-5500

[42]X. Gao, Spin injection into semiconductors and organic materials, Thèse,2019,Université de Lorraine,

[43]L. Xie and X. Cui, Manipulating spin-polarized photocurrents in 2D transition metal dichalcogenides, PNAS 2016,113,14

[44]S. Wang, Y. Rong, Y. Fan, M. Pacios, H. Bhaskaran, K. He and J. H. Warner, Shape Evolution of Monolayer MoS_2 Crystals Grown by Chemical Vapor Deposition, Adv. Mater.,2014,26,22,6371-6379

[45]L. H. Bo Li, Mianzeng Zhong, Nengjie Huo, Yongtao Li, Shengxue Yang, Chao Fan, Juehan Yang, Wenping Hu, Zhongming Wei, Jingbo Li, Synthesis and Transport Properties of Large-Scale Alloy Co0.16Mo0.84S2 Bilayer Nanosheets, ACS Nano,2015,9,2,1257

[46]B. Li, T. Xing, M. Zhong, L. Huang, N. Lei, J. Zhang, J. Li and Z. Wei, A two-dimensional Fe-doped SnS_2 magnetic semiconductor, Nat. Commun.,2017,8,1,1958

[47]K. F. Mak, C. Lee, J. Hone, J. Shan and T. F. Heinz, Atomically Thin MoS_2: A New Direct-Gap Semiconductor, Phys. Rev. Lett.,2010,105,13,136805

[48]B. Radisavljevic, A. Radenovic, J. Brivio, V. Giacometti and A. Kis, Single-layer MoS_2 transistors, Nat. Nanotechnol.,2011,6,3,147-150

[49]D. Xiao, G.-B. Liu, W. Feng, X. Xu and W. Yao, Coupled Spin and Valley Physics in Monolayers of MoS2and Other Group-VI Dichalcogenides, Phys. Rev. Lett.,2012,108,19,196802

[50]K. F. Mak, K. He, J. Shan and T. F. Heinz, Control of valley polarization in monolayer MoS_2 by optical helicity, Nat. Nanotechnol.,2012,7,8,494-498

[51]G. Sallen, L. Bouet, X. Marie, G. Wang, C. R. Zhu, W. P. Han, Y. Lu, P. H. Tan, T. Amand, B. L. Liu and B. Urbaszek, Robust optical emission polarization in MoS2monolayers through selective valley excitation Phys. Rev. B,2012,86,7,081301(R)

[52]H. Zeng, J. Dai, W. Yao, D. Xiao and X. Cui, Valley polarization in MoS_2 monolayers by optical pumping, Nat. Nanotechnol.,2012,7,8,490-493

[53]M. Xu, T. Liang, M. Shi and H. Chen, Graphene-Like Two-Dimensional Materials, Chem. Rev. ,2013,113,5,3766-3798

[54]K. Ko´smider, J. W. Gonz´alez and J. Fern´andez-Rossier, Large spin splitting in the conduction band of transition metal dichalcogenide monolayers, Phys. Rev. B,2013,88,245436

[55]W. Yang, J. Shang, J. Wang, X. Shen, B. Cao, N. Peimyoo, C. Zou, Y. Chen, Y. Wang, C. Cong, W. Huang and T. Yu, Electrically Tunable Valley-Light Emitting Diode

(vLED) Based on CVD-Grown Monolayer WS_2, Nano Lett.,2016,16,3,1560-1567

[56]H. Ochoa and R. Roldán, Spin-orbit-mediated spin relaxation in monolayer MoS_2, Phys. Rev. B 2013,87,24,245421

[57]M. Cardona, P. Fulde, K. v. Klitzing, R. Merlin, H.-J. Queisser and H. Störmer, Spin Physics in Semiconductors, Springer,2008,

[58]M. W. Wu, J. H. Jiang and M. Q. Weng, Spin dynamics in semiconductors, Phys. Rep.,2010,493,2-4,61-236

[59]L. Wang and M. W. Wu, Electron spin relaxation due to D'yakonov-Perel' and Elliot-Yafet mechanisms in monolayerMoS2: Role of intravalley and intervalley processes, Phys. Rev. B,2014,89,11,115302

[60]L. Wang and M. W. Wu, Electron spin diffusion in monolayerMoS_2, Phys. Rev. B,2014,89,20,205401

[61]M. I. Dyakonov and V. L. Perel, Optical orientation / F. Meier, B.P. Zakharchenya, Amsterdam,1984,8,22-24

[62]B. Huang, G. Clark, E. Navarro-Moratalla, D. R. Klein, R. Cheng, K. L. Seyler, D. Zhong, E. Schmidgall, M. A. McGuire, D. H. Cobden, W. Yao, D. Xiao, P. Jarillo-Herrero and X. Xu, Layer-dependent ferromagnetism in a van der Waals crystal down to the monolayer limit, Nature,2017,546,7657,270-273

[63]Z. Wang, D. Sapkota, T. Taniguchi, K. Watanabe, D. Mandrus and A. F. Morpurgo, Tunneling Spin Valves Based on Fe_3GeTe_2/hBN/Fe_3GeTe_2 van der Waals Heterostructures, Nano Lett.,2018,18,7,4303-4308

[64]W. Zhang, P. K. J. Wong, X. Zhou, A. Rath, Z. Huang, H. Wang, S. A. Morton, J. Yuan, L. Zhang, R. Chua, S. Zeng, E. Liu, F. Xu, Ariando, D. H. C. Chua, Y. P. Feng, G. van der Laan, S. J. Pennycook, Y. Zhai and A. T. S. Wee, Ferromagnet/Two-Dimensional Semiconducting Transition-Metal Dichalcogenide Interface with Perpendicular Magnetic Anisotropy, ACS Nano,2019,13,3353-2261

[65]H. Yang, A. D. Vu, A. Hallal, N. Rougemaille, J. Coraux, G. Chen, A. K. Schmid and M. Chshiev, Anatomy and Giant Enhancement of the Perpendicular Magnetic Anisotropy of Cobalt–Graphene Heterostructures, Nano Lett.,2015,16,1,145-151

[66]W. Wang, A. Narayan, L. Tang, K. Dolui, Y. Liu, X. Yuan, Y. Jin, Y. Wu, I. Rungger,

S. Sanvito and F. Xiu, Spin-Valve Effect in NiFe/MoS_2/NiFe Junctions, Nano Lett.,2015,15,8,5261-5267

[67]K. Dolui, A. Narayan, I. Rungger and S. Sanvito, Efficient spin injection and giant magnetoresistance inFe/MoS_2/Fejunctions, Phys. Rev. B,2014,90,4,041401

[68]T. Garandel, R. Arras, X. Marie, P. Renucci and L. Calmels, Electronic structure of the Co(0001)/MoS_2 interface and its possible use for electrical spin injection in a single MoS_2 layer, Phys. Rev. B,2017,95,7,075402

[69]A. Fert and H. Jaffrès, Conditions for efficient spin injection from a ferromagnetic metal into a semiconductor, Phys. Rev. B,2001,64,18,184420

[70]S. Liang, H. Yang, P. Renucci, B. Tao, P. Laczkowski, S. Mc-Murtry, G. Wang, X. Marie, J. M. George, S. Petit-Watelot, A. Djeffal, S. Mangin, H. Jaffres and Y. Lu, Electrical spin injection and detection in molybdenum disulfide multilayer channel, Nat. Commun.,2017,8,14947

[71]H. X. Yang, M. Chshiev, B. Dieny, J. H. Lee, A. Manchon and K. H. Shin, First-principles investigation of the very large perpendicular magnetic anisotropy at Fe|MgO and Co|MgO interfaces, Phys. Rev. B 2011,84,5,054401

[72]S. Ikeda, K. Miura, H. Yamamoto, K. Mizunuma, H. D. Gan, M. Endo, S. Kanai, J. Hayakawa, F. Matsukura and H. Ohno, A perpendicular-anisotropy CoFeB–MgO magnetic tunnel junction, Nat. Mater.,2010,9,9,721-724

[73]B. S. Tao, P. Barate, J. Frougier, P. Renucci, B. Xu, A. Djeffal, H. Jaffrès, J. M. George, X. Marie, S. Petit-Watelot, S. Mangin, X. F. Han, Z. G. Wang and Y. Lu, Electrical spin injection into GaAs based light emitting diodes using perpendicular magnetic tunnel junction-type spin injector, Appl. Phys. Lett.,2016,108,15,152404

[74]S. H. Liang, T. T. Zhang, P. Barate, J. Frougier, M. Vidal, P. Renucci, B. Xu, H. Jaffrès, J. M. George, X. Devaux, M. Hehn, X. Marie, S. Mangin, H. X. Yang, A. Hallal, M. Chshiev, T. Amand, H. F. Liu, D. P. Liu, X. F. Han, Z. G. Wang and Y. Lu, Large and robust electrical spin injection into GaAs at zero magnetic field using an ultrathin CoFeB/MgO injector, Phys. Rev. B 2014,90,8,085310

[75]B. Tao, P. Barate, X. Devaux, P. Renucci, J. Frougier, A. Djeffal, S. Liang, B. Xu, M. Hehn and H. Jaffres, Atomic-scale understanding of high thermal stability of the

Mo/CoFeB/MgO spin injector for spin-injection in remanence, Nanoscale,2018,10,10213-10220

[76]F. Cadiz, A. Djeffal, D. Lagarde, A. Balocchi, B. Tao, B. Xu, S. Liang, M. Stoffel, X. Devaux, H. Jaffres, J.-M. George, M. Hehn, S. Mangin, H. Carrere, X. Marie, T. Amand, X. Han, Z. Wang, B. Urbaszek, Y. Lu and P. Renucci, Electrical Initialization of Electron and Nuclear Spins in a Single Quantum Dot at Zero Magnetic Field, Nano Lett.,2018,18,4,2381-2386

[77]A. E. Giba, X. Gao, M. Stoffel, X. Devaux, B. Xu, X. Marie, P. Renucci, H. Jaffrès, J.-M. George, G. Cong, Z. Wang, H. Rinnert and Y. Lu, Spin Injection and Relaxation in p-Doped (In,Ga)As/GaAs Quantum-Dot Spin Light-Emitting Diodes at Zero Magnetic Field, Phys. Rev. Appl.,2020,14,3,034017

[78]P. Barate, S. Liang, T. T. Zhang, J. Frougier, M. Vidal, P. Renucci, X. Devaux, B. Xu, H. Jaffrès, J. M. George, X. Marie, M. Hehn, S. Mangin, Y. Zheng, T. Amand, B. Tao, X. F. Han, Z. Wang and Y. Lu, Electrical spin injection into InGaAs/GaAs quantum wells: A comparison between MgO tunnel barriers grown by sputtering and molecular beam epitaxy methods, Appl. Phys. Lett.,2014,105,1,012404

[79]Schulman, Daniel, S., Arnold, Andrew, J., Das and Saptarshi, Contact engineering for 2D materials and devices, Chem. Soc. Rev.,2018,47,3037

[80]Q. Ji, M. Kan, Y. Zhang, Y. Guo, D. Ma, J. Shi, Q. Sun, Q. Chen, Y. Zhang and Z. Liu, Unravelling Orientation Distribution and Merging Behavior of Monolayer MoS_2 Domains on Sapphire, Nano Lett.,2014,15,1,198-205

[81]H. Li, Q. Zhang, C. C. R. Yap, B. K. Tay, T. H. T. Edwin, A. Olivier and D. Baillargeat, From Bulk to Monolayer MoS_2: Evolution of Raman Scattering, Adv. Funct. Mater. ,2012,22,7,1385-1390

[82]T. Zhu, Y. Yang, R. C. Yu, H. Ambaye, V. Lauter and J. Q. Xiao, The study of perpendicular magnetic anisotropy in CoFeB sandwiched by MgO and tantalum layers using polarized neutron reflectometry, Appl. Phys. Lett.,2012,100,20,202406

[83]Y. Jang, C. Nam, K.-S. Lee, B. K. Cho, Y. J. Cho, K.-S. Kim and K. W. Kim, Variation in the properties of the interface in a CoFeB⁄MgO⁄CoFeB tunnel junction during thermal annealing, Appl. Phys. Lett.,2007,91,10,102104

[84]E. D. Whitney , R. F. and G. Jun., Reaction of Platinum and Boron under Pressure, Nature,1963,197,1293

[85]Q. Yan, T. Kim, A. Purkayastha, P. G. Ganesan, M. Shima and G. Ramanath, Enhanced Chemical Ordering and Coercivity in FePt Alloy Nanoparticles by Sb-Doping, Adv. Mater. ,2005,17,18,2233-2237

[86]G. Kresse and J. Hafner, Ab initio molecular-dynamics simulation of the liquid-metal–amorphous-semiconductor transition in germanium, Phys. Rev. B,1994,49,20,14251-14269

[87]G. Kresse and J. Furthmu¨ller, Efficient iterative schemes for ab initio total-energy calculations using a plane-wave basis set, Phys. Rev. B,1996,54,16

[88]P. E. Blöchl, Projector augmented-wave method, Phys. Rev. B,1994,50,24,17953-17979

[89]J. P. Perdew, K. Burke and M. Ernzerhof, Generalized Gradient Approximation Made Simple, Phys. Rev. Lett. ,1996,77,3865

[90]H. J. Monkhorst and J. D. Pack, Special points for Brillouin-zone integrations, Phys. Rev. B 1976,13,12,5188-5192

[91]S. Grimme, S. Ehrlich and L. Goerigk, Effect of the damping function in dispersion corrected density functional theory, J. Comp. Chem. ,2011,32,7,1456-1465

[92]S. Grimme, J. Antony, S. Ehrlich and H. Krieg, A consistent and accurate ab initio parametrization of density functional dispersion correction (DFT-D) for the 94 elements H-Pu, J. Chem. Phys. ,2010,132,15,154104

[93]H. B. Michaelson, Work function of elements and its periodicity, J Appl Phys.,1977,48,11,4729-4733

[94]Y. Lu, J. C. Le Breton, P. Turban, B. Lépine, P. Schieffer and G. Jézéquel, Band structure of the epitaxial Fe/MgO/GaAs(001) tunnel junction studied by x-ray and ultraviolet photoelectron spectroscopies, Appl. Phys. Lett. ,2006,89,15,152106

[95]S. Liang, H. Yang, A. Djeffal, B. Tao, S. Mc-Murtry, S. Mangin and Y. Lu, Electrical transport properties of black phosphorus based field-effect transistor with Au/Co/MgO tunneling contacts, J. Appl. Phys. ,2017,122,16,164301

[96]W., H., Butler, X.-G., Zhang, T., C., Schulthess, J. and M., Spin-dependent

tunneling conductance ofFe|MgO|Fesandwiches, Phys. Rev. B,2001,63,5,54416-54416

[97]G. Konstantatos, I. Howard, A. Fischer, S. Hoogland, J. Clifford, E. Klem, L. Levina and E. H. Sargent, Ultrasensitive Solution-Cast Quantum Dot Photodetectors, Nature,2006,442,180-183

[98]S. A. McDonald, G. Konstantatos, S. Zhang, P. W. Cyr, E. J. Klem, L. Levina and E. H. Sargent, Solution-Processed PbS Quantum Dot Infrared Photodetectors and Photovoltaics, Nat. Mater.,2005,4,138-142

[99]T. Mueller, F. Xia and P. Avouris, Graphene Photodetectors For High-Speed Optical Communications, Nat. Photon.,2010,4,297-301

[100]M. Zhong, X. Wang, S. Liu, B. Li, L. Huang, Y. Cui, J. Li and Z. Wei, High-Performance Photodetectors Based on Sb_2S_3 Nanowires: Wavelength Dependence and Wide Temperature Range Utilization, Nanoscale,2017,9,34,12364-12371

[101]H. Pettersson, J. Trägårdh, A. I. Persson, L. Landin, D. Hessman and L. Samuelson, Infrared Photodetectors in Heterostructure Nanowires, Nano Lett.,2006,6,229-232

[102]C. Soci, A. Zhang, B. Xiang, S. Dayeh, D. Aplin, J. Park, X. Bao, Y. Lo and D. Wang, ZnO Nanowire UV Photodetectors with High Internal Gain, Nano Lett.,2007,7,1003-1009

[103]Y. Liu, R. Cheng, L. Liao, H. Zhou, J. Bai, G. Liu, L. Liu, Y. Huang and X. Duan, Plasmon Resonance Enhanced Multicolour Photodetection by Graphene, Nat. Commun.,2011,2,579

[104]X. Li, W. Cai, J. An, S. Kim, J. Nah, D. Yang, R. Piner, A. Velamakanni, I. Jung, E. Tutuc, S. S. Banerjee, L. Colombo and R. Ruoff, Large-Area Synthesis of High-Quality and Uniform Graphene Films on Copper Foils, Science,2009,324,1312-1314

[105]Y. Cui, B. Li, J. Li and Z. Wei, Chemical Vapor Deposition Growth of Two-Dimensional Heterojunctions, Sci. China-Phys. Mech. Astron.,2018,61,016801

[106]E. Zhang, P. Wang, Z. Li, H. Wang, C. Song, C. Huang, Z. Chen, L. Yang, K. Zhang, S. Lu, W. Wang, S. Liu, H. Fang, X. Zhou, H. Yan, J. Zou, X. Wan, P. Zhou, W. Hu and F. Xiu, Tunable Ambipolar Polarization-Sensitive Photodetectors Based on High-Anisotropy $ReSe_2$ Nanosheets, ACS Nano,2016,10,8,8067-8077

[107]D. Zheng, H. Fang, P. Wang, W. Luo, F. Gong, J. Ho, X. Chen, W. Lu, L. Liao, J.

Wang and W. Hu, High-Performance Ferroelectric Polymer Side-Gated CdS Nanowire Ultraviolet Photodetectors, Adv. Funt. Mater.,2016,26,7690-7696

[108]P. Venuthurumilli, P. Ye and X. Xu, Plasmonic Resonance Enhanced Polarization-Sensitive Photodetection by Black Phosphorus in Near Infrared, ACS Nano,2018,12,4861-4867

[109]J. Wang, M. Gudiksen, X. Duan, Y. Cui and C. Lieber, Highly Polarized Photoluminescence and Photodetection From Single Indium Phosphide Nanowires, Science,2001,293,1455-1457

[110]S. Niu, G. Joe, H. Zhao, Y. Zhou, T. Orvis, H. Huyan, J. Salman, K. Mahalingam, B. Urwin, J. Wu, Y. Liu, T. E. Tiwald, S. B. Cronin, B. M. Howe, M. Mecklenburg, R. Haiges, D. J. Singh, H. Wang, M. A. Kats and J. Ravichandran, Giant Optical Anisotropy in A Quasi-One-Dimensional Crystal, Nat. Photon.,2018,12,392-396

[111]Q. Wang, K. Kalantar-Zadeh, A. Kis, J. N. Coleman and M. S. Strano, Electronics And Optoelectronics of Two-Dimensional Transition Metal Dichalcogenides, Nat. Nanotechnol.,2012,7,699-712

[112]C. Wang, Q. He, U. Halim, Y. Liu, E. Zhu, Z. Lin, H. Xiao, X. Duan, Z. Feng, R. Cheng, N. Weiss, G. Ye, Y. C. Huang, H. Wu, H. C. Cheng, I. Shakir, L. Liao, X. Chen, W. A. Goddard, III, Y. Huang and X. Duan, Monolayer Atomic Crystal Molecular Superlattices, Nature,2018,555,231-236

[113]K. S. Novoselov, A. K. Geim, S. V. Morozov, D. Jiang, M. I. Katsnelson, I. V. Grigorieva, S. V. Dubonos and A. A. Firsov, Two-Dimensional Gas of Massless Dirac Fermions in Graphene, Nature,2005,438,197-200

[114]X. Wang, A. Jones, K. Seyler, V. Tran, Y. Jia, H. Zhao, H. Wang, L. Yang, X. Xu and F. Xia, Highly Anisotropic And Robust Excitons In Monolayer Black Phosphorus, Nat. Nanotechnol.,2015,10,6,517-521

[115]M. Zhong, K. Zhou, Z. Wei, Y. Li, T. Li, H. Dong, L. Jiang, J. Li and W. Hu, Highly Anisotropic Solar-Blind UV Photodetector Based on Large-Size Two-Dimensional α-MoO_3 Atomic Crystals, 2D Mater.,2018,5,035033

[116]M. Amani, E. Regan, J. Bullock, G. H. Ahn and A. Javey, Mid-Wave Infrared Photoconductors Based on Black Phosphorus-Arsenic Alloys, ACS

Nano,2017,11,11,11724-11731

[117]F. Liu, S. Zheng, X. He, A. Chaturvedi, J. He, W. L. Chow, T. R. Mion, X. Wang, J. Zhou, Q. Fu, H. J. Fan, B. K. Tay, L. Song, R.-H. He, C. Kloc, P. M. Ajayan and Z. Liu, Highly Sensitive Detection of Polarized Light Using Anisotropic 2D ReS_2, Adv. Funt. Mater.,2016,26,1169-1177

[118]B. Liu, M. Kopf, A. N. Abbas, X. Wang, Q. Guo, Y. Jia, F. Xia, R. Weihrich, F. Bachhuber, F. Pielnhofer, H. Wang, R. Dhall, S. B. Cronin, M. Ge, X. Fang, T. Nilges and C. Zhou, Black Arsenic-Phosphorus: Layered Anisotropic Infrared Semiconductors with Highly Tunable Compositions and Properties, Adv. Mater.,2015,27,4423-4429

[119]S. Y. Kang, Y. S. Yoon, N. W. Park, W. Y. Lee, G. S. Kim, Y. G. Yoon, J. H. Koh, S. M. Koo, A. Umar and S. K. Lee, Electrical Properties of Exfoliated Multilayer Germanium Selenide (GeSe) Nanoflake Field-Effect Transistors, Sci Adv Mater,2018,10,11,1596-1600

[120]X. S. Lv, W. Wei, C. Mu, B. B. Huang and Y. Dai, Two-dimensional GeSe for high performance thin-film solar cells, Journal of Materials Chemistry A,2018,6,12,5032-5039

[121]K. Lee, S. Kamali, T. Ericsson, M. Bellard and K. Kovnir, GeAs: Highly Anisotropic van der Waals Thermoelectric Material, Chem. Mater.,2016,28,2776-2785

[122]J. Guo, Y. Liu, Y. Ma, E. Zhu, S. Lee, Z. Lu, Z. Zhao, C. Xu, S. J. Lee, H. Wu, K. Kovnir, Y. Huang and X. Duan, Few-Layer GeAs Field-Effect Transistors and Infrared Photodetectors, Adv. Mater.,2018,30,1705934

[123]S. Yang, Y. Yang, M. Wu, C. Hu, W. Shen, Y. Gong, L. Huang, C. Jiang, Y. Zhang and P. M. Ajayan, Highly In-Plane Optical and Electrical Anisotropy of 2D Germanium Arsenide, Adv. Funt. Mater.,2018,28,1707379

[124]W. A. Eaton and J. Hofrichter, Polarized Absorption and Linear Dichroism Spectroscopy of Hemoglobin, Method. Enzymol.,1981,76,175-261

[125]J. Qiao, X. Kong, Z. X. Hu, F. Yang and W. Ji, High-Mobility Transport Anisotropy and Linear Dichroism in Few-Layer Black Phosphorus, Nat. Commun.,2014,5,4475

[126]L. Huang, L. Tao, K. Gong, Y. Li, H. Dong, Z. Wei and J. Li, Role of Defects in

Enhanced Fermi Level Pinning at Interfaces Between Metals and Transition Metal Dichalcogenides, Phys. Rev. B,2017,96,20,205303

[127]L. Huang, B. Li, M. Zhong, Z. Wei and J. Li, Tunable Schottky Barrier at $MoSe_2$/Metal Interfaces with a Buffer Layer, J. Phys. Chem. C 2017,121,9305-9311

[128]G. Kresse and D. Joubert, From Ultrasoft Pseudopotentials to the Projector Augmented-Wave Method, Phys. Rev. B,1999,59,1758-1775

[129]L. Zhou, Y. Guo and J. Zhao, GeAs and SiAs Monolayers: Novel 2D Semiconductors With Suitable Band Structures, Phys. E.,2018,95,149-153

[130]X. Zhang, Q. H. Tan, J. B. Wu, W. Shi and P. H. Tan, Review on the Raman spectroscopy of different types of layered materials, Nanoscale,2016,8,12,6435-50

[131]H. B. Ribeiro, M. A. Pimenta and C. J. S. Matos, Raman spectroscopy in black phosphorus, J. Raman. Spectrosc.,2018,49,1,76-90

[132]T. Sriv, K. Kim and H. Cheong, Low-Frequency Raman Spectroscopy of Few-Layer 2H-SnS2, Sci. Rep.,2018,8,1,10194

[133]N. Prasad and B. Karthikeyan, A Raman spectral probe on polar w-ZnS nanostructures and surface optical phonon modes in nanowires, Nanoscale,2019,11,11,4948-4958

[134]L. J. Allen, A. J. D'Alfonso, B. Freitag and D. O. Klenov, Chemical mapping at atomic resolution using energy-dispersive x-ray spectroscopy, Mrs. Bull.,2012,37,1,47-52

[135]F. Ricci, W. Chen, U. Aydemir, G. J. Snyder, G. M. Rignanese, A. Jain and G. Hautier, An ab initio electronic transport database for inorganic materials, Sci. Data.,2017,4,6,170085

[136]H. R. Fuh, C. R. Chang, Y. K. Wang, R. F. Evans, R. W. Chantrell and H. T. Jeng, Newtype single-layer magnetic semiconductor in transition-metal dichalcogenides VX2 (X = S, Se and Te), Sci. Rep.,2016,6,9,32625

[137]J. Yuan, Q. Xie, N. Yu and J. Wang, Surface regulated arsenenes as Dirac materials: From density functional calculations, Appl. Surf. Sci.,2017,394,10,625-629

[138]A. Ryabov, I. Akhatov and P. Zhilyaev, Neural network interpolation of exchange-correlation functional, Sci. Rep.,2020,10,1,8000

[139]L. Huang, M. Zhong, H. Deng, B. Li, Z. Wei, J. Li and S. Wei, The Coulomb interaction in van der Waals heterostructures, Sci. China. Phys. Mech.,2018,62,3,037311

[140]A. J. Smith, P. E. Meek and W. Y. Liang, Raman scatterig studies of SnS_2 and $SnSe_2$, J. Phys. C: Solid State Phys.,1977,10,1321-1333

[141]Y. Huang, X. Chen, D. Zhou, H. Liu, C. Wang, J. Du, L. Ning and S. Wang, Stabilities, Electronic and Optical Properties of SnSe2(1–x)S2xAlloys: A First-Principles Study, J. Phys.Chem. C,2016,120,10,5839-5847

Appendix I Contents of Published articles

1. **Zhou, Ziqi**[§]; Long, Mingsheng[§]; Pan, Longfei.; Wang, Xiaoting.; Zhong，Mianzeng; Blei, Mark; Wang, Jianlu; Tongay, Sefaattin; Hu, Weida; Li, Jingbo; Wei, Zhongming; Perpendicular Optical Reversal of the Linear Dichroism and Polarized Photodetection in 2D GeAs. *ACS Nano* **2018**, *12* (12), 12416−12423. (Co-first-author)
2. **Zhou, Ziqi**; Cui, Yu; Tan, Pingheng; Liu, Xuelu; Wei, Zhongming; Optical and Electrical Properties of Two-dimensional Anisotropic Materials. *J. Semicond.* **2019**, *40* (6), 061001.
3. **Zhou, Ziqi**; Cui, Yu; Deng, Huixiong.; Huang, Le; Wei, Zhongming; Li, Jingbo; Modulation of Electronic and Optical Properties in Mixed Halide Perovskites $CsPbCl_{3x}Br_{3(1-x)}$ and $CsPbBr_{3x}I_{3(1-x)}$. *Appl. Phys. Lett.* **2017**, *110* (11), 113901.
4. **Zhou, Ziqi**; Paul, Marcon; Xavier, Devaux; Lionel, Calmels; Phillipe, Pigeat; Alexandre, Bouché; Sylvie, Migot; Abdallah, Jaafar; Remi, Arras; Michel, Vergnat; Lei Ren; Cedric Robert; Xavier Marie; Jean-Marie George; Henri-Yves Jaffrès; Mathieu Stoffel; Hervé Rinnert; Zhongming Wei; Pierre Renucci; Yuan Lu; Large Perpendicular Magnetic Anisotropy in Ta/CoFeB/MgO Structure on Full Coverage Monolayer MoS_2. *ACS Appl. Mater. Interfaces* **2021**, *13* (27), 32579-32589.
5. Cui, Yu[§]; **Zhou, Ziqi**[§]; Wang , Xiaoting; Ren, Zhihui; Pan Longfei, Yang Juehan; Wavelength-selectivity Polarization Dependence of Optical Absorption and Photoresponse in SnS Nanosheets. *Nano Res.* **2021**, *14* (7), 2224-2230.（Co-first-author）
6. Cui, Yu; **Zhou, Ziqi**.; Li, Tao; Wang, Kaiyou; Li, Jingbo; Wei, Zhongming, Versatile Crystal Structures and (Opto)electronic Applications of the 2D Metal Mono-, Di-, and Tri-Chalcogenide Nanosheets. *Adv. Funct. Mater.* **2019**, *29* (24), 1900040.
7. Fang, Jingzhi; **Zhou, Ziqi**; Xiao, Mengqi; Lou, Zheng; Wei, Zhongming; Shen, Guozhen; Recent Advances in Low-dimensional Semiconductor Nanomaterials and

Their Applications in High-performance Photodetectors. *InfoMat.* **2020**, *2* (10), 291-317.

8. Yang, Juehan; **Zhou, Ziqi;** Fang, Jingzhi; Wen, Hongyu; Lou, Zheng; Shen, Guozhen; Wei, Zhongming; Magnetic and Transport Properties of a Ferromagnetic Layered Semiconductor $MnIn_2Se_4$. *Appl. Phys. Lett*. **2019**, *115* (22), 222101.
9. Yang, Huai; Pan, Longfei; Wang, Xiaoting; Deng, Huixiong; Zhong, Mianzeng; **Zhou, Ziqi**; Lou, Zheng; Shen, Guozhen; Wei, Zhongming; Mixed-Valence-Driven Quasi-1D $Sn^{II}Sn^{IV}S_2$ with Highly Polarization-Sensitive UV-vis-NIR Photoresponse. *Adv. Funct. Mater*. **2019**, *29* (38), 1904416.
10. Li, Yongtao; Huang, Le; Li, Bo; Wang, Xiaoting; **Zhou, Ziqi**; Li, Jingbo; Wei, Zhongming; Co-Nucleus 1D/2D Heterostructures with Bi_2S_3 Nanowire and MoS_2 Monolayer:One-Step Growth and Its Defect-Induced Formation Mechanism. *ACS Nano* **2016**, *10* (9), 8938-8946.